Thermal Radiation, Scaling and Flame Stability in Semi-Industrial Oxyfuel Combustion

Vom Fachbereich Maschinenbau
an der Technischen Universität Darmstadt
zur
Erlangung des Grades eines Doktor-Ingenieurs (Dr.-Ing.)
genehmigte

Dissertation

vorgelegt von

M.Sc. Marcel Richter

aus Göppingen

Erstgutachter:	Prof. Dr.-Ing. Bernd Epple
Zweitgutachter:	Apl. Prof. Dr.-Ing. Martin Schiemann
Tag der Einreichung:	09.10.2024
Tag der mündlichen Prüfung:	10.12.2024

Darmstadt 2024

D17

Richter, Marcel: *Thermal Radiation, Scaling and Flame Stability in Semi-Industrial Oxyfuel Combustion*

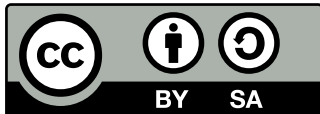Darmstadt, Technische Universität Darmstadt,

Jahr der Veröffentlichung der Dissertation auf TUprints: 2025

URN: urn:nbn:de:tuda-tuprints-289702

Tag der mündlichen Prüfung: 10.12.2024

"Essentially, all models are wrong, but some are useful."

– George Edward Pelham Box

Abstract

The oxyfuel technology enables combustion processes producing exhaust gases consisting almost entirely of CO_2. Thus, CO_2 can be efficiently captured from the combustion off-gases by using Carbon Capture and Storage (CCS) to prevent CO_2 from being emitted into earth's atmosphere. Compared to conventional firing with air, the main gas component is CO_2, which has different material properties than N_2 and therefore changes the combustion characteristics. This concerns, e.g. the ignition behavior of the fuel, the pollutant emissions and the heat transfer. Especially the heat transfer changes due to the strongly absorbing properties of CO_2 in the thermal spectrum. While many studies investigated this combustion process on a laboratory scale using coal as fuel, a semi-industrial scale is considered here for the combustion of pulverized biomass under oxyfuel conditions.

First, an existing laboratory oxyfuel burner was scaled up to a semi-industrial size. Numerical simulations and dimensionless quantities were used for this purpose. Based on the geometric results of this procedure, a $500\,kW_{th}$ burner was manufactured and installed in a semi-industrial combustion chamber. The results suggest that regardless of the fuel, a strong recirculation zone near the burner is important to aerodynamically stabilize the flame. This means that all combustion parameters, such as a higher thermal power or less O_2 content in the oxidant, which both lead to a higher momentum ratio between secondary and primary flow, intensify the recirculation zone. Also, the velocity of the secondary stream should be high enough to carry the particles. However, the O_2 content in the oxidant cannot be reduced arbitrarily. CO emissions increase significantly for biomass below $27\,vol\%$, whereas coal requires lower O_2 enrichment in the oxidant. It is assumed that this is mainly due to the smaller particles of the coal.

A heat flux sensor was used to measure the radiative heat flux in absolute terms at the combustion chamber wall. The combustion of biomass shows a higher radiative heat flux for all O_2 concentrations in the case of oxyfuel than in the case of combustion with air. For lignite, on the other hand, the measurement results for oxyfuel are all below those of air combustion. When comparing the thermal radiation of biomass and lignite, the biomass shows significantly higher radiative heat transfer; it is assumed that the higher volatile content in the biomass leads to a stronger local heat release and therefore a higher radiative heat flux. In case of a natural gas flame, the radiative heat flux for all oxyfuel conditions is higher than for air-firing. This can probably be attributed to a local displacement of the main reaction zone.

In order to efficiently calculate the radiative exchange in oxyfuel combustion with numerical simulations, several gas radiation models were implemented and tested in the open-source code OpenFOAM®. The Full Spectrum Correlated-k (FSCK) and Weighted Sum of Gray Gases (WSGG) models showed good approximations of the wall-incident radiative heat flux with the measured data in the combustion chamber, whereby the WSGG has a lower computing time than the FSCK.

I

Kurzfassung

Die Oxyfuel-Technologie ermöglicht Verbrennungsprozesse, bei denen die Abgase fast vollständig aus CO_2 bestehen. Daher kann das CO_2 aus den Verbrennungsabgasen durch Carbon Capture and Storage (CCS) Verfahren effizient abgeschieden werden, um zu verhindern, dass CO_2 in die Erdatmosphäre gelangt. Im Vergleich zur herkömmlichen Verbrennung mit Luft ist die Hauptgaskomponente CO_2, welche andere Materialeigenschaften als N_2 aufweist und daher die Verbrennungseigenschaften verändert. Dies betrifft z.B. das Zündverhalten des Brennstoffs, die Schadstoffemissionen und die Wärmeübertragung. Insbesondere die Wärmeübertragung verändert sich aufgrund der stark absorbierenden Eigenschaften von CO_2 im thermischen Spektrum. Während viele Studien diesen Verbrennungsprozess im Labormaßstab mit Kohle als Brennstoff untersuchten, wird hier ein halbindustrieller Maßstab für die Verbrennung von gemahlener Biomasse unter Oxyfuel-Bedingungen betrachtet.

Zunächst wurde ein bestehender Oxyfuel-Laborbrenner auf eine halbindustrielle Größe skaliert. Hierfür wurden numerische Simulationen und dimensionslose Größen verwendet. Auf Grundlage der geometrischen Ergebnisse dieses Verfahrens wurde ein $500\,kW_{th}$-Brenner hergestellt und in einer halbindustriellen Brennkammer installiert. Die Ergebnisse deuten darauf hin, dass unabhängig vom Brennstoff eine starke Rezirkulationszone in der Nähe des Brenners für die aerodynamische Stabilisierung der Flamme maßgebend ist. Dies bedeutet, dass alle Verbrennungsparameter, wie z.B. eine höhere thermische Leistung oder ein geringerer O_2-Gehalt im Oxidationsmittel, die beide zu einem höheren Impulsverhältnis zwischen Sekundär- und Primärstrom führen, die Rezirkulationszone verstärken. Außerdem sollte die Geschwindigkeit des Sekundärstroms hoch genug sein, um die Partikel zu tragen. Der O_2-Gehalt im Oxidationsmittel kann jedoch nicht beliebig reduziert werden. CO-Emissionen nehmen bei Biomasse unterhalb von $27\,vol\%$ deutlich zu, während Kohle eine geringere O_2-Anreicherung im Oxidationsmittel erfordert. Es wird angenommen, dass dies hauptsächlich auf die kleineren Partikel der Kohle zurückzuführen ist.

Ein Wärmestromsensor wurde zur Messung des absoluten Strahlungswärmestroms an der Brennkammerwand verwendet. Bei der Verbrennung von Biomasse ist der Strahlungswärmestrom bei allen O_2-Konzentrationen im Falle von Oxyfuel höher als bei der Verbrennung mit Luft. Bei Braunkohle hingegen liegen die Messergebnisse für Oxyfuel durchweg unter denen der Luftverbrennung. Beim Vergleich der Wärmestrahlung von Biomasse und Braunkohle zeigt die Biomasse einen deutlich höheren Strahlungswärmestrom; es wird angenommen, dass der höhere Gehalt an flüchtigen Bestandteilen in der Biomasse zu einer stärkeren lokalen Wärmefreisetzung und damit zu einem höheren Strahlungswärmestrom führt. Bei einer Erdgasflamme ist der Strahlungswärmestrom bei allen Oxyfuel-Bedingungen höher als bei der Luftfeuerung. Dies kann vermutlich auf eine lokale Verschiebung der Hauptreaktionszone zurückgeführt werden.

Um den Strahlungsaustausch bei der Oxyfuel-Verbrennung mit numerischen Simulationen ef-

fizient berechnen zu können, wurden mehrere Gasstrahlungsmodelle in den Open-Source-Code OpenFOAM® implementiert und getestet. Die Modelle Full Spectrum Correlated-k (FSCK) und Weighted Sum of Gray Gases (WSGG) zeigen gute Näherungen des Strahlungswärmestroms an die gemessenen Daten in der Brennkammer, wobei das WSGG eine geringere Rechenzeit hat als das FSCK.

Acknowledgement

Ehrenwörtliche Erklärung

Hiermit erkläre ich, dass ich die vorliegende Arbeit, abgesehen von den in ihr ausdrücklich genannten Hilfen, selbständig verfasst habe. Die "Grundsätze zur Sicherung guter wissenschaftlicher Praxis an der Technischen Universität Darmstadt" und die "Leitlinien zum Umgang mit digitalen Forschungsdaten an der TU Darmstadt" wurden in den jeweils aktuellen Versionen bei der Verfassung der Dissertation beachtet.

Die Arbeit wurde bisher keiner anderen Prüfungsbehörde vorgelegt und noch nicht veröffentlicht.

Darmstadt, den 8. Januar 2025

_____

Marcel Richter

Contents

Nomenclature

Latin Symbols

Symbol	Unit	Description
A	m²	Area
A	1/s	Frequency factor
A^*	–	Dimensionless area
A_s	Pa s/K$^{0.5}$	Sutherland coefficient
a	–	Non-gray stretching factor for FSK
a_i	–	Weight for WSGG model
C	molecule/m³	Number density
C_1, C_2		Constants for Planck-function
c	–	Reaction progress variable
c	–	Clearance-to-wavelength ratio
c_0	m/s	Speed of light in vacuum
c_p	J kg^{-1} K^{-1}	Specific heat capacity at constant pressure
c_v	J kg^{-1} K^{-1}	Specific heat capacity at constant volume
D	m²/s	Mass diffusion coefficient
d	m	Diameter
$\boldsymbol{d}_i$	–	Direction vector of solid angle
E	J/kmol	Activation energy
E	W/m³	Power contribution per volume
E_b	W/m²	Total blackbody emission
E''	cm^{-1}	Lower-state energy
$\boldsymbol{F}$	N	Force
f_v	–	Soot volume fraction
G	W/m²	Incident radiation
G_k	m²/s³	Turbulent kinetic energy production rate
$\boldsymbol{g}$	m/s²	Gravity
g	–	Asymmetry factor
g	–	cumulative k-distribution or non-dimensional wavenumber
H_u	J/kg	Lower calorific value

h_s	J/kg	Specific sensible enthalpy
h	J s	Planck's constant (6.6261×10^{-34} J s)
$\hbar$	J s/sr	Modified Planck's constant ($= h/2\pi$)
Δh_f	J/kmol	Enthalpy of formation
I	kg m/s	Momentum
I	W cm^{-2} sr^{-1}	Radiative intensity
I	–	Isotopologue number
I	–	Turbulence intensity
$I_{b\eta}$	W cm^{-2} sr^{-1}	Spectral blackbody intensity
K	J/kg	Specific mechanical energy
k		Reaction rate coefficient
k	J/K	Boltzmann's constant (1.3807×10^{-23} J/K)
k	cm^{-1}	Absorption coefficient variable
k	–	Complex value for complex index of refraction
k	J/kg	Turbulent kinetic energy
k^*	cm^{-1}	Correlated absorption coefficient variable
L	kg m^2/s	Angular momentum
L	m	Path length
L_{mix}	m	Turbulent mixing length
l_0	m	Internal length scale
l_η	m	Kolmogorov length scale
M	kg/kmol	Molar mass
M	–	Molecule number
m	kg	Mass
m	–	Complex index of refraction
$\dot{m}$	kg/s	Mass flow
n	–	Refractive index
n	–	Temperature-dependent exponent for γ_{air}
n	–	Real value for complex index of refraction
n	–	Dispersion coefficient
$\hat{\boldsymbol{n}}$	–	Cell-face normal vector
N	–	Number

N_A	molecule/mol	Avogadro constant ($6.022141076 \times 10^{23}$ 1/mol)
p	Pa	Pressure
Q	J	Thermal energy
$\dot{Q}$	W	Thermal power
$\dot{q}$	W/m^2	Heat flux density
R	m	Outer radius
R	J mol^{-1}K^{-1}	Gas constant (8.314462618 J mol^{-1}K^{-1})
$\dot{R}$	kg m^{-3}s^{-1}	Reaction rate
r	m	Radius
S	–	Swirl number
S		Source term
S	cm^{-1}/(molecule$\times$cm^{-2})	Intensity
s	m	Distance
$\hat{\boldsymbol{s}}$	–	Unit vector
s_L	m/s	Laminar burning velocity
s_T	m/s	Turbulent burning velocity
T	K	Temperature
T_a	K	Activation temperature
T_s	K	Sutherland temperature
t	s	Time
t_0	s	Macroscopic time scale
t_L	s	Chemical/laminar flame time scale
t_η	s	Kolmogorov time scale
$\boldsymbol{u}$	m/s	Velocity
u^*	–	Dimensionless velocity
V	m^3	Volume
$\dot{V}$	m^3/s	Volume flow
w_i	–	Gaussian quadrature weight
x	mol/mol	Mole fraction
x	–	Size parameter
x_i	–	Gaussian abscissas
Y	kg/kg	Mass fraction

Z	–	Mixture fraction

Greek Symbols

Symbol	Unit	Description
α	rad	Angle
α	$\mathrm{W\,m^{-2}K^{-1}}$	Heat transfer coefficient
α	$\mathrm{m^2/s}$	Thermal diffusivity
β	$\mathrm{cm^{-1}}$	Extinction coefficient
β	–	Exponent for artificial k-distribution
Γ	–	Diffusion coefficient
γ	$\mathrm{cm^{-1}\,atm^{-1}}$	Line half-width
γ_{air}	$\mathrm{cm^{-1}\,atm^{-1}}$	Air-broadened half-width
γ_{self}	$\mathrm{cm^{-1}\,atm^{-1}}$	Self-broadened half-width
δ_L	m	Laminar flame thickness
ϵ	$\mathrm{m^2/s^3}$	Turbulence dissipation rate
ϵ	–	Emissivity
η	$\mathrm{cm^{-1}}$	Wavenumber
θ	rad	Scattering angle
θ	rad	Polar angle
κ	$\mathrm{cm^{-1}}$	Absorption coefficient
λ	–	Oxidant-fuel equivalence ratio
λ	µm	Wavelength
λ	$\mathrm{W\,m^{-1}\,K^{-1}}$	Thermal conductivity
μ	$\mathrm{Pa\,s}$	Dynamic viscosity
ν	$\mathrm{m^2/s}$	Kinematic viscosity
ν	–	Stoichiometric mass ratio
ν'	–	Stoichiometric coefficient reactant
ν''	–	Stoichiometric coefficient product
ξ^*	–	Fine structures length scale
ρ	$\mathrm{kg/m^3}$	Density
ρ_N	$\mathrm{cm^{-3}}$	Number density
σ	Pa	Cauchy stress tensor

σ	W cm^{-2} K^{-4}	Stefan-Boltzmann-Constant (5.670... $\times$ 10^{-12} W cm^{-2} K^{-4})
σ_s	cm^{-1}	Scattering coefficient
$\boldsymbol{\tau}$	Pa	Shear-rate tensor
τ^*	s	Fine structures time scale
Φ	–	Scattering phase function
$\boldsymbol{\phi}$	–	Vector for thermodynamic state of T, p and x_i
φ	rad	Angle
φ	rad	Azimuthal angle
ψ	–	Stream function
Ω	sr	Solid angle

Dimensionless Quantities

Symbol	Description
CFL	Courant number ($= u\,\Delta t/\Delta x$)
Da	Damköhler number ($= t_0/t_L$)
Ka	Karlovitz number ($= t_L/t_\eta$)
Nu	Nusselt number ($= \alpha\,d/\lambda$)
Pr	Prandtl number ($= \mu\,c_p/\lambda$)
Re	Reynolds number ($= \rho\,u\,d/\mu$)
Re$_t$	Turbulent Reynolds number ($= (l_0/l_\eta)^{4/3}$)
Sc	Schmidt number ($= \nu/D$)

Subscripts

Subscript	Description
0	Reference
a	Atmospheric
ax	Axial
b	Burned
b	Blackbody
c	Circumferential
c	At band center
$chem$	Chemical

D	Doppler
d	Drag
dep	Deposition
$diff$	Diffusion
eff	Effective
f	Cell-face
fix	Fixed
g	Gravity
$glob$	Global
L	Lorentz
lam	Laminar
loc	Local
mix	Mixture
$mois$	Moisture
N	Neighbor-cell
NB	Narrow band
P	Owner-cell
P	Planck
p	Particle
$prim$	Primary
$prod$	Product
pt	Point
r	Rotation
$reac$	Reactant
rnd	Random
s	Species
s	Scattering
sec	Secondary
st	Stoichiometric
sw	Swirled
tet	Tertiary
tot	Total

$turb$	Turbulent
v	Vibration
vol	Volatile
w	Wall
η	Spectral resolved
η_0	Wavenumber in line center

Abbreviations

Abbreviation	Description
ADF	Absorption Distribution Function
AR	As received
BECCS	Biomass Energy Carbon Capture and Storage
BW	Beech wood
CAD	Computer Aided Design
CCS	Carbon Capture and Storage
CFD	Computational Fluid Dynamics
CDF	Rosin–Rammler cumulative Distribution Function
CDSD	Carbon Dioxide Spectroscopic Database
CK	Constant volume to Kinetic energy
CM	Constant volume to jet Momentum
CRT	Constant Residence Time
CV	Constant Velocity
DAF	Dry and ash free
DNS	Direct Numerical Simulation
DOM	Discrete Ordinates Model
NBCK	Narrow Band Correlated-k model
EWB	Exponential Wide Band model
EST	Institute of Energy Systems and Technology
FSK	Full Spectrum k model
FSCK	Full Spectrum Correlated-k model
FVM	Finite Volume Method
HITEMP	High-temperature molecular spectroscopic database

HITRAN	High-resolution transmission molecular absorption database
IRZ	Inner recirculation zone
JANAF	Joint Army Navy NASA Air Force
KDLR	Kinetic Diffusion Limited Rate
LBL	Line-by-line
LES	Large Eddy Simulation
NBCK	Narrow Band Correlated-k model
NDIR	Non-dispersive infrared
NG	Natural gas
PDF	Probability Density Function
RANS	Reynolds-Averaged Navier-Stokes
RBK	Rhenish lignite (german: Rheinische Braunkohle)
RDT	Rapid Distortion Theory
RHF	Radiative heat flux
RTE	Radiative transfer equation
SIMPLE	Semi Implicit Method for Pressure Linked Equations
SNB	Statistical Narrow Band model
TB	Torrefied biomass
WBCK	Wide Band Correlated-k model
WS	Walnut shells
WSA	Institute of Heat and Mass Transfer
WSGG	Weighted Sum of Gray Gases

Mathematical Operators

Operator	Description
ϕ	Scalar value
$\boldsymbol{\phi}$	Vectorial value
$\overline{\boldsymbol{\phi}}$	Averaged (vectorial) value
ϕ'	(vectorial) fluctuation
$\tilde{\boldsymbol{\phi}}$	Favre-averaged (vectorial) value
Δ	Difference

$$\boldsymbol{I} = \begin{bmatrix} 1 & 0 & 0 \\ 0 & 1 & 0 \\ 0 & 0 & 1 \end{bmatrix}$$ Identity matrix

$$\nabla\phi = \begin{pmatrix} \partial\phi/\partial x_1 \\ \partial\phi/\partial x_2 \\ \partial\phi/\partial x_3 \end{pmatrix}$$ Gradient of a scalar

$$\nabla\boldsymbol{\phi} = \begin{bmatrix} \partial\phi_1/\partial x_1 & \partial\phi_1/\partial x_2 & \partial\phi_1/\partial x_3 \\ \partial\phi_2/\partial x_1 & \partial\phi_2/\partial x_2 & \partial\phi_2/\partial x_3 \\ \partial\phi_3/\partial x_1 & \partial\phi_3/\partial x_2 & \partial\phi_3/\partial x_3 \end{bmatrix}$$ Gradient of a vector

$$\nabla \cdot \boldsymbol{\phi} = \frac{\partial\phi_1}{\partial x_1} + \frac{\partial\phi_2}{\partial x_2} + \frac{\partial\phi_3}{\partial x_3}$$ Divergence of a vector

$$\nabla \cdot \boldsymbol{\tau} = \begin{pmatrix} \partial\tau_{11}/\partial x_1 + \partial\tau_{12}/\partial x_2 + \partial\tau_{13}/\partial x_3 \\ \partial\tau_{21}/\partial x_1 + \partial\tau_{22}/\partial x_2 + \partial\tau_{23}/\partial x_3 \\ \partial\tau_{31}/\partial x_1 + \partial\tau_{32}/\partial x_2 + \partial\tau_{33}/\partial x_3 \end{pmatrix}$$ Divergence of a tensor

$$\nabla \cdot (\nabla\phi) = \frac{\partial^2\phi}{\partial x_1^2} + \frac{\partial^2\phi}{\partial x_2^2} + \frac{\partial^2\phi}{\partial x_3^2}$$ Laplace operator

1 Introduction

Global warming caused by emission of greenhouse gases, mainly from combustion of fossil fuels in the energy sector, is a key challenge for engineers and scientists in the current century. Carbon dioxide, beside fluorinated gases, nitrogen- and hydrocarbon compounds, makes up the majority of greenhouse gases. To counteract climate change, measures were taken at the Paris Climate Conference of the United Nations in 2015 to reduce carbon dioxide emissions to net zero by 2050 and limit the rising of global average temperature to $1.5\,°C$, or a maximum of $2\,°C$, relative to the pre-industrial levels [1]. To achieve the goals of the Paris climate agreement, CO_2 emissions must be drastically reduced worldwide. It is assumed that the current global primary energy demand will increase by approx. $24\,\%$ by the year 2040 according to the International Energy Agency [2]. Especially in developing and emerging countries, where fossil fuels are still predominant, a strong increase in primary energy demand is expected [2]. In order to counteract CO_2 emissions from the energy sector, a variety of mechanisms must be implemented. A first step towards reducing CO_2 emissions in the energy sector is to increase the efficiency of existing fossil powered system and accelerate the installation of renewable energy sources to replace fossil fueled power plants. However, not all thermal processes can be operated CO_2 neutral, such as the production of cement. For this, the separation of CO_2 from the exhaust gas is a reasonable solution.

For the separation of CO_2, industries mainly focus on three promising combustion processes: *pre-combustion*, *post-combustion* and *oxyfuel*. Pre-combustion is the separation of carbon from the fuel before combustion to gain a flue gas without CO_2 content. This can be done by gasification of solid fuels containing carbon to produce a synthetic gas which consists of H_2, CO and CO_2. After cleaning the synthetic gas from ash, residual char, tars, sulphur- and nitrogen compounds as well as other accompanying substances, the H_2 content of the synthetic gas can be increased through a water gas shift reaction. Hydrogen can be used as carbon free fuel for gas turbines to produce electricity and heat without CO_2 emissions [3]. In post-combustion, CO_2 is captured after flue gas cleaning of a solid fuel combustion process, which includes dedusting, desulphurization, and denitrification. The capturing of CO_2 is performed by chemical absorption (e.g. amine scrubbing or carbonate looping), adsorption, cryogenic separation, or membrane processes [3]. Carbon Capture and Storage (CCS) technologies can be used to avoid CO_2 emissions if the exhaust gas consists of pure CO_2. This can be achieved with oxyfuel combustion. Using biomass as fuel, negative CO_2 emissions in the power sector can be achieved through Biomass Energy Carbon Capture and Storage (BECCS) [4].

The oxidant in an oxyfuel process consists mainly of O_2, CO_2 and H_2O. This implies that the fuel is not burned with ambient air as in conventional combustion processes. Thus, carbon dioxide is present in high concentrations in the exhaust gas after the combustion of the fuel. The residual water vapor in the off-gas can be condensed, to obtain flue gas consisting of almost pure CO_2. An advantage of this processes is the possibility to retrofit existing power

plants at reasonable costs [5, 6]. A major disadvantage of oxyfuel is the provision of oxygen, as the separation of oxygen from the air, reduces the efficiency of the entire process. Together with the compression of CO_2, this results in a net efficiency loss of $8 - 10\,\%$ for power plants [7, 8]. The oxyfuel combustion technology is currently ranked at Technology Readiness Level 7 out of 9 [9]. This means that oxyfuel combustion has already been demonstrated at a sub-scale, fully functional prototype and is about to be completely qualified for commercial demonstration. An example is the coal-fired $30\,MW_{th}$ oxyfuel pilot plant in Schwarze Pumpe, Germany, which was operated by the company Vattenfall [10]. An overview of different oxyfuel fired systems and pilot-plants in the range from 1.2 to $35\,MW_{th}$ is given by Guo et al. [11]. In 2024, Thyssenkrupp began with the construction of a large-scale industrial oxyfuel plant for the production of cement in Schleswig-Holstein, Germany. The plant is scheduled to be commissioned in 2028 [12]. Despite the high degree of maturity of this firing concept, there are still open questions, particularly with regard to oxyfuel combustion with biomass.

1.1 Motivation

Compared to conventional combustion with air, the main component of the combustion atmosphere is CO_2 instead of N_2, which has different chemical and thermodynamic properties than N_2. Thus, combustion characteristics change. In the last few decades, oxyfuel combustion has been studied almost exclusively for the combustion of coal, as the focus has been on retrofitting coal-fired power plants. However, biomass combustion has gain more attention in recent years. Only few studies exist for the combustion of pure pulverized biomass under oxyfuel conditions. Most of these investigations are done in laboratory combustion chambers and chambers with refractory-lined walls [13–15]. It is therefore difficult to transfer the experimental results from the laboratory scale to industrial boilers, which are usually equipped with water-cooled steel walls. While refractory-lined walls store most of the heat, water-cooled membrane walls dissipate the absorbed heat from the combustion chamber. The cooled walls and the high volatile content of the biomass affect, for example, the ignition time, heat transfer, flame stability, burnout of solids, soot formation and the pollutant emissions. In particular, the properties of thermal radiation change in combustion chambers with cooled walls compared to those of chambers with refractory-lined walls. The up-scaling of a laboratory oxyfuel burner firing biomass should thus provide information on the impact of the scale and water-cooled walls on flame stability, heat transfer and pollutant emissions. In addition, the step from laboratory scale to semi-industrial scale should demonstrate geometric and operational measures for the further step to an industrial application.

1.2   Research Objectives

Since a large amount of heat transfer in combustion chambers with non-premixed flames are caused by thermal radiation, a first step in this work is to implement and verify theoretical gas radiation models in a Computational Fluid Dynamics (CFD) code, which have already shown good results in a stand-alone code for the calculation of radiative heat transfer in virtual oxyfuel boilers [5]. The objective here is to demonstrate the suitability of the radiation models for a real, semi-industrial application, as only a few studies exist in this area. An overview of the state of the art is given in Chapter 3.

A further objective of this work is to answer the questions of how to scale up an oxyfuel laboratory burner to a semi-industrial scale. While in the literature the scaling of a burner is mostly done without geometric restrictions, in this work the design of the new oxyfuel burner is strongly limited by the geometric constraints of the existing $1\,\mathrm{MW_{th}}$ combustion chamber. For this reason, the focus here is on finding a new approach for scaling a pulverized fuel burner, based on an laboratory oxyfuel burner to semi-industrial scale for an existing combustion chamber. An overview of burner scaling methods that have already been investigated in the literature is given in Chapter 5.

Furthermore, the flame stability and pollutant emissions under oxyfuel conditions for different pulverized biomass and different combustion parameters are investigated to find stable operating conditions. To establish comparability with a reference laboratory burner, lignite is also being investigated as a reference fuel. The objective is to clarify which combustion parameters are essential for a stable flame in a semi-industrial combustion chamber, firing biomass under oxyfuel conditions while keeping pollutant emissions to a minimum. More information on the state of the art can be found in Chapter 7.

The wall-incident radiative heat flux inside the chamber is measured, to validate the radiation models, integrated in a CFD code. The measurements are also used to determine the radiation behavior of biomass and natural gas under oxyfuel conditions in a semi-industrial combustion chamber with cooled walls. Since heat transfer by radiation dominates in the region of the evaporator inside industrial boilers, it is important to know, as in the case of air-firing, at which combustion settings similar heat fluxes can be expected under oxyfuel conditions. This can be useful when retrofitting an air-fired boiler with an biomass fueled oxyfuel system, as the combustion parameters can be adjusted without changing the thermal output. The natural gas flame is measured to show the influence of a particle-laden flow on the radiation properties. Studies already carried out by other authors in this area are shown in Chapter 7.

1.3   Thesis Outline

This work is divided into 9 chapters. The following chapter describes the basics of oxyfuel combustion and the difference to conventional combustion with air. Subsequently, the basics

of turbulent premixed flames and the theory for non-premixed flames as well as their quantification methods are shown. Furthermore, the model concept of solid fuel combustion is addressed. In addition, the influences that affect the stability of a flame are described, as well as the classification of flame types in industrial combustion. Finally, this chapter describes the necessary fundamentals of gas, soot and particle radiation relevant to this work.

Chapter 3 deals with the modeling of gas radiation in combustion processes. Starting with radiative heat transfer and its modeling using the Discrete Ordiante Model (DOM) and P_1 model. Subsequently, the modeling of gas radiation and the calculation of radiation absorption at the molecular level are described. The state of the art regarding the modeling of gas radiation in oxyfuel combustion is also given here. The described models, which are implemented in a CFD code, are applied here to test cases to verify the code. The next chapter covers the basic transport equations for reactive flows with solid particles. Furthermore, the modeling of turbulent flows, heterogeneous and homogeneous combustion processes, as well as thermoynamic properties are described.

Chapter 5 discusses the up-scaling of a reference laboratory scale oxyfuel burner. First, the state of the art is given and some of the methods described there are applied and evaluated for the current up-scaling. The properties of the reference burner are addressed. Subsequently, a new approach is described for scaling the burner to a semi-industrial dimension. For this purpose, numerical simulations are used, the results are compared with simulation data of the reference burner to show the similarity.

Chapter 6 describes the entire oxyfuel facility that was used to carry out the experiments. The combustion chamber, the burner, the fuel dosing and the measuring systems as well as the used fuels are described.

Chapter 7 discusses the experimental results using the up-scaled oxyfuel burner in the semi-industrial combustion chamber. In the first section of this chapter, the effects of the firing parameters on NO and CO emissions for biomass and lignite are considered. The next section focuses on the combustion parameters and their effects on flame stability for different solid fuels. In the last section of this chapter, the measurements of the wall-incident radiative heat flux in an air and oxyfuel atmosphere for various solid fuels and natural gas are discussed. The results of the wall-incident radiative heat flux for biomass and lignite are compared to the measurement results of the reference combustion chamber in relative terms.

In the penultimate chapter, the CFD code with the implemented and verified radiation models, which is discussed at the beginning of the thesis, is applied to a real natural gas-fired case with oxyfuel and air atmosphere. For this purpose, the operating conditions and measurement data from the previous chapters are used for validation of the radiative heat flux.

The last chapter summarizes the most important results and provides an outlook for further investigations.

2 Theoretical Background

An overview of the differences between air-firing and oxyfuel combustion is given in this chapter. Since this work focuses on turbulent solid fuel combustion and thermal radiation, the most relevant fundamentals of turbulent flames, stability, industrial non-premixed flame types, solid fuel combustion and thermal radiation will be briefly described. A short description of premixed flames is given to provide a clearer understanding of non-premixed flames.

2.1 Oxyfuel versus Air Combustion

In conventional air combustion systems, the oxidant consists of approx. $21 \, \text{vol}\%$ oxygen and $79 \, \text{vol}\%$ nitrogen. In an oxyfuel fired system, however, the oxidant consists of $70 - 90 \, \text{vol}\%$ CO_2. The CO_2 content depends on whether wet flue gas recirculation is used or if the water is condensed from the flue gas (dry recirculation). The recirculated flue gas replaces the missing N_2 and provides sufficient volume flow to transport the heat through the combustion system. The temperature of the flame can also be controlled with the recirculated flue gas [7].

Several studies have shown that with oxyfuel combustion lower temperatures are reached, heat transfer is changed, ignition is delayed, and the flame is more unstable. Moreover, NO_x and SO_x emissions are reduced for oxyfuel conditions. Most of these effects can be attributed to the different gas properties of N_2 and CO_2. The molar mass of CO_2 is higher than that of N_2, thus CO_2 has a higher density. With identical mass flow, oxyfuel firing therefore results in lower velocities and higher residence times for particles in the combustion chamber than in air-firing. CO_2 has a higher heat capacity than N_2, which reduces the adiabatic flame temperature. To counteract this, the flame temperature can be increased by a higher O_2 content in the oxidant. The availability of oxygen is reduced at the char surface, since the diffusion rate of oxygen in CO_2 is lower than in nitrogen. Flame propagation speed is lower due to lower thermal diffusivity. Furthermore, CO_2 has strongly absorbing bands in the thermal spectrum, which leads to a change in the radiative properties in the combustion chamber compared to conventional air combustion [7, 16–18]. The thermal properties of CO_2 and N_2 are summarized in Tab. 2.1 according to Toporov and Martin [7, 19].

Tab. 2.1 Properties of CO_2 and N_2 at $900 \, °C$ and $1 \, \text{bar}$ according to Toporov and Martin [7, 19].

Thermal property	Symbol	Unit	N_2	CO_2	CO_2/N_2
Molecular mass	M	kg/kmol	28.01	44.01	1.57
Density	ρ	kg/m^3	0.29	0.45	1.55
Molar heat capacity	c_p	kJ kmol^{-1}K^{-1}	33.6	56.1	1.67
O_2 diffusion coeff. $\times 10^{-4}$	D_{O_2}	m^2/s	3.074	2.373	0.77
Thermal diffusivity $\times 10^{-7}$	α	m^2/s	2168	1420	0.65
Thermal conductivity $\times 10^{-3}$	λ	W m^{-1}K^{-1}	74.67	81.69	1.09

In addition to differences in thermal properties, endothermic gasification reactions occurring at the char surface in a CO_2-rich atmosphere provoke flame instability in case of solid fuel combustion [7].

2.2 Turbulent Combustion

Since the focus of this work is on semi-industrial combustion of pulverized fuels under oxyfuel conditions, using non-premixed, turbulent flames, the fundamentals of turbulent combustion are described in the following.

The mixing processes in turbulent combustion are significantly faster than in laminar combustion. An advantage of turbulent combustion is e.g. more compact combustion chambers through shorter flames [20]. In comparison to laminar combustion processes, continuous fluctuations in velocity and scalar quantities occur in turbulent combustion processes due to the formation of vortices. The vortices are formed by high shear forces if two fluid streams with different velocities flow beside each other. The vortices increase the boundary layer between the fluids, which enhances the molecular mixing process. An example is shown in Fig. 2.1 where two flows of different velocities flow from left to right. It can be seen how the vortices increase in size. The change from laminar to turbulent flow can be described using the Reynolds number Re, Eq. (2.1) [20]:

$$\mathrm{Re} = \frac{\rho\,u\,d}{\mu},\qquad(2.1)$$

where ρ is the density, u the velocity and μ the dynamic viscosity of the fluid. d is the characteristic diameter of the geometry. The Reynolds number describes the relationship between destabilizing inertia forces and stabilizing friction forces. If the destabilizing forces dominate, turbulence occurs. For tube flow, the critical value above the changeover to turbulence occurs is $\mathrm{Re} \approx 2300$ [21]. Fig. 2.2 shows the flame length vs. the Reynolds number. As the Reynolds number increases, the flame length rises until a turbulent flame is formed, which shows a short and bushy shape.

The velocity in a turbulent flow can be described by splitting u into a mean velocity $\overline{u}$ and the fluctuating velocity deviation from the mean velocity $u'(t)$, Eq. (2.2):

$$u(t) = \overline{u} + u'(t).\qquad(2.2)$$

To describe turbulent processes, various scales are required, such as length scales. The largest length scale in a turbulent process is the geometric length of the system, the *integral length scale* l_0 (macro length). The growth of the vortices depends on their non-linear generation

and dissipation. Large vortices break down into smaller vortices with shorter wavelengths and higher frequencies. The decay of vortices is known as an *energy cascade*. The smallest vortices dissipate their kinetic energy into thermal energy due to frictional forces. The smallest vortex scale is reached when turbulent mixing occurs faster than diffusion. This length scale is known as the *Kolmogorov-length scale* l_η [20]. The *turbulence intensity* or turbulent fluctuation velocity u' can be calculated by the root-mean-square of the transient velocity deviation $u'(t)$ in Eq. (2.2). The turbulent Reynolds number Re_t can be determined using the integral length scale, the turbulent fluctuating velocity and the dynamic viscosity, Eq. (2.3):

$$\mathrm{Re}_t = \frac{u'\,\overline{\rho}\,l_0}{\mu} = \left(\frac{l_0}{l_\eta}\right)^{4/3}. \tag{2.3}$$

The turbulent Reynolds number can be used to establish a relationship between the integral length scale and the Kolmogorov-length scale. It can be used to characterize a turbulent flow and is therefore more feasible than Re. If the turbulent Reynolds number is less than 1, laminar combustion takes place. If $\mathrm{Re}_t > 1$, turbulent combustion is taking place [20].

2.2.1 Premixed flames

In turbulent premixed flames, the fuel and the oxidant are already mixed before chemical reaction initiates. A temporal resolution displays angled and fractured flame fronts with strongly fluctuating structures [20].

The burning velocity or ignition speed is the speed at which a combustion front propagates into a fuel-oxidant mixture. For laminar flames, the burning velocity s_L results from the cone angle of the combustion front φ and the flow velocity u of the fresh mixture, Eq. (2.4):
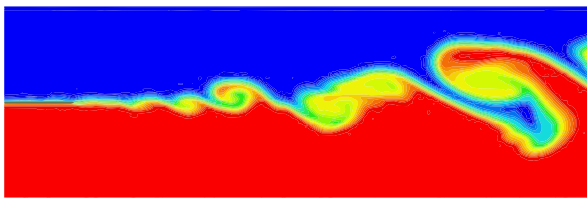

Fig. 2.1 Formation of turbulence in a shear layer (Direct Numerical Simulation). Adapted from [22, 23].
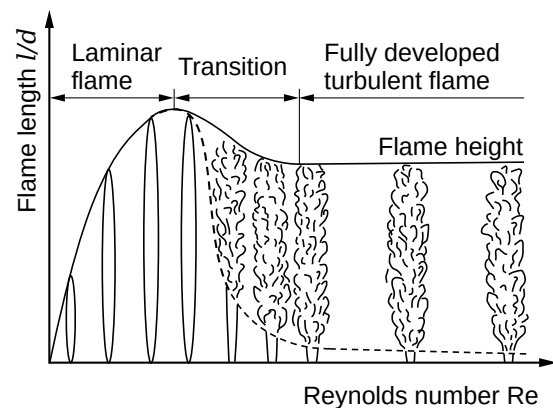

Fig. 2.2 Turbulence transition for a non-premixed jet flame. Adapted from [24–26].

$$s_L = u \cdot \sin \varphi. \tag{2.4}$$

Similarly to the laminar burning velocity, the turbulent burning velocity s_T can be calculated using the mean velocity of the fresh mixture, Eq. (2.5) [20]:

$$s_T = \overline{u} \cdot \sin \varphi. \tag{2.5}$$

Damköhler's theory establishes a relationship between the laminar and turbulent burning velocity for wrinkled, laminar flame surfaces using Eq. (2.6) [27]:

$$\frac{s_T}{s_L} = 1 + \frac{u'}{s_L}. \tag{2.6}$$

Numerous correlations for the calculation of the turbulent burning velocity exist in the literature. For example Zimont and Lipatnikov [28], Bradley et al. [29] or Metghalchi and Keck [30] who experimentally determined correlations for burning velocities of different mixtures at high pressure and temperature.

The *turbulent Karlovitz number* Ka can be used to describe the ratio of the laminar flame time scale ($t_L = \delta_L/s_L$) to the Kolmogorov time scale, Eq. (2.7):

$$\mathrm{Ka} = \frac{t_L}{t_\eta}, \quad \text{with} \quad t_\eta = \sqrt{\frac{\mu}{\rho\,\tilde{\epsilon}}}, \tag{2.7}$$

where δ_L is the laminar flame thickness and $\tilde{\epsilon}$ the dissipation rate of the turbulent kinetic energy. For $\mathrm{Ka} < 1$, the Kolmogorov time scales are larger than those of the laminar flame; in the Borghi diagram in Fig. 2.3, the flame is located below the line $\mathrm{Ka} = 1$ in the area of the corrugated flames.

The *Damköhler number* Da is used to describe the relationship between the macroscopic time scale t_0 and the chemical time scale t_L, Eq. (2.8):

$$\mathrm{Da} = \frac{t_0}{t_L} = \frac{l_0\,s_L}{u'\,\delta_L}. \tag{2.8}$$

With $\mathrm{Da} < 1$, the chemical reactions need more time than the physical mixing. Above the line $\mathrm{Da} = 1$, the area is referred to a *perfect stirred reactor*. The area of thickened reaction zones is located between $\mathrm{Da} = 1$ and $\mathrm{Ka} = 1$. In these zones, the vortices with a length scale l_η smaller than δ_L are located in the flame front [20].
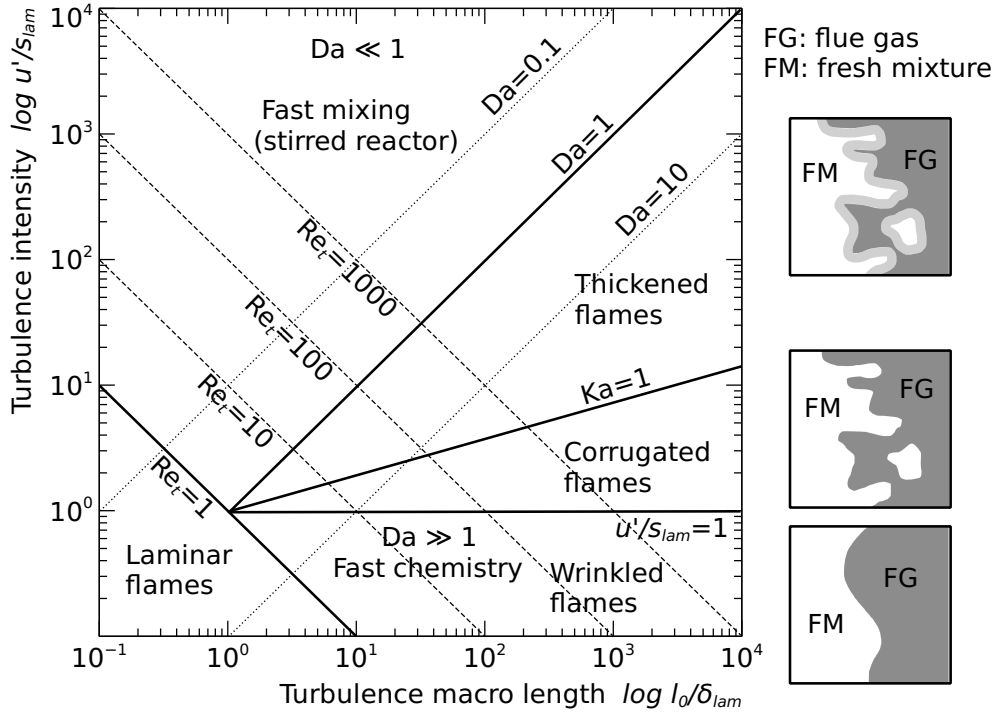
Fig. 2.3 Flame structure diagram according to Borghi [31, 32].

In premixed combustion processes, the temperature, density or mixture is often described as a function of the reaction progress. For this purpose, the reaction progress variable is defined, which can be applied to all scalar variables that do not have extreme values, but fall or rise continuously [20]. The progress variable c implies a one-step reaction. The actual value is normalized with the product mass fraction (here e.g. CO_2), Eq. (2.9):

$$c = \frac{Y_{CO_2} - Y_{CO_2,u}}{Y_{CO_2,b} - Y_{CO_2,u}}.$$

(2.9)

The subscript u stands for *unburned* and the subscript b for *burned* quantities [33].

2.2.2   Non-premixed flames

If the fuel is mixed with the oxidant inside the combustion chamber, the flames are referred as non-premixed flames or diffusion flames. The chemical conversion depends on mixing. A simple way to describe a non-premixed flame is the mixture fraction model according to Burke and Schumann [34]. For simple combustion models, it can be assumed that only diffusion needs to be taken into account, while the chemical reactions are assumed to be infinitely fast. Further assumptions for this are a single-step reaction and an one-directional reaction. In this case, fuel and oxidizer cannot coexist. However, this assumption only means that the slow, mixture-controlled processes dominate. Thus, the mixture fraction can also be applied to equilibrium and multi-step reactions [20]. The mixture fraction Z in Eq. (2.10) indicates

the mass fraction of the fuel stream in the mixture:

$$Z = \frac{m_1}{m_1 + m_2} = \frac{\nu\, Y_{fuel} - Y_{O_2} + Y_{O_2,2}}{\nu\, Y_{fuel,1} + Y_{O_2,2}}. \tag{2.10}$$

The fuel mass m_1 is designated by subscript one and the oxidizer mass m_2 by subscript two. Both the fuel stream and the oxidizer stream may contain additional inter species such as nitrogen. The right-hand side of the equation represents the mixture fraction with oxygen mass fraction in the oxidizer $Y_{O_2,2}$ ($Y_{O_2,2} = 0.232$ for air) and the fuel mass fraction in the fuel stream $Y_{fuel,1}$. The stoichiometric mass ratio ν is calculated according to Eq. (2.11) [33]:

$$\nu = \left(\frac{Y_{O_2,u}}{Y_{fuel,u}} \right)_{st} = \frac{\nu'_{O_2}\, M_{O_2}}{\nu'_{fuel}\, M_{fuel}}, \tag{2.11}$$

where M is the molar mass and ν' is the stoichiometric coefficient of the reactants. The stoichiometric mixture fraction Z_{st} is expressed by Eq (2.12):

$$Z_{st} = \frac{Y_{O_2,2}}{\nu\, Y_{fuel,1} + Y_{O_2,2}}. \tag{2.12}$$

The maximum heat release and thus the highest possible temperature of the reaction is located at the stoichiometric position. The adiabatic flame temperature can be expressed using the mixture fraction, Eq. (2.13) and Eq. (2.14):

$$T_b(Z) = \frac{Q\, Y_{fuel,1}}{c_p\, \nu'_{fuel}\, M_{fuel}}\, Z + T_u(Z) \quad \text{for } Z \leq Z_{st}, \tag{2.13}$$

$$T_b(Z) = \frac{Q\, Y_{O_2,2}}{c_p\, \nu'_{O_2}\, M_{O_2}}\, Z + T_u(Z) \quad \text{for } Z \geq Z_{st}, \tag{2.14}$$

where Q is the reaction heat release and c_p the specific heat capacity at constant pressure [33]. Fig. 2.4 shows the linear relation between the mass fraction and the mixture fraction. At the stoichiometric position Z_{st}, the oxygen and the fuel have been completely converted into reaction products. At position 0 there is pure oxygen and at point 1 pure fuel. Fig. 2.5 shows the relation between temperature and mixture fraction. The maximum temperature is reached at the stoichiometric point.
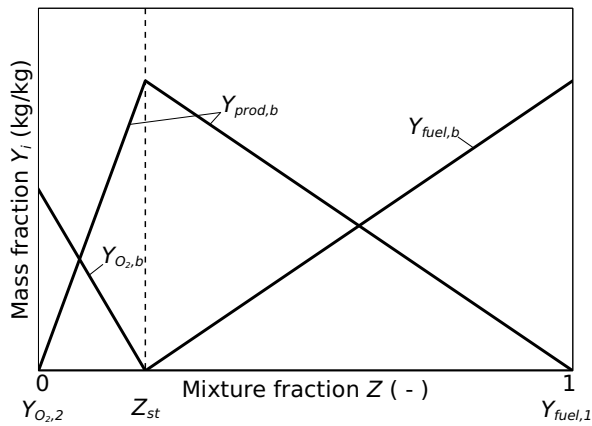
Fig. 2.4 Burke-Schumann-diagram for the mass fraction of oxidizer, fuel and products, plotted against the mixture fraction [33].
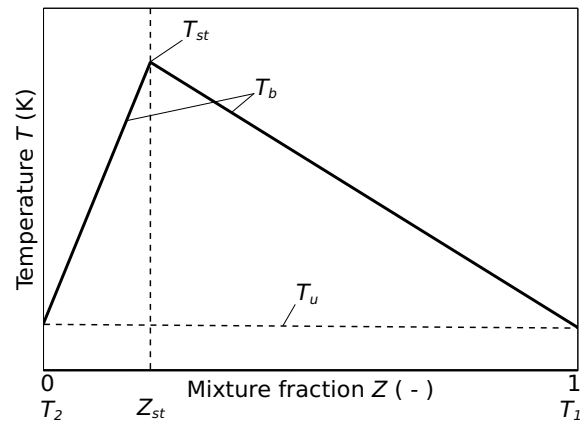
Fig. 2.5 Burke-Schumann-diagram for the adiabatic flame temperature, plotted against the mixture fraction [33].

2.2.3 Solid fuel combustion

The stability of a dust-flame also depends on the ignition properties and the burnout behavior of the fuel, therefore the basics of solid fuel combustion are briefly described here. The combustion of solid biomass can generally be described by the combustion behavior of solid fuels. In the literature, the combustion of solids is usually described based on coal, since the ignition of coal particles has been a subject of research for almost 180 years [35].

Biomass and coal, as well as polymers are char forming solids. They release volatile species during the heat-up phase. Particles are heated-up by convection and/or thermal radiation from several sides. At approx. $100\,°C$, the moisture in the particle mostly evaporates and desorption of stored gases in the pores of the particle takes place. The *pyrolysis* starts at approx. $300\,°C$. At low temperatures, the *primary pyrolysis* begins, where weak bridges in the macromolecular structures are broken up, tars and chars are formed from the fuel. Yield volatiles consist of short-chain hydrocarbons. During the *secondary pyrolysis*, which begins at further increasing particle temperature, tars are broken up into low-molecular hydrocarbons or deposit on solids. The composition of the pyrolysis gas depends on the fuel, the particle temperature and heating rate [20, 36]. The actual amount of volatiles yield is approx. $1.3 - 2.0$ times higher in combustion systems than under standardized determination methods where the temperature is significantly lower [20, 37]. The volatile components react homogeneously in the gas phase. Whether the oxidation of the volatiles or the surface reaction on the particle dominates, depends on the ambient temperature and the transport of oxygen through the boundary layer on the particle surface. The molecular diffusion in the macropores, as well as the Knudsen diffusion in the meso- and micropores determine the macroscopic transport of the oxidant into the internal particle surface. The products of this process are primarily CO and CO_2 [20]. Fig. 2.6 illustrates the steps during combustion of a solid fuel particle.

In comparison to volatiles and H_2O, which react in the homogeneous gas phase, a heterogeneous reaction takes place on the surface of the char particle. CO_2 and O_2 react on the surface

of the particle to form CO. The resulting CO reacts in the gas phase mainly through OH to CO_2. Many sub-processes take place during char burnout, such as absorption of molecules on the surface, surface reactions, desorption of the products, diffusion through the pores of the particle and diffusion into the gas phase. The overall reaction rate is determined by the slowest process. Fig. 2.7 shows the reaction rate determining zones during the combustion of char particles in an Arrhenius diagram. At high temperatures (zone III), chemical reactions are fast and pore diffusion and diffusion into the gas phase are reaction rate limiting. In zone II, at intermediate temperatures, the reaction rate is controlled by pore diffusion and chemical reaction. Most of the particles in a pulverized fuel combustion system are burned in this zone. At low particle temperatures (zone I), the chemical reaction is the reaction rate determining process. In addition, the burning velocity depends on the volatile and ash content of the fuel [20].
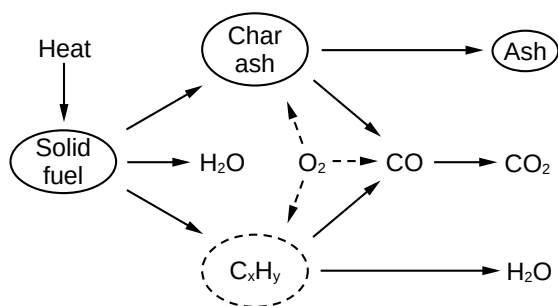
Fig. 2.6 Schematic illustration of the processes involved in pulverized fuel combustion. Adapted from [20, 38].
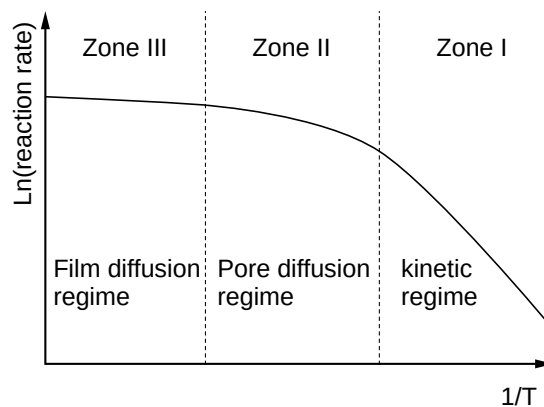
Fig. 2.7 Arrhenius diagram of reaction rate controlling zones. Adapted from [39, 40].

2.2.4 Flame Stability

Flame stability is used as a synonym for ignition stability. In this context, Günther [41] describes a flame as stable if minor fluctuations in flame parameters such as air preheating temperature, equivalence ratio or pressure loss do not affect the flame [32]. To maintain the stability of a flame, heat and radicals must be continuously transferred to the reaction zone in order to sustain chemical reactions. Radicals are transferred to the reaction zone solely by diffusion, while heat is transferred by convection and heat conduction. Both effects can be controlled by recirculation of hot flue gas and mixing with fresh gas. No reactions can take place near walls, as large masses absorb and remove the heat that is released. Therefore, a flame cannot touch the burner. For top-down fired burners, the flame velocity must be higher than the convective buoyancy created by hot flue gases to avoid flame extinction. Turbulence can stabilize a flame by intense mixing, but it can also destabilize it if the turbulence is too strong and the fresh gas is diluted with exhaust gas [20].

The capability of ignition and therefore the flame stability of solid fuel combustion mainly depends on the volatile content of the fuel. The volatile reactions in the gas phase are much faster than the surface reaction of the char particles. An ideal fuel for a stable flame has a high volatile content and a low moisture and ash content. Another important property of the solid fuel is the particle size. Small particles follow the streams better than coarse particles and the fuel is heated up faster since the surface of the particle cloud is larger. The aerodynamics near the burner are also important for a stable flame, since the mixing rate of the fuel with oxygen is determined by the flow field. In this context, the swirl is important as it creates an inner recirculation zone (IRZ) that transports hot combustion products into the reaction zone and thus provides heat transfer to the fuel. The high velocity gradients at the boundary of the IRZ further enhance turbulent diffusion. Furthermore, the burner geometry has an influence on the flow field [42]. Fig. 2.8 shows a solid fuel burner with quarl and swirl generated IRZ. A disadvantage of the intensive mixing through the IRZ is higher NO_x formation. NO_x formation can be counteracted by air staging [43].
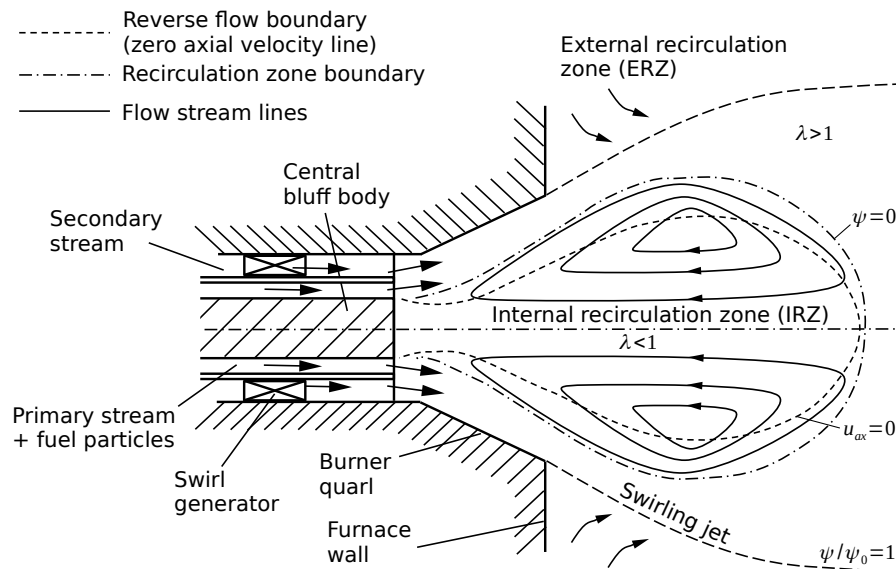
Fig. 2.8 Illustration of swirl stabilization in a pulverized fuel burner. Adapted from [44, 45].

In most coaxial industrial burners, the fuel input or primary stream is located in the center of the burner. The primary stream is surrounded by the secondary stream which supplies the combustion air. The secondary stream has a higher velocity than the primary. This difference in velocity causes the primary stream to be drawn into the secondary stream. In addition to mixing with the fuel, the high velocity of the secondary stream also ensures that hot gases are mixed in [46]. To aerodynamically stabilize a flame, large vortices are created to obtain ignitable mixing [20]. These vortices can be created with swirl chambers or swirl vanes inside the burner. The swirl of a burner can be expressed by the swirl number S in Eq. (2.15), which is the ratio of the circumferential and the axial momentum [20]

13

$$S = \frac{1}{R} \frac{\int_0^R (u_c\, r)\, \rho\, u_{ax}\, 2\, \pi\, r\, dr}{\int_0^R u_{ax}\, \rho\, u_{ax}\, 2\, \pi\, r\, dr + \int_0^R p\, 2\, \pi\, r\, dr}, \tag{2.15}$$

where p is the pressure, u_c the circumferential, u_{ax} the axial velocity and R the characteristic radius. If the dependence of the circumferential and axial velocity on the radius is neglected, as well as the pressure term, the simple relationship in Eq. (2.16) is obtained [20]:

$$S = \frac{2}{3} \frac{u_c}{u_{ax}}. \tag{2.16}$$

Schmid et al. [43] investigated the interaction between the primary air jet and the swirl-induced vortices. For this purpose, they investigated geometric variations of the fuel injection, the quarl geometry, the position of the primary air and the ratio of the momentum between primary and secondary flow. As a result of this investigation they defined four different flame types for industrial applications (Fig 2.9).
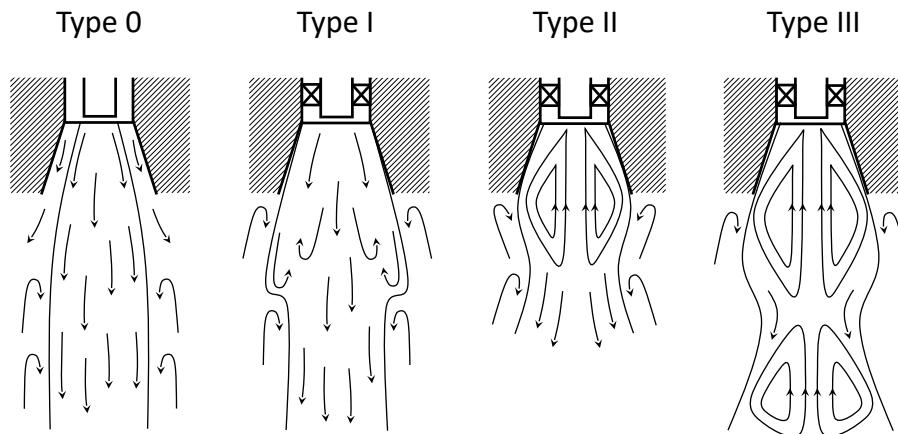
Fig. 2.9 Flame types for industrial applications according to Schmid et al. [43].

- **Type 0:** long non-swirled jet flame, which stabilize on the fuel injector. Typically used in corner fired boilers.
- **Type I:** the flame is a combination of a IRZ stabilized flame (type II) and a long non-swirled flame (type 0). The fuel penetrates the IRZ. Used as low NO_x emitter.
- **Type II:** IRZ stabilized, short flame with high secondary air swirl. This flame type is used in wall fired boilers.
- **Type III:** very high secondary air swirl stabilized flame. A long flame with a secondary IRZ downstream. Not commonly used in industrial applications.

Schmid and co-workers recommend a physical distance between the primary and secondary channel of 0.6 or higher for a type II flame. This value refers to the ratio of the primary channel diameter to the secondary channel diameter. Too high primary momentum destroys

the IRZ and forms a jet flame (type 0). Therefore, a lower primary air momentum increases the strength of the IRZ [43].

2.3 Thermal Radiation in Combustion

In oxyfuel combustion, the atmosphere consists of a high amount of CO_2 compared to air combustion where N_2 is the major component. While N_2 is a non-radiating gas, CO_2 and water vapor have strongly absorbing bands in the thermal spectrum, which lead to changes in radiative properties inside the combustion chamber. The heat transfer in the region of the flame is primarily caused by radiative heat transfer in the case of non-premixed flames. Convection is less relevant here [47]. For the numerical investigation of heat transfer by thermal radiation, the fundamentals are discussed in this chapter.

2.3.1 Gas radiation

In contrast to surfaces, radiative properties of gases or molecules are strongly dependent on the electromagnetic wavelength. A *gray* approximation, which means that radiative properties are independent of the wavelength, is not recommended for gases [48, 49]. Heat transfer by thermal radiation occurs by means of electromagnetic waves or photons expanding at the speed of light. Photons can be absorbed, reflected or transmitted by materials [50]. The spectrum of electromagnetic waves is illustrated in Fig. 2.10.
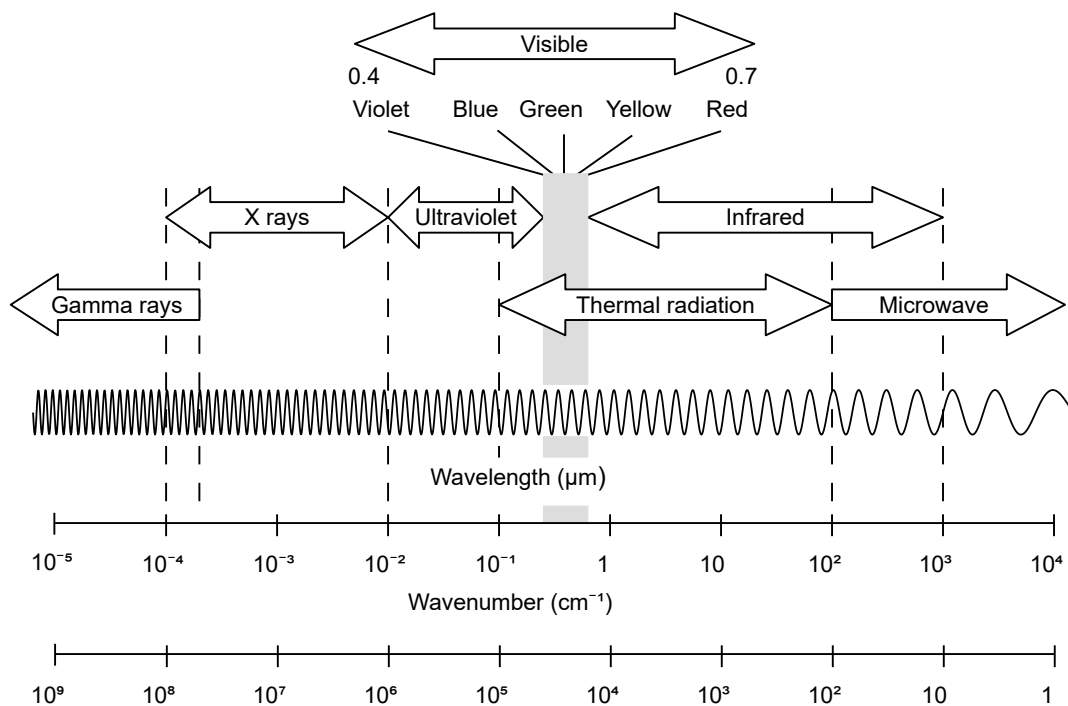

Fig. 2.10 Spectrum of electromagnetic waves in vacuum depending on wavelength or wavenumber [48].

A molecule can raise its energy level when it absorbs an electromagnetic wave (photon). It can lower its energy level by emitting photons or scatter the photons in an other direction. Scattering by gas molecules can always be neglected in heat transfer application because the molecules are far too small to scatter photons [48]. For solid fuel combustion, however, the scattering of the fuel particles must be considered.

Different factors determine the internal energy of a molecule. For example the electrons spinning with different distances around the nucleus, atoms of a molecule rotate around other atoms in the molecule bonding or vibrate against each other. Since the energy of a photon is directly proportional to the frequency, for *bound-bound* transitions (transitions between non-dissociated atomic or molecular states) a certain wavelength is necessary in order to change the energy level by capturing or releasing of the photon. For changing the orbit of an electron, high energy or short wavelengths are necessary in the range of $0.01\,\mu m$ up to $1.5\,\mu m$. For changing of vibration energy levels with wavelengths between $1.5\,\mu m$ and $10\,\mu m$ are required where for change of rotation the wavelengths can be higher than $10\,\mu m$. Since the change in vibration energy level usually occurs in conjunction with the change in rotational energy, the spectral lines are often close together. Due to line broadening, overlaps occur which leads to *vibration-rotation bands* in the infrared. For temperatures in combustion systems the emissive power has its maximum in the infrared ($1\,\mu m - 6\,\mu m$) so the *bound-bound* transitions and *vibration-rotation bands* are the most important [48]. The molecules can rotate and vibrate as illustrated in Fig. 2.11.
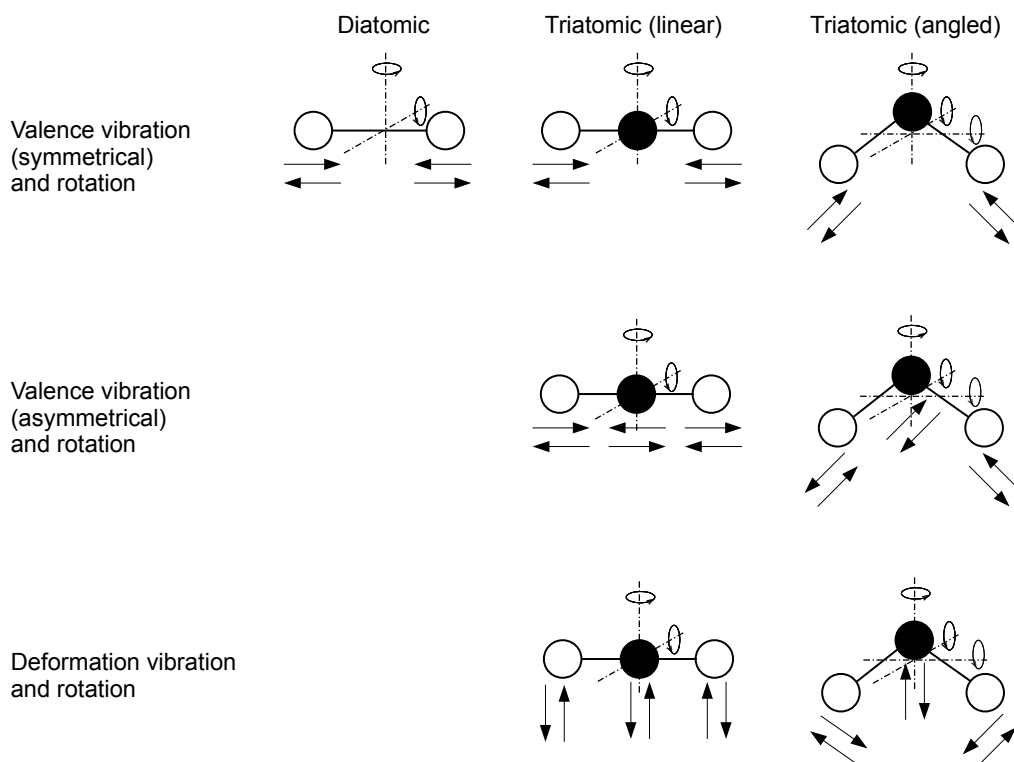

Fig. 2.11 The vibration and rotational degrees of freedom for diatomic, linear and non-linear triatomic molecule structures [51].

Diatomic and polyatomic molecules have three degrees of translation freedom for the molecule in a Cartesian coordinate system and $3N - 3$ degrees of freedom for relative motion between the atoms in a molecule bounding where N is the number of atoms in the molecule.

The atoms in diatomic molecules can rotate around their gravity center where the rotation motion in a plane is equal to two degrees of freedom for each atom. The last degree of freedom leads to the vibration mode. For linear triatomic molecules (e.g. CO_2) there are also only two rotation modes but four vibration modes since the molecule has three atoms (3×3 - $3 = 6$). An angled triatomic molecule (e.g. H_2O) has three degrees of freedom for rotation so there are just three motions left for vibration. An electric dipole is necessary for rotational lines, thus diatomic molecules such as O_2 or N_2 have no rotational transitions. Symmetric molecules show a rotational spectrum only in combination with vibration transition [48, 52]. Fig. 2.12 shows the energy level over the wavenumber spectrum for a rigid rotator (left) and for vibration modes, the harmonic oscillator (right).
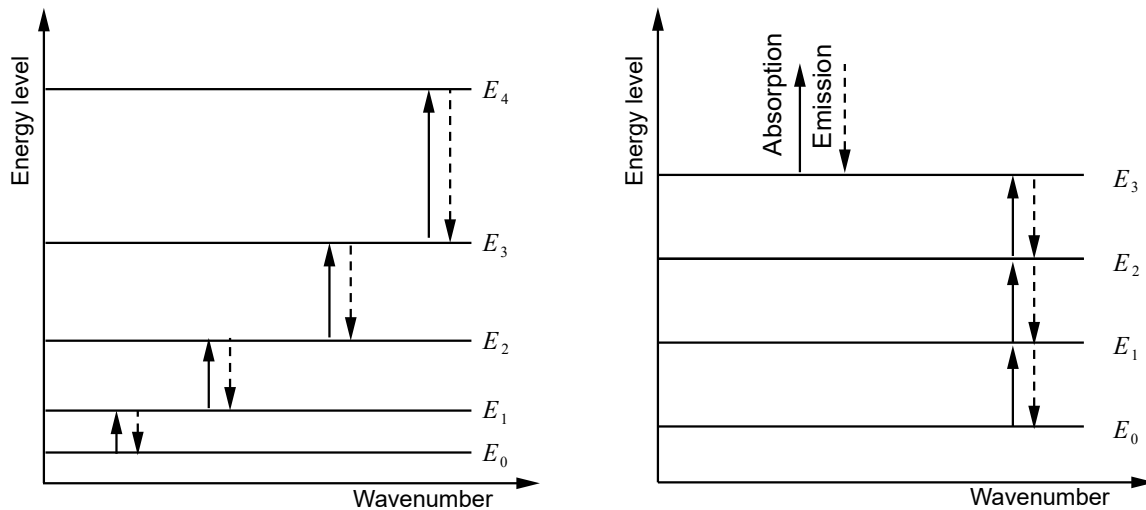
Fig. 2.12 Left: energy level and spectral position for a rigid rotator. Right: energy level and spectral position for a harmonic oscillator [48].

The vibration of molecules is described with point masses connected by massless, perfectly elastic springs. Such a model is called *harmonic oscillator*. In Fig. 2.13 the energy level for each vibration mode and the distance between two atoms is shown. The solid line delimits the horizontal lines which are the energy levels and marks the possible distance between the two atoms during vibration. If the energy level becomes too high, molecules can dissociate.

The required energy to change the vibration state is significantly higher than the energy for changing the rotating state. In addition, both motions often occur at the same time. This results in many lines laying close together called *vibration-rotation band* [48].

The emission of photons from a molecule can either be *spontaneous*, *induced* or *stimulated*. Spontaneous emission is random and isotropic, this means the intensity is equally emitted in all directions. The maximum spectral blackbody intensity $I_{b\eta}$ at given wavenumber η and
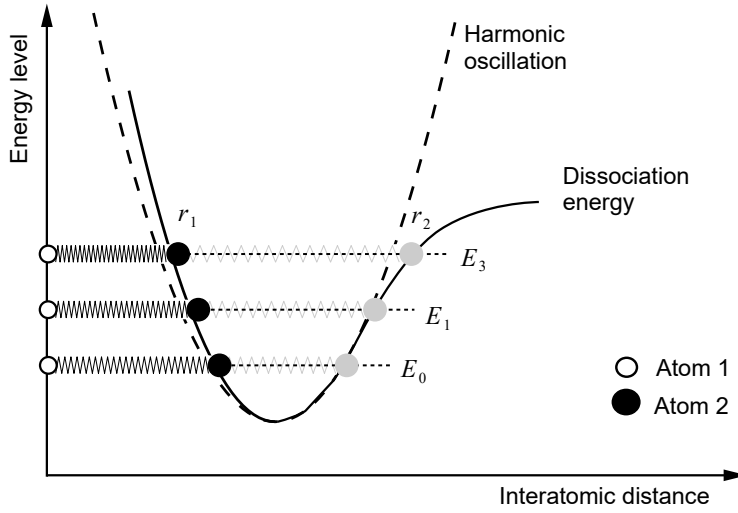
Fig. 2.13 Energy levels and interatomic distance for molecular vibration. Molecular bounding is illustrated by a mechanical spring [48]. The gray spring-mass sketches represent the maximum possible deflection.

temperature T can be described by the *blackbody emissive power* distribution or *Planck's law*, Eq. (2.17):

$$I_{b\eta}(T,\eta) = \frac{1}{\pi} \frac{C_1 \, \eta^3}{n^2 \, e^{C_2 \, \eta/T} - 1}. \tag{2.17}$$

The parameter n is the *refractive index* of the medium and is equal to 1.00029 for air at room temperature. The radiation constants C_1 and C_2 in the blackbody emissive power equation are defined as:

$$C_1 = 2\pi \, h \, c_0^2 = 3.7428 \times 10^{-12} \text{ W\,cm}^2,$$
$$C_2 = h \, c_0/k = 1.4388 \text{ cm\,K},$$

where h is the *Planck constant*, c_0 the speed of light in vacuum or the velocity of the photons and k is the *Boltzmann constant* [48]. The integration of Eq. (2.17) over the entire spectrum leads to the *total blackbody intensity*:

$$I_b(T) = \int_0^\infty I_{b\eta}(T,\eta) \, d\eta = \frac{n^2 \, \sigma \, T^4}{\pi}, \tag{2.18}$$

where σ is the so called *Stefan-Boltzmann constant* which has a value of $\sigma = 5.670 \times 10^{-12}$ W\,cm^{-2}K^{-4}. This equation shows that a small change in temperature, due to the power of 4, causes a significant change in radiative intensity. The spectral blackbody intensity is illustrated in Fig. 2.14 for different temperatures.

Absorption and emission of a gas strongly depends on the temperature, pressure and concen-
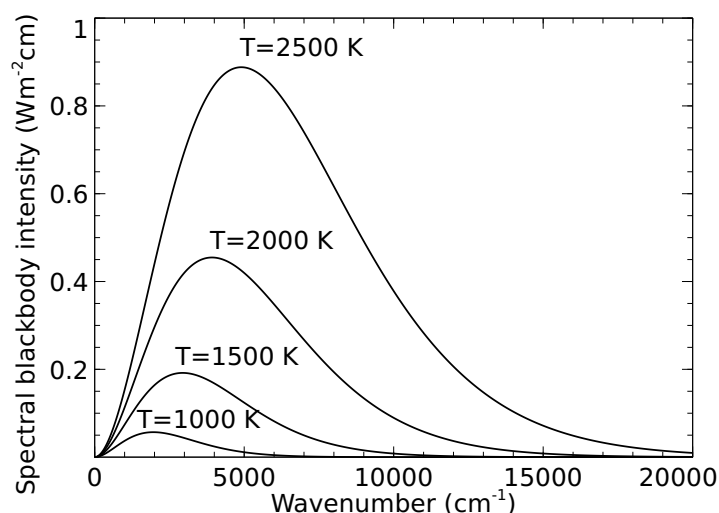
Fig. 2.14 Spectral blackbody intensity for different temperatures plotted against the wavenumber [50].

tration of the medium, as well as the wavelength of the photon passing through the medium. In Chapter 3 it is shown how the absorption coefficients of different gases and mixtures can be calculated from a spectral database for use in radiation models.

2.3.2 Particle radiation

In solid fuel combustion, a high amount of radiative heat transfer is caused by glowing fuel particles. The heat-up of fuel particles and therefore the ignition depends primarily on the absorption of thermal radiation from hot gases [46, 48]. Some radiative emissions from the flame have wavelengths where no vibration-rotation bands exists for the species composition and therefore the flame sending out light, visible to the human eye called *luminous*. The luminous emission comes from very small particles during the oxidation of soot [53].

In atmospheres containing small particles, electromagnetic waves or a photon can either be absorbed and/or scattered, changing the radiative intensity. The strength and direction of scattering depends on [53]:

- Particle shape

- Material of the particle

- The relative size

- The clearance between particles

Scattering is caused by three effects: *diffraction*, where electromagnetic waves have no contact with particles but are affected by their presence, *reflection in a particle* and *reflection by a particle*. Scattering is called *independent scattering* when the scattering effect at one particle is not effected by surrounding particles. Most of the electromagnetic waves scattered *elastically*

which means that their wavelength remain unchanged. The radiative properties of a particle cloud[1] can be expressed with three parameters [53]:

$$\text{Complex index of refraction: } m = n - i\,k, \tag{2.19}$$

$$\text{Size parameter: } x = \pi\,d/\lambda, \tag{2.20}$$

$$\text{Clearance-to-wavelength ratio: } c = x/\lambda, \tag{2.21}$$

where n is the real part and k the imaginary part of the complex index of refraction. The wavelength is designated as λ and d is the particle diameter. Instead of the clearance-to-wavelength parameter c, the volume fraction f_v according to Eq. (2.22) can be used:

$$f_v = \int_0^\infty \frac{1}{6}\,\pi\,d^3\,n(d)\,d\,d, \tag{2.22}$$

where $n(d)$ is the *particle distribution function*. In engineering applications, the particle shape is often approximated as a sphere. The particle clouds can be treated as independent since the volume fraction is mostly smaller than 0.006, or higher than 0.5 for the clearance-to-wavelength ratio according to Tien et al. [54]. The limits for the independent scattering are shown in Fig. 2.15, depending on their application.
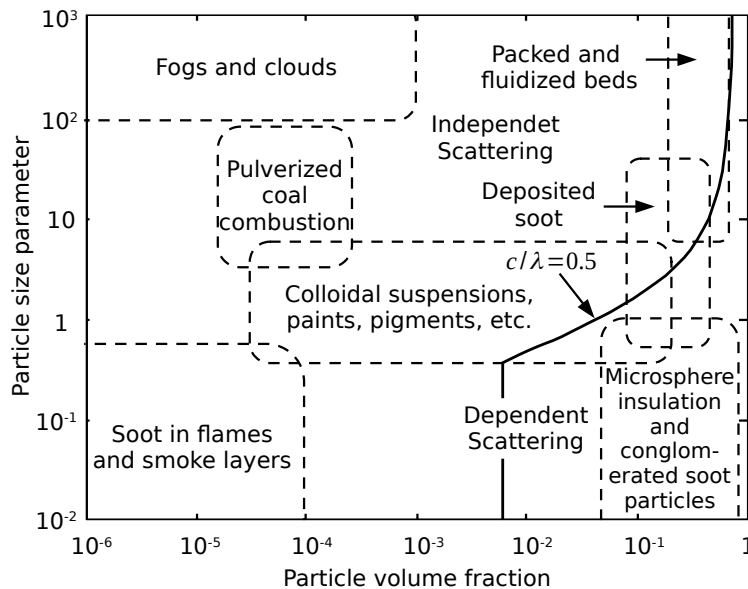
Fig. 2.15 Map of independent and dependent scattering with application areas for particle size parameter plotted against particle volume fraction [54].

If the particle is approximated as perfect single sphere, for very small particles $x \ll 1$ scattering can be neglected compared to the absorption. For large particles, most of the photons scattered in the forward direction. This effect can be calculated with the *Mie-Theory* [55].

---

[1]Particle clouds are a collection of uniform size, or non-uniform size (spherical) particles for easier handling of a large number of particles in the domain.

Since the scattering direction calculated by the Mie-Theory is too time expensive for practical applications, the scattering angle θ can be described by an averaged cosine, called the *asymmetry factor* g which can also be expressed with the scattering phase function $\Phi(\theta)$ integrated over all solid angles Ω, Eq. (2.23):

$$g = \overline{\cos(\theta)} = \frac{1}{4\pi} \int_{4\pi} \Phi(\theta) \cos(\theta) \, d\Omega. \tag{2.23}$$

The scattering of the electromagnetic wave by the particle depends on the wavelength and the diameter of the particle. An example for ray scattering on different particle-wavelength relation is shown in Fig. 2.16. For *isotropic scattering*, which means the same amounts scattered in all directions, the scattering phase function becomes 1 and the asymmetry factor is 0 [53]. This effect is also called the Rayleigh scattering [56] (c.f. Fig. 2.16, top). If g becomes 1, most of the radiative intensity is scattered in the forward direction. If g becomes -1, most of the radiative intensity is scattered in the backward direction.
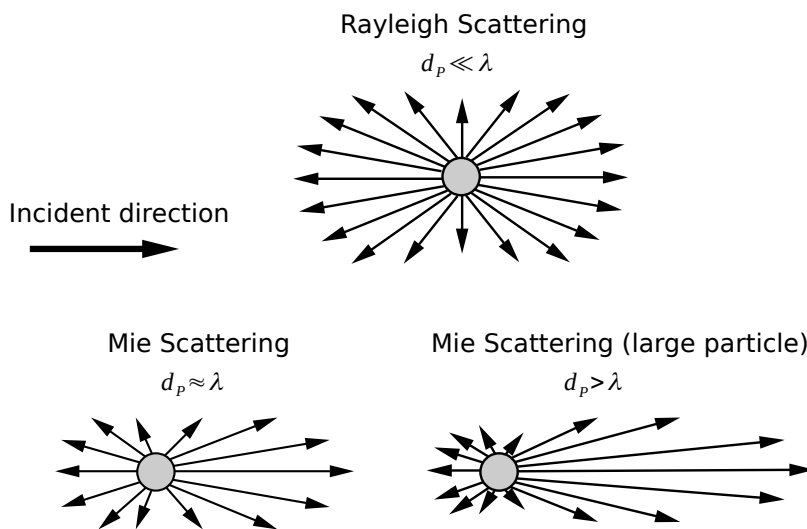
Fig. 2.16 Mie and Rayleigh scattering on a particle with different particle-wavelength relations.

2.3.3 Soot radiation

Soot is formed in almost all combustion processes where hydrocarbon gases or carbonaceous solids are oxidized. Soot occurs as an end product of incomplete combustion or as an intermediate product in flames. While soot as an end product is considered an environmentally harmful emission and should be avoided if possible, it is desirable as an intermediate product in many combustion processes to increase heat transfer through thermal radiation [57]. Particularly in diffusion flames, a high soot loading up to 10^{-4} % [48, 58–60] of the flame occurs, whereby a high proportion of the heat transfer takes place through thermal radiation. The formation mechanism of soot is still the subject of research today, as there are still unanswered

questions. Since soot has a very small size parameter x in the infrared spectrum, scattering of electromagnetic waves by soot particles can be assumed with Rayleigh theory and therefore scattering can be neglected, only the absorption of soot have to be taken into account. Since soot particles have diameters of a few nanometers, they can be assumed to have the same temperature as the gas phase [48].

The formation of soot increases the heat loss through radiation in a flame and thus reduces the reaction efficiency. The formation of soot in a combustion process depends on the ratio of elementary oxygen to carbon content in the fuel, Eq. (2.24) [61]:

$$\frac{\mathsf{O}}{\mathsf{C}} = \frac{n_{\mathsf{O}_2}/n_{fuel}}{(n_{\mathsf{O}_2}/n_{fuel})_{st}}. \tag{2.24}$$

As the O/C values increase, the formation of soot decreases. Where $n_{\mathsf{O}_2}/n_{fuel}$ is the molar ratio of oxidizer and fuel and $(n_{\mathsf{O}_2}/n_{fuel})_{st}$ the molar ratio of oxidizer and fuel at stoichiometric conditions [25, 61]. In pulverized fuel combustion, the soot concentration is relatively low compared to the particle concentration and is therefore neglected for the calculation of radiative heat transfer [50].

3 Modeling of Radiative Heat Transfer

Thermal radiation can be described most accurately with a line-by-line method (LBL) in which a conservation equation is solved in the system for each spectral line and all thermal rays are traced through the entire domain. LBL calculations are very computationally intensive and therefore not practical in engineering applications. Modeling of thermal radiation, especially for application in CFD codes, is mainly limited to simple models for ray directions as well as absorption, emission and scattering within the participating medium. However, it is important that the models provide accurate results despite their simplicity.

The C++ based open-source code OpenFOAM® version 2006 was used for calculation of radiative heat transfer. The models for gas and soot radiation absorption, which are described in this chapter, have been implemented into the original code. In addition, the code has been extended to allow integration using the Gaussian-quadrature method. This enables coupling with CFD and combustion simulations. Furthermore, a description is given of how the necessary absorption coefficients and absorption distribution functions of the combustion gases, used in the absorption models, are calculated from a spectral database using a stand-alone C++ code. In the last section of this chapter, the code implemented in OpenFOAM® is verified with the results by Kez et al. [62] who analyzed the described models in a stand-alone radiation solver based on the programming language Fortran 95.

3.1 Radiative Heat Transfer Equation

A radiative intensity ray or photon with a fixed direction traveling through an media, can either be absorbed by the media, scattered or increasing its intensity by *in-scattering* from an other direction, illustrated in Fig. 3.1.
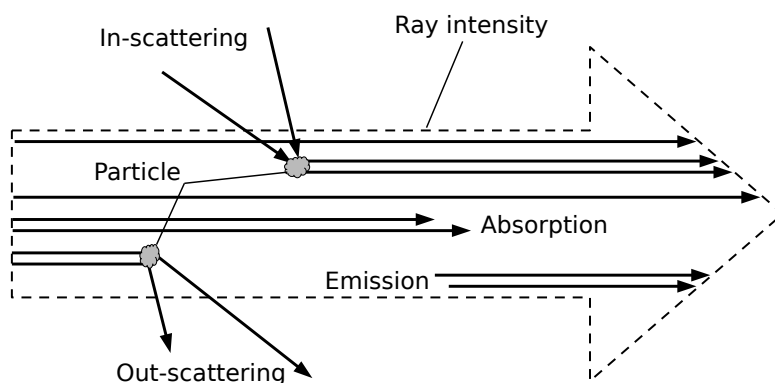
Fig. 3.1 Considered ray with photon beams (solid arrows) traveling trough a media. Increasing ray intensity by emission and in-scattering; decreasing by absorption and out-scattering. The radiative intensity is illustrated as a dashed arrow.

The increase or decrease of radiative intensity I can be described by Eq. (3.1) the so-called *Radiative Transfer Equation* (RTE). A peculiarity of this partial differential equation is that it contains an integral term resulting in an *integro-differential equation*. This term describes the

sum of all rays from other directions which are scattered into the considered ray.

$$\frac{dI_\eta}{ds} = \kappa_\eta \, I_{b\eta} - \beta_\eta \, I_\eta + \frac{\sigma_{s,\eta}}{4\pi} \int_{4\pi} I(\hat{s}') \, \Phi_\eta(\hat{s}' \to \hat{s}) \, d\Omega'. \tag{3.1}$$

The absorption by gas molecules and particles is described with the spectral absorption co-efficient κ_η. The spectral extinction coefficient $\beta_\eta = \kappa_\eta + \sigma_{s,\eta}$ is the sum of absorption and out-scattering. The spectral scatter coefficient $\sigma_{s,\eta}$ describes the amount of out-scattered intensity. The spectral *scattering phase function* $\Phi_\eta(\hat{s}' \to \hat{s})$ indicates the probability of in-scattering with a numerical range from zero to one. The unit vector $\hat{s}'$ is the incoming direction and $\hat{s}$ the outgoing direction [50].

A common quantity in the field of radiative heat transfer calculations is the *incident radiation* G, which results from the integration of the radiation intensity over all solid angles Ω_i, Eq. (3.2) and Eq. (3.3):

$$G_\eta = \int_{4\pi} I_\eta \, d\Omega \approx \sum_i^{N_{ray}} I_{i,\eta} \, \Delta\Omega_i, \tag{3.2}$$

$$G = \int_0^\infty G_\eta \, d\eta \approx \sum_i^{N_{band}} G_{i,\eta} \, \Delta\eta. \tag{3.3}$$

To calculate the enthalpy in a system, the radiation energy must be taken into account. This is done by calculating the divergence of the heat flux density $\nabla \cdot q$ within the medium, Eq. (3.4) and Eq. (3.5) the so-called *radiative source term*. The radiative energy stored in the volume, emitted and absorbed are balanced [48].

$$\nabla \cdot q_\eta = \kappa_\eta \, (4\pi \, I_{b\eta} - G_\eta) \approx \kappa_\eta \left(4\pi \, I_{b\eta} - \sum_i^{N_{ray}} I_{i,\eta} \, \Delta\Omega_i \right), \tag{3.4}$$

$$\nabla \cdot q = \int_0^\infty \nabla \cdot q_\eta \, d\eta \approx \sum_i^{N_{band}} \nabla \cdot q_{i,\eta} \, \Delta\eta. \tag{3.5}$$

For practical applications, the *radiative heat flux* on the boundaries is the most important value to get knowledge about the amount of transferred heat by thermal radiation to the walls. In most industrial boilers the evaporator is located at the walls of the chamber where radiative heat transfer dominates in the flame region. Furnace walls can be assumed as diffusely emitting and reflecting, so the radiative intensity is independent of direction [50, 63]. The

total radiative heat flux q_{tot} in Eq. (3.8) consists of the incident radiative heat flux $q_{\eta,in}$ into the wall Eq. (3.6), the emitted and reflected radiative heat flux by the wall $q_{\eta,out}$ Eq. (3.7). If the wall is assumed as blackbody ($\epsilon_{\eta,w} = 1$) $q_{\eta,out}$ only depends on the wall temperature.

$$q_{\eta,in} = \int_{\hat{\boldsymbol{s}} \cdot \hat{\boldsymbol{n}} > 0} I_\eta \left(\hat{\boldsymbol{s}} \cdot \hat{\boldsymbol{n}} \right) d\Omega, \tag{3.6}$$

$$q_{\eta,out} = \epsilon_{\eta,w} \, \pi \, I_{b\eta,w} + \left(1 - \epsilon_{\eta,w} \right) \int_{\hat{\boldsymbol{s}} \cdot \hat{\boldsymbol{n}} > 0} I_\eta \left(\hat{\boldsymbol{s}} \cdot \hat{\boldsymbol{n}} \right) d\Omega, \tag{3.7}$$

$$q_{tot} = \int_0^\infty q_{\eta,in} \, d\eta - \int_0^\infty q_{\eta,out} \, d\eta. \tag{3.8}$$

3.2   Angular Discretization

In order to describe the directions of radiative beams or photons traveling through the domain, different procedures exist in the literature. The most precise method is the *Ray Tracing Method*, where a huge amount of rays traced through the whole domain. However, this method is far too computationally intensive for practical applications. The *Monte Carlo Method* can provide a remedy here, which uses a certain number of random directions to approximate ray tracing of all possible directions. Simpler methods for modeling ray directions that are commonly used in CFD codes as the *Discrete Ordinates Model* (DOM) and the P_1 model are described below. The equations are described according to the implementation in the open-source code OpenFOAM® version 2006 and are used in this form for the radiation calculations.

3.2.1   Discrete Ordinates Model

The DOM in the source-code is a derived model by Murthy and Mathur [64] for application of the original DOM by Carlson and Lathrop [65] to finite volume methods. Therefore the change of radiative intensity in a specific direction can be described with a general transport equation (cf. Eq. (4.1) in the next chapter). This version of the DOM is also called the *Finite Volume Discrete Ordinates Model*. A hemisphere is divided in equally spaced zones by defining a fixed number of *solid angles*[1]. Fig. 3.2 shows the spatial properties in a hemisphere for a single solid angle.

The angular discretization is described by an azimuthal angle φ and a polar angle θ in a polar coordinate system. The direction vector in the center of the solid angle $\boldsymbol{d}_i$ is calculated according to Eq. (3.9):

---

[1]A solid angle is the pendant to an angle in a two dimensional area. It is the three dimensional share of the entire volume.
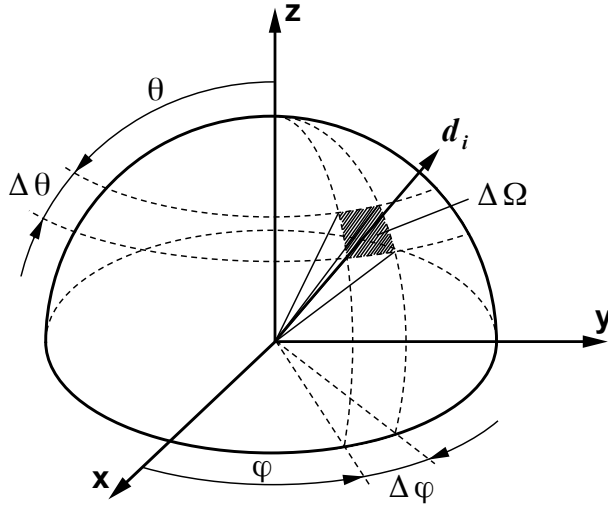
Fig. 3.2 Properties of a solid angle for angular discretization using the Finite Volume Discrete Ordinates Model.

$$
\boldsymbol{d}_i = \begin{pmatrix} \sin(\theta_i) \sin(\varphi_i) \\ \sin(\theta_i) \cos(\varphi_i) \\ \cos(\theta_i) \end{pmatrix}. \tag{3.9}
$$

To account for the proportion of a solid angle inside the volume, the averaged direction vector $\overline{\boldsymbol{d}_i}$ is determined by Eq. (3.10):

$$
\overline{\boldsymbol{d}_i} = \begin{pmatrix} \sin(\varphi_i) \sin\left(\frac{1}{2}\Delta\varphi_i\right)\left(\Delta\theta_i - \cos\left(2\theta_i\right)\sin\left(\Delta\theta_i\right)\right) \\ \cos(\varphi_i) \sin\left(\frac{1}{2}\Delta\varphi_i\right)\left(\Delta\theta_i - \cos\left(2\theta_i\right)\sin\left(\Delta\theta_i\right)\right) \\ \frac{1}{2}\Delta\varphi_i \sin(2\theta_i) \sin(\Delta\theta_i) \end{pmatrix}. \tag{3.10}
$$

To transfer $\overline{\boldsymbol{d}_i}$ to the numerical mesh, the inner product $(\overline{\boldsymbol{d}_i} \cdot \boldsymbol{n}_f)$ of $\overline{\boldsymbol{d}_i}$ and the normal vector of the cell faces $\boldsymbol{n}_f$ is calculated. The result of this calculation is illustrated in Fig. 3.3, by means of a single mesh-cell.
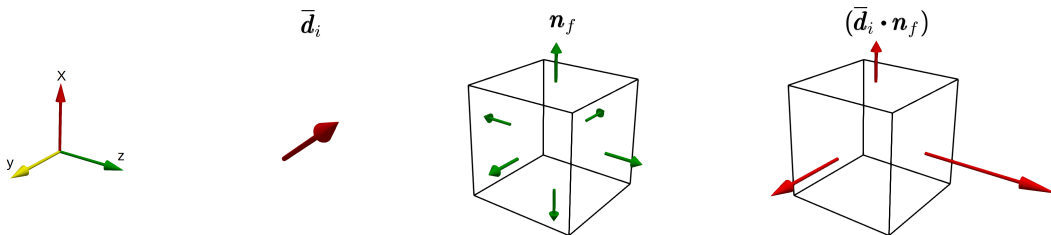
Fig. 3.3 Left: vector example for a solid angle to be calculated (red). Middle: normal vectors on the cell faces (green). Right: resulting vectors of the solid angle for each cell face after inner product with the face normal vectors (red).

The solid angle $\Delta\Omega_i$ is used in the RTE of the DOM as a weight parameter for the intensity. It can be calculated with Eq. (3.11) using both distances $\Delta\varphi = \pi/2/n_\varphi$ and $\Delta\theta = \pi/n_\theta$ of two adjoining direction vectors [66]:

$$\Delta\Omega_i = 2\sin(\theta_i)\sin\left(\frac{\Delta\theta}{2}\right)\Delta\varphi. \tag{3.11}$$

The total number of rays results in $4 \times n_\varphi \times n_\theta$. The RTE of the DOM is given in Eq. (3.12). For a conservative formulation of the RTE, the radiative intensity multiplied by the absorption coefficient and the weight factor is transferred to the left hand side of the equation:

$$\nabla \cdot \left[(\bar{\boldsymbol{d}}_i \cdot \hat{\boldsymbol{n}}_f)\, I_{i,\eta} \right] + \kappa\, I_{i,\eta}\, \Delta\Omega_i = \frac{1}{\pi}\left(\kappa_\eta\, E_{b\eta} + E_\eta\right)\Delta\Omega_i, \tag{3.12}$$

where $E_{b\eta}$ and E_η are the volumetric contributions of blackbody emission and an additional source term, which is not used here. The absorption coefficient consists of gas absorption and particle absorption ($\kappa_\eta = \kappa_{gas,\eta} + \kappa_{p,\eta}$). In Fig. 3.4 a varying number for the azimuthal and the polar angle is shown, by means of a single mesh-cell.
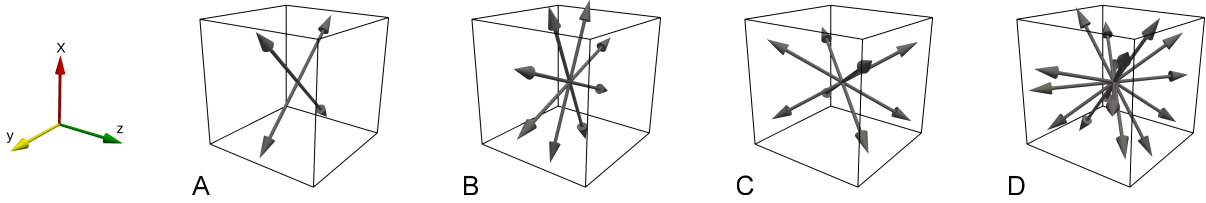
Fig. 3.4 Variation of solid angles: (A) $n_\varphi = 1$, $n_\theta = 1$ (B) $n_\varphi = 2$, $n_\theta = 1$ (C) $n_\varphi = 1$, $n_\theta = 2$ (D) $n_\varphi = 2$, $n_\theta = 2$.

The boundary conditions of the DOM are set to an opaque wall condition with diffuse reflecting radiation. The radiative heat flux at the wall of the domain can be calculated according to Eq. (3.8). The standard DOM in OpenFOAM® includes two integration loops, one integration over spectral bands, second integration over solid angles. An additional loop is implemented to account for Gaussian-quadrature, which is explained later.

3.2.2 P₁ approximation model

This model is based on the spherical harmonics method (P_N), which develops a series of functions, orthogonal to the unit-sphere, for the spectral intensity. The P_1 model is a first order approximation where the function is developed until the fourth term. This results in a differential equation which can be described as transport equation, so the radiative energy is conserved [48, 67]. The transported quantity is the incident radiation G. The P_1 is often used in engineering applications, because of its simplicity and fast calculation. A disadvantage of

this model is that it is only accurate in linear near-isotropic radiative intensity. It also fails if the intensity has strong directional gradients, which is often the case for optically thin media [48, 68].

A scalar function on the surface of the sphere with a unit radius is developed with a two-dimensional generalized Fourier series in Eq. (3.13):

$$I(\boldsymbol{r},\,\hat{\boldsymbol{s}}) = \sum_{n=0}^{\infty} \sum_{m=-n}^{n} I_n^m(\boldsymbol{r})\, Y_n^m(\hat{\boldsymbol{s}}). \tag{3.13}$$

The radiative intensity uses $\hat{\boldsymbol{s}}$ as direction unit vector and is surrounding the point $\boldsymbol{r}$. The *spherical harmonics basis functions* $Y_n^m(\theta, \psi)$ expressed with polar and azimuthal angles (θ and ψ) is given in Eq.(3.14) [48]:

$$Y_n^m(\theta, \psi) = \begin{cases} \cos(m\psi)\, P_n^m(\cos\theta), & m \geq 0 \\ \sin(m\psi)\, P_n^m(\cos\theta), & m \leq 0 \end{cases}. \tag{3.14}$$

The *associated Legendre polynomials* are expressed by

$$P_n^m(\mu) = (-1)^m\, \frac{(1-\mu^2)^{|m|/2}}{2^n\, n!}\, \frac{d^{n+|m|}}{d\mu^{n+|m|}}\, (\mu^2 - 1)^n, \tag{3.15}$$

where Eq. (3.15) includes a differential of the order $n + |m|$. For the P_1 approximation, n in Eq. (3.13) is set to 1. Using the first order approximation in combination with the general RTE, Eq. (3.1) leads to the final spectral formulation in Eq. (3.16):

$$\nabla \cdot (\Gamma_\eta\, \nabla G_\eta) - \kappa_\eta\, G_\eta = -4\, \kappa_\eta\, \sigma\, T^4 - E_\eta, \tag{3.16}$$

where E_η is an additional source term. The *diffusion coefficient* Γ_η for the diffusion term in transport Eq. (3.16) is substituted with

$$\Gamma_\eta = \frac{1}{3\, \kappa_\eta + C\, \sigma_{s,\eta}}. \tag{3.17}$$

The factor C is the linear-anisotropic phase function with a range of -1 (backward scattering) to 1 (forward scattering) and 0 (isotropic scattering).

At the walls of the geometry, the *Marshak boundary condition* [69] is used for the P_1 to eliminate the angular dependency [70]. This boundary condition is defined according to Eq. (3.18) as the negative product of Γ_η and the surface normal gradient of the incident radiation

on a diffuse surface:

$$q_{\eta,tot} = -\Gamma_\eta \frac{\partial G_\eta}{\partial \boldsymbol{n}} = -\frac{\epsilon_w}{2\,(2-\epsilon_w)}\,(4\,\pi\,I_{b\eta,w} - G_{\eta,w})\,. \tag{3.18}$$

P_N approximations with an order higher than one can quickly become complex, even for simple geometries [48]. Therefore, most CFD codes probably do not include them. In Fig. 3.5 the real part of some spherical harmonics are illustrated [68]. For $m = n = 0$ spherical harmonics become a positive sphere.
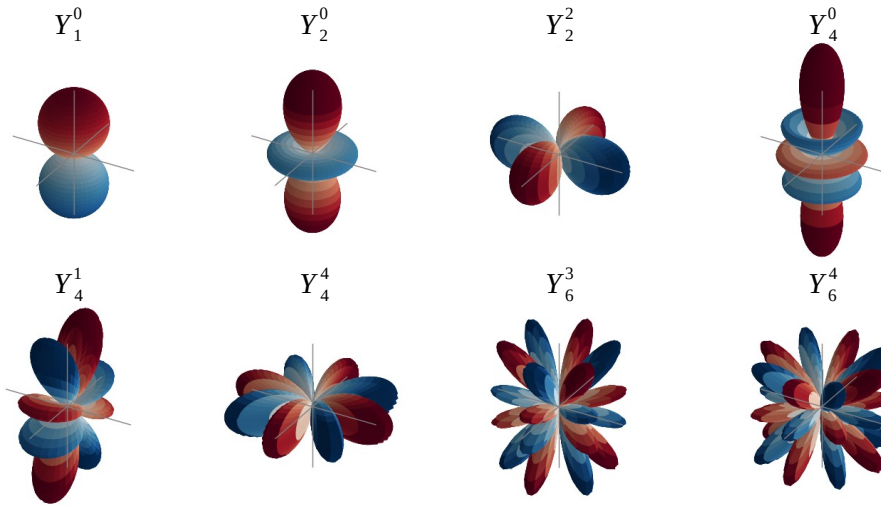
Fig. 3.5 Examples visualization of the real part for spherical harmonics. The blue color indicates where the function is negative and red where the function is positive [68].

The standard P_1 model of OpenFOAM® version 2006 was also extended to allow the use of k-distribution models and Gaussian-quadrature.

3.3   Gas Radiation

The strong wavelength, temperature and pressure dependency of some gas molecules requires models able to predict the variations of gas radiation during simulations. A wide range of different models exist in the literature, for example Statistical Narrow Band models (SNB), Exponential Wide Band models (EWB), Absorption Distribution Function models (ADF) like the Wide Band Correlated-k model (WBCK) and the Full Spectrum k-distribution model (FSK). In CFD, global models are widely used due to their low computing time e.g. the Weighted Sum of Gray Gases model (WSGG) by Hottel and Sarofim [71]. A large number of studies have been carried out in the past on radiation models in an oxyfuel atmosphere. A brief overview is provided here.

Kez et al. [62] compared the spectral resolved Narrow Band Correlated-k model (NBCK) with the Full Spectrum Correlated-k model (FSCK) and WBCK using a virtual coal fired boiler under

oxyfuel conditions with dry and wet flue gas recirculation. They used a stand-alone Fortran 95 code and a Gaussian-Legendre-quadrature for integration. The results of the FSCK were almost identical to the results of the NBCK model with a mean deviation from the radiative source term less than 2 %. The WBCK models showed deviations of up to 29 %. In addition, they compared results of the WSGG with different parameters to the NBCK benchmark solution [62, 72]. Deviations less than 15 % were reached using the WSGG model with parameters of Bordbar et al. [73] and Kangwanpongpan et al. [74]. Liu et al. [75] investigated an hybrid correlated-k solution scheme for the FSCK model, the original FSCK model by Modest and Zhang [76] and the FSCK by Cai and Modest [77] on a 2D laboratory scale dry oxyfuel flame. They used line-by-line (LBL) solutions as benchmark. They concluded based on their investigations that the results of the original FSCK are strongly dependent on the reference temperature, while the FSCK from Cai and Modest exhibits large errors at low temperatures. The hybrid model overcomes these disadvantages [75]. Leiser [78] used the WBCK and the gray Leckner [79] model for the simulation of radiative heat transfer in a 100 kW$_{th}$ gas fired combustion chamber. He came to the conclusion that the high computational effort of the WBCK does not justify the improvement in accuracy [78]. Clements et al. [80] performed CFD simulations of a 250 kW$_{th}$ coal-fired pilot-scale combustion chamber under oxyfuel and air condition, using the FSCK and WSGG model. The results show improved agreement with measurements using an LES instead of a RANS simulation. However, the different radiation models do not show any significant differences in their results [80].

The open-source code OpenFOAM® has become more and more popular for CFD simulation in recent years. Many scientists around the world are developing models based on this code. Therefore, the NBCK, FSCK and WSGG model were implemented here in OpenFOAM® to enable an integration in CFD. The NBCK was implemented to create benchmark solutions. The WSGG was implemented since it is one of the most common used models in CFD applications. The FSCK model is less common in CFD applications, but is a highly accurate global absorption model and was therefore also integrated into the used CFD code. In addition, separate stand-alone codes for the calculation of the spectral absorption coefficients and the absorption distribution were implemented in C++, which are described below.

3.3.1 Determination of spectral absorption coefficients

The absorption models used in this work NBCK, FSCK and WSGG are based on the spectral absorption of combustion gases. These models require a database with spectral absorption coefficients for various gases at different concentrations and temperatures. The spectral absorption coefficients can be calculated from the High Resolution Transmission Molecular Absorption (HITRAN) database which is provided by the Harvard-Smithsonian Center for Astrophysics [81–86]. This database in the version 2010 includes 114.7 million spectral lines for H_2O and 11.2 million for CO_2 which result in 18 and 1.7 GB of data storage, respectively.

The database is calculated theoretically and validated with experimental data [48]. For H_2O, the database shows acceptable results compared to experimental measurements, whereas the CO_2 database overpredicts emissivities above 1000 K. Therefore, more accurate data were produced in Russia for CO_2 leading to the carbon dioxide spectroscopic database (CDSD) with 628 million lines, which aims to be accurate up to 4000 K [48]. The CDSD was incorporated in the current 2010 version of HITRAN [87]. To determine the absorption coefficients, the High-Temperature Molecular Spectroscopic (HITEMP2010) database [87] is used, which corresponds to the HITRAN database for high temperatures. This section provides an overview of the steps to calculate the spectral absorption coefficients as implemented in a stand-alone C++ code to create a database of spectral absorption coefficients.

The spectral absorption in the center of the spectral line is calculated with Eq. (3.19):

$$\kappa_{\eta_0} = \frac{S_{\eta_0}}{\pi \, \gamma_c}, \tag{3.19}$$

where η_0 is the wavenumber in the line center, S the intensity in cm^{-1}/(molecule$\times$cm^{-2}) at standard temperature 296 K and γ the line half-width. The intensity, different from the reference temperature in the database (296 K), is calculated according to Eq. (3.20):

$$S_k(T) = S_k(T_0) \, \frac{Q(T_0)}{Q(T)} \, \frac{1 - e^{-C_2\eta/T}}{1 - e^{-C_2\eta/T_0}} \, \exp\left(\frac{C_2 \, E''}{T_0} - \frac{C_2 \, E''}{T}\right), \tag{3.20}$$

where $S_k(T)$ is the spectral line intensity for the kth transition line and E'' is the lower-state energy. The spectral absorption coefficient can then be calculated using Eq. (3.21) [74]:

$$\kappa_\eta = \rho_N \sum_k S_k(T) \, f_k(\eta). \tag{3.21}$$

Here ρ_N is the number density and $f_k(\eta)$ the line shape function of the kth transition line. The number density in Eq. (3.21) is calculated by using Eq. (3.22):

$$\rho_N = \frac{N_A}{R \, T} \, x_s \, p_a. \tag{3.22}$$

N_A is the Avogadro constant, equal to 6.022141076$\times 10^{23}$ molecules/mole, R is the gas constant, equal to 8.314462618 J mol^{-1} K^{-1}, x_s is the species mole fraction in mole/mole and p_a is the atmospheric pressure (1 atm = 1.01235 bar).

Collision broadening is the most important effect in engineering applications (at pressures of 1 bar or higher and temperatures not far above 2000 K). In Eq. (3.21) the *Lorentz profile*

$f_k(\eta)$ is used for approximation of the *line shape function* and can be calculated using Eq. (3.23). It is a combined effect of collision and natural line broadening [48]:

$$f_k(\eta) = \frac{1}{\pi} \frac{\gamma_k}{\gamma_k^2 + (\eta - \eta_k)^2}. \tag{3.23}$$

Starting from the center of the line, all contributions are summed up for ascending and descending wavenumbers by the program code. Since broadening contribution to other absorption coefficients gets smaller with distance from the line center η_0, the summation is stopped at contributions smaller than 1×10^{-28} cm/molecule and wavenumbers with distances from the center line greater than $50\,\mathrm{cm}^{-1}$ for CO_2 and $500\,\mathrm{cm}^{-1}$ for H_2O. This cut is done to reduce calculation time for the spectral database according to Riviére et al. [88]. Fig. 3.6 shows the spectral line shape for the Lorentz profile. In addition, the shapes of Doppler and Voigt broadening are shown.
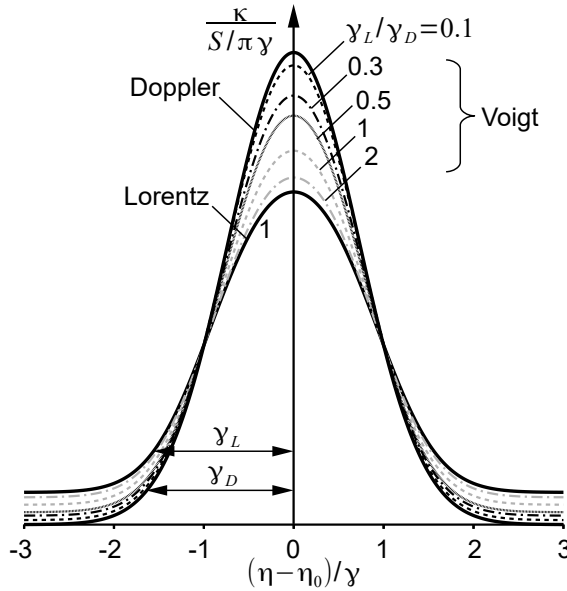
Fig. 3.6 Lorentz, Doppler and Voigt broadening shape for spectral lines. [48].

The pressure broadened line half-width γ_k is calculated according to Eq. (3.24):

$$\gamma_k = \left[\gamma_{self}\, x_s + \gamma_{air}\, (1 - x_s)\right] \left(\frac{T_0}{T}\right)^n p_a, \tag{3.24}$$

where γ_{self} is the self-broadened halfwidth at 296 K, γ_{air} the air-broadened halfwidth at 296 K, n the temperature-dependence coefficient for γ_{air} and T_0 the reference temperature (296 K). The temperature directly affects the contribution from the *partition function $Q(T)$* and the *stimulated emission term* $\exp(-C_2\,\eta/T)$. The partition function is a summation over all possible rotation and vibration energy levels of the molecule. Since the determination of this function is difficult, a separation of the vibration and rotation contribution is a good approximation and leads to Eq. (3.25) [48]:

$$Q(T) \simeq Q_v(T)\, Q_r(T). \tag{3.25}$$

Assuming a harmonic oscillator, the vibration partition function can be calculated by Eq. (3.26) [48, 89]:

$$Q_v(T) = \prod_k \frac{1}{(1 - e^{-C_2 \eta_m / T})^{g_m}}. \tag{3.26}$$

Tab. 3.1 Vibration parameters g_m and η_m for CO_2, H_2O, CO, CH_4, NO and SO_2 [49].

	m	CO_2	H_2O	CO	CH_4	NO	SO_2
g_m	1	1	1	1	1	1	1
	2	2	1		2		1
	3	1	1		3		1
	4				3		1
η_m	1	1351	3652	2143	2914	1876	1151
	2	667	1595		1526		519
	3	2396	3756		3020		1361
	4				1306		

Here η_m are the harmonic oscillation wavenumbers and g_m are the degeneracies of the vibration modes. These quantities can be determined with values from Edwards et al. [49]. The rotation partition function depends on the molecular structure and can be approximated according to Eq. (3.27) [48, 89, 90]:

$$\text{Linear molecules:} \qquad Q_r(T) = \frac{1}{\sigma} \frac{2\, I\, k\, T}{\hbar^2} \sim T, \tag{3.27a}$$

$$\text{Angled molecules:} \qquad Q_r(T) = \frac{1}{\sigma} \prod_{i=x,y,z} \left(\frac{2\, I_i\, k\, T}{\hbar^2} \right)^{1/2} \sim T^{3/2}, \tag{3.27b}$$

where $\hbar$ is the modified Planck's constant $(= h/2\pi)$ and I the isotopologue number, ordering by terrestrial abundance [48].

The spectral absorption coefficient can be averaged by introducing the *Planck-mean-absorption coefficient*. Each spectral absorption coefficient is weighted by their spectral blackbody intensity at the same wavenumber summed up and divided by the total blackbody emission in Eq. (3.28):

$$\kappa_P = \frac{\pi}{\sigma \, T^4} \int_0^\infty I_{b\eta}(T) \, \kappa_\eta \, d\eta. \tag{3.28}$$

The Planck-mean absorption coefficient can be used for evaluation of total intensity or heat flux divergence [48]. In Fig. 3.7 the Planck-mean absorption coefficients, calculated using the HITEMP2010 database for pure CO_2, H_2O and CO at 1 bar, are plotted against temperature and compared to the results of Modest [48] to verify the correctness of the implemented code.
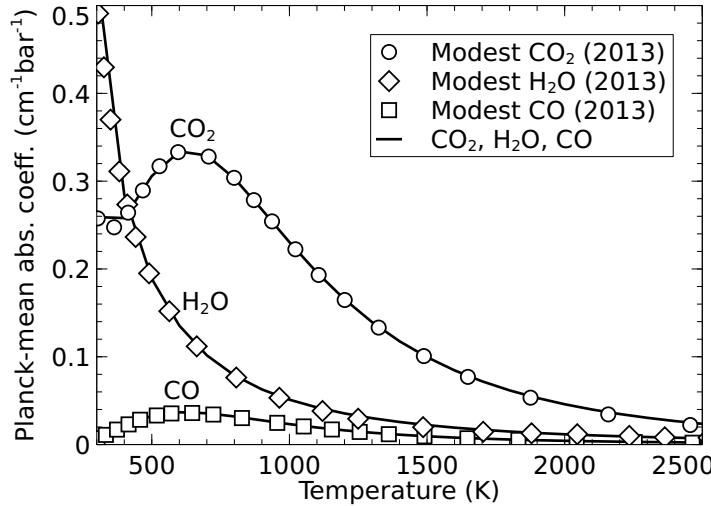

Fig. 3.7 Planck-mean absorption coefficient for pure CO_2, H_2O and CO at 1 bar calculated form the HITEMP2010 spectroscopic database and verification with the results from Modest [48].

The deviation of CO_2 at approx. 250 K is due to the temperature steps of every 100 K used for calculation of the absorption coefficients.

3.3.2 Line-by-line calculation

LBL is the most precise method to calculate the radiative intensity but at the same time the most computing intensive procedure, which make its use not recommended for practical applications. If homogeneous media without scattering is assumed, the RTE becomes:

$$\frac{dI_\eta}{ds} = \kappa_\eta \left(I_{b\eta} - I_\eta \right). \tag{3.29}$$

Since Eq. (3.29) is a first order differential equation, it can be integrated analytically. The integration results in Eq. (3.30):

$$I_\eta(L) = I_{b\eta} \left(1 - e^{-\kappa_\eta L} \right) + I_\eta(0) \, e^{-\kappa_\eta L}. \tag{3.30}$$

This equation can be used to calculate the spectral intensity along a distance L for a certain wavenumber, temperature and absorption coefficient at this wavenumber.

3.3.3 Narrow Band Correlated-k model

To simplify the integration over the spectral range, all absorption coefficients are sorted in ascending order, resulting in a monotonically increasing function, the k-*distribution*. This distribution also avoids multiple calculations of the same absorption coefficient. k-distribution models are mainly studied in the field of radiative heat transfer by Rivière, Soufiani, Taine [88, 91, 92] and Modest [48].

The narrow band model assumes small variation of blackbody intensity within a spectral band, thus the blackbody intensity is set constant within a band. The blackbody intensity is calculated in the center of the narrow band and remains constant in the whole band. Fig. 3.8 shows on the left side the absorption coefficients κ_η for a small spectral range and on the right side the same absorption coefficients as reordered k-distribution.
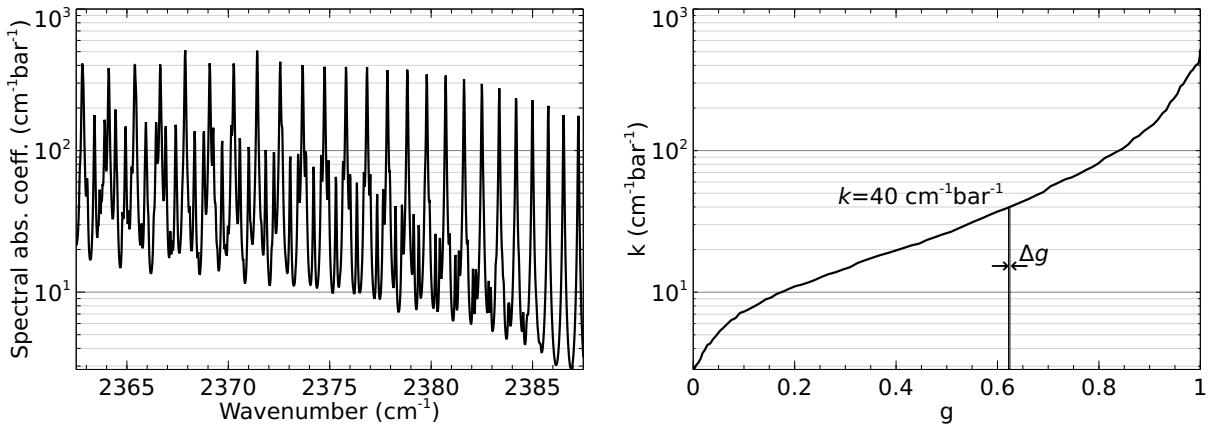

Fig. 3.8 Left: spectral absorption coefficient of pure CO_2 at 1000 K and 1 bar for a bandwidth of 25 cm^{-1}. Right: the same absorption coefficient and range reordered, resulting in the cumulative k-distribution.

In this figure, it can be seen that Δg can be regarded as the share of an absorption coefficient within a band. The cumulative k-distribution $g(k)$ is calculated according to Eq. (3.31):

$$g(k) = \frac{1}{\Delta\eta_{NB}} \int_{\Delta\eta_{NB}} H(k - \kappa_\eta) d\,\eta, \qquad (3.31)$$

where $\Delta\eta_{NB}$ is the width of a narrow band and $H(k)$ is the *Heaviside's unit step function*. It is defined as shown in Eq. (3.32):

$$H(x) = \begin{cases} 0, & x < 0 \\ 1, & x \geq 0 \end{cases}. \qquad (3.32)$$

In this work, equally spaced bandwidths of 25 cm^{-1} in the range of 12.5 cm^{-1} up to 11262.5 cm^{-1} according to Kez [5] are used. This results in a total number of 450 bands. For integration of the k-distribution, the Gauss-Chebyshev-quadrature is used [93]. All k-distributions in

the NBCK database are precalculated for 100 Gaussian abscissas and 450 bands. To reduce calculation time during simulations, the k-distribution for 100 Gaussian points is approximated with seven Gaussian points. Thus, the program has to solve $450 \times 7 = 3150$ RTEs per ray. This constellation is used according to Kez et al. [72].

The implemented NBCK program code first calculates an artificial k-distribution using the highest and lowest absorption coefficient in the considered band to create a distribution. For this, a power distribution is used, as it places more points at smaller k-values than a linear function, but less than a logarithmic function. The artificial distribution is calculated according to Eq. (3.33):

$$k_i = \left[\kappa_{min}^{\beta} + i\,\Delta(k^{\beta}) \right]^{1/\beta}, \quad i = 1, 2 \dots N_k \quad \text{and} \quad \Delta(k^{\beta}) = \frac{\kappa_{max}^{\beta} - \kappa_{min}^{\beta}}{N_k - 1}, \tag{3.33}$$

where β is used as skewness parameter of this function with an empirical value of 0.05 and $N_k = 5000$ for the number of k-points according to Modest and Riazzi [94]. In a next step the code executes two interleaved loops, searching for an artificial k value, similar to the considered absorption coefficients, inside the band. The number of artificial k-point where $k_j \leq \kappa_{\eta} < k_{j+1}$ is then divided by the bandwidth. Therefore the cumulative k-distribution can be expressed numerically by Eq. (3.34):

$$g(k_{i+1}) = g(k_i) + \frac{1}{\Delta\eta_{NB}} \sum_{\eta} H(k_{i+1} - \kappa_{\eta})\,\Delta\eta, \quad i = 0 \dots N_{pt} - 1. \tag{3.34}$$

For conventional reasons, the first bin of the $g(k)$ distribution is set to 0 and the last bin is set to 1. To get the $k(g)$ distribution, the $g(k)$ distribution has to be inverted. This can be done by using the Newton-Raphson scheme [48]. Since the Gaussian abscissas also have a range from 0 to 1, the k-values can be transferred to the Gaussian points.

During simulations in non-homogeneous media, different species mole fractions, different volume fractions of soot and different temperatures occur. To create a mixture cumulative k-distribution a 5D linear interpolation using the NBCK look-up table is done. The look-up table is described in a later section. The RTE of the NBCK model is shown in Eq. (3.35):

$$\frac{dI_{g\eta}}{ds} = k^*(\boldsymbol{\phi}, g)\,(I_{b\eta} - I_{g\eta}) - \sigma_{s\eta}\left(I_{g\eta} - \frac{1}{4\pi} \int_{4\pi} I_{g\eta}(\hat{\boldsymbol{s}}')\,\Phi_{\eta}(\boldsymbol{s}' \rightarrow \boldsymbol{s})\,d\Omega' \right), \tag{3.35}$$

where $k^*(\boldsymbol{\phi}, g)$ is the *correlated k-distribution* and $\boldsymbol{\phi}$ is a vector containing the thermodynamic state of pressure, temperature and mole fraction [48]. Eq. (3.36) shows the numerical calculation of the total radiative intensity for a single ray:

$$I = \int_0^\infty \int_0^1 I_{g\eta} \, dg \, d\eta \approx \sum_{j=0}^{N_\eta} \sum_{i=0}^{N_g} I_{g\eta,i,j} \, w_i \, \Delta\eta_j, \tag{3.36}$$

where w_i is the Gaussian weight.

In this code the maximum deviation of NBCK from the LBL average absorption coefficient is smaller than 2 % for all bands. For the most bands it is smaller than 10^{-4}. In Fig. 3.9, the spectral intensity over a wavenumber range of 12.5 cm^{-1} to 11262.5 cm^{-1} at a pressure of 1 bar and a temperature of 1650 K is calculated with LBL and NBCK. The gas mixture consists of 90 mol% CO_2 and 10 mol% H_2O. Since the LBL method computes a high number of spectral lines, more maxima and minima are visible than for the NBCK. The narrow bands are equally spaced with $\Delta\eta = 25$ cm^{-1} which results in 450 bands. The intensity is calculated along a small path length of 1 m.
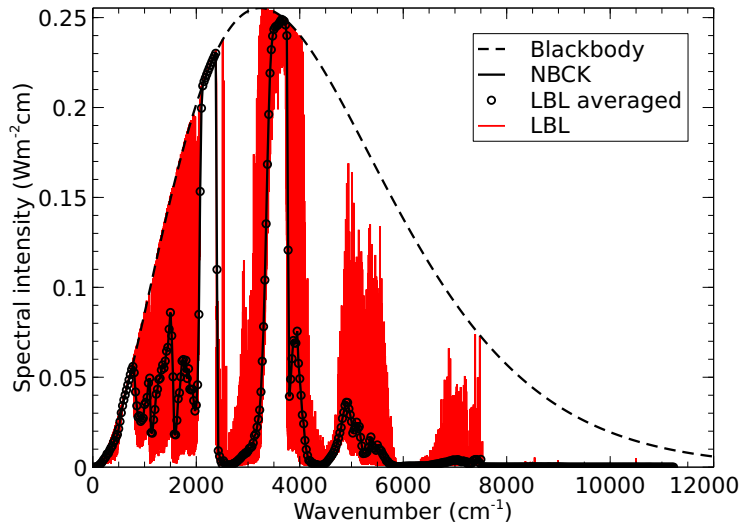

Fig. 3.9 Solutions of RTE calculations over the infrared spectrum using LBL and NBCK along a small path length of 1 m. The gas mixture consists of 90 mol% CO_2 and 10 mol% H_2O. The temperature is 1650 K and the pressure 1 bar.

Since no differences can be seen in the LBL results due to the high amount of spectral lines, the LBL calculation is shown averaged, in addition. The LBL calculation is averaged over each calculated band (25 cm^{-1}) of the NBCK. It can be seen that there is good agreement between the averaged LBL calculation and the NBCK model.

3.3.4 Full Spectrum Correlated-k model

In comparison to the NBCK model which assumes constant blackbody intensity within a narrow band, this assumption can not be made for the FSCK model since the RTE is integrated over the entire spectrum. Therefore no other property except of the absorption coefficient varies over the spectrum. Similar to the NBCK model, the distribution of the absorption coefficients for the FSCK is reordered in a monotonically increasing k-distribution. As already mentioned the RTE is integrated over the full spectrum, the blackbody intensity has to vary. This model is also valid for arbitrary scattering media and reflecting surfaces [48, 53, 76]. Before

the correlated version of this model is described, the determination of the Full Spectrum k-distribution (FSK) is shown first.

Full spectrum k-distribution   The cumulative k-distribution of the FSK can be calculated using Eq. (3.37):

$$g(T_P, \boldsymbol{\phi}, k) = \frac{1}{E_b(T_P)} \int_0^\infty H\left(k - \kappa_\eta(\boldsymbol{\phi})\right) \, E_{b\eta}(T_P) \, d\eta, \qquad (3.37)$$

where $E_b(T_P)$ is the total blackbody emission over the entire spectrum at Planck temperature and $\boldsymbol{\phi} = (p, T, x_i)$ for the local conditions. The k values are calculated by inverting Eq. (3.37). Therefore an artificial distribution similar to the NBCK distribution is created with Eq. (3.33). Now k_{min} is the minimum and k_{max} the maximum absorption coefficient of the entire spectrum. The artificial full spectrum k-distribution is calculated similar to the narrow band distribution using a number of 5000 bins i and and an exponent of 0.1 according to Modest [48]. This leads to the numerical calculation in Eq. (3.38):

$$g(T_P, \boldsymbol{\phi}, k_{i+1}) = g(T_P, \boldsymbol{\phi}, k_i) + \frac{1}{E_b(T_P)} \sum_\eta H(k_{i+1} - \kappa_\eta) \, E_{b\eta}(T_P), \qquad (3.38)$$

$$\text{with } i = 0 \dots N_{pt} - 1,$$

where $g(T_P, \boldsymbol{\phi}, k_{i=0})$ is set to 0 by definition [48]. An example for a full spectrum cumulative k-distribution is shown in Fig. 3.10 for 10 mol% CO_2, 90 mol% N_2, 1 bar and a temperature of 1000 K. The spectral absorption coefficients are calculated wit HITEM2010, once with a wing cut-off of 50 cm^{-1} and an intensity cut-off of 10^{-28} cm/molecule. In addition, one distribution is calculated only with an intensity cut.
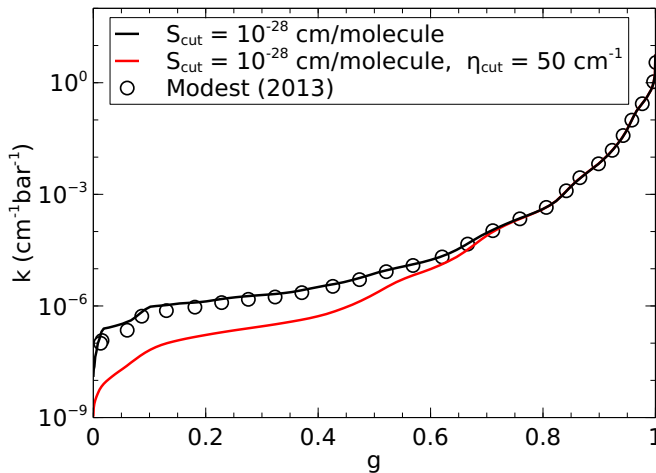

Fig. 3.10 Full spectrum k-distribution calculated with 10 mol% CO_2 and 90 mol% N_2, at 1 bar and 1000 K. Results without broadening limitation (black line) and limitation of 50 cm^{-1} (red line). Verification with the results of Modest (circles) [48].

Both results are compared to the distribution created by Modest [48] to verify the correctness of the implemented code. Since the distributions only differ significantly from Modest k-distribution at values below 10^{-4} cm^{-1}bar^{-1}, the limit of 50 cm^{-1} for CO_2 is acceptable. A wing cut of 500 cm^{-1} is used for H_2O and CO to reduce the calculation time, according to Rivière and Soufiani [88].

Correlated k-distribution Since the creation of a full spectrum k-distribution for each possible thermodynamic state would be time expensive and leading to large data storage, different versions of the FSCK model exist. Correlated k-distributions can either be found by correlations [95] or multidimensional linear interpolation using a look-up table [77, 96]. Even more advanced methods based on machine learning exist [97]. Fig. 3.11 shows the spectral distribution of reference absorption coefficients $\kappa_\eta(\boldsymbol{\phi}_0)$ for a small fictional band and $\kappa_\eta(\boldsymbol{\phi})$. The lower horizontal line shows all intersections with $\kappa_\eta(\boldsymbol{\phi}_0)$ where the distribution has one and the same absorption coefficient. In this small band this absorption coefficient repeats eight times. The correlated version of the absorption coefficient has exactly the same number of an unique absorption coefficient at the same wavenumber [95].
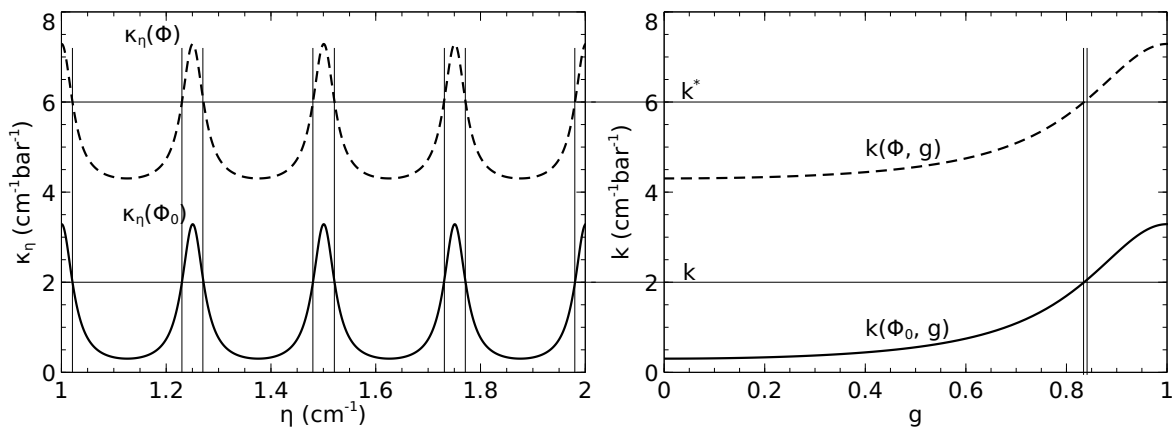

Fig. 3.11 Left: example of correlation between a reference spectral absorption distribution $\kappa_\eta(\phi_0)$ and its correlated absorption distribution $\kappa_\eta(\phi)$ in a small band. Right: amount of the same absorption coefficients for the reference $k(\phi_0, g)$ and correlated $k(\phi, g)$ distribution [53, 76].

Wang et al. Implementation Wang and co-workers developed a look-up table of k-distributions for non-homogeneous mixtures and different temperatures. The mixture consists of CO_2, H_2O, CO and soot. Different variations of the composition are tabulated. The pressure is always 1 bar. The k-distribution of a certain composition can then be determined by multidimensional interpolation. In addition, they introduced a new method to obtain the correlated k-distribution, which is described in this section [98].

Wang's implementation requires two interpolation steps to obtain the correlated k-distribution [77, 98]. The individual steps of the method can be described as follows:

1. Using the look-up table, a 5D interpolation is performed three times to receive $k(T, T, x, g_0)$, $k(T, T_0, x, g_0)$ and $k(T_0, T_0, x, g_0)$.

2. First interpolation step: Find g^* by solving $k(T_0, T_0, x, g_0) = k(T, T_0, x, g_0)$.

3. Second interpolation step: Find k^* by solving $g^* = g_0(T, T, x, k)$.

This procedure of finding the correlated k-distribution is illustrated in Fig. 3.12. The conservation of total emission can be shown by Eq. (3.39) using the the correlated k-distribution [98]:

$$
\begin{aligned}
\int_0^1 k^*(g_0)\, a(g_0)\, dg_0 &= \int_0^1 k(T, T, x)(g(T_0, T_0, x))\, \frac{dg(T, T_0, x)}{dg(T_0, T_0, x)}\, dg(T_0, T_0, x) \\
&= \int_0^1 k(T, T, x)(g(T, T_0, x))\, \frac{dg(T, T_0, x)}{dg(T_0, T_0, x)}\, dg(T_0, T_0, x) \\
&= \int_0^1 k(T, T, x)(g(T, T_0, x))\, dg(T_0, T_0, x) \\
&= \kappa_P.
\end{aligned}
\tag{3.39}
$$
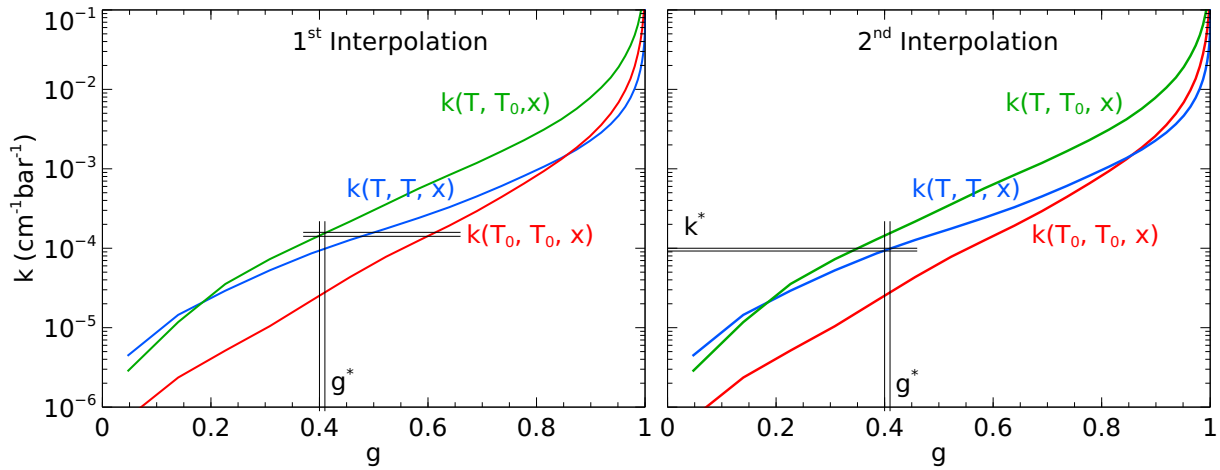
Fig. 3.12 Visualization of the both interpolation steps to find the correlated k-distribution as proposed by Wang et al. [98].

To verify the correctness of the implemented code, the method by Wang and co-workers was applied to a homogeneous medium with 10 mol% H_2O, a temperature of 1000 K and a pressure of 1 bar (Fig. 3.13). The results for $k(T_0, T_0, x)$, $k(T, T_0, x)$, $k(T, T, x)$ and k^* are in agreement with those of Wang et al. [98]. It can be seen that the calculated distributions do not extend to $g=0$, which is due to the wing and intensity cut-off (cf. Fig. 3.10).

To account for the variation of the blackbody intensity over the full spectrum, the *stretching-function* $a(g_0)$ or weight function is introduced into the RTE. The stretching function is calculated according to Eq. (3.40):

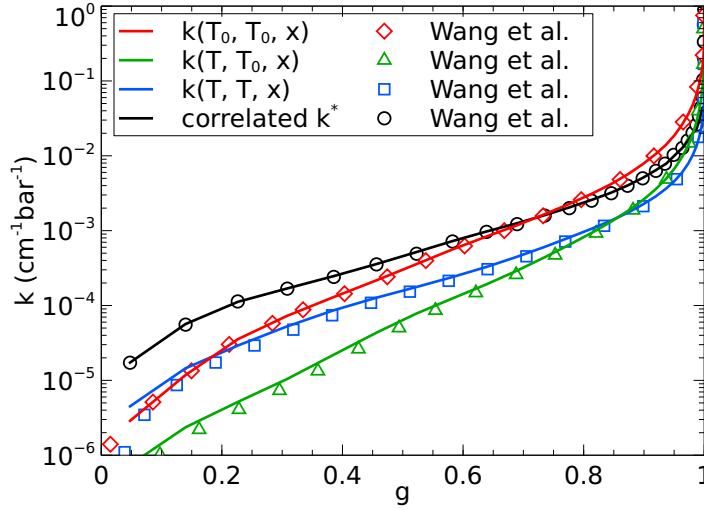**Fig. 3.13** Verification of the created look-up table and the two-step interpolation procedure with the results from Wang et al. [98] for 10 mol% H_2O at 1 bar and 1000 K.

$$a(g_{i,0}) = \frac{dg(T,T,x,k_i)}{dg(T_0,T_0,x,k_i)} \simeq \frac{g(T,T,x,k_{i+1}) - g(T,T,x,k_{i-1})}{g(T_0,T_0,x,k_{i+1}) - g(T_0,T_0,x,k_{i-1})}. \tag{3.40}$$

Since $k(T,T,x)(g(T_0,T_0,x)) = k(T,T,x)(g(T,T_0,x)) = k^*(g_0)$, the RTE for the FSCK model for non-homogeneous media can be written as Eq. (3.41) [98]:

$$\frac{dI_g}{ds} = k^*(g_0) \left[a(g_0) \, I_b(T) - I_g \right] - \sigma_s \left[I_g - \frac{1}{4\pi} \int_{4\pi} I_g(\hat{\boldsymbol{s}'}) \, \Phi(\boldsymbol{s'} \to \boldsymbol{s}) \, d\Omega' \right]. \tag{3.41}$$

The RTE is solved for each quadrature point, therefore the subscript g is used for the I. If the RTE has been solved at all Gaussian-quadrature points, the intensity can be integrated according to Eq. (3.42):

$$I = \int_0^1 I_g \, dg \approx \sum_{i=0}^{N_g} I_{g,i} \, w_i. \tag{3.42}$$

For homogeneous media, where the k-distribution is not correlated with a reference state or the distribution is calculated directly from the k-distribution database without interpolation between the database points, the FSK is an exact method and the results are equivalent to an LBL calculation with a few RTE solutions instead of millions [48]. To illustrate this, it is considered that $T = T_0$ so $a(T_0, T_0, g_0) = dg(T_0, \boldsymbol{\phi}_0, k)/dg_0(T_0, \boldsymbol{\phi}_0, k) = 1$ and thus the weighting function in the RTE (3.41) is unnecessary [48].

Reference state   A single state is used as reference for the FSCK model. Therefore, a reference mole fraction, temperature and pressure has to be calculated for the whole domain. If the pressure is assumed to be constant, the reference mole fraction x_0 and reference temperature

T_0 can be calculated according to Eq. (3.43) – (3.45):

$$x_0 = \frac{1}{V} \int_V x \, dV, \tag{3.43}$$

$$\left(\kappa_P \, T^4\right)_0 = \frac{1}{V} \int_V \kappa_P \, T^4 \, dV, \tag{3.44}$$

$$T_0 = \frac{\int_V T \left[4 \, \sigma \, \kappa_P(T,p,x) \, T^4\right] dV + \int_A T \left[\epsilon \, \sigma \, T^4/\pi\right] dA}{\int_V \left[4 \, \sigma \, \kappa_P(T,p,x) \, T^4\right] dV + \int_A \left[\epsilon \, \sigma \, T^4/\pi\right] dA}. \tag{3.45}$$

Modest and Zhang investigated different reference temperatures and concluded, that the *Planck mean temperature* Eq. (3.44) and the *emission weighted temperature* Eq. (3.45) are the best choice for realistic combustion systems [76].

3.3.5 Weighted Sum of Gray Gases model

The WSGG was first presented by Hottel [48, 71]. The basic idea of this model is to approximate a non-gray gas by several gray gases. Therefore, the radiation intensity is calculated individually for each gray gas and then summed up. For this model, the temperature can vary in the domain but the composition of the media should be constant. Different authors have developed correlations for the WSGG model in oxyfuel combustion, e.g. one of the most promising correlations was found by Bordbar et al. [73] and Kangwanpongpan et al. [74]. Both authors performed a line-by-line calculation based on the HITEMP2010 database and created graphs for total emittance for different pressure path lengths, temperatures and H_2O/CO_2 molar fractions at atmospheric pressure. Since the concept of the WSGG is identical for both authors, but different parameters are used, only the version by Kangwanpongpan and co-workers is described in this section. The parameters of both authors are listed in Tab. B.1 in the appendix. The LBL lines for molar ratio of 0.125, 0.25, 0.5, 0.75 (dry flue gas recirculation) and values above 1.0, 2.0, 4.0 (wet flue gas recirculation) are plotted in Fig. 3.14. The total emittance was fitted by Kangwanpongpan and co-workers using the Levenberg–Marquardt [99, 100] algorithm and non-linear multiple regression analysis [74], while Bordbar and co-workers used the LSQCURVEFIT function of the software Matlab [73].

The total emittance ϵ_{tot} for a given path length L can be calculated by Eq. (3.46):

$$\epsilon_{tot} = \sum_{i=1}^{N_g} a_i \left(1 - e^{-\kappa_i \, p_a \, L}\right), \tag{3.46}$$
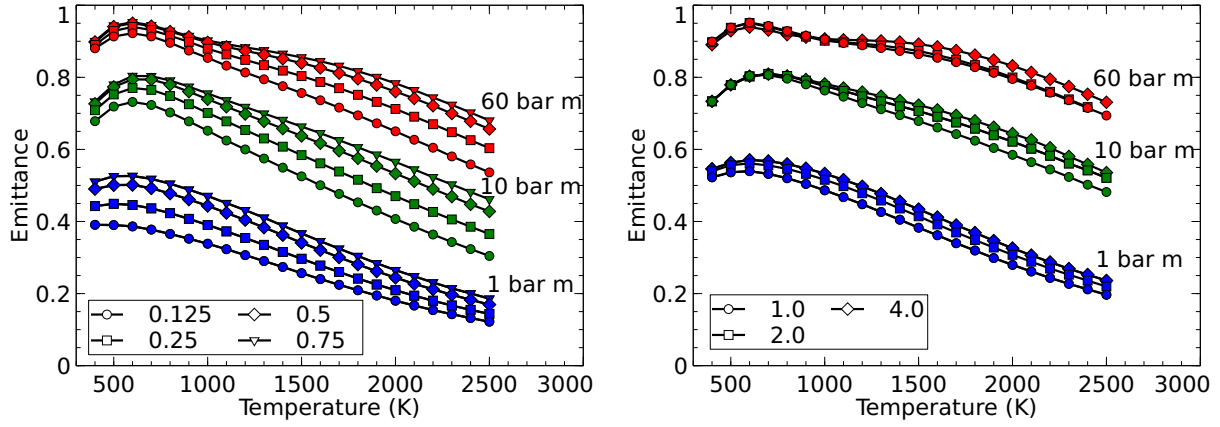
Fig. 3.14 Total emittance calculated from HITEMP2010 database with LBL for different molar ratios (symbols) and path lengths by Kangwanpongpan et al. [74]. Left: emittance for dry flue gas recirculation. Right: wet flue gas recirculation [74].

where a_i are the weighting factors, N_g the number of gray gases and p_a the pressure, calculated according to Eq. (3.47):

$$p_a = p \left(x_{CO_2} + x_{H_2O} \right).$$ (3.47)

Using tabulated values, pre-calculated by Kangwanpongpan et al. [74], the absorption coefficient for a gray gas can be directly calculated with the polynomina in Eq. (3.48):

$$\kappa_i = \sum_{k=1}^{N_k} CK_{i,k} \, MR^{k-1},$$ (3.48)

where MR is the molar ratio x_{H_2O}/x_{CO_2}. The WSGG parameters $CK_{i,k}$ are taken from tables (appendix Tab. B.1). The weighting factors a_i for Eq. (3.46) are calculated according to Eq. (3.49):

$$a_i = \sum_{j=1}^{N_j} c_{i,j} \left(\frac{T}{T_0} \right)^{j-1}.$$ (3.49)

The temperature is normalized by a reference temperature T_0 to reduce errors [74]. The coefficient $c_{i,j}$ for Eq. (3.49) is calculated according to the polynomina in Eq. (3.50):

$$c_{i,j} = \sum_{k=0}^{N_k} C_{i,j,k} \, MR^k.$$ (3.50)

A long path length is necessary to get a hundred percent absorptivity. Therefore κ_0 is equal

to zero to allow a *spectral window* [48]. The weighting factor a_0 is then calculated using Eq. (3.51):

$$a_0 = 1 - \sum_{i=1}^{N_g} a_i. \tag{3.51}$$

If the intensity of each gray gas is calculated individually, the RTE results in Eq. (3.52) for the WSGG. The gray absorption coefficient κ_{tot} can be calculated by rearranging Eq. (3.46) and setting the weighting factor to one. This results in $\kappa_{tot} = -\ln(1-\epsilon_{tot})/L$. Therefore, the RTE only has to be calculated once for each ray direction using the total absorption coefficient. However, this simplification leads to large errors but reduces the computation time.

$$\frac{dI_i}{ds} = \kappa_i(T, x_i) \; [a_i(T, x_i) \, I_b(T) - I_i] - \sigma_s \left[I_i - \frac{1}{4\pi} \int_{4\pi} I_i(\hat{\boldsymbol{s}}') \, \Phi_i(\boldsymbol{s}' \rightarrow \boldsymbol{s}) \, d\Omega' \right]. \tag{3.52}$$

The equivalence path length L which is required for Eq. (3.46) can be approximated by Eq. (3.53). Where A is the surface area of the radiating gas volume and V the volume [101]:

$$L \approx 3.6 \frac{V}{A}. \tag{3.53}$$

3.3.6 k-distribution look-up table

Wang et al. [98] proposed a precalculated look-up table (shown in Tab. 3.2) with full spectrum k-distributions at different thermodynamic states using 32 Gauss-Chebyshev-quadrature points. This table includes different gas compositions containing CO_2, H_2O, CO and soot at an atmospherically pressure of 1 bar. The absorption coefficients at different thermodynamic states for k-distributions in the look-up table are calculated using Eq. (3.54), where the subscript *p* indicates the pressure-based absorption coefficient [102]. This look-up table enables the determination of a full spectrum k-distribution for a specific thermodynamic state using a 5D linear interpolation. More points placed on low mole fractions in the table since strong non-linearity appears here [96].

$$\kappa_\eta = \left(x_{CO_2} \, \kappa_{p\eta,CO_2} + x_{H_2O} \, \kappa_{p\eta,H_2O} + x_{CO} \, \kappa_{p\eta,CO} \right) p + \kappa_{\eta,soot}. \tag{3.54}$$

In this work, the spectral absorption coefficients are calculated form the HITEMP2010 database. The look-up table is created according to Wang et al. [96, 102] for the FSCK model. This results in 93288 data files ($23\times13\times13\times6\times4$) where each file contains 736 (23×32) reference temperatures with Gaussian-quadrature points. For the NBCK model, a second database

Tab. 3.2 Properties of spectral absorption coefficient look-up table proposed by Wang et al. [98].

Parameter	Range	Values	Number of points
x_{CO_2}	0.0 − 0.05	every 0.01	13
	0.25 − 1.0	every 0.25	
x_{H_2O}	0.0 − 0.05	every 0.01	13
	0.25 − 1.0	every 0.25	
x_{CO}	0.0 − 0.5	0.0, 0.01, 0.05, 0.1,	6
		0.25, 0.5	
$f_{v,soot}$	0.0 − 10^{-5}	0.0, 10^{-7}, 10^{-6}, 10^{-5}	4
T	300 K − 2500 K	every 100 K	23
p	1 bar	const.	1

is created using the same concept of the presented look-up table with some modifications. The database also includes 93288 data files but each file has 45000 (450×100) bands with Gaussian-quadrature points.

3.3.7 Gaussian-quadrature

The Gaussian-quadrature is used for numerical integration of the k-distributions. The quadrature scheme is based on the formulation in Eq. (3.55):

$$\int_a^b f(x)\,dx \approx \sum_i^N f(x_i)\,w_i. \tag{3.55}$$

The Gaussian abscissas x_i, ranging from 0 to 1 (or Gaussain points) and the associated weights w_i are precalculated values. This procedure can be used for simple integration of monotonically increasing functions. Two different quadrature schemes are shown in Fig. 3.15. Both schemes are illustrated with 32, 16 and 8 quadrature points.

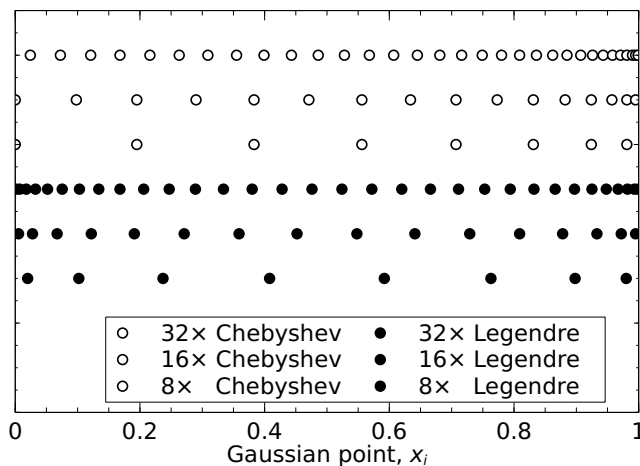| ○ | 32× Chebyshev | ● | 32× Legendre |
| ○ | 16× Chebyshev | ● | 16× Legendre |
| ○ | 8× Chebyshev | ● | 8× Legendre |

Fig. 3.15 Comparison of Gaussian-quadrature distributions for 32, 16 and 8 quadrature points using Gauss-Chebyshev and Gaussian-Legendre-quadrature.

It is obvious that the Gaussian-Legendre scheme places more points near 0 and 1 whereas in the center field are less points located. For the Gaussian-Chebyshev scheme, quadrature points are increasing in the direction of 1. In this work, the *odd-ranked* implementation of the Gauss-Chebyshev by Wang and Modest [93] is used which is an extension of the original implementation by Davis and Rabinowitz [103], where x_i = -1 ... 1. A transformation factor of 2 is used to generate more points at higher x_i-values since higher absorption coefficients located there, which dominate radiative heat transfer [93, 98].

3.3.8   Verification of gas radiation models

In this section, the test case and results of Kez et al. [62] are used to verify that all radiation models are correctly implemented. In addition, a similar test case by Porter et al. [104] is used and the results are compared to their benchmark solution.

In their work, they used an 3D virtual oxyfuel coal fired boiler to test different radiation models. The models they used are implemented in the program language Fortran 95. The temperature and species distributions inside the boiler are described with mathematical functions according to Kez et al. [62] while the interior pressure is set to 1 bar. These artificial distribution based on simulation results of Ströhle et al. [105], who calculated radiative heat transfer in an oxyfuel boiler with bituminous coal. Here, the test case of Kez and co-workers for dry flue gas recirculation is used. The boilers dimensions are 50 m × 20 m × 20 m (L_x × L_y × L_z). The walls are assumed as black walls with fixed temperatures. The temperature distribution inside the boiler is shown in Fig. 3.16. In Fig. 3.17 the temperature, CO_2 and H_2O concentrations against the center axis (z-axis) of the virtual boiler is shown, where the species and temperature distribution of Kez and co-workers are compared with the current distributions set in OpenFOAM®. The domain is discretized with 22491 cells (21 × 21 × 51).

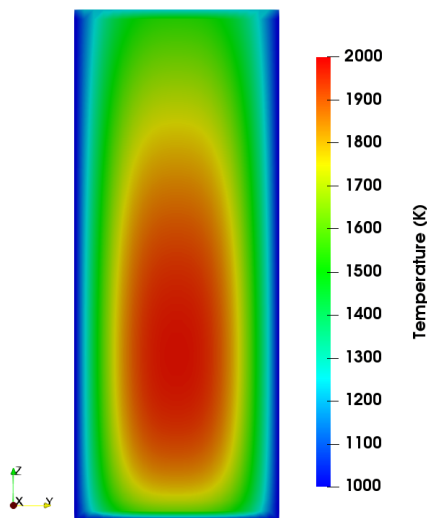**Fig. 3.16** Temperature distribution in the 3D virtual boiler test case of Kez et al. [62].
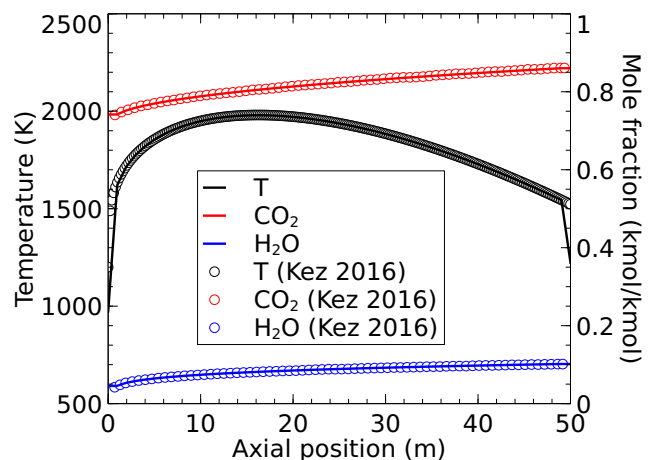

Fig. 3.17 Temperature, CO_2 and H_2O distributions on the center line inside the virtual boiler verified with the data by Kez et al. [62].

The curves in Fig. 3.17 are identical except for the temperature at the boundaries. The temperature profile shows an significant drop from the last interior cell to the fixed temperature at the wall. The wall and inlet patches are set to 973 K and the outlet patch to 1223 K according to Kez et al. [62]. This is due to the different treatment of numerical cells in both codes.

As can be seen in Fig. 3.18, the NBCK model implemented in OpenFOAM$^\circledR$ is almost consistent with the benchmark solution by Kez and co-workers. Small deviations may come from a different angular discretization, since Kez and co-workers use a DOM with T_7 approximation, while the current simulation uses a finite volume DOM with 48 rays (n_φ=4, n_θ=3). For the spatial discretization, the first order upwind scheme is used. A linear scheme resulted in no convergence. It is unclear which interpolation scheme is used by Kez et al. [62].
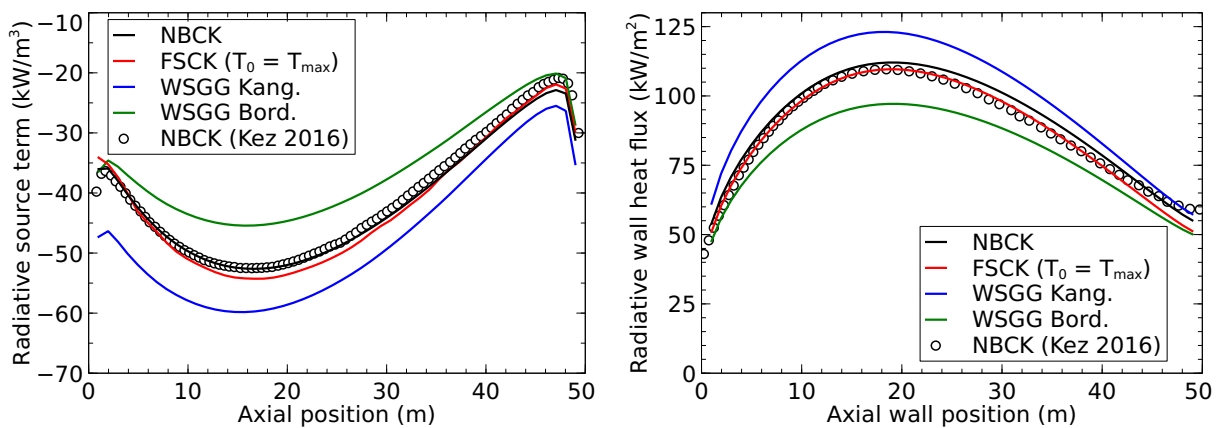

Fig. 3.18 Verification of different gas radiation models with the NBCK and the results by Kez et al. [62]. Left: radiative source term plotted against the central boiler axis. Right: radiative wall heat flux plotted against the central boiler axis.

Considering the global radiation models, the FSCK model with 32 Gaussian-quadrature points has the lowest deviation for the radiative source term of max. 4 % from the NBCK model. In the work of Kez and co-workers, the deviation of the FSCK from the benchmark solution amounts to a maximum of 2 %. This is due to different implementations of the FSCK model. For the radiative wall heat flux, the FSCK model has maximum deviations of 6 %. The accuracy of the FSCK model depends strongly on the reference temperature used to describe the entire domain. In this work, the maximum temperature in the domain, for reference temperature, shows the best results; while other authors use the emission weighted Planck mean temperature as reference [62, 76, 104]. The WSSG model, using parameters according to Kangwanpongpan et al. [74], shows deviates up to 30 % for the radiative source term and up to 13 % for the radiative wall heat flux. The WSSG model using parameters from Bordbar et al. [73] has a maximum deviation of 14 % from the radiative source term of the NBCK model and 13 % from the radiative wall heat flux. The FSCK model is more time consuming than the WSGG model, requiring a CPU time of 19 s using 32 quadrature points and 6 s using 12 quadrature points. The WSGG model requires a CPU time of 3 s for the test case. The NBCK model takes multiple days for calculating the benchmark solution, so it can only be

used as benchmark at the moment.

A second test case by Porter et al. [104], a virtual 3D flame under oxyfuel conditions is considered. The temperature distribution is calculated using mathematical functions similar to the previous test case. In contrast, the species concentrations are set constant to 85 mol% CO_2, 10 mol% H_2O and 5 mol% N_2. The pressure is set to 1 bar in the entire 2 m $\times$ 2 m $\times$ 4 m $(L_x \times L_y \times L_z)$ domain. The domain is discretized with 16 $\times$ 16 $\times$ 32 cells. The surrounded walls are black and set to a fixed temperature of 300 K. The temperature field of this test case is shown in Fig. 3.19.
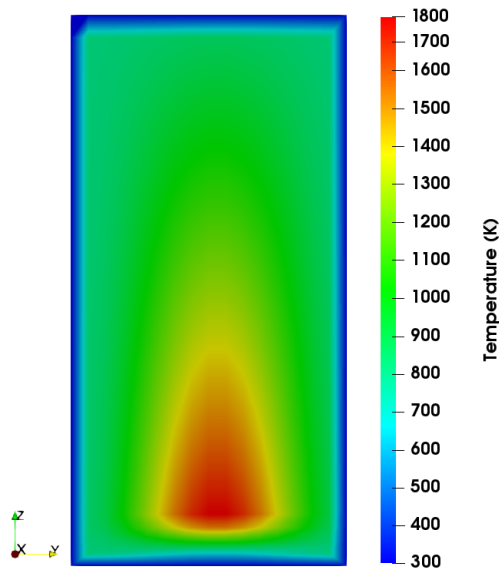
Fig. 3.19 Temperature field inside the virtual 3D oxyfuel test case by Porter et al. [104].

Porter and co-workers used a ray tracing method and the SNB model to solve the RTE. The results of Porter and co-workers are used as benchmark for comparison with the current results. Fig. 3.20 shows the results of the FSCK and WSGG model in comparison to the benchmark solution by Porter et al. [104].

Fig. 3.20 Comparison of different gas radiation models with the benchmark results by Porter et al. [104]. Left: radiative source term plotted against central chamber axis. Right: radiative wall heat flux plotted against central chamber axis.

In this case, the finite volume DOM was discretized with 64 rays (n_φ=4, n_θ=4) according to

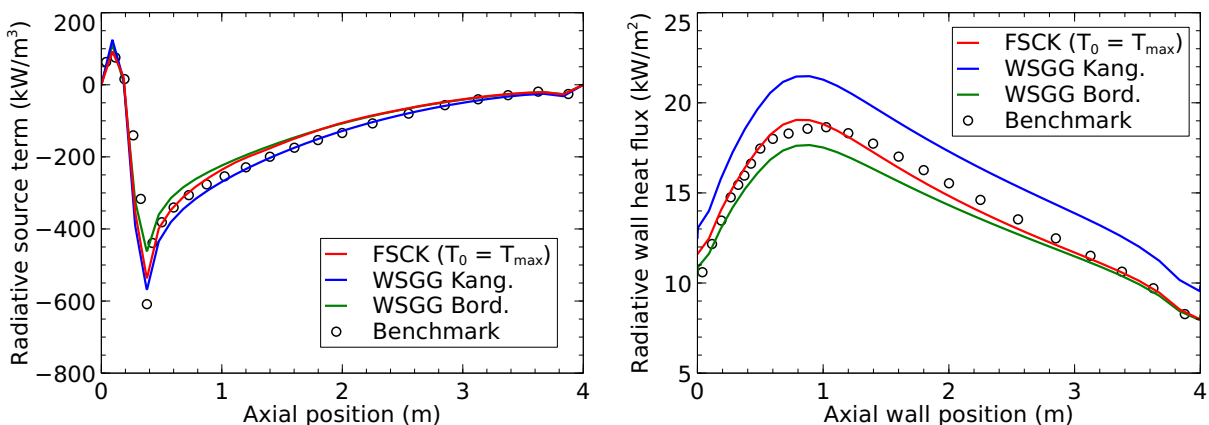Porter et al. [104] and a mesh with $16 \times 16 \times 32$ cells is used. The FSCK model has maximum deviations of $12\,\%$ considering the radiative source term and $6\,\%$ for the wall radiative heat flux. The WSSG model by Kangwanpongpan and co-workers has maximum deviation of $7\,\%$ from the radiative source term and $16\,\%$ from the wall radiative heat flux. The WSGG model by Bordbar and co-workers has deviations of maximum $24\,\%$ from the radiative source term and $8\,\%$ from the benchmark of the wall radiative heat flux.

The verification with the results of Kez and co-workers has shown that the new implementations in OpenFOAM® are correct and ready to be used in CFD and combustion simulations. Only minor deviations can be seen, which might be due to a different spatial discretization or a different treatment of the numerical cells in both codes. Additional results using the P_1 model for the discussed test cases can be found in the appendix Chapter A.1.

3.4   Soot Radiation

Since strongly radiating soot is produced in nearly all combustion systems with non-premixed flames and low O/C ratios, the effect of soot on radiative heat transfer has to be taken into account. Soot can be treated as a cloud of non-uniform sized small particles, since it is not a uniquely defined substance. For a wavelength dependent modeling of the soot absorption coefficient with limitation to the Rayleigh scattering, the correlation in Eq. (3.56) by Chang and Charalampopoulos [102, 106] for the *complex index of refraction* m is used:

$$\kappa_\lambda = \frac{36\,\pi\,n\,k}{\left(n^2 - k^2 + 2\right)^2 + 4\,n^2\,k^2} \frac{f_v}{\lambda}, \tag{3.56}$$

where f_v is the volume fraction of soot particles. The correlations for the parameters n and k in Eq. (3.56), which are the real and complex part of the complex index of refraction ($m = n - i\,k$) are calculated as:

$$n = 1.811 + 0.1263\,\ln\lambda + 0.027\,\ln^2\lambda + 0.0417\,\ln^2\lambda,$$
$$k = 0.5281 + 0.1213\,\ln\lambda + 0.2309\,\ln^2\lambda + 0.01\,\ln^2\lambda.$$

The formation of soot in non-premixed flames is a complex process and still subject of research. There are numerous models for the formation of soot, for example the model of Khan and Greeves [107] or the model of Moss-Brookes [108]. Since the formation of soot in models is associated with large uncertainty, it makes no sense to use a complex absorption model for soot. Furthermore, the radiation models in the last chapter of this work are only applied to natural gas combustion under oxyfuel conditions, which has a high O/C ratio and therefore the soot

radiation is of less importance. Therefore, a simple soot model, which is already implemented in the OpenFOAM® program code called *mixtureFractionSoot*, is used. No additional transport equation is solved for this model. It is a purely state model, which uses a reference species for the spatial distribution of the soot. The mass fraction of the soot is also calculated based on the reference species [109]. CO is used as reference species here, as it is also an intermediate product of combustion and, like soot, formed in regions with low oxygen content. The soot mass fraction is calculated according to Eq. (3.57):

$$Y_{soot} = Y_{soot,max,st} \frac{Y_{prod,0}}{Y_{prod,0,st}}, \qquad (3.57)$$

where Y_{soot} is the soot mass fraction, $Y_{prod,0}$ the mass fraction of the reference product, $Y_{prod,0,st}$ the mass fraction of the reference product at stoichiometric conditions and $Y_{soot,max,st}$ is the maximum soot mass concentration that can be produced, calculated with Eq. (3.58):

$$Y_{soot,max,st} = \frac{x_{soot} M_{soot}}{\sum_i x_{i,prod} M_{i,prod}}. \qquad (3.58)$$

The mole fraction for soot x_{soot} and the product species $x_{i,prod}$ are calculated in Eq. (3.59):

$$x_{soot} = \frac{\nu_{soot}}{\sum_i |\nu_i''|}, \qquad x_{i,prod} = \frac{|\nu_i''|}{\sum_i |\nu_i''|}, \qquad (3.59)$$

where ν_{soot} is the soot yield, which must be predefined and ν_i'' are the stoichiometric coefficients for products of a single step chemical reaction.

4 Modeling of Two Phase Reacting Flows

For the up-scaling process of an oxyfuel burner in Chapter 5 and the simulation of the thermal gas radiation inside the experimental combustion chamber in Chapter 8, the following describes the equations used for the reactive flow simulations. The equations and models are presented as they are implemented in OpenFOAM® version 2006 for the in-house solver *simpleOxyTR129ParcelFoam* which is a modification of the standard solver *simpleCoalParcelFoam*.

4.1 Continuous Phase

The transport of mass, species, momentum and energy are described by partial differential equations for the change in time and space. All transport equations of the continuous phase based on the following general formulation [38]:

$$\underbrace{\frac{\partial (\rho\,\phi)}{\partial t}}_{\text{Transient}} + \underbrace{\nabla \cdot (\rho\,\boldsymbol{u}\,\phi)}_{\text{Convection}} = \underbrace{\nabla \cdot (\Gamma\,\nabla\phi)}_{\text{Diffusion}} + \underbrace{\sum S_\phi}_{\text{Source/Sink}}. \tag{4.1}$$

In Eq. (4.1), ρ is the density of the medium, $\boldsymbol{u}$ the velocity vector, ϕ a general balance quantity, Γ the diffusion coefficient, S_ϕ the source and sink term for the balance quantity, and t the time. Since the continuous phase is simulated stationary here, the transient terms in the following transport equations are omitted.

For a Direct Numerical Simulation (DNS) of turbulent flows, it is necessary to resolve the turbulent structures down to the smallest scales (Kolmogorov scales). This leads to a high computational effort and is currently only possible for simple geometries [21]. The Large Eddy Simulation (LES) is used to calculate the large vortex structures directly, whereas the small structures are simulated using a turbulence model [25]. For large geometries, even nowadays a LES is still associated with a high computational effort. To minimize the computing time, the Reynolds-Averaged Navier-Stokes (RANS) equations and eddy viscosity turbulence models are used for all simulations. Turbulence models are statistical averages of the general transport equations. For most applications with turbulent flows, time averaging is used since the flow variables strongly fluctuate in time but remain constant on average. In the process of combustion, high fluctuations in temperature and consequently in density occur, so it is more appropriate to use a density-weighted *Favre-averaging* according to Eq. (4.2) instead of time averaging [25]:

$$\tilde{\phi} = \frac{\overline{\rho\,\phi}}{\overline{\rho}}. \tag{4.2}$$

Time-averaged quantities are overlined and Favre-averaged quantities are marked with a tilde above the quantity.

4.1.1 Mass transport equation

Eq. (4.3) shows the continuity equation of fluid mechanics. This equation is used to ensure the conservation of mass flows:

$$\nabla \cdot (\overline{\rho}\, \tilde{\boldsymbol{u}}) = S_p. \tag{4.3}$$

Since there is a two-phase coupling between gas and particle phase, the subscript p in the source term S_p corresponds to the disperse phase. This source term in the continuous equation is used for mass exchange with the particle phase. Quantities referring to the gas phase are not designated with an additional subscript.

4.1.2 Momentum transport equation

The conservation of momentum in Newtonian fluids is composed of convective terms and momentum changes due to pressure and friction forces, as shown on the left-hand side in Eq. (4.4). The effective shear-rate tensor $\tilde{\boldsymbol{\tau}}_{eff}$ and pressure forces are combined in the effective *Cauchy stress tensor* $\tilde{\boldsymbol{\sigma}}_{eff}$. The program code calculates the Cauchy stress tensor for laminar and turbulent transport phenomena in Eq. (4.4). Therefore, the subscript eff is used. More information on this representation of the momentum equation can be found in the work of Holzmann [110]. The gravitational vector $\boldsymbol{g}$ and a source term for the disperse phase S_p is included on the right-hand side of the equation [25]:

$$\nabla \cdot (\overline{\rho}\, \tilde{\boldsymbol{u}}\, \tilde{\boldsymbol{u}}) - \nabla \cdot \tilde{\boldsymbol{\sigma}}_{eff} = \overline{\rho}\, \boldsymbol{g} + S_p. \tag{4.4}$$

Since there is no explicit equation for the pressure, this complicates the solution of the continuity and momentum equation. A pressure correction method is therefore used. This is a frequently used approximation in which the deviations of the momentum equation are substituted into the continuity equation. Pressure calculation and continuity equation are coupled with each other. The pressure equation can only be treated fully or partially implicitly. For an explicit formulation, the equation cannot be satisfied. This pressure correction method is called *SIMPLE* algorithm (Semi Implicit Method for Pressure Linked Equations) [21, 111]. More details can be found in the work of Laurien and Oertel [21].

4.1.3 Species transport equation

Eq. (4.5) shows the conservation of species. The effective dynamic viscosity μ_{eff} on the left side of this equation includes the laminar and turbulent portion. The laminar part μ_{lam} is calculated by using the Sutherland correlation [112]. In the OpenFOAM® program code, the assumption is made so that the Schmidt number is $\mathrm{Sc} = 1$, and thus the mass diffusion corresponds to the dynamic viscosity. Other authors use values of 0.7 [66, 113]. However, the Schmidt number can vary depending on the application. Since the molecular transport in turbulent combustion is minor compared to turbulent mixing, the code remains unchanged at this point:

$$\nabla \bullet (\overline{\rho}\, \tilde{\boldsymbol{u}}\, \tilde{Y}_i) - \nabla \bullet (\mu_{eff}\, \nabla \tilde{Y}_i) = \dot{R}_i + S_p. \tag{4.5}$$

The balance quantity Y_i is the mass fraction of species i, and $\dot{R}_i$ on the right-hand side of Eq. (4.5) is the reaction rate which contributes the change of a species by chemical reaction in the gas phase. The reaction rate is determined using combustion models which will be presented later. S_p is an additional source therm which belongs to the disperse phase. The sum of all species must be equal to one. Therefore it is only necessary to solve $n-1$ transport equations. Where n is the number of species involved. The nth species results from Eq. (4.6):

$$Y_n = 1 - \sum_{n-1}^{i=1} Y_i. \tag{4.6}$$

The numerical stability increases if the most abundant species is defined as n^{th} species. For combustion processes using air as oxidant, nitrogen would be the nth species [66] and in oxyfuel combustion, carbon dioxide.

4.1.4 Enthalpy transport equation

The enthalpy conservation Eq. (4.7) determines the spatial change of specific sensible enthalpy h_s. Assuming low Mach numbers, it can be written in the form of Eq. (4.7). On the right side of Eq. (4.7) the source term S_h is located, for energy release due to combustion, increasing or decreasing enthalpy caused by thermal radiation and heat exchange with the disperse phase S_p:

$$\nabla \bullet (\overline{\rho}\, \tilde{\boldsymbol{u}}\, \tilde{h}_s) + \nabla \bullet (\overline{\rho}\, \tilde{\boldsymbol{u}}\, K) - \nabla \bullet \left(\alpha_{eff}\, \nabla \tilde{h}_s\right) = \overline{\rho}\, \tilde{\boldsymbol{u}}\, \boldsymbol{g} + S_h + S_p. \tag{4.7}$$

The mechanical energy is summarized as $K = 1/2 |\overline{\boldsymbol{u}}|^2$. The second term on the left cor-

responds to heat transfer by conduction and turbulent diffusion [50]. The effective thermal diffusivity is calculated using the turbulent Prandtl number $\alpha_{eff} = \mu_{eff}/\mathrm{Pr}_{turb}$.

4.1.5 Turbulence modeling

Turbulence is an unsteady, three-dimensional and chaotic flow. It arises from a three-dimensional instability caused by a predominance of destabilizing inertial forces over stabilizing frictional forces [21]. Using RANS, the momentum equation yields *Reynolds stresses*, which requires a closure approximation. This fluctuation term can be solved explicitly with the Reynolds Stress Model [114] using a transport equation for each stress. Since this method is computationally intensive, eddy viscosity models for isotropic turbulence are used, which have shown reasonable results for industrial boilers in the literature [50, 115]. The effective dynamic viscosity μ_{eff}, as already included in the previous equations, provides the turbulent contribution by addition with the laminar viscosity μ_{lam} in Eq. (4.8):

$$\mu_{eff} = \mu_{lam} + \mu_{turb}. \tag{4.8}$$

The k–ϵ–turbulence model

The Standard k-ϵ-model is the most commonly used turbulence model and is characterized by its robustness against inaccurate inflow conditions and its moderate complexity [21]. It was also used in the field of oxyfuel firing by Toporov et al. [116], whereas the Realizable k-ϵ-model was used by Bohnstein et al. [117] and the RNG k-ϵ-model by Askarizadeh et al. [118] for oxyfuel. The Standard k-ϵ-model is used in this work, as it has proven to be the most stable model in the simulations carried out. A comparison of two eddy viscosity turbulence models can be found in the appendix, Chapter A.3.

The eddy viscosity μ_{turb}, or turbulent viscosity can be calculated using a two-equation model for *turbulent kinetic energy* k and the *dissipation rate* ϵ. The turbulent kinetic energy is calculated by Eq. (4.9). The equations for the k-ϵ turbulence model are formulated on an empirical basis, assuming isotropic turbulence [50, 119, 120]:

$$\underbrace{\nabla \cdot (\overline{\rho}\, \tilde{\boldsymbol{u}}\, \tilde{k})}_{\text{Convection}} - \underbrace{\nabla \cdot \left(\frac{\mu_{turb}}{\sigma_k}\, \nabla \tilde{k} \right)}_{\text{Diffusion}} = \underbrace{\overline{\rho}\, G_k - \frac{2}{3}\, \overline{\rho}\, (\nabla \cdot \tilde{\boldsymbol{u}})\, k}_{\text{Production}} - \underbrace{\overline{\rho}\, \tilde{\epsilon}}_{\text{Dissipation}} + \underbrace{S_k}_{\text{Source}}. \tag{4.9}$$

Turbulence is produced at a given location in the flow field and transported to another location by convection and diffusion, where it eventually dissipates by friction [21]. According to the Boussinesq approximation, the turbulence production is composed of the *turbulent kinetic energy production rate* G_k and $2/3\overline{\rho}(\nabla \cdot \tilde{\boldsymbol{u}})k$ [67, 121]. In addition, a source term S_k is

included in Eq. (4.9).

The dissipation rate ϵ is given by Eq. (4.10). The second term on the right-hand side provides the contribution of *Rapid Distortion Theory* (RDT) in compressible flows to the the production term, introduced by El Tahry [120]. In addition, a source term S_ϵ on the right-hand side of Eq. (4.10) is included:

$$
\underbrace{\nabla \cdot (\overline{\rho}\, \tilde{\boldsymbol{u}}\, \tilde{\epsilon})}_{\text{Convection}} - \underbrace{\nabla \cdot \left(\frac{\mu_{turb}}{\sigma_\epsilon}\, \nabla \tilde{\epsilon} \right)}_{\text{Diffusion}} = \underbrace{C_{1\,\epsilon}\, \overline{\rho}\, G_k\, \frac{\tilde{\epsilon}}{\tilde{k}} - \left(\frac{2}{3}\, C_{1\,\epsilon} - C_{3\,\text{RDT}} \right) \overline{\rho}\, (\nabla \cdot \tilde{\boldsymbol{u}})\, \tilde{\epsilon}}_{\text{Production}}
$$

$$
\qquad\qquad - \underbrace{C_{2\,\epsilon}\, \overline{\rho}\, \frac{\tilde{\epsilon}^2}{\tilde{k}}}_{\text{Dissipation}} + \underbrace{S_\epsilon}_{\text{Source}} .
\tag{4.10}
$$

The eddy viscosity μ_{turb} is obtained by Eq. (4.11) after solving the k and ϵ transport equation. An empirical factor C_μ and the density is multiplied with the ratio of the turbulent kinetic energy and the dissipation rate:

$$
\mu_{turb} = C_\mu\, \overline{\rho}\, \frac{\tilde{k}^2}{\tilde{\epsilon}}.
\tag{4.11}
$$

Initial conditions for the two-equation k-ϵ-turbulence model, the turbulence intensity I, and the characteristic mixing length L_{mix} can be determined for fully developed pipe flows using the correlations in Tab. 4.1 [122–124].

Tab. 4.1 Determination of initial values for k and ϵ.

Initial value		Correlation	
Turbulent kinetic energy	$k_0 = 1.5\, (I|\boldsymbol{u}_0|)^2$	Turbulence intensity	$I = 0.16\, \text{Re}^{-1/8}$
Dissipation rate	$\epsilon_0 = C_\mu^{0.75}\, k^{1.5}\, L_{mix}^{-1}$	Turbulent mixing length	$L_{mix} = 0.07\, d$

The empirical parameters used in Eq. (4.9) and Eq. (4.10) are tabulated in Tab. 4.2.

Tab. 4.2 Empirical parameters used for the k-ϵ-turbulence model [21, 119, 124].

C_μ	σ_k	σ_ϵ	$C_{1\epsilon}$	$C_{2\epsilon}$	$C_{3\text{RDT}}$
0.09	1.0	1.3	1.44	1.92	0

4.1.6 Spatial discretization and solution

All transport equations described in this section and Chapter 3 have the general structure of Eq. (4.1). The investigated geometries in this work are discretized using the finite volume method

according to Eq. (4.12) where all terms of the general transport equation are integrated over the cell volumes V:

$$\int_V \frac{\partial (\rho \boldsymbol{\phi})}{\partial t} \, dV + \int_V \nabla \cdot (\rho \boldsymbol{u} \boldsymbol{\phi}) \, dV = \int_V \nabla \cdot (\Gamma \nabla \boldsymbol{\phi}) \, dV + \int_V S_\phi \, dV. \qquad (4.12)$$

The *Gaussian theorem* can be used to convert the volume integral into a surface integral. The integration of the terms in the general transport equation using the surface integral is summarized in Tab. 4.3.

Tab. 4.3 Surface integral of the terms in the general transport equation.

Term	Integration	Eq.
Divergence	$\int_V \nabla \cdot \boldsymbol{\phi} \, dV = \oint_S d\boldsymbol{S} \cdot \boldsymbol{\phi} = \sum_i^{N_{face}} \boldsymbol{S}_{f,i} \cdot \boldsymbol{\phi}_{f,i}$	(4.13a)
Convection	$\int_V \nabla \cdot (\rho \boldsymbol{u} \boldsymbol{\phi}) \, dV = \oint_S d\boldsymbol{S} \cdot (\rho \boldsymbol{u} \boldsymbol{\phi}) = \sum_i^{N_{face}} \boldsymbol{S}_{f,i} \cdot (\rho \boldsymbol{u})_{f,i} \, \boldsymbol{\phi}_{f,i}$	(4.13b)
Laplacian	$\int_V \nabla \cdot (\Gamma \nabla \boldsymbol{\phi}) \, dV = \oint_S d\boldsymbol{S} \cdot (\Gamma \nabla \boldsymbol{\phi}) = \sum_i^{N_{face}} \Gamma_{f,i} \boldsymbol{S}_{f,i} \cdot (\nabla \boldsymbol{\phi})_{f,i}$	(4.13c)
Gradient	$\int_V \nabla \boldsymbol{\phi} \, dV = \oint_S d\boldsymbol{S} \boldsymbol{\phi} = \sum_i^{N_{face}} \boldsymbol{S}_{f,i} \boldsymbol{\phi}_{f,i}$	(4.13d)

Where $\boldsymbol{S}_{f,i}$ is the surface area vector. Since the cell-faces lie between the adjoining cells (illustrated as gray surface in Fig. 4.1) the value of the cell-centers are interpolated on the cell-faces. The calculation domain is discretized with a numerical mesh which can consists of orthogonal and non-orthogonal cells. Each *owner-cell* ϕ_P consists of a cell center, *cell-faces* ϕ_f and *neighbor-cells* ϕ_N. Values are stored in the cell center. To get the information how a quantity is transported through the domain, an interpolation between the cell centers of adjoining cells is necessary.
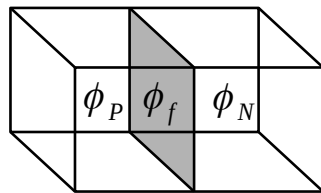

Fig. 4.1 Two three dimensional adjoining cells. Owner-cell with cell center ϕ_P, neighbor-cell with cell center ϕ_N and cell-face between both cells ϕ_f.

There are different interpolation methods in the literature for divergence, convection, Laplacian and gradient terms based on Eq. (4.14). Most methods optimize the parameter γ in this equation. Popular methods are the *step scheme* or *upwind scheme* and the *linear scheme*.

$$\phi_f = \phi_N + \gamma (\phi_P - \phi_N) = \gamma \, \phi_P + \phi_N (1 - \gamma). \qquad (4.14)$$

Upwind differencing scheme   The upwind interpolation scheme sets γ to zero. The value on the cell-face depends on the flux on the face. If the flux is positive, it becomes the value of the owner-cell, if the flux is negative it becomes the value of the neighbor-cell. This can be expressed as:

$$\phi_f = \begin{cases} \phi_P, & \text{flux on cell-face} > 0 \\ \phi_N, & \text{flux on cell-face} < 0 \end{cases}. \tag{4.15}$$

Central differencing scheme   For the linear interpolation scheme, or *central differencing scheme*, γ is set so 0.5, so the cell-face gets 50 % of its value from the owner-cell and 50 % from the neighbor-cell:

$$\phi_f = \frac{1}{2}\left(\phi_P + \phi_N\right). \tag{4.16}$$

The upwind scheme is a first order scheme. It is stable and robust but it is less accurate and can lead to numerical diffusion [21]. The linear scheme is a second order scheme. It reduces numerical diffusion but is sensitive for numerical instabilities. For divergence terms, the upwind scheme is more advisable than a linear scheme because of strong gradients [67]. More information about the available interpolation methods can be found in the OpenFOAM® code guide [124, 125]. Since the upwind scheme is highly stable, it is used for all terms at the beginning of the simulations, except for the Laplacian term which uses a linear scheme. Once a stationary state has been reached in the simulation, the schemes are switched to higher order. However, the divergence terms remain discretized with the upwind scheme.

The discretization of Eq. (4.12) leads to an algebraic system of equations, which can be solved using different numerical methods. An overview of the available solution methods can also be found in the OpenFOAM® code guide [124, 125]. In this work, the PCG solver [126] is used for symmetric and the preconditioned Bi-CGSTAB solver [127] for asymmetric matrices, as these solvers have proven to be the most stable in this work.

4.2 Disperse Phase

The motion of particles is described transiently by the Lagrangian approach. In order to determine the position and properties of the particles; equations of motion, mass and energy change are used. A more detailed description of the particle treatment in OpenFOAM® can be found in the work of Christ [66] and Kasper [128]. Tracking *parcels*, rather than individual particles, is a widely used method in CFD codes to reduce computation time and storage. Parcels are particle packages whit a predefined, initial mass and contain a certain number of particles

with identical properties. The introduced mass is divided evenly between a specified number of parcels; the number of particles per parcel is calculated with a particle size distribution. To avoid runtime errors, the volume of all particles per parcel should not exceed the volume of the smallest cell of the numerical mesh.

4.2.1   Velocity and momentum

The trajectory of a particle can be described by the momentum Eq. (4.17). This equation is calculated for a single particle which is representative for all particles inside the considered parcel. The momentum of the particle is obtained by summation of all forces acting on the particle. The drag force in the gas phase $\boldsymbol{F}_d$ and the gravitation $\boldsymbol{F}_g$ are most relevant for the simulation of the pulverized fuel [115]. Additional forces acting on the particle are neglected. The position of the particle results from the integration of the particle velocity over time [21, 66, 129].

$$m_p \frac{\partial \boldsymbol{u}_p}{\partial t} = \sum_i \boldsymbol{F}_i = \boldsymbol{F}_g + \boldsymbol{F}_d = m_p \, \boldsymbol{g} \, \left(1 - \frac{\rho}{\rho_p} \right) + \frac{0.75 \, m_p \, \mu \, \mathrm{Re}_p \, C_d}{\rho_p \, d_p^2} (\tilde{\boldsymbol{u}} - \boldsymbol{u}_p). \qquad (4.17)$$

In Eq. (4.17) m_p is the mass of a single particle, d_p the diameter of the particle, Re_p the particle Reynolds number and C_d the drag coefficient. The boundary conditions at the geometry patches are defined to ensure that particles bounce elastically from walls and leave the system if they have contact with an outlet.

4.2.2   Change in mass

During the combustion of solid fuel, the mass of the particle changes due to drying, pyrolysis and char burnout. The change of different mass components is represented by summation of source terms $S_{p,i}$ in Eq. (4.18):

$$\frac{\partial m_p}{\partial t} = \sum_i S_{p,i}. \qquad (4.18)$$

After full combustion of the fuel particle, ash is the only remaining mass in the particle, which is not transferred to the gas phase and is not chemically converted.

4.2.3   Change of particle temperature

The temperature change of the particles in Eq. (4.19) is determined by convective heat exchange, thermal radiation and the source/sink terms $S_{p,i}$ caused by heterogeneous reactions.

The source terms are composed of the heat extraction by pyrolysis, which is neglected here, and the heat released by surface reaction of the particle:

$$m_p \, c_{p,\,p} \frac{\partial T_p}{\partial t} = \underbrace{\alpha_p \, A_p (T - T_p)}_{\text{Convection}} + \underbrace{\epsilon_p \, A_p \left(\frac{G}{4} - \sigma \, T_p^4 \right)}_{\text{Thermal radiation}} + \underbrace{\sum_i S_{p,\,i}}_{\text{Source/sink}}, \qquad (4.19)$$

where $A_p = \pi \, d_p^2$ is the projected surface area of the particle, $c_{p,\,p}$ is the specific heat capacity and ϵ_p is the emission ratio of the particle. The convective heat exchange between particle and gas phase is calculated with the heat transfer coefficient α_p, which is calculated using the Nusselt correlation according to Ranz and Marshall [130, 131] in Eq. (4.20):

$$\text{Nu}_p = \frac{\alpha_p \, d_p}{\lambda} = 2.0 + 0.6 \, \text{Re}_p^{0.5} \, \text{Pr}^{0.33}. \qquad (4.20)$$

4.2.4 Turbulence modeling for particles

The turbulence dispersion model for the particle phase is based on the *eddy-life time model* by Gosman and Ioannides [132]. An artificial fluctuation $\boldsymbol{u}'$ is calculated and added to the averaged velocity of the gas phase $\tilde{\boldsymbol{u}}$. Using the turbulent kinetic energy $\tilde{k}$, the instantaneous velocity is calculated according to Eq. (4.21):

$$\boldsymbol{u} = \tilde{\boldsymbol{u}} + \boldsymbol{u}' = \tilde{\boldsymbol{u}} + x_{rnd} \, \boldsymbol{e} \, \sqrt{\frac{2}{3} \, \tilde{k}}, \qquad (4.21)$$

where $\sqrt{2/3 \, \tilde{k}}$ is the standard deviation, factor x_{rnd} is a random value reproducing a probability density function (PDF) and the direction vector $\boldsymbol{e}$ indicates the direction of the fluctuation pointing in a random direction. The particle must be in contact with the fluctuations for a certain amount of time in order to be influenced by the turbulence. The particle is only deflected when it completely passes through an eddy. The following turbulent time scale in Eq. (4.22) serves as a measure [66]:

$$t_{turb} = \min \left\{ \frac{\tilde{k}}{\tilde{\epsilon}}, \ 0.16432 \frac{\tilde{k}^{3/2}}{\tilde{\epsilon} |\tilde{\boldsymbol{u}} - \boldsymbol{u}_p|} \right\}. \qquad (4.22)$$

Since the solution of the particle motion is transient, the time steps Δt are accumulated by the dispersion model. If $\sum \Delta t \geq t_{turb}$, the fluctuating velocity $\boldsymbol{u}'$ is updated [66]. After a certain time step Eq. (4.17) is integrated over time, resulting in the particle velocity $\boldsymbol{u}_p$ [50]. The time step results from the Courant number $\text{CFL} = \tilde{\boldsymbol{u}} \, \Delta t / \Delta x$, which is set to 0.3.

4.2.5 Particle size distribution

In CFD codes, the particle size distribution is often approximated with a fixed number of particle classes. Another widely used approach is the *Rosin-Rammler distribution*. The Rosin-Rammler *cumulative distribution function* (CDF) is determined with a constant characteristic particle diameter $\overline{d}$ and an exponent or *dispersion coefficient* n. As the computational effort required to simulate each particle individually would be too high, *parcels* are used. An initial mass is specified, which usually corresponds to the fuel mass flow, and a constant number of parcels. The initial mass is distributed evenly among all parcels. Within a parcel, all particles have the same properties. Depending on the parcel mass and the particle size, the number of particles varies from parcel to parcel. Yoon et al. [133] state in their work that the difference between the particle distribution and the parcel distribution is $f(d)_{parcel} = d^3 \, f(d)_{particle}$. To take this into account, they formulate the CDF in Eq. (4.23):

$$\text{CDF}_{parcel} = \frac{1}{\overline{d}^3 \Gamma(3/n+1)} \int_0^d d^3 \frac{n \, d^{n-1}}{\overline{d}^n} \exp\left[-\left(\frac{d}{\overline{d}}\right)^n\right] d\,d. \qquad (4.23)$$

In OpenFOAM® version 2006, the computation based on Eq. (4.23) is implemented for the parcel diameter d_{parcel} according to Eq. (4.24):

$$d_{parcel} = \overline{d} \left[\Gamma\left(\frac{3}{n} + 1, \ x_{rnd}\right) \right]^{1/n}. \qquad (4.24)$$

The parcel diameter is calculated depending on the characteristic particle diameter $\overline{d}$, the dispersion coefficient n, a random generated number x_{rnd} between 0 and 1 and the incomplete gamma function. The parcel diameter is the particle diameter that is representative for all particles within a parcel.

4.3 Thermophysical Properties

The following section gives an overview of correlations used for the calculation of thermophysical properties of the gas phase, which are used in the CFD simulations. Further thermophysical models, implemented in OpenFOAM®, can be found in the code guide [124, 134]. Constant material properties are assumed for the liquids and solids.

4.3.1 Ideal gas law

The ideal gas law is valid for low pressures and densities, which is true for atmospheric firing. Molecules are assumed as mass points with large distances to other molecules, so they do not

interact [135]. The heat capacity at constant pressure and constant volume is assumed to be constant resulting in a *perfect gas*. This allows the calculation of the density using the ideal gas law according to Eq. (4.25):

$$\rho = \frac{p}{R\,T}. \tag{4.25}$$

4.3.2 Transport models for gases

The dynamic viscosity μ is calculated using the correlation according to Sutherland Eq. (4.26) for the ideal gas state [134]. Species based values of the Sutherland coefficient A_s and the Sutherland temperature T_s are used for this correlation:

$$\mu = \frac{A_s\,\sqrt{T}}{1 + T_s/T}. \tag{4.26}$$

If the Sutherland correlation is applied for the calculation of the dynamic viscosity, the thermal conductivity is calculated using the correlation in Eq. (4.27) by Poling et al. [136]:

$$\lambda = \mu\,c_v\left(1.32 + \frac{1.77\,R_i}{c_v}\right). \tag{4.27}$$

R_i is the specific gas constant and c_v the specific heat capacity at constant volume.

4.3.3 Heat capacity of gases

Polynomial sets are usually used instead of tables for the calculation of the specific heat capacity in CFD simulations. Thus, additional interpolation procedures are not necessary [25]. In OpenFOAM®, JANAF-Polynomials (Joint Army Navy NASA Air Force) are used for the calculation of heat capacity, enthalpy and entropy of gases. In order to obtain a higher accuracy, Eq. (4.28) is evaluated for low temperatures $T < 1000\,\text{K}$ and high temperatures $T \geq 1000\,\text{K}$. Thus, there are always two parameter sets for the polynomial [25, 134]:

$$c_p(T) = R\left(a_0 + a_1\,T + a_2\,T^2 + a_3\,T^3 + a_4\,T^4\right). \tag{4.28}$$

The values for a_0 to a_4 for the respective species are taken from the CHEMKIN software and tabulated in the work of Kronenburg [137].

4.3.4   Enthalpy of gases

The specific sensible enthalpy is calculated using an additional parameter a_5 which is specified in the parameter set of the JANAF-Polynomials. The total specific enthalpy h_{tot} in Eq. (4.29) is reduced by the standard enthalpy of formation Δh_f in Eq. (4.30) to obtain the specific sensible enthalpy h_s in Eq. (4.31) [134]:

$$h_{tot}(T) = R \left(a_0 T + \frac{a_1}{2} T^2 + \frac{a_2}{3} T^3 + \frac{a_3}{4} T^4 + \frac{a_4}{5} T^5 + a_5 \right), \qquad (4.29)$$

$$\Delta h_f = R \left(a_0 T_0 + \frac{a_1}{2} T_0^2 + \frac{a_2}{3} T_0^3 + \frac{a_3}{4} T_0^4 + \frac{a_4}{5} T_0^5 + a_5 \right), \qquad (4.30)$$

$$h_s(T) = h_{tot}(T) - \Delta h_f. \qquad (4.31)$$

The standard enthalpy of formation is calculated using standard conditions at a reference temperature T_0 of 25 °C (298.15 K).

4.4   Heterogeneous Chemistry

In solid fuel combustion, chemical interactions take place between different phases. In pulverized fuel combustion, the heterogeneous reactions are pyrolysis and char burnout [38]. Since combustion processes are very complex and the objective of this work is primarily the up-scaling of a burner with numerical calculations and the simulation of gas radiation in oxyfuel combustion, simple models are used for the combustion of solids in order to reduce the computational effort. The models presented are widely used for solid fuel combustion and can be found in most CFD codes.

4.4.1   Pyrolysis modeling

The moisture content in the particle evaporates before pyrolysis initiates. The evaporation of the moisture is modeled with OpenFOAM® model *LiquidEvaporation*. More information about this model can be found in the source code [125], or in the ANSYS® Fluent® Theory Guide where the same model is described [70].

The *SingleKineticRateDevolatilisation* model calculates the mass transfer of volatiles from the particles into the gas phase by using an Arrhenius approach as shown in Eq. (4.32). The volatile mass loss rate of the fuel particle is determined with the frequency factor A and the activation energy E. The same amount of volatiles is transferred to the gas phase.

$$\frac{dm_{p,vol}}{dt} = -A \cdot \exp\left(-\frac{E}{RT}\right) m_{p,vol}. \tag{4.32}$$

The values for A and E are fuel-specific properties and have to be determined experimentally. Since the presented CFD model is used for the up-scaling of an oxyfuel burner for which experimental data are mostly available for the investigation of coal, the reference fuel is Rhenish lignite, instead of biomass and thus pyrolysis kinetics for coal are used here. The pyrolysis kinetics of Badzioch et al. [138] are integrated in many CFD codes for bituminous coal. Kinetics from Hamor et al. [139] used for lignite, since it represents the average of kinetics for lignite from other authors [67]. Values for the pyrolysis frequency factor A and the activation energy E can be found in Tab. 4.4. Further values are listed in the work of Epple et al. [67].

Tab. 4.4 Pyrolysis frequency factor and activation energy for the single kinetic rate model [67].

Author	Coal type	A (1/s)	E (J/kmol)
Fletcher et al. [140]	Bituminous coal	2.3×10^{14}	23.01×10^{7}
Badzioch et al. [138]	Bituminous coal	1.5×10^{5}	7.4×10^{7}
Hamor et al. [139]	Lignite	3.15×10^{5}	7.4×10^{7}
Anthony et al. [141]	Bituminous coal	1.64×10^{13}	21.26×10^{7}

Since pyrolysis occurs when the temperature reaches approx. $300\,^{\circ}\mathrm{C}$, this temperature is specified as the initial value. Pyrolysis will not occur until the particle temperature is above the pyrolysis temperature.

4.4.2 Surface reaction modeling

As described in Chapter 2, the rate of char burnout is limited by diffusion processes and chemical reactions. The widely used char burnout model by Baum and Street [142] named *COxidationKineticDiffusionLimitedRate* in OpenFOAM® considers diffusion rate k_{diff} and the chemical reaction rate k_{chem} as limiting for the burnout rate. Using the harmonic mean of k_{diff} and k_{chem}, the mass consumption of char is calculated according to Eq. (4.33):

$$\frac{dm_{char}}{dt} = -A_p\, \rho\, R\, T\, \frac{Y_{O_2}}{M_{O_2}} \left(\frac{1}{k_{diff}} + \frac{1}{k_{chem}}\right)^{-1}. \tag{4.33}$$

The particle surface $A_p = \pi\, d_p^2$ is treated simplified as a spherical surface. The chemical reaction rate k_{chem} is determined with an Arrhenius approach in Eq. (4.34):

$$k_{chem} = C_2 \exp\left(-\frac{E}{RT}\right). \tag{4.34}$$

The diffusion rate k_{diff} is calculated according to Eq. (4.35):

$$k_{diff} = \frac{C_1}{d_p} \left(\frac{T + T_p}{2} \right)^{0.75},$$
(4.35)

and the parameter C_1 using Eq. (4.36) [66, 143]:

$$C_1 = \frac{2\,M_{char}\,D_{O_2}}{R\,T^{1.75}}\,\delta = \frac{2\,M_{char}\,D_{O_2}(1600\text{ K}) \left(\frac{T}{1600\text{ K}} \right)^{1.75}}{R\,T^{1.75}}\,\delta,$$
(4.36)

where the oxygen diffusion coefficient in air combustion is $D_{O_2}(1600\text{ K}) = 3.49 \times 10^{-4}\,\text{m}^2/\text{s}$ [38]. The mechanism factor δ is set to $\delta = 1$ if the char oxidation product is CO and $\delta = 2$ if the product is CO_2 [143].

Toporov et al. [116] proposed values for C_1, C_2 and the activation energy E for Rhenish lignite, listed in Tab. 4.5, using high and low particle temperatures under oxyfuel conditions. The char is mainly oxidized to CO by oxygen in Eq. (4.37a). Because of the high amount of CO_2 in oxyfuel combustion the endothermic *Boudouard-reaction* in Eq. (4.37b) must be taken into account. Since small amounts of water vapor are also involved in the heterogeneous reactions, this is taken into account using reaction Eq. (4.37c).

Tab. 4.5 Reaction constants for the char burnout model for low and high particle temperatures of Rhenish lignite [116, 118].

Reaction equation	Range (K)	C_1 (s/K$^{0.75}$)	C_2 (s/m)	E (J/kmol)	Eq.
$C_{char} + \frac{1}{2}\,O_2 \rightarrow CO$	–	2.18×10^{-12}	5.0×10^{-3}	7.4×10^7	(4.37a)
$C_{char} + CO_2 \rightarrow 2\,CO$	< 1223	1.0×10^{-10}	1.35×10^{-4}	13.5×10^7	(4.37b)
	> 1223	1.0×10^{-10}	6.35×10^{-3}	16.2×10^7	
$C_{char} + H_2O \rightarrow CO + H_2$	< 1223	2.84×10^{-12}	3.19×10^{-1}	20.8×10^7	(4.37c)
	> 1223	2.84×10^{-12}	1.92×10^{-3}	14.7×10^7	

Since the char oxidation model in the standard OpenFOAM® code only allows the oxidation of carbon with oxygen to carbon dioxide, the code was extended with the equations in Tab. 4.5.

4.5 Homogeneous Chemistry

Once the volatile species from the solid fuel have been transferred into the gas phase, homogeneous reactions occur. An exact knowledge of the intermediate products resulting from chemical reactions in the gas phase is not of importance for the up-scaling of the oxyfuel burner and the calculation of gas radiation, which is done later. Therefore, detailed chemistry is omitted in favor of computing time and a global reaction mechanism is used.

4.5.1 Chemical reactions and kinetics

The combustion of volatile components in an oxyfuel atmosphere is described using a four-step mechanism according to Toporov et al. [116] and Askarizadeh et al. [118] for Rhenish lignite. Pyrolysis releases a mixture of gases composed of light and heavy gases such as tars. Since a large number of reaction equations have to be solved and this considerably increases the calculation time, the volatile species are summarized into the single species $C_xH_yO_lN_mS_n$ [144]. The volatile reaction is shown in Eq. (4.38):

$$C_xH_yO_lN_mS_n + \left(\frac{x}{2} + n - \frac{l}{2}\right)O_2 \; \rightarrow \; xCO + \frac{y}{2}H_2 + nSO_2 + \frac{m}{2}N_2. \tag{4.38}$$
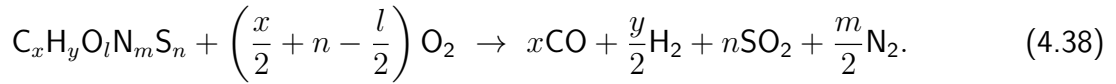
The kinetics for the volatile reaction are taken from Toporov et al. [116]. The mole-based coefficients for the representative species $C_xH_yO_lN_mS_n$ of the volatile components in the solid fuel are calculated using the values from the ultimate and the proximate analysis by means of Eq. (4.39):

$$x = \frac{M_{vol}}{M_C}\frac{Y_C^{DAF} - Y_{C_{fix}}^{DAF}}{Y_{vol}^{DAF}}, \tag{4.39a}$$

$$y = \frac{M_{vol}}{M_H}\frac{Y_H^{DAF}}{Y_{vol}^{DAF}}, \tag{4.39b}$$

$$l = \frac{M_{vol}}{M_O}\frac{Y_O^{DAF}}{Y_{vol}^{DAF}}, \tag{4.39c}$$

$$m = \frac{M_{vol}}{M_N}\frac{Y_N^{DAF}}{Y_{vol}^{DAF}}, \tag{4.39d}$$

$$n = \frac{M_{vol}}{M_S}\frac{Y_S^{DAF}}{Y_{vol}^{DAF}}. \tag{4.39e}$$

Since the volatile specie is a virtual gas, its enthalpy of formation Δh_f must be determined. It is therefore assumed that the experimentally determined calorific value H_u is composed of the enthalpy of formation for the fixed carbon and the volatile species Eq. (4.40):

$$H_{u,fuel}^{DAF} = H_{u,C_{fix}}^{DAF}\,Y_{C_{fix}}^{DAF} + H_{u,vol}^{DAF}\,Y_{vol}^{DAF}. \tag{4.40}$$

Assuming the char content as pure carbon, $H_{u,C_{fix}}^{DAF} = 32.76\,\text{MJ/kg}$ can be used for the calorific value. Rearranging Eq. (4.40), the calorific value of the volatile species can be calculated. Multiplying the calorific value by the molar mass gives the enthalpy for the combustion of the volatiles h_{vol}. If Hess' law is applied, which states that the change of enthalpy for a global reaction h_R corresponds to the sum of the change of enthalpy for all partial reactions in Eq.

(4.41), the enthalpy of formation for the volatile specie can be calculated with Eq. (4.42):

$$h_R = \sum h_{f,prod} - \sum h_{f,reac} = H_{u,vol}^{DAF} \, M_{vol}. \tag{4.41}$$

Eq. (4.42) corresponds to the general Eq. (4.41) rearranged to $\Delta h_{f,vol}$:

$$\Delta h_{f,vol} = x \, \Delta h_{f,\text{CO}} + \frac{y}{2} \, \Delta h_{f,\text{H}_2} + n \, \Delta h_{f,\text{SO}_2} + \frac{m}{2} \, \Delta h_{f,\text{N}_2}$$
$$- \left(\frac{x}{2} + n - \frac{l}{2} \right) \Delta h_{f,\text{O}_2} - h_R. \tag{4.42}$$

The enthalpy of formation of all other species are calculated using data from the literature. The molar mass of the volatile species has to be estimated [144]. In this work the molar mass and transport properties of methane are assumed for $C_x H_y O_l N_m S_n$. This assumption is based on the work of different authors [67, 78, 145] where methane is used as representative hydrocarbon compound for volatile species. The reaction in Eq. (4.38) is followed by CO and H_2 oxidation and the *water-gas-shift* reaction, which is only considered in one direction, as used by Askarizadeh et al. [118]. All reactions implemented in the simulation are shown in Tab. 4.6 with the corresponding reaction rate.

Tab. 4.6 Frequency factor and activation temperature for the combustion of volatile matter [116, 118].

Reaction equation	A (1/s)	T_a (K)	Eq.
$CO + \frac{1}{2} O_2 \rightarrow CO_2$	1.3×10^{11}	15155	(4.43a)
$H_2 + \frac{1}{2} O_2 \rightarrow H_2O$	2.2×10^9	13110	(4.43b)
$CO + H_2O \rightarrow CO_2 + H_2$	2.75×10^{11}	10.07	(4.43c)

4.5.2 Turbulent chemical interaction

To close the partial differential equation system of turbulent, reactive flows for species conservation the source term $\dot{R}_i$ in Eq. (4.5) must be determined. Chemical reactions can only take place if there is a sufficiently high temperature and the reactants are perfectly mixed at the molecular level. In turbulent flows, the reaction progress is thus strongly influenced by the mixing through vortex structures [67]. If a vortex decays, it generates numerous smaller vortices, which subsequently disintegrate into even smaller ones. Eventually, the smallest vortex structures dissipate their kinetic energy into heat. Based on the idea of this energy cascade, the total volume is divided into microscopic areas called *fine structures* and macroscopic areas. The mixing of the reactants takes place only at the microscopic level, as they represent the smallest scales of the energy cascade. There, viscous forces dominate and energy dissipates to

heat. Outside the smallest structures, no reaction takes place because there is no molecular mixing [67].

Due to the high turbulence of industrial firing, the Eddy Dissipation Concept (EDC) model is used here, since it is suitable for highly turbulent flows and nevertheless takes chemical time scales into account. This model is also used by other authors in the field of oxyfuel combustion simulation [7, 66, 146]. The EDC is derived from the Eddy Dissipation Model (EDM). According to Magnussen [147, 148], the ratio of the dissipation rate ϵ and the turbulent kinetic energy k are used as a measure for the dissipation of the vortices. The ratio ϵ/k has the unit $1/s$ and is multiplied by the time-averaged concentration of the reacting species. Thus, a small turbulent time scale results in a high reaction turnover [67].

The length fraction ξ^* of the fine structures is calculated according to Eq. (4.44):

$$\xi^* = C_\xi \left(\frac{\nu_{lam}\,\epsilon}{k^2} \right)^{1/4}. \tag{4.44}$$

Quantities with '$*$' as superscript refer to the fine structures. To obtain the volume fraction of the fine structures, $(\xi^*)^3$ is calculated. The constant for the volume fraction is given by C_ξ = 2.1377. The fine structure time scale τ^* is used to solve the system of reaction equations. The mass fractions within the fine structure are calculated by applying the Arrhenius chemical reaction rates in the previous section under fine structure conditions [7]. The fine structure time scale is calculated using Eq. (4.45):

$$\tau^* = C_\tau \left(\frac{\nu_{lam}}{\epsilon} \right)^{1/2}, \tag{4.45}$$

where the constant $C_\tau = 0.4082$. The reaction rate $\dot{R}_i$ for the mean species i is then calculated with Eq. (4.46). The fine structures mass fraction of species i is designated as Y_i^* which results from the reaction calculations over the time τ^* [70].

$$\dot{R}_i = \frac{\rho\,(\xi^*)^2}{\tau^*\,[1 - (\xi^*)^3]}(Y_i^* - Y_i). \tag{4.46}$$

Compared to the EDM, the EDC has the advantage that it takes the reaction rate of the individual chemical reactions into account, whereas the EDM is only controlled by turbulence. Therefore, the EDM should only be used for global one-step reactions. However, different chemical time scales can lead to stiff differential equation systems using the EDC. Implicit solution methods can be used to solve stiff differential equation systems. In this work the implicit Euler method is used [125].

4.6 Wall Conditions

In industrial steam generators, the walls consist of parallel tubes through which water/steam flows. Depositions on these tubes reduce the heat transfer between fluid and the combustion chamber interior [50]. Since the inflow and outflow temperature as well as the pressure of the water in the cooling system of the experimental combustion chamber used in this work are known, the wall heat flux density q_w can be estimated in conjunction with the surfaces of the combustion chamber wall. Only the surfaces in the area of the visible flame, where heat transfer by radiation dominates, are considered. This assumption is made since, according to Schneider [38], it is assumed that the heat transfer by convection is less than 10 % of the radiative heat transfer. The wall heat flux density q_w, taking the thickness of the deposit layer d_{dep} into account, is calculated by Eq. (4.47) [50]:

$$q_w = \frac{\lambda_{dep}}{d_{dep}} \left(T_w - T_{tube} \right),$$

(4.47)

where T_w is the wall temperature and T_{tube} the temperature at the tubes. The thermal conductivity of the deposit λ_{dep} is assumed to be an average value of $1.0 \, \text{Wm}^{-1}\text{K}^{-1}$ and the deposit thickness is set to $2 - 4 \, \text{mm}$ according to Ströhle [50]. Furthermore, a temperature difference between water/steam and the wall is caused by two temperature gradients, one inside the wall of the tubes and another inside the fluid itself. The qualitative temperature profile between the combustion chamber interior and the water/steam is shown in Fig. 4.2 [50].
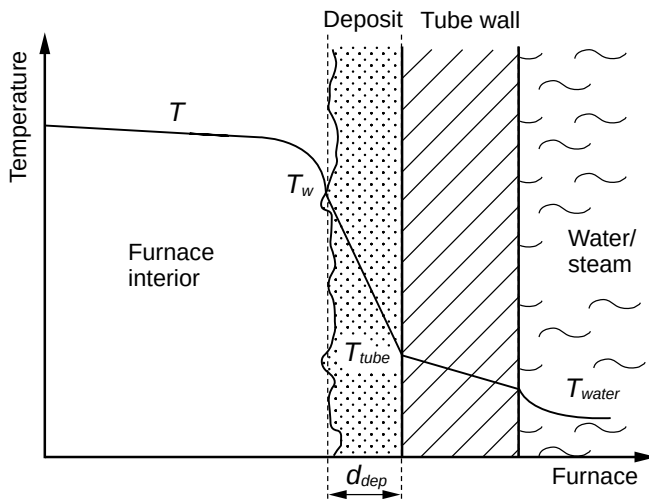
Fig. 4.2 Qualitative temperature profile from the interior of the combustion chamber through the deposits and the membrane wall to the water/steam [50].

For the numerical simulations in this work, the wall heat flux density q_w and the water/steam temperature T_{water} are calculated analytically from measurement data. The wall temperature T_w is selected so that the corresponding wall heat flux density results according to Eq. (4.47). The wall temperature is set constant in the simulations for the entire combustion chamber wall since it was not possible to measure a wall temperature profile.

5 Up-Scaling of an Oxyfuel Burner

To investigate the combustion of biomass under oxyfuel conditions in a semi-industrial combustion chamber with water-cooled walls, a laboratory-scale reference oxyfuel burner was scaled up. The reference oxyfuel burner, designed and investigated at WSA RWTH Aachen University has a thermal output of 40 kW (WSA40). Toporov et al. [149] developed this oxyfuel burner for pulverized coal with stable flames at low oxygen concentrations in the oxidant. They achieved flame stability by means of a strong inner recirculation zone (IRZ) in front of the burner, which compensates heat losses due to the high heat capacity of CO_2 by returning hot gases back into the reaction zone. The reference burner was investigated numerically and experimentally by different authors [116, 150–153]. A down-scaled version of the WSA40 burner also exists and is described in the work of Becker et al. [154]. Investigations of the down-scaled burner were done by different authors [14, 155–158].

This chapter presents the procedure of up-scaling an oxyfuel reference burner which led to the semi-industrial burner used for the experiments in this work. For this purpose, established scaling methods for up-scaling the reference burner are applied and discussed in a first step. Afterwards a new method based on dimensional analysis and numerical simulations is presented. The following section provides an overview of the state of the art in the field of up-scaling industrial burners.

The effort of up-scaling can be reduced by mathematical correlations. These correlations are intended to obtain similar values for emissions, heat transfer rate and flame stability of the up-scaled burner to those of the reference burner. The parameter of interest in most scaling studies is NO_x formation [159]. Weber and Mancini [160] applied the *constant velocity* (CV) and *constant residence time* (CRT) approach of Hawthorne et al. [161] for scaling in the range of $0.176 - 50 \, MW_{th}$ for pulverized coal-fired, swirl-stabilized burners. Experiments proved both approaches to be representative for full-scale industrial applications above $4 \, MW_{th}$. However, for less than $1 \, MW_{th}$, the CRT approach is more suitable. For penetrating flames (type 0), in contrast, both methods are suitable for the entire thermal input range investigated by Weber and Mancini [160]. The idea behind the CRT approach is a constant ratio of burner diameter to inlet velocity, which represents the large macro turbulent mixing time scale for fuel and oxidant. Adequate mixing of the fuel and oxidizer provides stable combustion [162, 163]. By using CV and CRT, Maldonado [162] down-scaled an oxyfuel-fired clinker burner from $47 \, MW_{th}$ to $0.5 \, MW_{th}$. The author opted for the CV approach due to limitations in the manufacture of the burner. The geometry of a clinker burner is much more complex than most industrial burners, which are coaxial and shell-shaped. Therefore, it was not possible to down-scale all geometrical attributes of the burner by the same factor and consequently the number of nozzles had to be reduced. Two approaches were presented by Pramanik and Ravikrishna [164], a *constant volume to jet momentum ratio* (CM) and a *constant volume to jet kinetic energy ratio* (CK), to scale up a $3.3 \, kW_{th}$ combustion chamber to $25 \, kW_{th}$. Their

study showed that the CK and CM criterion is very similar to the CV approach and therefore applicable to the up-scaling of reverse-flow combustors [165].

5.1 Reference Combustion Chamber

The $40\,\text{kW}_\text{th}$ laboratory burner was specially designed for the investigation of oxyfuel firing by Toporov et al. [116]. This burner serves as a reference for up-scaling to a semi-industrial scale in this work. In Fig. 5.1 the WSA combustion chamber with the axial movable reference burner and the geometry of the WSA40 itself is shown. The carrier gas together with the pulverized fuel is entering the chamber through the primary inlet. The oxidant is distributed to the secondary, tertiary and purge channel. The secondary stream is swirled and the degree of swirl can be adjusted. The channel at the wall serves as purging, since the burner is movable in axial direction [7]. The quarl has an angle of approx. $21°$. The chamber walls are refractory-lined and equipped with electrical heating elements. More details about the burner and the combustion chamber can be found, for example, in the work of Toporov et al. [7, 116] and Zabrodiec et al. [153].
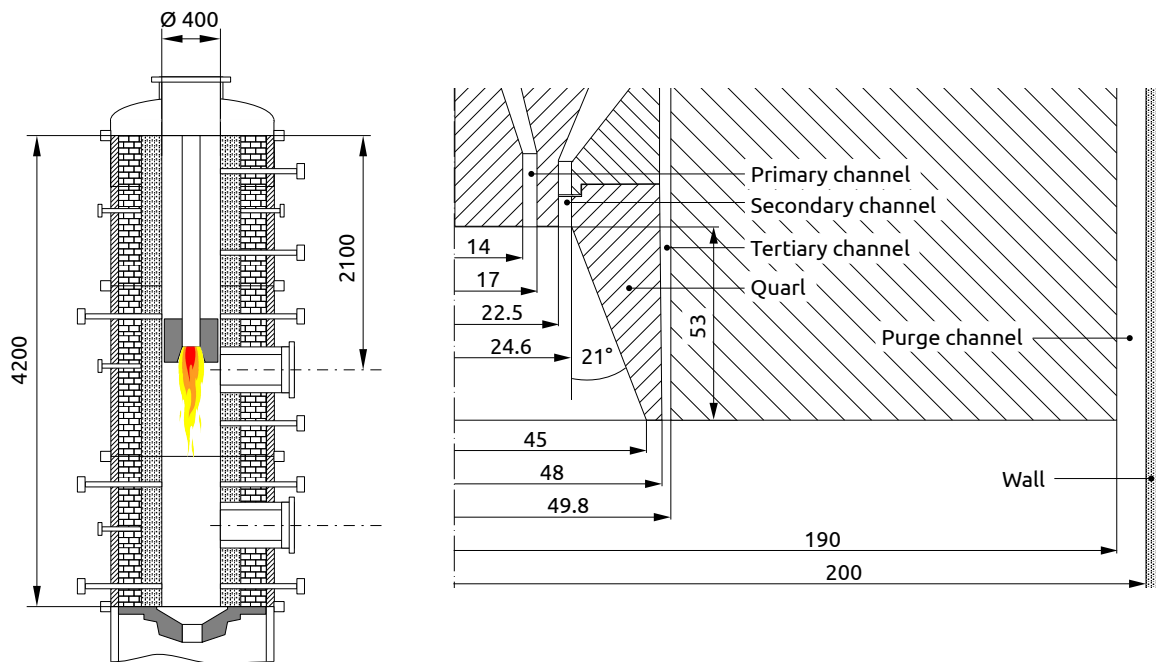
Fig. 5.1 Left: cross-section of the WSA combustion chamber. Right: symmetrical half of the WSA40 reference oxyfuel burner. Dimensions in millimeters [116].

5.2 Initial Conditions

The following section shows the basic parameters that are used for the further up-scaling process of the burner up to a nominal thermal power of $500\,\text{kW}$. This burner is designated

here as EST500. The coaxial channel arrangement of the WSA40, as shown in the previous section, is also used for the EST500. The primary channel for the solid fuel is located in the center and is surrounded by the secondary channel. The tertiary channel is located outside of the quarl. The mass flow of the fuel is calculated by dividing the nominal power of $500\,\mathrm{kW_{th}}$ by the calorific value of the reference fuel, Rhenish lignite[1]. Biomass is not investigated during the process of up-scaling, since no experimental data currently exist for the reference burner. The particle load of the primary flow has to be low so that the particles are able to follow the stream. In this case, $\dot{m}_{fuel}/\dot{m}_{prim}$ should be lower than 0.5 according to Effenberger [47]. This results in a primary carrier gas mass flow of $177\,\mathrm{kg/h}$ for a fuel mass flow of $88.5\,\mathrm{kg/h}$. An oxidant composition of $18\,\mathrm{vol\%}$ O_2 and $82\,\mathrm{vol\%}$ CO_2 is used for the primary flow, similar to Heil et al. [166] and Toporov et al. [116]. This results in a primary gas volume flow of approx. $100\,\mathrm{Nm^3/h}$. The required oxidizer volume flow is calculated using Eq. (5.1) – (5.5), whereby the primary flow rate is constant for all thermal loads [165]:

$$\dot{V}_{O_2,st} = \frac{\dot{m}_{fuel}}{\rho_{O_2}} \left(Y_C \frac{M_{O_2}}{M_C} + \frac{1}{2} Y_H \frac{M_{O_2}}{M_{H_2}} + Y_S \frac{M_{O_2}}{M_S} - Y_O \frac{M_{O_2}}{M_{O_2}} \right), \tag{5.1}$$

$$\dot{V}_{O_2,loc} = \lambda_{loc} \dot{V}_{O_2,st}, \tag{5.2}$$

$$\dot{V}_{O_2,glob} = \lambda_{glob} \dot{V}_{O_2,st}, \tag{5.3}$$

$$\dot{V}_{O_2,sec} = \dot{V}_{O_2,loc} - \dot{V}_{O_2,prim}, \tag{5.4}$$

$$\dot{V}_{O_2,tet} = \dot{V}_{O_2,glob} - \dot{V}_{O_2,prim} - \dot{V}_{O_2,sec}. \tag{5.5}$$

The mass fractions Y_i in Eq. (5.1) result from the ultimate analysis. For the EST combustion chamber, the local oxidant-fuel equivalence ratio refers only to the primary and secondary channel, since the combustion chamber does not have a purge channel in contrast to the WSA chamber. The global oxidant-fuel equivalence ratio is achieved with the tertiary nozzles. Detailed dimensions of the chamber and the final burner design can be found in Chapter 6.

5.3   Scaling Correlations

This section discusses established scaling correlations from the literature regarding their applicability to the up-scaling of the WSA40. Eq. (5.6) is the fundamental equation which

---

[1]Calorific value, ultimate and proximate analysis are tabulated in Chapter 6.

establishes a relationship between the thermal output and the burner diameter. The thermal power $\dot{Q}$ is determined from the mass flow rate of the fuel and the calorific value. The calorific value and $\pi/4$ are substituted into the constant scaling factor K. Here, the diameter of the burner is used as characteristic value. After the new diameter has been calculated by means of the correlation, any other burner dimensions can be calculated, as the geometric similarity is retained [159, 162].

$$\dot{Q} = \dot{m}_{fuel}\, H_u = u\, \rho\, \frac{\pi}{4}\, d^2 H_u = K\, u\, \rho\, d^2. \tag{5.6}$$

To obtain the relationship for the constant velocity, Eq. (5.6) is solved for the velocity u, resulting in Eq. (5.7), where the subscript 0 denotes the reference and 1 the scaled parameter:

$$u = const. \;\Rightarrow\; u_0 = u_1 \;\Rightarrow\; \frac{\dot{Q}_0}{K\, \rho\, d_0^2} = \frac{\dot{Q}_1}{K\, \rho\, d_1^2}. \tag{5.7}$$

The same is done for the constant residence time. Here, Eq. (5.6) is solved for d/u, resulting in the relationship in Eq. (5.8). Therefore Eq. (5.6) has to be divided by u^3:

$$d/u = const. \;\Rightarrow\; \frac{d_0}{u_0} = \frac{d_1}{u_1} \;\Rightarrow\; \frac{\dot{Q}_0}{K\, \rho\, u_0^3} = \frac{\dot{Q}_1}{K\, \rho\, u_1^3}. \tag{5.8}$$

Since the right-hand equation in Eq. (5.8) does not contain a diameter, the middle part of Eq. (5.8) must be solved for u_1 and substituted into the right-hand part of Eq. (5.8). For both, the constant velocity and the constant residence time, this results in the general formulation Eq. (5.9):

$$d_{scaled} = d_1 = d_0 \left(\frac{\dot{Q}_1}{\dot{Q}_0} \right)^{C}. \tag{5.9}$$

All authors mentioned above use Eq. (5.9) with some restrictions described in the work of Drubetskoi et al. [159]. Differences are only due to the exponent C in Eq. (5.9). Tab. 5.1 summarizes the values for the exponent [165].

Tab. 5.1 Values for the exponent C in correlation Eq. (5.9) [161, 164, 165].

	CV	CRT	CM	CK
C	0.5	0.33	0.25	0.43

Tab. 5.2 summarizes the results of scaling WSA40 to $500\,\text{kW}_{\text{th}}$ applying the various scaling approaches. In addition, the actual geometric properties of both burners are shown in the

table. Results of all approaches lead to a quarl angle of approx. 21°, equivalent to the angle of the WSA40. The quarl length is between 99.7 and 187.4 mm [165].

Tab. 5.2 Results using correlations from the literature for up-scaling WSA40 to 500 kW$_{th}$ [165].

	Load $\dot{Q}$	Primary A	Secondary A	Quarl L	Quarl d
	kW$_{th}$	mm^2	mm^2	mm	mm
Actual	40	292.2	310.7	53.0	90.0
geometry	500	3782.0	10307.6	235.0	438.0
CV	500	9833.0	11157.0	187.4	318.2
CRT	500	1547.4	1645.7	122.0	207.1
CM	500	1033.0	1098.6	99.7	169.2
CK	500	2564.3	2727.3	157.0	266.6

However, due to the constructive limitations of the EST combustion chamber, the quarl length can not be smaller than 235 mm and the burner diameter is limited by the connection port with a diameter of 265 mm. Considering the results for the primary channel inlet using the CRT method, the area of the primary channel inlet is 2.4 times smaller than in the final geometry of the EST500. According to the principle of continuity, the velocity in the channel increases by the same factor. With a factor of 1.5, the CK method shows the smallest difference to the EST500. For the CRT method, the velocity of the secondary channel is approx. 6.3 times higher and for the CK method 3.8 times higher. Using the CV method, the burner channel surfaces are adjusted in such a way that the velocities correspond to the reference burner. Since the velocities of approx. 5 m/s for the primary channel and 12 m/s for the secondary channel [167] do not correspond to a semi-industrial burner, this method can be discarded. Fig. 5.2 illustrates a simplified comparison of the reference burner WSA40, EST500 and the burner scaled using the CRT method [165].
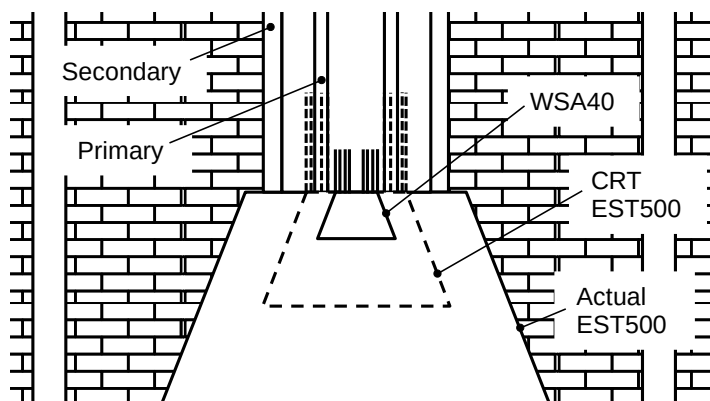
Fig. 5.2 Geometric comparison of the quarl and channels for the actual EST500 with WSA40 and the result of the scaling method CRT (dashed lines) [165].

5.4   Dimensional Analysis

Before the reference burner is scaled up to a semi-industrial burner, it is crucial to determine which characteristic properties of the laboratory burner should be transferred to the large-scale burner. For most industrial burners, the focus is on pollutant emissions and stable operation. When developing the reference burner, the main focus was on aerodynamic flame stabilization with low oxygen concentrations, which is achieved by a strong IRZ at the outlet of the burner [166]. Since the IRZ is the most characteristic property of the reference burner, there should be a correlation between the IRZ of the laboratory burner and the IRZ of the semi-industrial burner. A frequently used mathematical method in fluid mechanics for similarity analyses is *dimensional analysis*. This mathematical method is able to reduce the number of physical quantities to a number necessary to describe a physical problem. The dimensional analysis can be used to describe how many independent parameters are actually required. Buckingham's Π-theorem states that a function with m dimensional parameters, which in turn are made up of n physical base units, can be described with $m - n$ independent dimensionless quantities [21, 168]. A detailed description on how to perform a dimensional analysis can be found in the work of Laurien [21].

The first step of a dimensional analysis is to create a list of physical variables that have an influence on the flow process under consideration. The quarls surface A_{quarl} is calculated as a truncated cone. It is used for similarity investigation since the angle and the radius of the quarl have an impact on the shape of the IRZ. The IRZ is approximated with the surface of an ellipsoid A_{IRZ}. It includes all negative velocities in the axial direction in the area of the quarl. Here the reader is referred to Fig. 2.8 in Chapter 2 ($u_{ax} = 0$ m/s). The velocity u and the density ρ of the fluid are responsible for the flows momentum. The dynamic viscosity μ is also included here as it provides the shear stress in the flow. Tong et al. [169] demonstrate the effect of velocity differences between primary and secondary flow for a bluff-body-stabilized premixing flame. An IRZ is formed for $u_{sec} > u_{prim}$. In the case of $u_{prim} \gg u_{sec}$, the centrally located primary flow penetrates the IRZ resulting in the formation of a type 0 jet flame [169]. Since the IRZ is also formed in a flow without combustion, thermal variables are neglected here. This results in five characteristic quantities. The surface of the quarl A_{quarl}, and the density of the fluid ρ are chosen as the *repeating values*. The surface of the IRZ A_{IRZ} and the dynamic viscosity of the fluid μ are the *dependent values*. All these quantities can be described with the basic units metres m, seconds s and weight kg. Consequently, $m - n = 5 - 3 = 2$ equations are necessary. These two equations are Eq. (5.10) and Eq. (5.11) [165]:

$$\Pi_1 = \mu \, A_{quarl}^{x_1} \, u^{x_2} \, \rho^{x_3}, \tag{5.10}$$

$$\Pi_2 = A_{IRZ}\, A_{quarl}^{x_1}\, u^{x_2}\, \rho^{x_3}. \tag{5.11}$$

The following applies to the dimensionless representation in Eq. (5.12) and Eq. (5.13) by introducing the exponents $x_1 \ldots x_3$:

$$\frac{kg}{m\,s}\, (m^2)^{x_1} \left(\frac{m}{s}\right)^{x_2} \left(\frac{kg}{m^3}\right)^{x_3} = 1, \tag{5.12}$$

$$m^2\, (m^2)^{x_1} \left(\frac{m}{s}\right)^{x_2} \left(\frac{kg}{m^3}\right)^{x_3} = 1. \tag{5.13}$$

Applying Eq. (5.12) to the three dimensions in Eq. (5.14):

$$
\begin{aligned}
kg : &\qquad\qquad\qquad 1 + x_3 = 0 &\Rightarrow&\qquad x_3 = -1, \\
m : &\qquad -1 + 2x_1 + x_2 - 3x_3 = 0 &\Rightarrow&\qquad x_1 = -\frac{1}{2}, \\
s : &\qquad\qquad\qquad -1 - x_2 = 0 &\Rightarrow&\qquad x_2 = -1.
\end{aligned}
\tag{5.14}
$$

Likewise for Eq. (5.13):

$$
\begin{aligned}
kg : &\qquad\qquad\qquad x_3 = 0 &\Rightarrow&\qquad x_3 = 0, \\
m : &\qquad 2 + 2x_1 + x_2 - 3x_3 = 0 &\Rightarrow&\qquad x_1 = -1, \\
s : &\qquad\qquad\qquad -x_2 = 0 &\Rightarrow&\qquad x_2 = 0.
\end{aligned}
\tag{5.15}
$$

If the values for x_1, x_2 and x_3 from Eq. (5.14) are inserted into Eq. (5.10) and the results from Eq. (5.15) into Eq. (5.11), the following quantities result:

$$\Pi_1 = \frac{\mu}{A^{0.5}\, u\, \rho} = \frac{2}{\sqrt{\pi}}\, \mathrm{Re}^{-1}, \tag{5.16}$$

$$\Pi_2 = \frac{A_{IRZ}}{A_{quarl}} = A^*. \tag{5.17}$$

Π_1 results in the Reynolds number. The Reynolds number is the most commonly used parameter in fluid mechanics for comparison. For laboratory-scale burners, however, the Reynolds numbers are lower than on a semi-industrial scale. The Scaling-400 study [170–175] found that the smallest burner with $30\,\mathrm{kW_{th}}$ produces a Reynolds number of 16300 and the largest burner with $12\,\mathrm{MW_{th}}$ a Reynolds number of 331400. Industrial burners can reach high Reynolds

numbers, approaching half a million [160, 170, 171]. Hence, a comparison between laboratory scale and semi-industrial scale using the Reynolds number is difficult [165]. Π_2 results in a ratio of two surfaces. The ellipsoidal surface of the IRZ, normalized by the surface of the quarl, is designated as the dimensionless surface A^*. The exact calculation of A^* is shown in Eq. (5.18):

$$A^* = \frac{2\,\pi\,a\,\left[a + \frac{c^2}{\sqrt{c^2-a^2}}\arcsin\left(\frac{\sqrt{c^2-a^2}}{c}\right)\right]}{\pi\,\left[r^2 + R^2 + \sqrt{(R-r)^2 + \left(\frac{R-r}{\tan\alpha}\right)^2}(r+R)\right]}, \quad \text{for } c > a. \tag{5.18}$$

Here, c and a refer to the height and width of an ellipsoid, which is used to approximate the IRZ. The result of Eq. (5.16) and Eq. (5.17) also implies that there is a functional relationship between Π_1 and Π_2, namely $A^* = f(\mathrm{Re})$. The recirculation zone will certainly change with a changed Reynolds number and thus A^*, but this relationship is not of interest in the further course of this work. An additional variable is used to characterize the flow field, namely the dimensionless velocity u^* in Eq. (5.19):

$$u^* = \frac{|u_{ax,min,IRZ}|}{u_{mix}}. \tag{5.19}$$

The mixture velocity u_{mix} is a vector addition of all inlet velocities inside the quarl according to Selvam and Isaev [176, 177]. They use this comparative quantity in their work for a T-junction where flows with different velocities are mixing. In this work, u^* is the ratio between the mixing velocity and the largest negative velocity in terms of amount within the IRZ. The dimensionless surface area in Eq. (5.18) and the dimensionless velocity in Eq. (5.19) are used below as comparative variables for up-scaling [165].

Since the velocity of the secondary channel is unknown, the annular gap was initially selected so that a velocity of approx. $20\,\mathrm{m/s}$ results. However, this value corresponds to a comparable burner that has been investigated in earlier studies in the same combustion chamber [178]. A CFD simulation is carried out with the specified values for the primary and secondary velocity as u^* requires information about the IRZ. In case the result differs from the u^* of the reference burner, either the secondary velocity is decreased or increased by changing the secondary channel geometry. For A^*, the procedure is the same. The angle of the quarl is corrected in this case. This method is intended to establish a relationship between the reference burner and the up-scaled burner. The swirl number, the local and global equivalence ratio remain constant [165].

5.5 Validation and Up-Scaling Results

This section is divided into two parts. First, to prove the applicability of the CFD model from Chapter 4 for the EST500 burner simulation, the model is validated in preliminary tests using existing experimental data from the WSA40 reference burner. Second, the numerical results of the up-scaling process for the EST500 are compared to the simulation results of the WSA40 using the same numerical model, fuel, and dimensionless quantities of the previous section.

5.5.1 Validation of the numerical model

Both the WSA and EST combustion chambers feature cyclic boundary conditions; the mesh represents one sixth of the entire combustion chamber. As the EST combustion chamber has a hexagonal cross-section, this is done for reasons of uniformity. Each mesh extends to the location where the off-gas leaves the combustion chamber. Fig. 5.3 shows the numerical meshes.
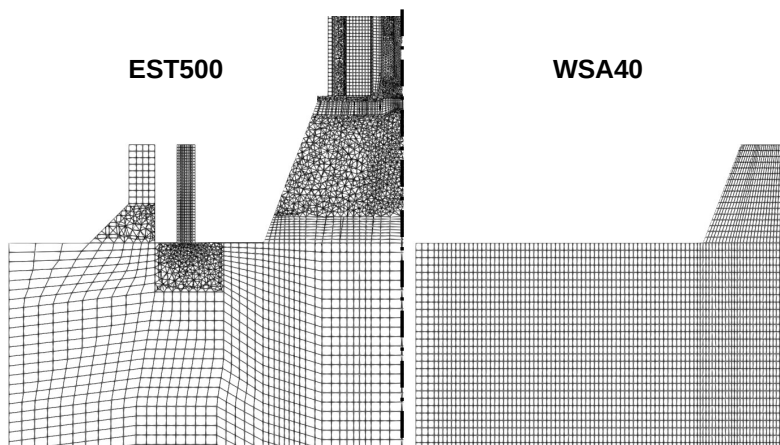
Fig. 5.3 Combustion chamber meshes in the upper area. Left: cross-section of the EST500. Right: cross-section of the WSA40 [165]. The meshes are displayed at different scales for better comparison.

WSA40 is discretized with 4.5×10^5 hexahedral cells. This has proven to be reasonably accurate after a mesh study with 8×10^5 and 20×10^5 cells. The EST500 mesh has 2.5 million cells. The mesh study of the EST500 can be found in the appendix Chapter A.2. There are two extensions on the EST500 mesh outside the quarl, corresponding to a niche and the tertiary air nozzle. More details can be found in Chapter 6. The boundary conditions for WSA40 and EST500 are shown in Tab. 5.3 [165].

For the WSA40, the primary, secondary and tertiary channels are not meshed; the inlet consists of a patch at each channel. The swirl channels of the EST500 extend to the inlet of the combustion chamber and therefore have meshed channels. Each simulation was carried out using the models in Chapter 4. A fixed wall temperature of 1173 K is used for the WSA chamber, as the wall temperature measurements during the experiments were in the same order of magnitude [152]. For the EST chamber, the equivalence ratio within the quarl is sub-stoichiometric $\lambda_{loc} = 0.8$ and the global ratio is $\lambda_{glob} = 1.4$, similarly to the WSA40. Furthermore, a maximum swirl number of 1.0 is used. However, the walls of the WSA combustion

Tab. 5.3 Boundary conditions at the inlets for the WSA40 [116] and EST500 simulation [165].

$\dot{Q}$ (kW)	Channel	$\dot{m}$ (kg/h)	O_2 (vol%)	CO_2 (vol%)	T (K)
	Coal	6.5	–	–	–
	Primary	17.6	19	81	313
40	Secondary	26.6	21	79	333
	Tertiary	1.5	21	79	333
	Purge	54.9	21	79	1173
	Coal	81	–	–	–
	Primary	177	18	82	293
500	Secondary (axial)	0	21	79	323
	Secondary (swirl)	482	21	79	323
	Tertiary	482	21	79	323

chamber are heated to a constant value. The EST combustion chamber features water-cooled walls, where in previous experiments at 500 kW$_{th}$ load a value of about 1000 K was reached on the inside near the wall. This temperature is applied for the simulation of the EST chamber [165].

Results for the velocity field in the axial direction, temperature and oxygen concentration are shown in Fig. 5.4, plotted in radial direction for the WSA40 case for different axial distances to the burner. The axial origin is located at the end of the quarl. At an axial position of 0.05 m, the velocity curve is in good agreement with the measurements. However, it increases close to the wall, since the velocity of the purge flow is even more pronounced in the simulation than in the measurements. Uncertainties also exist in the measurement near the wall. In the central region of the flame, the IRZ is underestimated by the simulation. The calculated axial velocity at 0.2 m shows a minor shift compared to the measurements. This may be due to uncertainties in the turbulence model. The simulation results at 0.3 m are similar to the measurements [165].

At an axial position of 0.05 m, in the center of the flame, the temperature is lower than the measured values. Measurements at this position are complicated due to the high temperature gradients in this region. Moreover, effects caused by thermal radiation can lead to inaccuracies. Since the secondary stream is located at this position, it is reasonable for the temperature to drop. There is a second leap along the radius leading to a lower temperature due to the more pronounced secondary flow in the simulation. The temperature decrease close to the wall is caused by the purge flow. Oxygen concentration results and measurements on the burner axis near the quarl are low, as a sub-stoichiometric condition is present here. A leap in the oxygen concentration can be seen at the radial position of 0.05 m, caused by the secondary flow. In the wall area, the high deviations are probably due to the coarse resolution of the mesh close
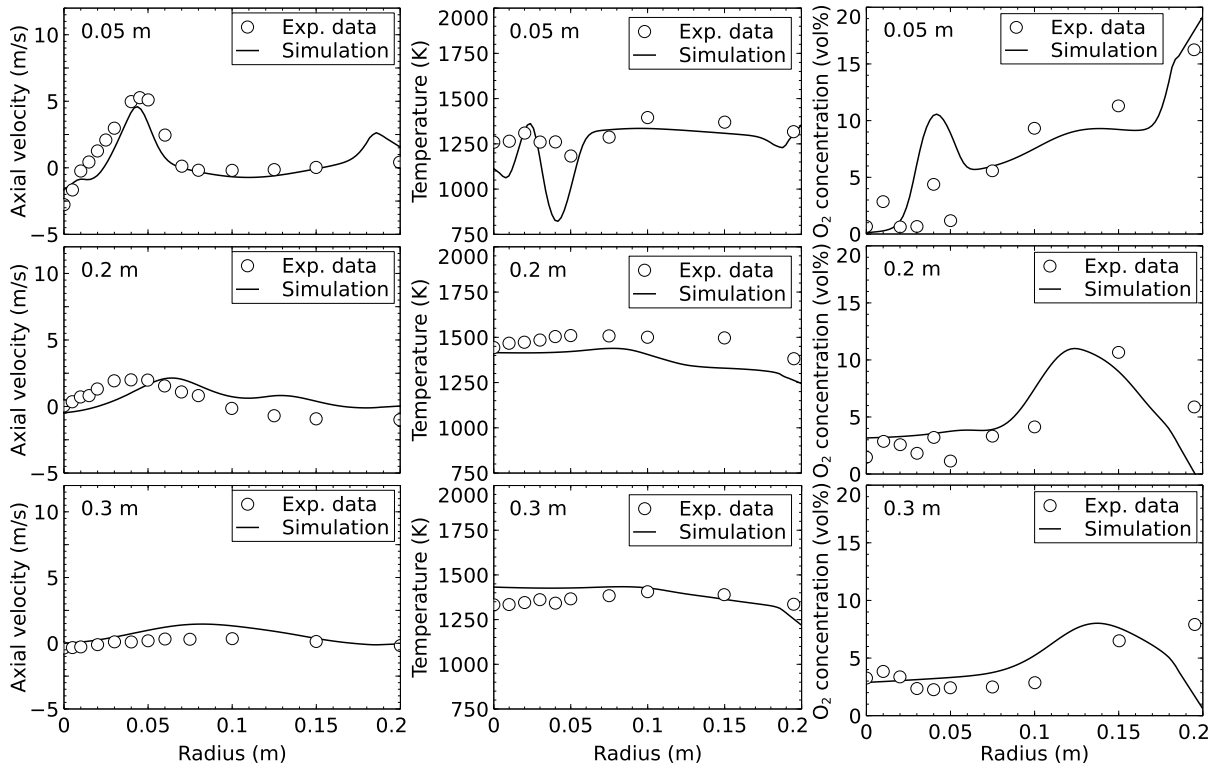
Fig. 5.4 CFD results for the axial velocity, temperature and oxygen concentration of the WSA40 burner plotted against the combustion chamber radius at axial position 0.05, 0.2 and 0.3 m. CFD results compared to the experimental data from Toporov et al. [116, 165].

to the wall [165].

The simulations of the WSA40 burner using simple numerical models from Chapter 4 showed acceptable deviations from the experimental data. In particular, these models are able to predict the IRZ with sufficient accuracy. The model validation should be reasonably accurate for the scope of this work, focusing on the flow field. Knowledge of the exact chemical processes, for example, is not required. Hence, this model is used for the EST500 simulation [165].

5.5.2 Up-scaling numerical results

This numerical up-scaling process can be considered as a parameter study. It involves numerous simulations, therefore only simple numerical models are used in order to keep the computing time to a minimum. Starting the simulations with the same quarl angle as the WSA40 (21°), the dimensionless surface results in a value of approx. 2.2 and thus equals the same value as A^* for the WSA40. Therefore, no further adjustments are made to the quarl angle. Previous simulations have shown that with an opening angle of approx. 27°, the stream is directed towards the combustion chamber wall. After a few additional simulations and adjustments to the secondary channel of the EST500, a value of 0.2 is obtained for u^*, which corresponds to the WSA40. This results in a velocity of 18 m/s for the secondary stream [165].

The results for the velocity field in the axial direction of the EST500 burner compared to the

WSA40 burner are shown in Fig. 5.5. The dimensions of the IRZ are shown in the illustrations. The recirculation zones can also be identified by the zero axial velocity line ($u_{ax} = 0\,\mathrm{m/s}$).
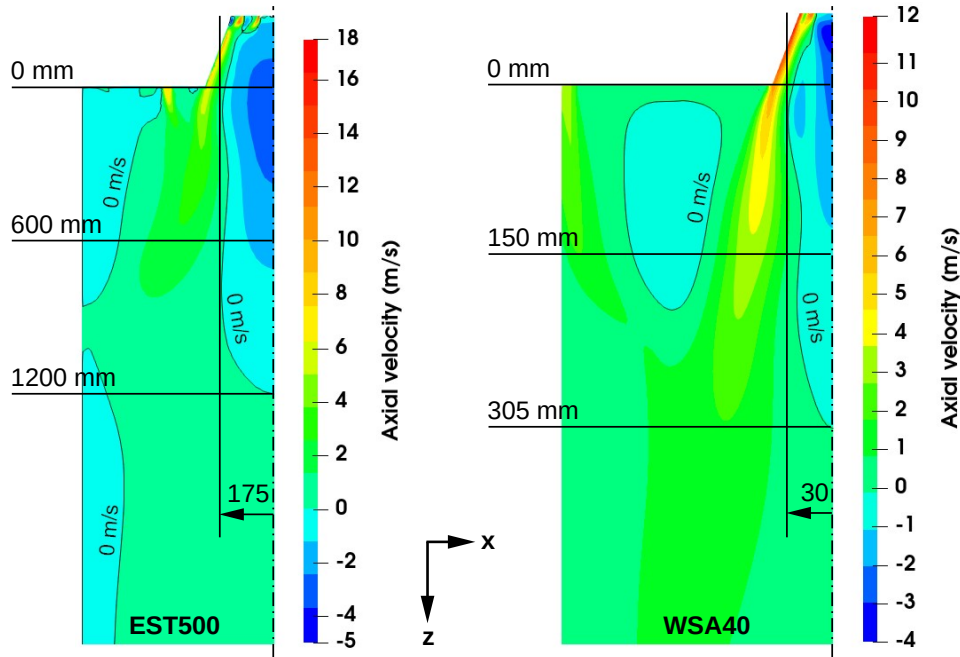
Fig. 5.5 Axial velocity (z) fields resulting from CFD simulations. Left: results of the EST500. Right: results of the WSA40. Geometries are displayed at different scales for better comparison [165].

The WSA and EST combustion chamber velocity fields have a pronounced IRZ along the center axis. The IRZ is important for flame stabilization. An additional external recirculation zone can be recognized on the WSA40 between the purge channel and the tertiary channel. The EST500, on the other hand, shows an outer recirculation zone in the upper and lower area of the wall. As the EST combustion chamber does not have a purge channel, the flow conditions outside the flame zone are different. Furthermore, the WSA chamber introduces around half of the total oxidant volume through the purge channel. This means that the oxidant volume must be divided among the primary, secondary and tertiary channels for the EST500 in order to achieve an equivalence ratio of 0.8 in the flame core and a total value of 1.4 [165].

Fig. 5.6 shows the normalized axial velocity, tangential velocity and pressure plotted against the normalized radius of the WSA40 and EST500 at different axial positions. The velocity and pressure are shown in dimensionless form. The velocities are normalized by the mixing velocity u_{mix}. The radius r and the axial height z are normalized by the quarl diameter d of the respective burner. The pressure is given as a percentage deviation from the reference pressure $(p - p_0)/p_0$. The reference pressure is set to $101325\,\mathrm{Pa}$. At $z/d = 0.6$ it can be seen that the axial velocities for both burners are negative up to the half of the radius and then change into the positive range. The limit of the IRZ is located at the point of the transition. Furthermore, the relationship between the tangential velocity, which is caused by the swirl, and the negative pressure or backflow can be seen. At the height $z/d = 0.6$, the tangential
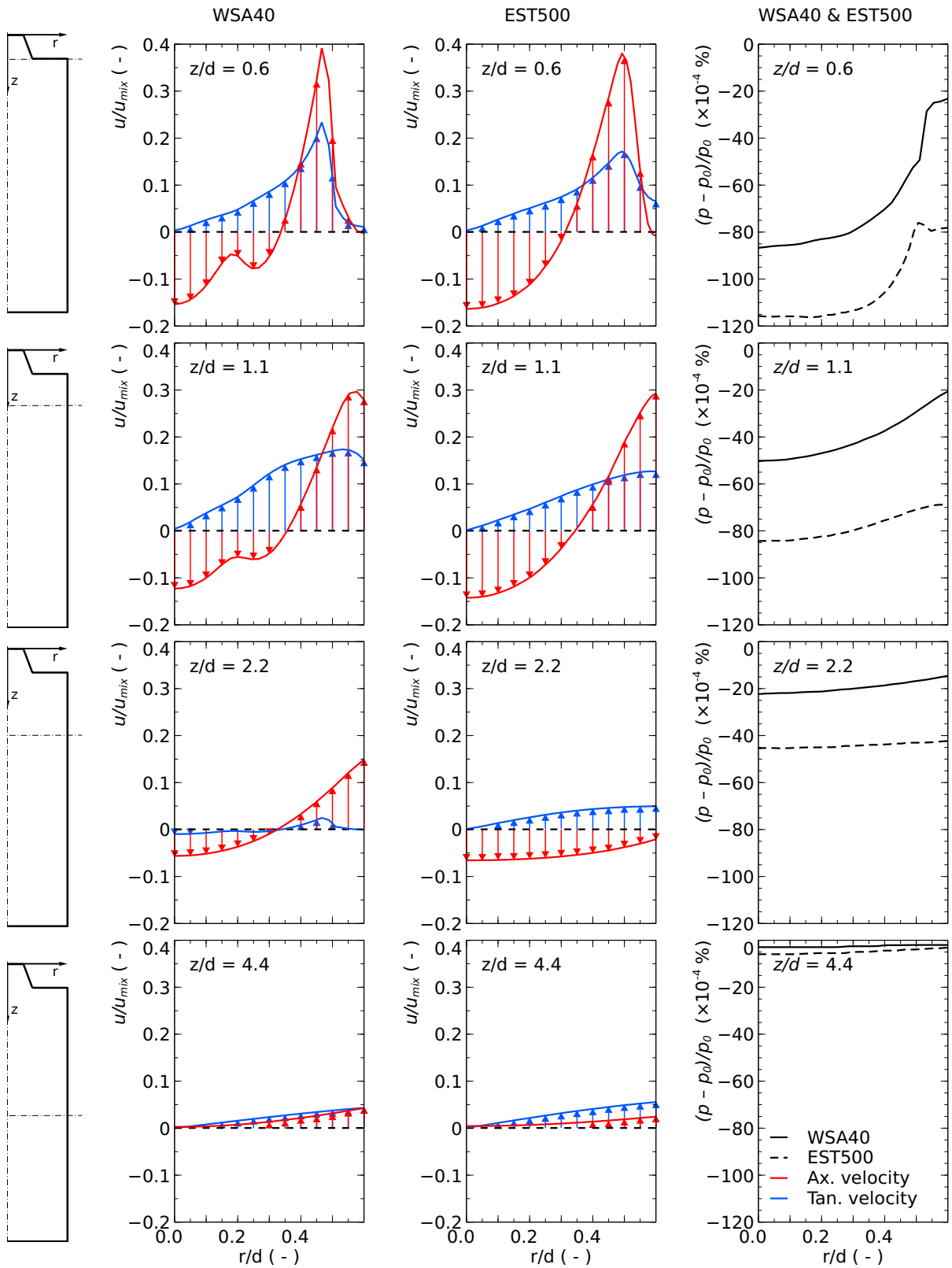
Fig. 5.6 Dimensionless axial velocity, tangential velocity and pressure plotted against the dimensionless radius of the combustion chamber at various axial positions. Velocities are normalized by the mixture velocity of each burner. The pressure is given as a percentage deviation from the reference pressure. The considered height in the combustion chamber is shown on the left-hand side.

velocity is at its maximum and the backflow and negative pressure are also most pronounced here. The WSA40 and EST500 show similar profiles for all the variables considered here. At $z/d = 0.6$ and $z/d = 1.1$, a fluctuation in the axial velocity can be seen at approx. $r/d = 0.2$. Presumably, the different distribution of the particles in the stream at both burners is responsible for the different velocity profile here. As the velocities of the EST500 are higher than those of the WSA40, the negative pressure is also slightly increased. As z/d increases, it can be seen that the tangential velocity and the IRZ, which can be recognized by the negative axial velocity, decrease. At $z/d = 4.4$, both velocities are in the positive range and the pressure has also equalized with the reference pressure. There is no more recirculation at this position. At $z/d = 2.2$, the profiles of both burners exhibit pronounced divergence. While the entire axial velocity profile of the EST500 is in the negative range, the WSA40 shows a transition between negative and positive velocities. This is due to the differences in the wall region of the combustion chambers, which can also be seen in Fig. 5.5. The flow characteristics differ significantly here, as the EST combustion chamber does not have a purge channel at the wall.

The ignition characteristics and thus the flame stability of solid fuel combustion significantly depend on the volatile content of the fuel and their consumption [42]. Non-premixed flames, where the mixing process dominates and the chemical reaction is assumed to be infinitely fast, can be described using the mixture fraction. Solid fuel combustion presents a particular case, as two fuels, volatiles and char, react with different rates [179]. Therefore the mixture fraction is split into individual mixture fractions for volatiles and char according to Domino and Smith [180], Flores and Fletcher [181] and Brewster et al. [182]. The mixture fraction for volatiles Z_{vol} is calculated according to Eq. (5.20):

$$Z_{vol} = \frac{m_{vol}}{m_2 + m_{vol} + m_{char}}. \tag{5.20}$$

The index 2 marks the gas mass originating from oxidant flow. In Fig. 5.7 the volatile mixture fractions for both burners are shown. The temperature is plotted against the volatile mixture fraction of WSA40 and EST500. The data obtained from the CFD simulation are shown as scatter plot in these diagrams. The adiabatic flame temperature is shown as a straight black line.

Since there is no pure fuel stream and the volatile species are yield from the solids during pyrolysis and carried by the transport fluid, both diagrams end on the abscissa considerably below one. Pyrolysis takes place at temperatures above $500\,\mathrm{K}$, so the fuel-rich area (from right to left in the diagram) starts at significantly higher temperatures than the oxidizer stream. However, the diagram of the WSA40 burner shows an accumulation of points between a mixture fraction of 0 and 0.12, in the upper area of the chart. This is due to the high temperature of the purge stream. While the EST500 shows a scattering of points around the adiabatic temperature line in the lean range. The mixing processes of the two burners
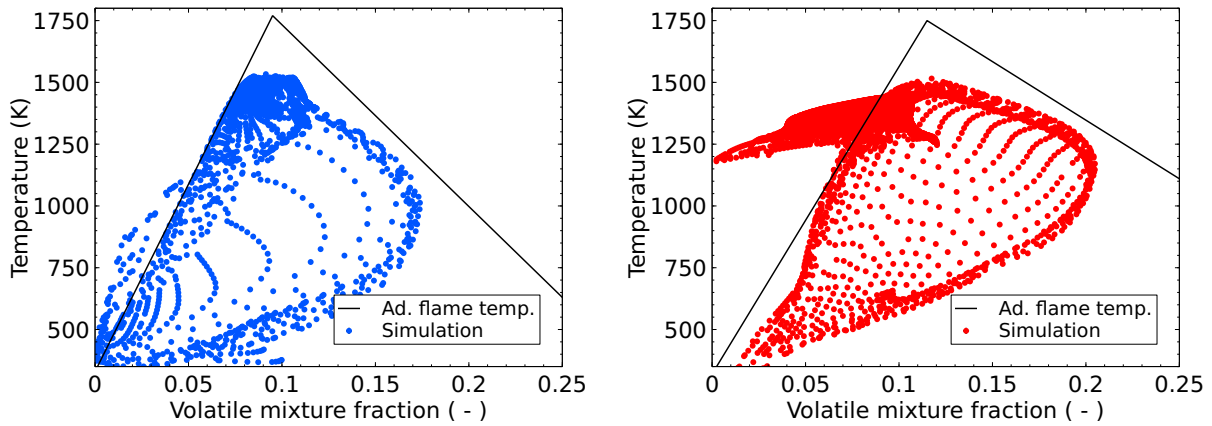
Fig. 5.7 Scatter plots for flame temperature against volatile mixture fraction resulting from CFD simulations. Left: scatter plot of the EST500. Right: scatter plot of the WSA40. Adiabatic flame temperature drawn as black solid line.

differ in this area. The overall structure of the mixture fraction and the areas of localized flame extinction are similar for both burners. The local release of volatile species in the WSA chamber is higher than in the EST chamber, which may be due to the heated walls. The maximum temperatures in both combustion chambers differ only slightly.

Fig. 5.8 shows the temperature contour of both burners resulting from the CFD simulation.
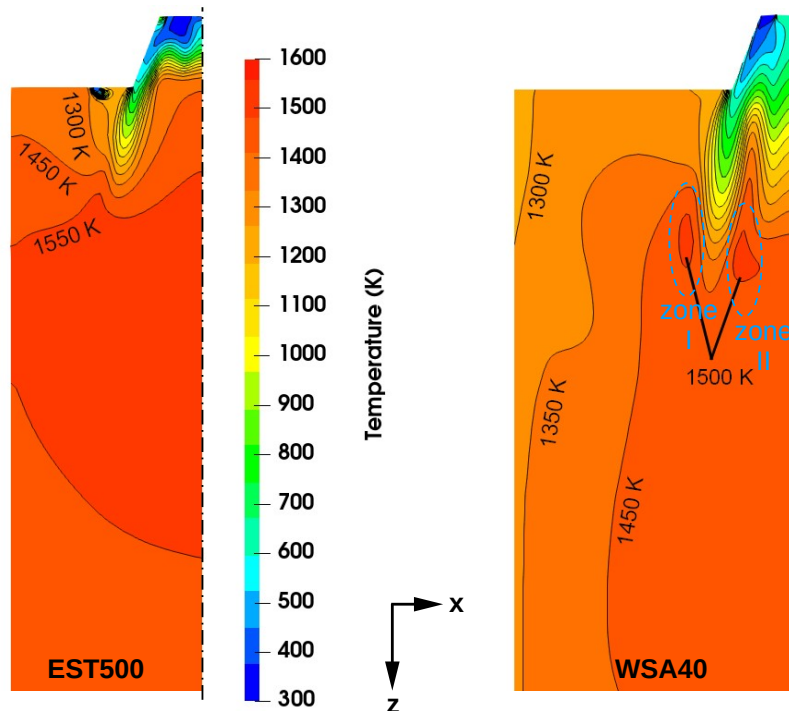
Fig. 5.8 Temperature contours in the upper section of the combustion chamber resulting from CFD simulations. Left: contour of the EST500. Right: contour of the WSA40. Geometries are displayed at different scales for better comparison [165].

The WSA40 shows two zones (marked in blue) at the end of the quarl in the horizontal direction in which the highest temperature occur. In contrast, only one zone exists for the EST500 [165]. As the IRZ is the same for both burners, the reason for the differences in the

reaction zones could be the distribution of the particles. The higher secondary velocities, close to the burner, in the EST combustion chamber cause the particles to follow the IRZ streams. This results in a uniform release of the volatile components in the area of the quarl. In contrast to the WSA40, the large particles do not follow the secondary stream. Consequently, the larger particles penetrate the IRZ and release the volatiles within the IRZ (zone II, Fig. 5.8), while the smaller particles follow the secondary flow and release the volatiles at the outer area of the IRZ (zone I, Fig. 5.8) [165]. Fig. 5.9 shows the distribution of particle diameter in the combustion chamber of the EST500 and WSA40 burner.
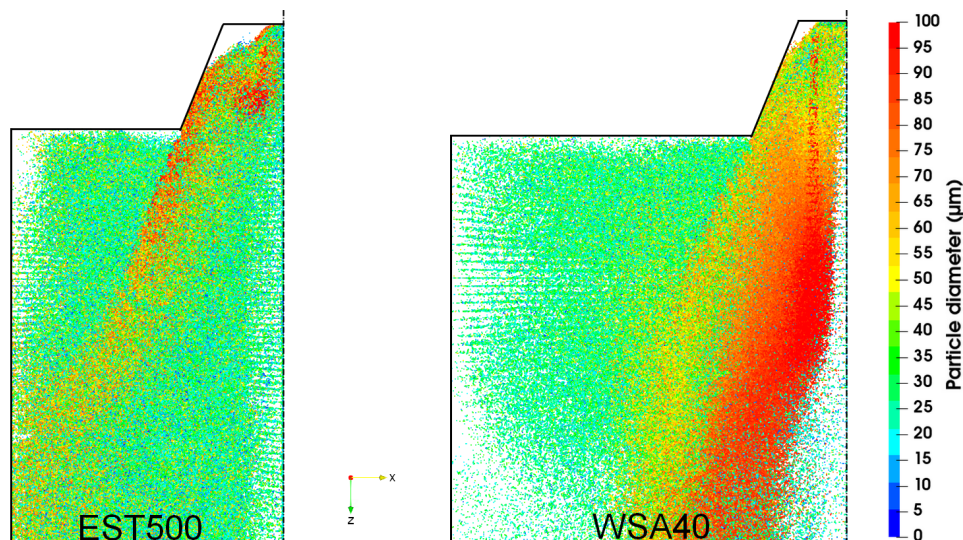
Fig. 5.9 Distribution of particle sizes in the upper part of the combustion chambers. Left: particle distribution in the EST chamber. Right: particle distribution in the WSA chamber. Geometries are displayed at different scales for better comparison [165].

The secondary flow of the EST500 carries the large particles ($>100\,\mu m$) directly after they exit the primary channel. The particles follow the secondary streams. In the case of the WSA40, larger particles in the secondary flow penetrate the IRZ and only a small amount of large particles follow the secondary stream. The high accumulation of large particles along the combustion chamber axis, which can be seen in the WSA40, suggests that burnout is slower than in the EST500, where only a small accumulation of larger particles can be seen due to the strong recirculation and thus enhanced mixing. It may therefore be advisable to additionally include the particle size for future scaling correlations [165].

The results of the simulation fulfill the criteria required here of an equal dimensionless velocity u^* and surface area A^* for both burners. This means flow conditions that ensure a compact IRZ in order to recirculate sufficient fuel particles, radicals and hot gases in the reaction zone near the burner, but do not divert the flow towards the combustion chamber wall. The temperatures are also within an appropriate range. The simulation can therefore be used as an orientation for the design of the new burner. The geometric data resulting from the simulation was used for the production of the burner [165]. The final geometry of the EST500 burner is described in the next chapter.

6 Experimental Setup

This chapter describes the configuration of the entire oxyfuel combustion system and the dimensions of the oxyfuel burner based on the up-scaling in Chapter 5. Furthermore, the measuring systems used to determine the gas concentrations, humidity and the sensor used to measure the wall-incident radiative heat flux are addressed. In addition, the properties of the fuels used for the combustion experiments are shown.

6.1 Oxyfuel Combustion Facility

The experimental oxyfuel plant of the EST at the Technical University Darmstadt is suitable for the combustion of pulverized solid fuel, and natural gas with a maximum thermal output of up to $1\,\mathrm{MW}$. In Fig. 6.1 a simplified scheme of the oxyfuel system is shown.
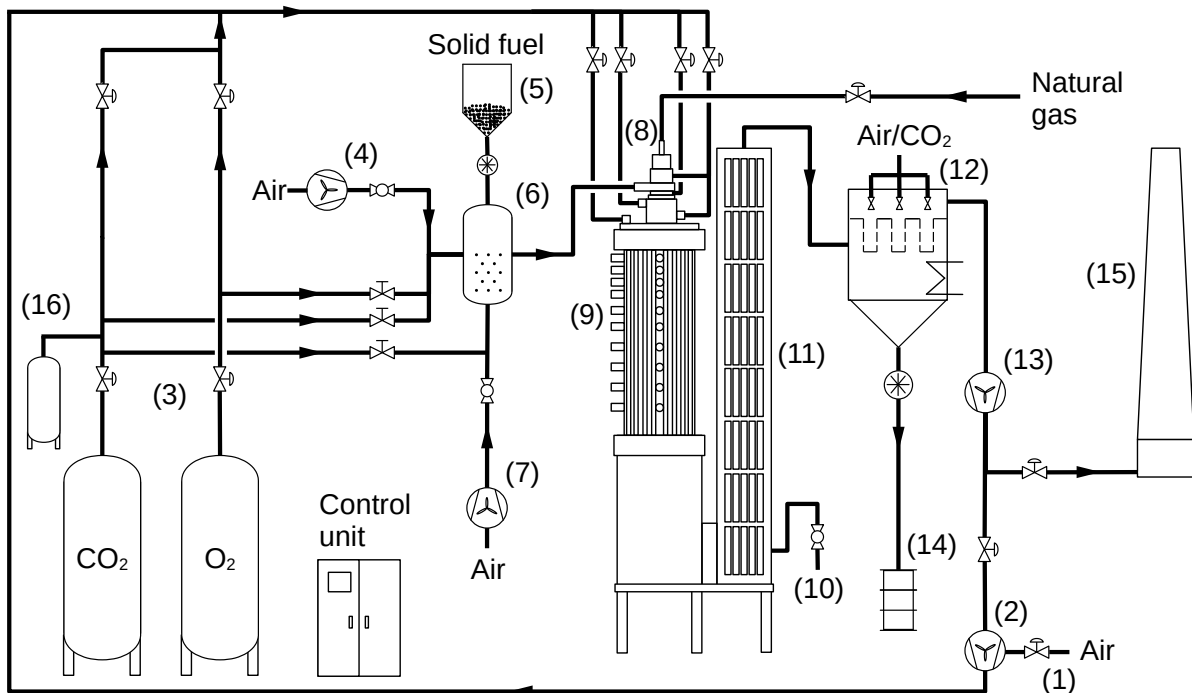
Fig. 6.1 Simplified scheme of the oxyfuel combustion system: (1) air valve, (2) combustion air fan or RF fan, (3) CO_2 and O_2 tanks, (4) transport air fan, (5) fuel supply container, (6) dosing device, (7) fluidization air fan, (8) burner, (9) combustion chamber, (10) ash sampling, (11) convective heat exchanger, (12) particulate filter, (13) ID fan, (14) ash barrel, (15) stack, (16) pressure compensating tank.

The combustion chamber is an approx. $10\,\mathrm{m}$ high top-down fired system. The chamber is operated at a negative pressure of approx. $-2\,\mathrm{mbar}$. The cooling system is pressurized by $16\,\mathrm{bar}$ and is capable of removing up to $1\,\mathrm{MW}$ heat. In the air-fired configuration, air is introduced into the system through the air valve (1). The fan (2) conveys the oxidant to the burner (8). Before the oxidant enters the burner, it is split up into four pipes for swirled

primary, axial secondary, swirled secondary and tertiary flow. The combustion chamber walls are made of parallel, welded, water-cooled steel tubes in the upper section, similar to the evaporator in coal-fired power plants. In the lower part of the combustion chamber, the flue gas changes its direction and flows upwards through a convective heat exchanger (11). The off-gas then passes through a particulate filter (12), which is equipped with filtration bags which are cleaned by periodic impulses of air or CO_2. The filter ash is collected in a barrel (14) for disposal. The particulate filter is heated at $200\,°C$ to prevent condensate formation inside the filter. The filtered flue gas is conveyed by an ID fan (13) to the stack (15) where it is released into the environment, or is partly recirculated by the fan (2) back to the burner. Natural gas and pulverized solid fuels are combustible with the same burner. Solid fuels are stored in *Big-Bags* or containers. The solid fuel is transported into a feed container (5) and is fed from there into the dosing device (6). The dosing device is a container with nozzles at the bottom which are fluidizing the pulverized fuel using a fluidizing fan (7). From the discharge line at the dosing system the fuel is transported to the burner. In air-fired operation, the transport air is provided by a fan (4), which has a constant volume flow of $210\,Nm^3/h$ regardless of the fuel mass flow. The thermal load is only varied by increasing the fuel dosage. In case of dry oxyfuel combustion, the oxidant and transport flow are supplied by the O_2 and CO_2 tanks (3). The transport flow and the O_2/CO_2 ratio is constant during all experiments. However, it can be adjusted with manual needle valves. If recirculated flue gas is used, the CO_2 tank is only necessary for the transport flow. The O_2 tank is required for the oxygen content in the transport medium of the solid fuel and for enriching the oxygen concentration in the recirculated flue gas. The O_2 enrichment for the oxidant is controlled by an automatic control valve, while the oxygen for the transport flow is adjusted with a manual needle valve. The O_2 concentration in the oxidant and the oxidant-fuel equivalence ratio are determined by the operator. The air for fluidization of the dosing device and the particulate filter cleaning device is replaced by CO_2 in oxyfuel operation. It is possible to take ash samples from the bottom of the combustion chamber via a screw conveyor (10). A pressure compensating tank (16) is connected to the CO_2 line to compensate pressure fluctuations which are mainly caused by the pulsing device inside the particulate filter.

Originally, this plant was only capable of burning fuel in an air atmosphere. To enable experiments with oxyfuel, the entire system was retrofitted in the context of this work. In addition to the oxyfuel burner and quarl, new pipes, fittings, measuring ports and a new control unit were installed. To enable flue gas recirculation, a new pipe was built between the combustion air fan, the oxidant line and the flue gas path. A connection to the oxygen line was created to enrich the recirculated flue gas with O_2. New O_2 and CO_2 pipes, each with a manual control valve, were installed to allow solid fuel transport with a constant volume flow. Two further CO_2 lines were constructed for the fluidization of the dosing system and for the CO_2 component in the oxidant when operating the plant in dry oxyfuel mode. The pulse cleaning

of the particle filter was modified so that the filter bags can be cleaned with CO_2 instead of air. Additional measurement ports were installed at the membrane wall of the combustion chamber. For this, new CO_2 lines were created to purge the measuring systems. The entire oxidant lines were thermally insulated to reduce the condensation of water vapor in the lines during flue gas recirculation. Since the oxyfuel operation is more complex than pure air-firing, a new control unit including a customized software had to be installed.

For safety reasons, the system is pre-ventilated for approx. 10 min during start-up. After pre-ventilation, the natural gas is ignited in air operation with a high-energy igniter. After a heating phase with natural gas at a load of approx. $300 \, kW_{th}$, the combustion air is enriched with oxygen. Subsequently, the air inlet on the fan is closed and the flap to the flue gas path is opened at the same time. The system is then in oxyfuel mode with flue gas recirculation. As soon as all control units have stabilized and a temperature of approx. $600 \, °C$ is reached in the combustion chamber, the system can be switched to solid fuel operation. Here, the system starts to gradually increase the feed of solid fuel into the combustion chamber up to the desired thermal load, while the natural gas volume flow is slowly reduced. The swirl number, oxidant-fuel equivalence ratio and oxygen content in the oxidant then need to be adjusted by the operator for solid fuel combustion.

6.2 Burner and Combustion Chamber

Fig. 6.2 shows the EST500 oxyfuel burner as a result of the up-scaling process described in Chapter 5.
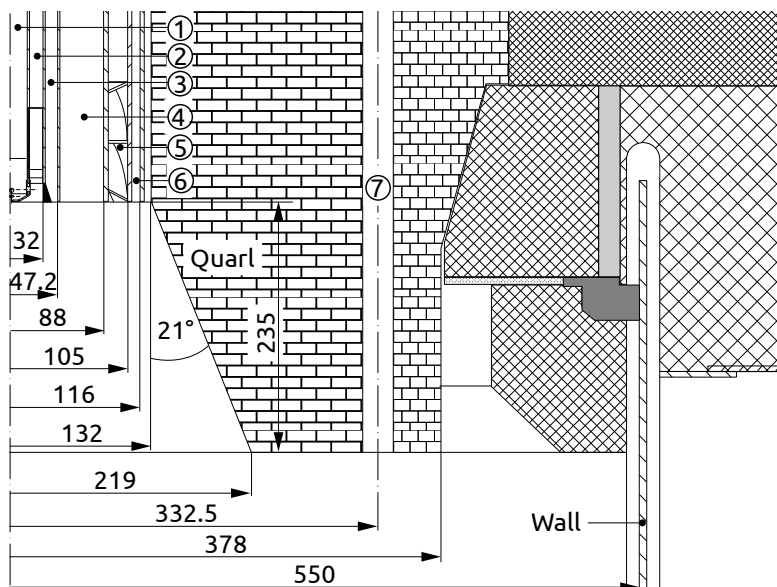
Fig. 6.2 Upper section of the combustion chamber, showing the coaxial EST500 oxyfuel burner and the quarl. Refractory stones are shown tiled and cross-hatched. (1) gas lance, (2) swirled primary channel, (3) primary channel/pulverized fuel, (4) cooling channel, (5) swirled secondary channel, (6) axial secondary channel, (7) tertiary nozzles. Dimensions in millimeters.

The coaxial burner consists of a natural gas lance in the center and a *swirled primary* channel which is used to support the gas flame with oxidizer during heat-up of the chamber with natural gas. The gas lance has an inner diameter of 25 mm and features 12 openings with a diameter of 4 mm. Pulverized fuel is introduced through the non-swirled *primary* channel, next to the swirled primary channel. A small bluff-body is welded at the end of the primary channel. The *cooling* channel is next to the primary channel for pulverized fuel. This channel can be used at high thermal loads to prevent ignition of the fuel inside the burner. However, in the experiments of this work, it was not used. Nevertheless, the cooling channel creates a certain gap between the primary and the secondary flows, forming a bluff-body. The secondary channels, providing the oxidant for combustion, are located at the outer edge of the burner. They are split up into a *swirled secondary* and an *axial secondary* channel. The swirl number of the burner can be adjusted by changing the flow ratio between swirled secondary and axial secondary channel. The burner is installed in a quarl (diffuser), which consists of 12 stones made of refractory concrete. The quarl has an opening angle of 21°. The quarl is surrounded by 24 *tertiary* nozzles. The nozzles are axial ducts through the refractory stones. These nozzles are used for air staging and provide additional oxidizer for combustion. The niche at 378 mm is the result of a design change, since the quarl of the previous burner (not used in this work) has a shorter height. The reason for the extension of oxyfuel burner and quarl is to reduce the distance of the quarl to the first measuring port.

Fig. 6.3 shows a cross-section of the combustion chamber and a CAD model of the chamber. The upper section of the combustion chamber is hexagonally shaped and consists of welded membrane plates through which cooling water flows. The lower part of the combustion chamber is circular and consists of refractory concrete. The upper part of the combustion chamber has 10 measuring levels along the height, at each of three corners. The axial (z) distance between the ports variates according to the sketch. The CAD model also shows the convective heat exchanger behind the combustion chamber and the connection to the chamber. The positions where the radiative heat flux measurements were carried out are numbered $1 - 4$. The gas temperature measurements near the combustion chamber wall are labeled T_1 and T_2. The camera used to record the flame during the experiments is shown as well.
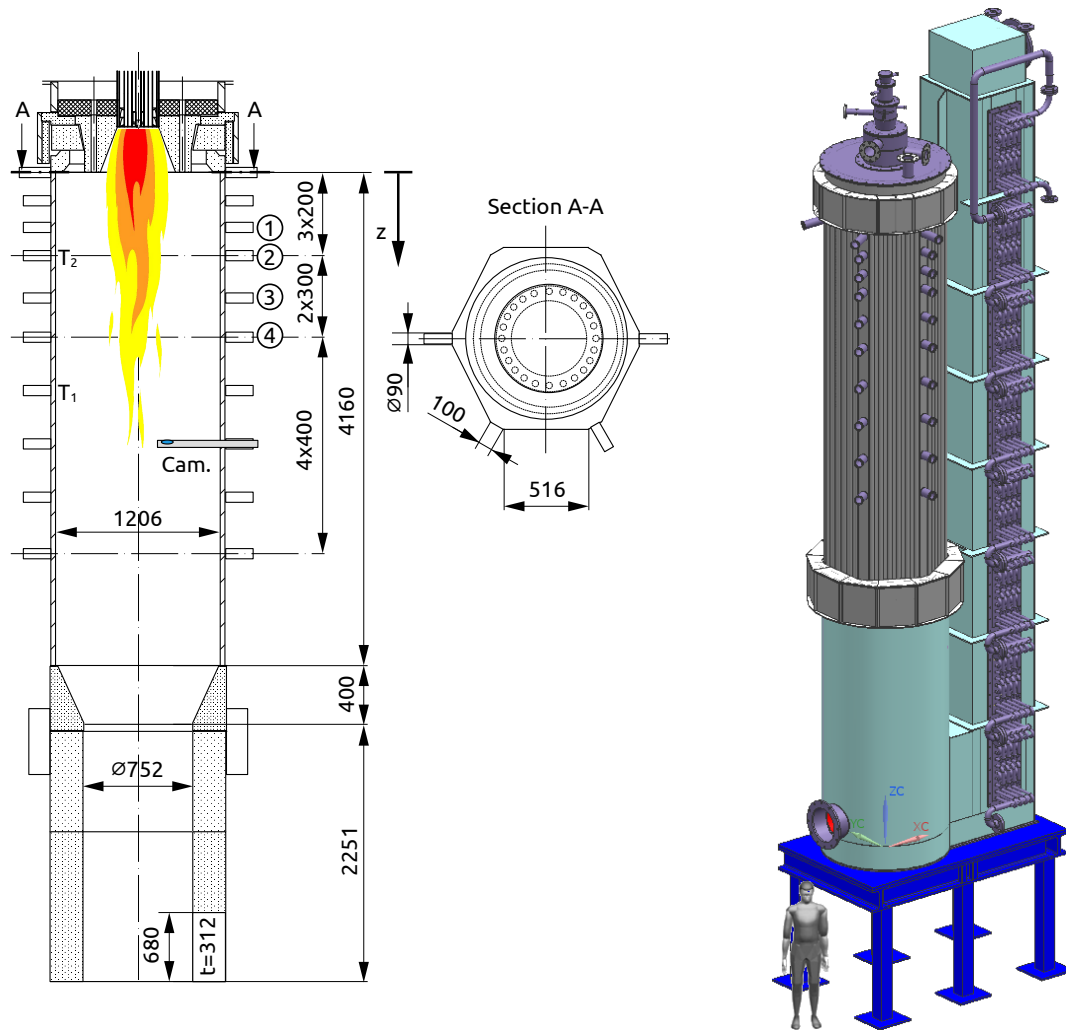
Fig. 6.3 Left: cross-section of the combustion chamber, positions of temperature measurement (T_1 and T_2) and observation camera (cam.). Positions of the used ports for the radiative heat flux measurements are enumerated from 1 to 4 (circles). Right: CAD model of the combustion chamber and convective heat exchanger. Dimensions in millimeters.

6.3 Dosing System

The dosing system of the combustion chamber is shown in Fig. 6.4. The dosing system is a $0.345\,\mathrm{m}^3$ container with fluidization nozzles at the bottom. There is a rotating perforated disk inside the container. The chambers of the disk are filled with the fluidized solid fuel. The perforated disk is located between two inlets and two outlet tubes, which are used to flush the fuel out of the disk chambers. The fuel dosage can be adjusted via the rotational speed of the perforated disk. The mass flow is determined through a delivery characteristics curve, which is a function of the rotational speed. The characteristic curve for the fuels has to be determined empirically. A gravimetric determination of the mass flow was not possible, as the vibrations in the facility have a direct impact on the gravimetric measurement. The dosing container is filled with solid fuel from above with a supply container as soon as the differential pressure in the dosing container falls below a predefined threshold.
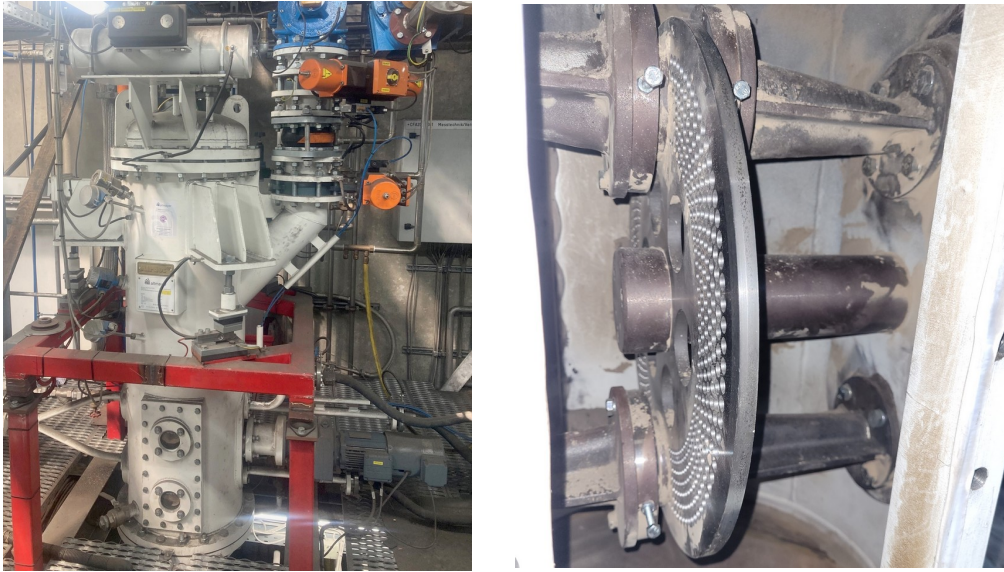
Fig. 6.4 Left: picture of the dosing container with connection (top right) to the fuel supply container. Right: picture of the double-flow perforated disk inside the dosing container.

6.4 Radiative Heat Flux Measurement

The total incident radiative heat flux at the wall, inside the combustion chamber, was measured with a Gardon gauge heat flux sensor type GG01-250 from the company HUKSEFLUX. It is a passive sensor with a fast response time and can be used in high-temperature environments. It is water-cooled and equipped with a sapphire glass (Al_2O_3) to protect the sensor from convective heat transfer in order to measure solely heat transfer by radiation. However, it reduces the hemispherical incidence angle of the radiation to $150°$ [183]. The resulting error is negligible, according to the manufacturer, as the cut-off part of the field of view has a very small angle of incidence to the sensors surface [184]. The sapphire window has a transmissivity of 86% at a wavelength of $1\,\mu m$ (Spectral range: $0.2 - 5.5\,\mu m$). The sensor generates an output voltage that is proportional to the incident thermal radiation. The total radiative heat flux is calculated by the voltage divided by a constant parameter. The constant results from the calibration according to ISO 14934-3 and is specified by the manufacturer [183, 185]. The sensor has a measuring range up to $250\,kW/m^2$ and is made of steel and copper. The manufacturer specifies the calibration error of the sensor to be approx. 5.8% [184].

In contrast to conventional thermopiles, which dissipate the absorbed heat to the environment by radiative or convective heat transfer, this sensor dissipates the heat to a heat sink by thermal conduction [186]. To explain its theoretical background, a sketch of the sensor is shown in Fig. 6.5. The sensor consists of a diffuse absorbing, blackened, thin, circular foil made of constantan. The foil is connected to the copper housing around the circumference. One wire is connected to the center of the foil, the second wire is placed at the water-cooled copper housing, which serves as a heat sink. This connection results in a thermocouple. The heat absorbed by the foil is conducted radially to the heat sink, which has a constant temperature.

90

This makes it possible to measure the temperature difference against the radius of the foil. The voltage output is proportional to the temperature difference and therefore proportional to the heat flux [186–188]. In addition, the sensor is installed in a lance, equipped with purge nozzles to prevent the sensor from ash depositions. CO_2 is used as purge gas in oxyfuel combustion. The lance has a diameter of 60 mm and a length of 405 mm. A flange is welded to the end of the lance to mount it at the measuring ports of the combustion chamber. The head of the sensor has a diameter of 25.4 mm. The mounted lance for measuring the radiative heat flux at the wall is shown in Fig. 6.6.
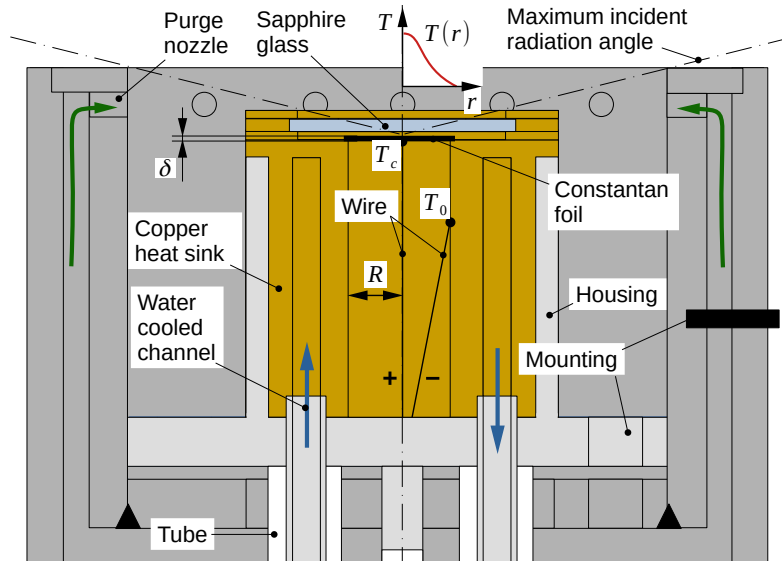
Fig. 6.5 Sketch of the Gardon gauge sensor (copper-colored and light grey) installed in the purge lance (dark gray). The red line shows the temperature profile against the radius of the foil [186–188].

Assuming that the thermal conductivity of the foil is independent of temperature, the heat flux can be calculated theoretically by Eq. (6.1):

$$\dot{q} = \frac{4\,\lambda\,\delta}{R^2}\,(T_c - T_0).$$

(6.1)

The exact derivation of Eq. (6.1) for converting the temperature difference to the heat flux is described in the work of Robert Gardon [186]. In practice, however, the equation for the heat flux results from calibration. The heat flux can be determined using a constant from the calibration and the output voltage. Fig. 6.6 on the left-hand side shows a picture of the lance including the heat flux sensor. The picture beside shows the lance during heat flux measurement at the fourth port. In addition, five narrow windows can be seen on the combustion chamber, which are used for laser optical measurements. If no measuring system is connected to the windows, the flame length can be estimated through the windows.
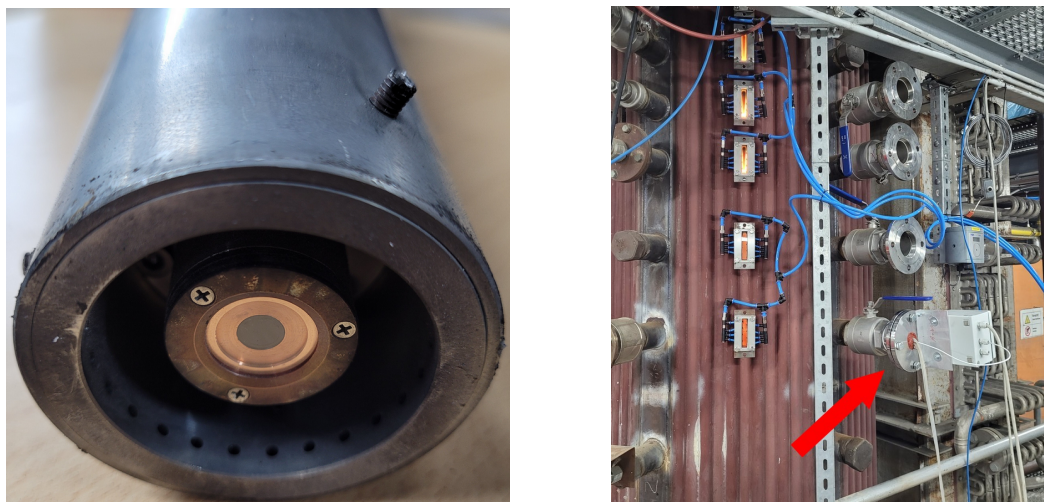
Fig. 6.6 Left: picture of the Gardon Gauge sensor installed in the purge lance. Right: sensor and lance during measurement in the combustion chamber at the fourth port.

6.5 Gas Composition Measurement

The composition of the flue gas from the combustion chamber is analyzed with an online gas analysis. The measuring position is located behind the particulate filter. The oxygen is measured using a paramagnetic measuring method. Due to its paramagnetic properties, the oxygen is drawn into an applied magnetic field where it is heated by a heating wire, causing the oxygen to lose its magnetic properties and be displaced from the magnetic field by the oxygen molecules flowing inside the magnetic field. This convection causes the heating wire to cool down, which leads to a change in electrical resistance that is detected by a bridge circuit [189]. Oxygen loses its paramagnetic properties above approx. 300 °C. As the flue gas temperature never reached this temperature during the experiments, a measurement using this principle was permanently possible. Cross-sensitivity due to other substances can be excluded. The species CO_2, CO, SO_2 and NO are measured using the non-dispersive infrared (NDIR) method. The measuring principle is based on the radiation absorption of gas molecules. With NDIR, there is no spectral decomposition of the radiation. A heating wire that serves as an infrared source emits thermal radiation through a sample channel through which the flue gas flows. The radiating gases in the flue gas absorb the radiation. As a result, the radiation reaches the receiver chamber, which comes after the sample channel, with reduced intensity. The gas to be measured is located in the receiver chamber. The absorption in the receiver chamber causes the molecules to vibrate, which increases the temperature and pressure in the chamber. This increase in pressure is detected by the membrane of a condenser microphone. More information about this measuring principle can be found in documentations from the ABB Group [190]. The measuring range and the principle of the measuring systems are summarized in Tab. 6.1.

The H_2O content in the flue gas is measured using the principle of psychrometrics. Two temperature measurements are taken in the same atmosphere. One of the thermocouples is

Tab. 6.1 Gas analysis systems used to determine the species concentrations in the flue gas of the combustion chamber [191].

Species	Range	Rel. uncertainty	Unit	Principle
H_2O	2 − 100	< 1	vol%	Psychrometric
O_2	0 − 100	< 0.5	vol%	Paramagnetic
CO_2	0 − 100	< 0.5	vol%	NDIR
CO	0 − 5	< 0.5	vol%	NDIR
SO_2	0 − 5	< 0.5	vol%	NDIR
NO	0 − 1010	< 0.5	ppm	NDIR

moistened so the convection causes cooling by means of enthalpy of vaporization. The ambient humidity can be determined using the temperature difference between these two thermocouples [189].

With exception of humidity measurement, all gases are measured in a dry state. For this purpose, the flue gas first passes through a particulate filter. Afterwards, the flue gas enters the first condenser through a heated tube. The gas is pumped to a second condenser and then passes through a flow meter into the gas analyzer.

6.6 Fuel Properties

Four different fuels were burned in oxyfuel and air atmosphere to investigate the flame stability and radiative heat transfer. The solid fuels were delivered milled, in comparable particle sizes and stored in Big-Bags or containers. The pulverized fuels are fed into the combustion chamber using the dosing device (cf. Section 6.3). Walnut shells (WS) and beech wood (BW) are used representative for biomass. In addition, Rhenish lignite (RBK) is used as reference fuel for comparison with the $40\,kW_{th}$ oxyfuel burner (cf. Chapter 5). Natural gas is also used to investigate gaseous fuel without particles to exclude the effect of heterogeneous reactions. The pulverized fuels are shown in Fig. 6.7.

Fig. 6.7 Picture of the three different pulverized fuels (from left to right): beach wood, walnut shells and Rhenish lignite.

The upper calorific value, density at standard conditions and the chemical composition of the natural gas used in this work is summarized in Tab. 6.2 [184, 192].

Tab. 6.2 Fuel composition of the natural gas. Data according to e-netz Südhessen AG [192].

H_u	ρ	CH_4	C_2H_6	C_3H_8	CO_2	N_2	Others
MJ/m³	kg/m³	mol%	mol%	mol%	mol%	mol%	mol%
41.41	0.784	92.05	4.82	0.82	0.92	0.99	0.4

The chemical properties of the solid fuels are summarized in Tab. 6.3. These are the results of a ultimate analysis according to ASTM D5291 and D5373 and proximate analysis according to German standards DIN 51718, DIN 51719 and DIN 51720. The calorific value is determined according to ISO 1928 standards.

Tab. 6.3 Lower and higher heating values (LHV and HHV) in MJ/kg, ultimate and proximate analysis of WS, BW and RBK in mass percent. As received (AR), dry, dry and ash free (DAF).

	Walnut shells			Beech wood[*]			Rhenish lignite		
	AR	Dry	DAF	AR	Dry	DAF	AR	Dry	DAF
C	47.60	51.26	51.65	45.29	47.69	48.04	57.07	63.92	68.12
H	6.04	6.50	6.55	4.46	4.70	4.73	4.99	5.59	5.96
O	38.16	41.09	41.41	44.32	46.67	47.01	19.86	22.24	23.70
N	0.36	0.39	0.39	0.21	0.22	0.22	1.77	1.98	2.11
S	0.00	0.00	0.00	0.01	0.01	0.01	0.09	0.10	0.11
Ash	0.70	0.75	–	0.69	0.73	–	5.51	6.17	–
Water	7.14	–	–	5.04	–	–	10.71	–	–
C (fix)	11.30	12.17	12.26	8.56	9.01	9.08	32.28	36.15	38.53
Volatiles	80.86	87.08	87.74	85.71	90.26	90.92	51.50	57.68	61.47
LHV	16.01	17.24	17.37	16.48	17.35	17.48	18.43	20.64	22.00
HHV	18.88	20.33	20.49	16.60	17.48	17.61	22.15	24.81	26.44

[*]According to Schneider et al. [14].

The particle size distribution of the solid fuels was analyzed at the WSA RWTH Aachen University using a laser-optical method, while a sieve analysis[1] was carried out at the EST TU Darmstadt. The particle size distributions of both methods are shown in Fig. 6.8. The mass fraction of the fuel that has particles with a diameter greater than the corresponding value of the abscissa is shown in these graphs.

The WS shows an almost uniform particle size for both analysis methods, with the laser optical method the average particle size is slightly larger than by using the sieve analysis. The sieve analysis shows a mass fraction of 90 % particles larger than 110 µm and a number of 50 % particles larger than 140 µm for WS. The WSA results show particle sizes larger than 150 µm

---

[1]The following mesh sizes are used: 425, 355, 300, 280, 250, 224, 200, 180, 160, 150, 125, 106, 90, 63, 40, 25 and 20 µm.
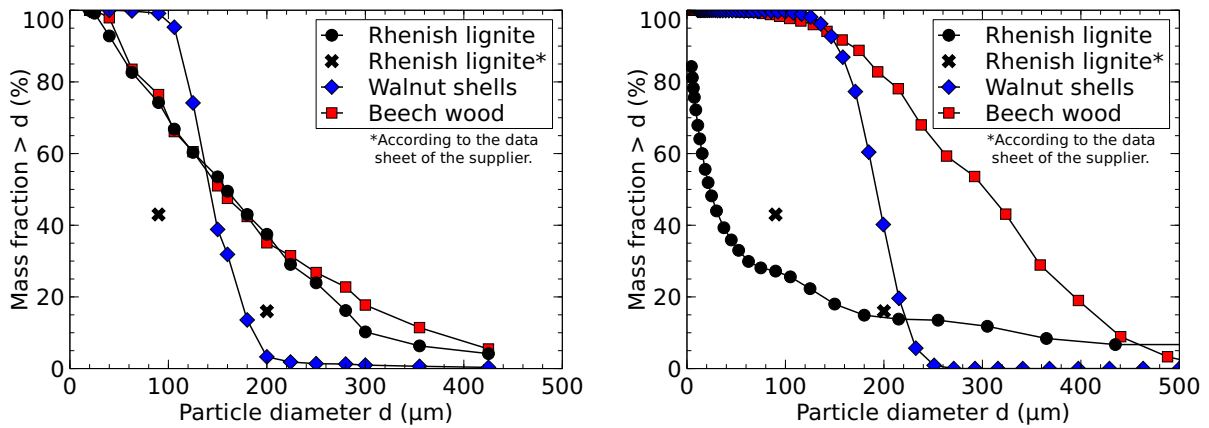
Fig. 6.8 Particle size distribution of the three solid fuels. Left: distribution of the EST sieve analysis. Right: distribution of the WSA laser optical analysis.

for 90 % of the fuel mass and particles larger than 190 µm for 50 % of the fuel mass. For the RBK, the sieve analysis shows that 90 % of the pulverized fuel mass consists of particles larger than 40 µm and 50 % of particles larger than 160 µm. With the optical method, 90 % of the fuel consists of particles larger than 4 µm and 50 % larger than 22 µm. The RBK was difficult to analyze using sieve analysis as it has lumpy properties and often clogged the meshes. The BW was the most problematic fuel to analyze, as its fibrous properties made it difficult to sieve. The sieve analysis shows a particle size larger than 5 µm for 90 % of the BW mass and a diameter larger than 150 µm for 50 % of the mass fraction. The analysis of the WSA results in a share of 90 % particles larger than 160 µm and a share of 50 % particles larger than 300 µm for BW.

Fig. 6.9 shows the Van Krevelen diagram, in which the atomic ratio of hydrogen to carbon is plotted against the ratio of oxygen and carbon. The drawn fields mark the typical range for different solid fuels.
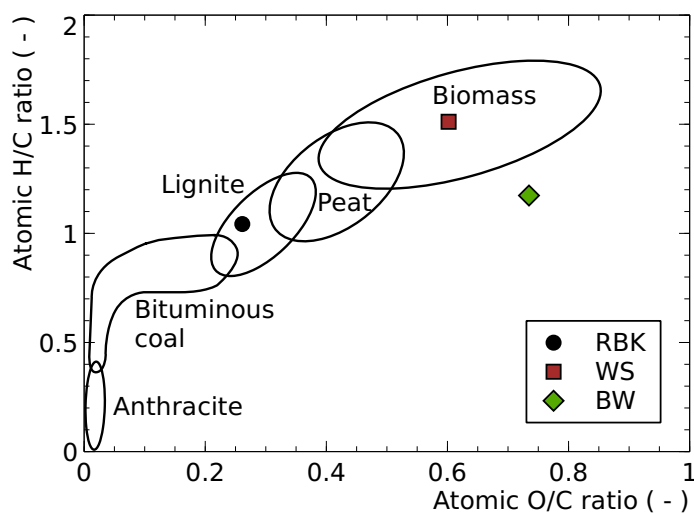
Fig. 6.9 Position of investigated fuels in the Van Krevelen diagram, according to Van Krevelen and Trif-Tordai [193, 194]. The fuels are marked with colored symbols in the diagram.

This diagram is useful for classifying fuels. It can be seen that anthracite, which consists almost entirely of carbon, has a low H/C and O/C ratio, while biomass has the highest H/C

and O/C ratios. The fuels used in the following experiments are marked in the diagram. It can be seen that RBK and WS are in the typical range for lignite and biomass. For BW, on the other hand, the O/C ratio is in the range of biomass, whereas the H/C ratio is lower. However, this does not mean any particularity of the fuels, as the fields shown for different fuels vary slightly depending on the literature. The fields in Fig. 6.9 refer to the original work of Van Krevelen [193, 194].

7 Experimental Results

To find the optimum operating conditions for the new oxyfuel burner, experiments at different thermal loads, swirl numbers and stoichiometric ratios were carried out. Various operating conditions were investigated for air-firing and transferred to oxyfuel combustion. Therefore, different fuels were used for air and oxyfuel firing. For oxyfuel combustion, the oxygen concentration in the oxidant was varied as well. Suitable operating conditions are characterized by low carbon monoxide content in the flue gas, as a high CO content indicates incomplete conversion of fuel and therefore poor combustion. Furthermore, the stability of the flame is an important criterion for the stationary operation of an industrial firing system. The stability of the flame was qualitatively determined on the basis of the optical flame properties. In addition, it was taken into account if the flame extinguishes without a natural gas support flame. For this purpose, pictures from the monitoring camera, which is located in the lower area of the combustion chamber (cf. Chapter 6), were analyzed. In addition, the radiative heat transfer of different fuels were investigated in an oxyfuel and air atmosphere. The measurement results of the wall-incident radiative heat flux are compared to the results of the reference burner WSA40 in the last part of this chapter.

The basic equation of the swirl number, presented in Chapter 2 (Eq. (2.15)) is calculated here for different operating conditions from measured data by using Eq. (7.1):

$$S = \frac{L_{sw}}{r I_{ax}} \approx \frac{r_{sw} \, \dot{V}_{sw} \, u_{sw} \cos(\varphi)}{r \left[\dot{V}_{sw} \, u_{sw} \sin(\varphi) + \dot{V}_{ax} \, u_{ax} \right]}, \tag{7.1}$$

where φ is the angle of the swirl vanes, r the radius of the vortex and r_{sw} the bulk radius of the swirl channel, I_{ax} the axial and L_{sw} the angular momentum. The vortex radius is approximated using the mean radius of axial and swirl channel [184]. A swirl number of 1.0 was not achieved during the experiments, as the axial flow valve did not completely close due to technical reasons.

7.1 CO and NO Emissions

Incomplete combustion is characterized by high CO emissions and is therefore taken into account in this work when evaluating flame stability. Additionally, NO emissions are considered in this section, as firing with high NO emissions has no practical use in industrial applications. Many studies on pulverized coal and biomass co-firing under oxyfuel conditions can be found in the literature. Only a few studies are currently available related to the use of pure biomass. Most studies using biomass under oxyfuel conditions are carried out in a fluidized bed reactor. A comprehensive review of biomass and biomass mixtures in oxyfuel combustion is given by

Ling et al. [13]. The following paragraph provides a brief overview of previous investigations using pulverized fuel combustion under oxyfuel conditions with coal and biomass focusing on pollutant emissions.

Experiments on the formation of NO_x were carried out by Stadler et al. [195] in a $100\,kW_{th}$ combustion chamber under air and oxyfuel conditions. Pulverized RBK was used as fuel. They investigated the effects of the different burner oxygen ratios with dry oxyfuel firing and recirculated flue gas. They showed that oxyfuel firing with recirculated flue gas (wet combustion) significantly reduces NO_x emissions compared to dry oxyfuel combustion. They assume that the water vapor inhibits the formation of NO. An increase in the burner oxygen ratio, on the other hand, leads to higher NO_x emissions. A burner for the production of cement under oxyfuel conditions was investigated by Carrasco et al. [196] in a $500\,kW_{th}$ combustion chamber. Pulverized, dried coal was used as fuel. The effects of the oxygen content in the oxidant and the swirl number on CO and NO formation were investigated. The results show that the CO concentration decreases with increasing swirl and increasing oxygen enrichment. In a comparison between oxyfuel firing with $29\,vol\%$ oxygen and air-firing, the oxyfuel firing shows higher NO emissions. Guo et al. [11] studied the effect of pollutant emissions, heat transfer and burnout caused by different oxygen concentrations in an oxyfuel pilot scale test furnace at $3\,MW_{th}$ with pulverized coal. They concluded that NO_x emissions are reduced by 30 to $50\,\%$ in an oxyfuel firing compared to a similar air-firing. Furthermore, they state that a high recirculation rate and low local oxygen content reduce NO_x emissions.

As mentioned above, most studies are based on oxyfuel combustion using coal as fuel. Thus, the effects of combustion parameters on biomass are investigated in this section. Since the new burner is based on a reference burner fired with RBK, biomass and RBK are examined. The following section presents the impact of combustion parameters such as thermal power, swirl, equivalence ratio, oxygen enrichment and flow conditions for WS, RBK and BW on CO and NO emissions.

7.1.1 Walnut shells

Pulverized walnut shells have excellent properties for conveying and dosing into the combustion chamber. Due to the non-fibrous properties compared to other biomass based fuels, there was no bridging in the fuel during the experiments. For the sake of simplicity, a parameter study with air-firing was carried out in advance, to serve as a reference for the oxyfuel cases in the remaining experiments with solid fuels. This involved reducing of the primary air (transport volume flow), increasing the thermal load and varying the swirl number and the equivalence ratio. Operating conditions are summarized in appendix Chapter C. A volume flow of $210\,Nm^3/h$ is set by default for the primary air of the combustion chamber system at the EST. In previous experiments, the volume flow was decreased to $160\,Nm^3/h$. Further reduction of the primary air from $160\,Nm^3/h$ to $100\,Nm^3/h$ reduced the CO content in the flue

gas by 2000 ppm at a thermal load of 285 kW (cf. appendix Tab. C.1, WSI). As a result of this measure, it is assumed that the flow field near the burner changed from a type I flame to a type II flame (cf. Chapter 7.2). Therefore, an air transport volume flow of 100 Nm³/h was used for all operating conditions with air described below. A further reduction of the volume flow was omitted to avoid depositions in the piping system.

Fig. 7.1 shows the influence of thermal power on CO emissions. By increasing the burner output from 285 kW$_{th}$ to 600 kW$_{th}$, with a constant global equivalence ratio of 1.7, the CO is reduced by 15000 ppm (cf. appendix Tab. C.1, WSIII), since more oxidant is required at a higher load and thus higher velocities occur in the burner channels. The higher velocities probably lead to better mixing of the fuel and oxidizer. The burner is designed for a secondary velocity of approx. $18 - 20$ m/s and a primary air velocity of approx. 10 m/s. The velocity ratio of $u_{sec}/u_{prim} \approx 2$, in combination with a high swirl number, an IRZ[1] is formed near the burner, which improves the stability of the flame, as well as the burnout of particles and oxidation of radicals (cf. Chapter 5). After increasing the thermal power to 600 kW, the influence of the swirl and the local equivalence ratio or $\dot{V}_{sec}/\dot{V}_{tet}$ ratio is now considered respectively. This is shown in Fig. 7.2, although it should be noted that the scaling of the CO axis is changed compared to the adjacent diagram. Increasing the $\dot{V}_{sec}/\dot{V}_{tet}$ ratio from 1.2 to 4.0 results in a swirl number of 0.97 (cf. appendix Tab. C.1, WSIV). As a result, the velocity of the secondary stream is increased from 11 m/s to 18 m/s. Consequently, the CO emissions reduce by 1500 ppm. No reduction in CO emissions can be achieved by further increasing the swirl number to 0.98, as it leads to an increase of CO as can be seen in Fig. 7.2 (hatched bars).
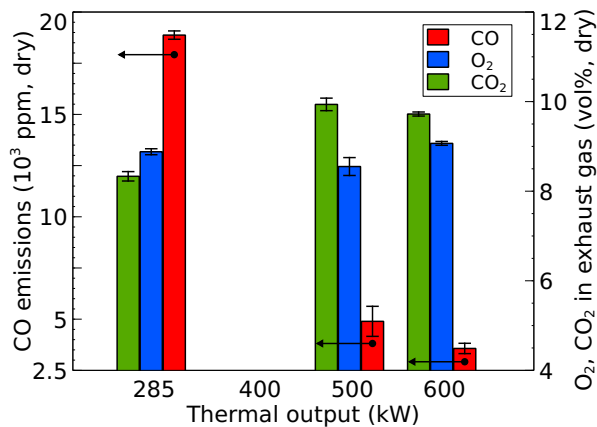
Fig. 7.1 Change in CO emission, O$_2$ and CO$_2$ content by increasing thermal power. CO emissions (red) on the left ordinate and O$_2$ (blue), CO$_2$ (green) content on the right ordinate plotted against thermal output.
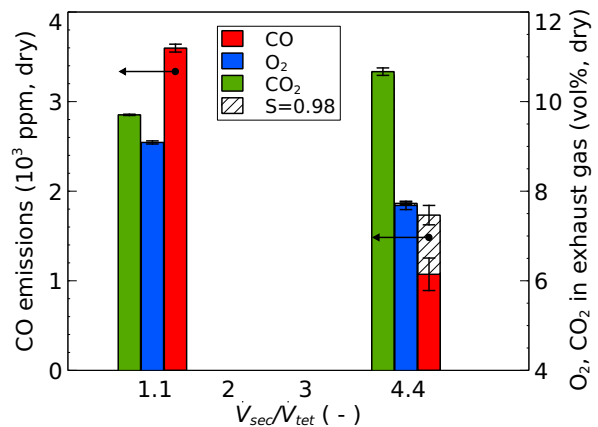
Fig. 7.2 Change in CO emission, O$_2$ and CO$_2$ content by increasing $\dot{V}_{sec}/\dot{V}_{tet}$ ratio and swirl. CO emissions (red) on the left ordinate and O$_2$ (blue), CO$_2$ (green) content on the right ordinate plotted against $\dot{V}_{sec}/\dot{V}_{tet}$.

Fig. 7.3 shows the influence of the global equivalence ratio on CO emissions. If the global equivalence ratio is reduced from 1.7 to 1.6, the CO emissions increase by approx. 1500 ppm;

---

[1]RBK, which has a 25 % higher oxygen demand than WS, was used as reference fuel for the burner design. As a result, higher volume flows and therefore higher velocities are achieved when burning RBK with the same oxygen enrichment in the oxidant.

a further reduction to $\lambda_{glob} = 1.5$ (cf. appendix Tab. C.1, WSVI) increases the CO content in the flue gas by 4000 ppm. Setting the global equivalence ratio to 1.8 does not result in any improvement in CO emissions compared to $\lambda_{glob} = 1.7$, but the O_2 content in the flue gas increases by 1 vol% and the CO_2 content decreases by 0.5 vol%. Thermal load had to be reduced at the last trials (WSIV and WSV), as the pulsing inside the particle filter was no longer able to sufficiently clean the filter bags at high particle mass flow. Fig 7.4 shows the influence of the parameter study discussed in the paragraph above in the same sequence on NO emissions. The reduction of the primary flow, which was mentioned earlier, leads to a decrease in NO emissions by approx. 30 ppm. This is probably due to less oxidizer being directly transported into the flame core. NO increases with an increase in thermal power from 285 to 600 kW since more fuel is introduced. The change in air distribution between the tertiary and secondary channel leads to an increase in NO. This measure also introduces more oxidizer into the flame core. A higher swirl has only a minor influence on NO emissions and is therefore not shown in the diagram. For all operating conditions with WS, NO emissions are below 60 ppm.
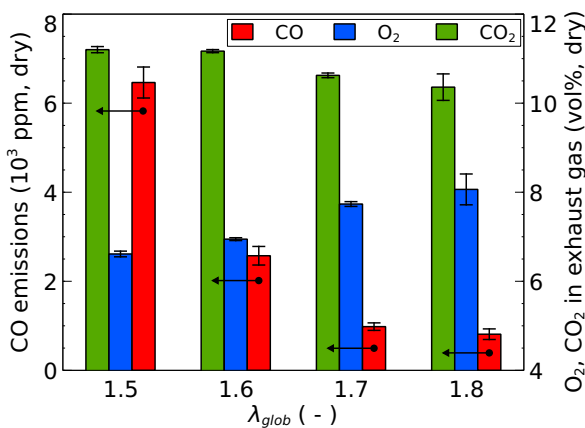
Fig. 7.3 Behavior of CO emission, O_2 and CO_2 content in the flue gas during variation of λ_{glob}. CO emission (red) on the left ordinate and O_2 (blue), CO_2 (green) content on the right ordinate plotted against global equivalence ratio.
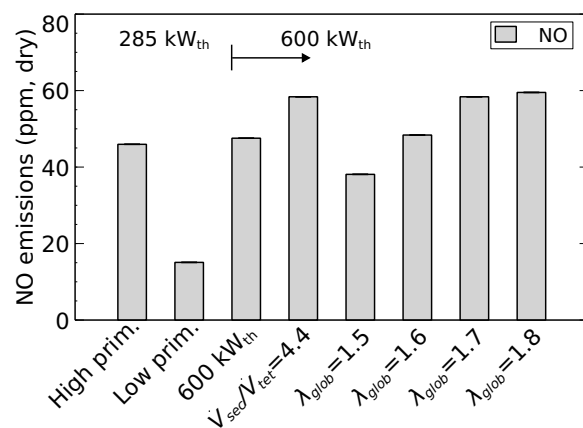
Fig. 7.4 NO emissions plotted against operating conditions. Change of NO emissions during the entire parameter study.

As can be seen in the diagrams discussed in this section, the residual oxygen content in the flue gas is between 6.5 and 9 vol% (dry). The humidity at all test cases here is 4.5 – 5 vol%. Furthermore, the filter cleaning of the combustion chamber introduces approx. 2.5 vol% (dry) oxygen into the flue gas and the purging of the measuring systems adds an additional 25.2 Nm^3/h of air into the combustion chamber, which leads to high residual oxygen in the exhaust gas. With respect to CO emissions and a low oxygen content in the flue gas, the best results for an global equivalence ratio of 1.7 and a swirl number of 0.97 are achieved in a range of 500 − 600 kW$_{th}$.

A thermal load of approx. 500 kW and a global equivalence ratio of 1.7 prove to be the most suitable combustion parameters regarding flame stability and low CO emissions for oxyfuel

combustion with WS.

After the discussion of parameter study results for the air-firing of WS, the combustion of WS under oxyfuel conditions is now considered. The optimum operating conditions from the previous paragraph were transferred to oxy-firing. While a constant mixture of O_2 and N_2 is given during air-firing, the O_2 concentration in oxyfuel combustion can be adjusted. The CO and NO emissions for the variation of the oxygen content in steps 27, 30 and 33 vol% (wet) in the oxidant for WS are considered (WS27, WS30, WS33, cf. appendix Tab. C.2), as well as the influence of a higher local equivalence ratio, which can also be expressed as $\dot{V}_{sec}/\dot{V}_{tet}$, to investigate the influence of higher velocities in the flame core. Fig. 7.5 shows the CO emissions of WS flames under oxyfuel conditions on two different days (circle and square), for three oxygen concentrations and two different local equivalence ratios (black and red). The measurement data of two different days are shown here to illustrate the reproducibility of the operating conditions with the semi-industrial plant. The error bars refer to the fluctuations over time during an individual trial. Further errors in the measurements are listed in Chapter 6. As can be seen, CO emissions decrease almost linearly with the increase in oxygen concentration from 27 to 33 vol% (wet). The CO emissions are reduced by 4650 ppm for a local equivalence ratio of approx. 1.0 ($\dot{V}_{sec}/\dot{V}_{tet} = 1.1$), while the oxygen content in the flue gas increases by 5 vol% (wet). By increasing the oxygen content from 27 to 33 vol% in the oxidant at λ_{loc} ≈ 1.6 ($\dot{V}_{sec}/\dot{V}_{tet} = 5.6$), the CO reduces by 3990 ppm while the oxygen content in flue gas increases by 3 vol% (wet). The NO emissions in Fig. 7.6 behave exactly the opposite to the CO emissions.
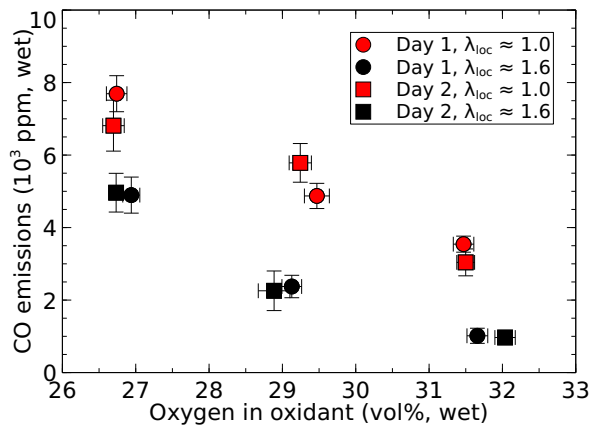
Fig. 7.5 CO emissions plotted against the oxygen concentration in the oxidant, on two days (circle and square), for two different local equivalence ratios (black and red).
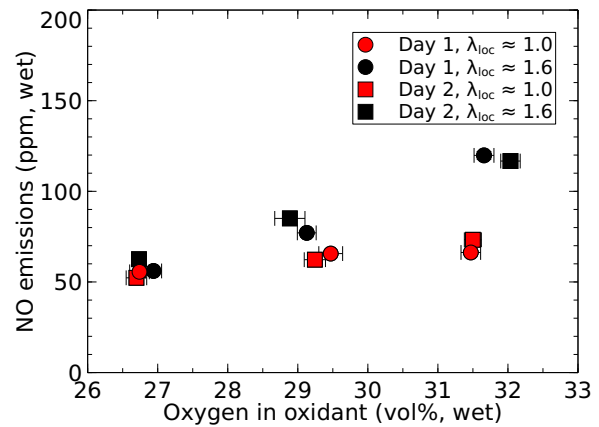
Fig. 7.6 NO emissions plotted against the oxygen concentration in the oxidant, on two days (circle and square), for two different local equivalence ratios (black and red).

With an increase of the oxygen concentration in the oxidant, the NO fraction for $\lambda_{loc} \approx$ 1.0 increases by approx. 10 ppm. With a local super-stoichiometric condition of 1.6, the NO emissions increase by approx. 65 ppm. As expected, NO formation increases with higher oxygen content in the flame core. A higher $\dot{V}_{sec}/\dot{V}_{tet}$ ratio can therefore also improve combustion

in oxyfuel operation, which is noticeable in lower CO formation, although the NO content increases slightly. The WS30 operating case with $\dot{V}_{sec}/\dot{V}_{tet} = 5.6$ ($\lambda_{loc} \approx 1.6$) represents a good compromise (cf. appendix Tab. C.2) regarding low CO and NO emissions. The residual oxygen content in the flue gas is between 4 and 8 vol% (wet). On average, the CO_2 concentration in the flue gas for WS is $51 - 53$ vol% (wet) and 15 to 16 vol% humidity, where the WS-air combustion just have an amount of 8 vol% H_2O, since there is no flue gas recirculation. The remaining component is N_2 from false air, caused by leakage in the system. The false air is mainly attributed to numerous leaking measuring systems that were connected to the combustion chamber during the experiments. Further leaks were found at the movable ignition lance and at the air valve of the fan for the oxidant supply. The negative pressure inside the combustion chamber additionally favored the leakage.

7.1.2 Rhenish lignite

RBK is the fuel that was initially used for the design of the EST500 oxyfuel burner (cf. Chapter 5). This section therefore discusses the burner operation under oxfuel conditions at 540 kW$_{th}$ with low local stoichiometric ratio, a global equivalence ratio of $1.4 - 1.6$ and a swirl number of 0.94, similar to the parameters of the reference laboratory burner WSA40, but at higher thermal power. In contrast to WS, RBK is difficult to transport in the pipes of the used dosing system. Blockages repeatedly occurred during experiments. Therefore, a systematic parameter study has proven to be difficult. The data set for the RBK is hence smaller than for WS.

Similarly to WS, it is not possible to handle low thermal power using RBK because of the low velocities. The CO emissions exceed 1000 ppm at a thermal output of less than 450 kW and, like WS, the flame pattern is unstable. In Fig. 7.7, the CO and NO emissions are plotted against the O_2 concentration in the oxidant. The single trials are marked with gray bars.
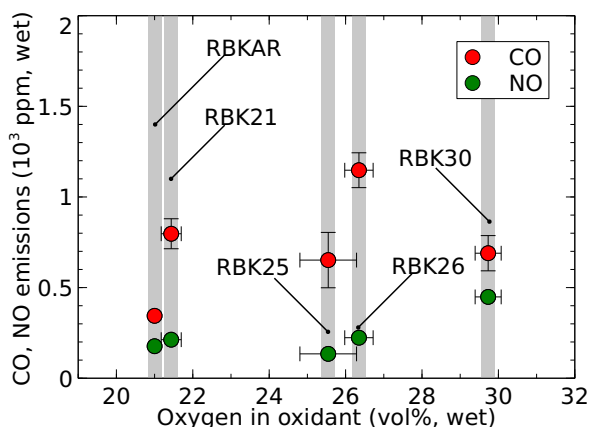
Fig. 7.7 Change in emissions due to variation of oxygen in the oxidant. CO (red) and NO (green) emissions plotted against the O_2 content in the oxidant.
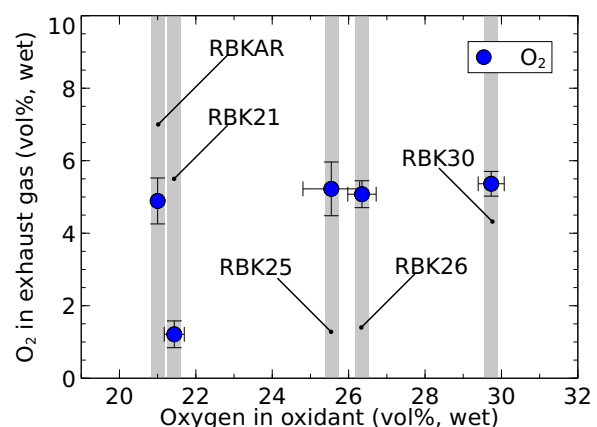
Fig. 7.8 Change in residual O_2 due to variation of oxygen in the oxidant. Residual O_2 plotted against O_2 content in the oxidant.

RBK30 and RBK26 (cf. appendix Tab. C.4) are derived from the operating conditions of WS with a secondary to tertiary ratio of 4.1. Due to fuel dosing problems in the system, the output of RBK30 (30 vol% O_2 in the oxidant) had to be reduced from 540 kW$_{th}$ to 510 kW$_{th}$ to ensure stable operation. Despite the lower power, RBK30 has twice the NO concentration in the flue gas than RBK26. This is probably due to the higher oxygen concentration in the oxidant and therefore favored NO formation. Carbon monoxide, on the other hand, is reduced by approx. 450 ppm from RBK26 (26 vol% O_2 in the oxidant) to RBK30, although it is not possible to determine whether this is due to the higher oxygen concentration or the lower fuel mass flow rate. RBK21 and RBK25 with an O_2 concentration of 21 and 25 vol% in the oxidant (cf. appendix Tab. C.4) both have a secondary to tertiary air ratio of $\dot{V}_{sec}/\dot{V}_{tet} =$ 1.8 and a fuel mass flow of 102 kg/h, which corresponds to an thermal output of approx. 540 kW. While the secondary flow is sub-stoichiometric for RBK21 ($\lambda_{loc} = 0.9$), the local equivalence ratio for RBK25 is just above one. Furthermore, both cases differ in the oxygen concentration in the oxidant which results in different global equivalence ratios. Despite a sub-stoichiometric zone, RBK21 shows a 78 ppm higher NO concentration in the flue gas. The CO concentration is also 145 ppm higher. However, the measurements for RBK25 show higher fluctuations, which indicates problems in fuel dosing. A comparison of RBK21 with the air case, both at $\lambda_{glob} = 1.4$ shows similar values for NO emissions, but more than twice the amount of CO emissions during oxyfuel combustion. The high CO_2 content and the high temperatures may favor Boudouard-reactions, which promote the formation of CO. It should also be taken into account that the load in the air-fired case is 510 kW$_{th}$. Comparable values at the same thermal output could therefore be slightly higher. Fig. 7.8 shows the residual oxygen content in the flue gas plotted against the O_2 enrichment in the oxidant. All RBK cases are between 5 and 6 vol% (wet), except of RBK21 where the residual oxygen is 1.2 vol% (wet). Among the oxyfuel cases, RBK21 has the lowest equivalence ratio of $\lambda_{glob} = 1.4$. RBK21 and RBK25 produce the lowest emissions and cover the operating range the burner was designed for. A reasonable range for the operation of the burner with RBK under oxyfuel conditions is therefore a thermal load between 500 and 600 kW, a high swirl number, $\lambda_{glob} = 1.4 - 1.6$, $\dot{V}_{sec}/\dot{V}_{tet} = 1.8$ and an oxygen enrichment in the oxidant between 21 and 25 vol%. The flue gas of the oxyfuel cases consists of $14 - 16$ vol% water vapor and $50 - 52$ vol% CO_2 (wet). Overall, the RBK has conspicuous lower CO emissions than WS. This could be a result of having more small particles compared to WS, which has a rather uniform particle size between 100 and 200 µm. Therefore, the residence time of small RBK particles inside the IRZ could favor combustion by producing radicals in the main reaction zone. In addition, the fine particles heat up more rapidly and provide faster ignition despite a lower volatile content than WS. This assumption is also supported in the work by Steffens et al. [197]. In their study, RBK and WS were numerically investigated in the reference laboratory combustion chamber used for up-scaling in this work. They came to the conclusion that compared to the RBK, a longer flame and a lower hot gas recirculation occurs with WS due to the larger particles and

thus slower heating of the particles. Slower heating of particles favors CO production through incomplete combustion processes. In case of larger particles, slower heating rates are caused by the reduced surface-to-volume ratio, slower heat transfer to the interior of the particle, less oxygen diffusion on the surface and increased required residence time [25, 198–200].

7.1.3 Beech wood

BW proved to be the most difficult fuel to dose due to its clumping properties. During the experiments, blockages repeatedly occurred in the pipes of the dosing system. Therefore, a systematic parameter study has proven to be difficult. Hence, only a small data set was recorded for BW. The results are discussed for various thermal loads in the range of 330 – 670 kW. The swirl number is approx. 0.93, the oxygen content in the oxidant is 35 vol% (wet) and the global equivalence ratio for thermal outputs higher than 500 kW is approx. 1.6 – 1.7. Lower thermal outputs have equivalence rations of 2.0 – 2.1. The operating conditions using BW in an oxyfuel atmosphere can be found in the appendix Tab. C.5.

Fig. 7.9 shows the CO and NO emissions when firing BW under oxyfuel conditions, plotted against the thermal load. Furthermore, the CO_2 and residual oxygen content in the flue gas are plotted against the thermal load in Fig. 7.10. The individual operating cases are marked with gray bars.
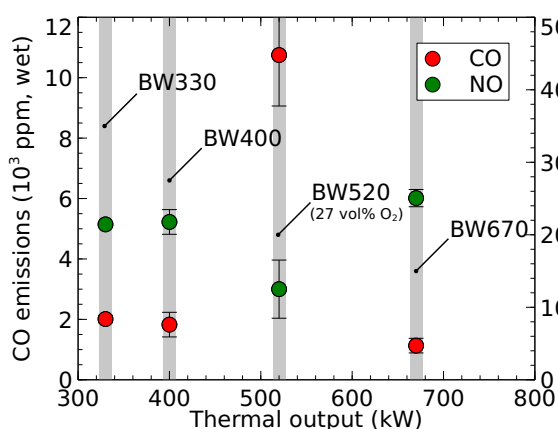
Fig. 7.9 Change in emissions due to variation of thermal load. CO (red, left ordinate) and NO (green, right ordinate) emissions plotted against thermal output. The oxygen content in the oxidant is 35 vol% (wet) except for BW520, which has an O_2 enrichment of 27 vol%.
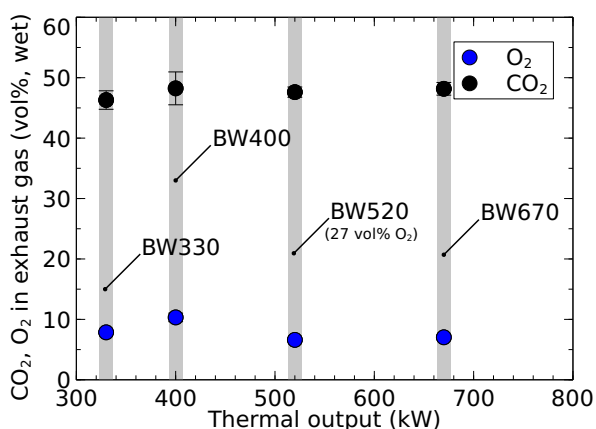
Fig. 7.10 Change in species concentrations due to variation of thermal load. Residual O_2 (blue) and CO_2 (black) flue gas content plotted against thermal output. The oxygen content in the oxidant is 35 vol% (wet) except for BW520, which has an O_2 enrichment of 27 vol%.

As already discussed for WS and RBK, CO emissions decrease at higher thermal power due to higher volume flows and thus higher velocities, which provide more effective mixing of oxidizer and fuel. With increasing thermal output, CO emissions reduce almost linearly from approx. 2010 ppm to 1130 ppm. An exception is given at 520 kW thermal power (BW520), as an oxygen enrichment of 27 vol% (wet) instead of 35 vol% (wet) in the oxidant was used. The low oxygen enrichment leads to high CO emissions, while the NO emissions are lowest here at

12 ppm. Furthermore, BW520 has the lowest residual oxygen of approx. 6 vol% (wet) in the off-gas. However, the large error bar of CO at BW520 also indicates fluctuations in the fuel dosing during this trial, whereas the oxidant flow remains unchanged. For BW330 and BW400 (thermal output of 330 and 400 kW), the NO emissions are approx. 21 ppm, and 25 ppm for BW670 (670 kW$_{th}$). The CO_2 content in the flue gas is between $46 - 48$ vol% (wet) for all operating conditions and 7 to 11 vol% humidity.

Again, it can be seen that a higher O_2 content in the oxidant favors NO formation. However, even at higher thermal power, a minimum oxygen content in the oxidant greater than 27 vol% is necessary to to avoid excessive CO emissions.

7.2 Flame Stability

This section focuses on the quantification of flame stability for pulverized biomass, lignite, and natural gas under oxyfuel conditions. Various methods for studying flame stability in pulverized fuel combustion can be found in the literature. Thermal loads, swirl rates, oxygen enrichment, etc. are analyzed. Aerodynamic stabilization is of major importance for a type II flame, which is investigated in this work for oxyfuel conditions.

Hassan et al. [42] used a water-cooled quarl to investigate the flame stability of pulverized coal flames up to 163 kW$_{th}$. In their work they analyzed the swirl number, excess air, burner power and the momentum ratio between secondary and primary flow. They state, high swirl numbers, high secondary to primary momentum ratios and high excess air generally improve flame stability. Schiemann et al. [201] used pulverized coal to investigate the ignition temperature and ignition delay under oxyfuel and air-fired conditions. Their study shows ignition at lower temperatures, whit increasing oxygen in the oxidant and higher volatile content in the fuel. Liu et al. [202] carried out numerical simulations of a 300 kW$_{th}$ type II oxyfuel flame. The stability criteria they used included the strength of the IRZ expressed as *gas internal recirculation ratio*. The stability of the flame was investigated with regard to blockage ratio, swirl number, recirculation rate and oxygen partial pressure ratio. Becker et al. [154] visualized the reaction zones and flame stabilization locations using planar laser induced fluorescence and broadband chemiluminescence for reacting conditions. The test rig consists of a 600 mm high combustion chamber with a burner quarl made of quartz for optical access. Methane is burned in an air and oxyfuel atmosphere with 25 and 30 vol% O_2 content in the oxidant. The thermal output of the type II methane flame is 20 kW$_{th}$. Habermehl et al. [203] investigated the flame stability of an oxyfuel, coal-fired type II flame with laser Doppler velocimetry and chemiluminescence imaging. They varied the local equivalence ratio for oxyfuel combustion at 21 and 25 vol% O_2 in the oxidant. In addition, for comparison they analyzed an air flame at the same thermal load of 60 kW. The oxyfuel flame with an enrichment of 25 vol% O_2 in the oxidant behaves similarly to the air flame. For the air case and the oxyfuel combustion at 25 vol%, a collapse of the central recirculation is observed at low local equivalence ratio. Due to the low O_2 content in

the oxidant in the 21 per cent oxyfuel flame, the CO_2 content increases. Since CO_2 has a higher molar mass than O_2, the momentum increases, which prevents the decay of the recirculation. They concluded that aerodynamic effects dominate flame stabilization. Schneider et al. [14] investigated the flame stability of various oxyfuel flames with an oxygen enrichment of 27, 30, 33 and 36 vol% in the oxidant using laser-optical diagnostics. They analyzed the velocity field, temperature field, local heat release, soot formation, particle concentration and volatile release. WS was used mainly as fuel. In addition, BW and RBK were investigated in an oxyfuel atmosphere with 33 vol%. They showed, for instance, how the particle size influences the characteristics of the IRZ.

However, a specific stability criterion for oxyfuel combustion in a semi-industrial chamber cannot be determined from the above studies. Based on the conclusion that a high momentum ratio between secondary and primary flow is important for a type II flame and thus a stable IRZ, a stability criterion can be derived which is based on measurable parameters in the plant. Since optical measurement data are not available at the moment, qualitative and indirect measurement methods are used for the semi-industrial combustion chamber investigated in this work. Following methods are used to evaluate the flame stability:

- The measured CO concentration in the exhaust gas, which is an indicator of poor combustion if the concentration reaches elevated levels (discussed in the previous section).

- The monitoring camera that is located in the combustion chamber can be used to obtain information about the flame profile, symmetry, fluctuations and luminosity of the flame. Furthermore, it is possible to recognize whether unburned particles are discharged from the flame.

- The momentum ratio between secondary and primary flow, as an indirect measurement, is used to make a statement about the stability of the flame, similar to the approach by Hassan et al. [42]. In this case, the ratio should always be greater than one for a stable IRZ ($I_{sec}/I_{prim} \gg 1$).

- The NG support flame can be switched off during pulverized fuel firing to see whether the flame continues burning without a pilot flame.

7.2.1 Natural gas

The NG flames were set to a maximum thermal output of 310 kW, the swirl varied between non-swirled ($S = 0$) and $S = 0.96$, the oxygen concentration in the oxidant is 28, 29 and 31 vol% (NG28, NG29, NG31) and the global equivalence ratio between 1.2 and 1.5. The NG flames show stable properties and CO emissions below 80 ppm at all operating conditions. The CO_2 content in the flue gas at oxyfuel operation is 60 vol% (wet), the water vapor content is 14 vol% and the residual oxygen in the flue gas is between 3 and 5 vol% (wet), depending on the

oxygen enrichment in the oxidant. Thus approx. 20 vol% (wet) nitrogen is in the system due to leakage. As the CO_2 content fluctuates only minimally and does not decrease, it is assumed that there is no nitrogen due to the changeover process from air-firing to oxyfuel combustion, since the nitrogen content in the recirculated flue gas should then decrease over time. Fig. 7.11 shows three 310 kW_{th} NG-air and NG-oxy flames at various operating conditions.

Fig. 7.11 Left: NG flame in air atmosphere (NGAR) with $S = 0.96$. Middle: non-swirled NG flame in air atmosphere (NGAR). Right: NG flame in oxyfuel atmosphere with 28 vol% oxygen content in the oxidant and $S = 0.93$ (NG28).

The left-hand image shows a NG flame with a swirl number of 0.96. The flame is much shorter compared to the solid fuel flames. This is also evident from the fact that changes in combustion parameters only cause a noticeable temperature change at the upper temperature sensor T_2, while the temperature of the thermocouple located at a lower position in the combustion chamber (T_1) barely changes. The image in the center shows the same flame without swirl. The result is a narrow, elongated type I flame. The image on the right-hand side shows the swirled flame under oxyfuel conditions with an enrichment of 28 vol% O_2 in the oxidant. Fig. 7.12 shows the temperature profile of T_1 and T_2 plotted against the three operating conditions shown in Fig. 7.11, whereby 3 oxygen variations are additionally plotted for the oxyfuel flame.
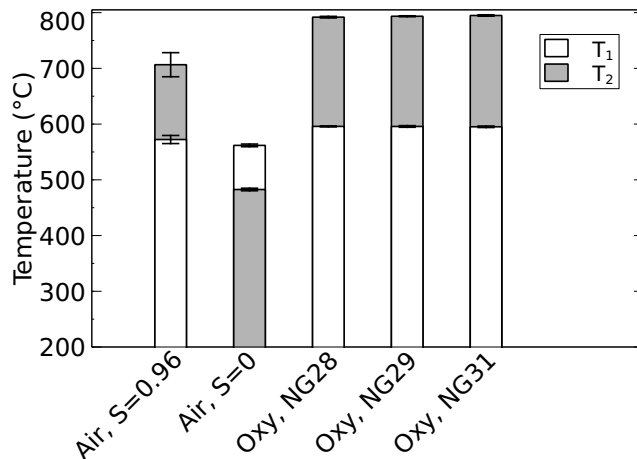
Fig. 7.12 Temperature variation during NG combustion in an air and oxyfuel atmosphere using different combustion parameters. Temperature of T_1 (white) and T_2 (gray) plotted against operating conditions.

The temperatures at T_2 drop by more than 200 K for a non-swirled flame, while the tem-

perature at T_1 decreases slightly. All NG flames in oxyfuel operation have 100 K higher gas temperatures near the combustion chamber wall than the NG-air flame. The three different oxygen concentrations in the oxidant have only a minor impact on the temperature during oxyfuel firing with natural gas.

7.2.2 Walnut shells

The WS flame discussed in the previous section at a local equivalence ratio of 1.6 ($\dot{V}_{sec}/\dot{V}_{tet}$ = 5.6) is shown in Fig. 7.13 on the left for an oxygen concentration of 27 vol% (WS27) and on the right for 33 vol% (WS33) in the oxidant. The flame is centered and can be operated without NG support flame. However, to compensate fluctuations in fuel mass flow, a low NG support flame of $1 - 1.5\,\mathrm{Nm^3/h}$ is used during the experiments. Moreover, it can be seen that the combustion chamber is brighter in the right-hand image than in the left-hand image, as the flame is more luminous due to the higher oxygen content.
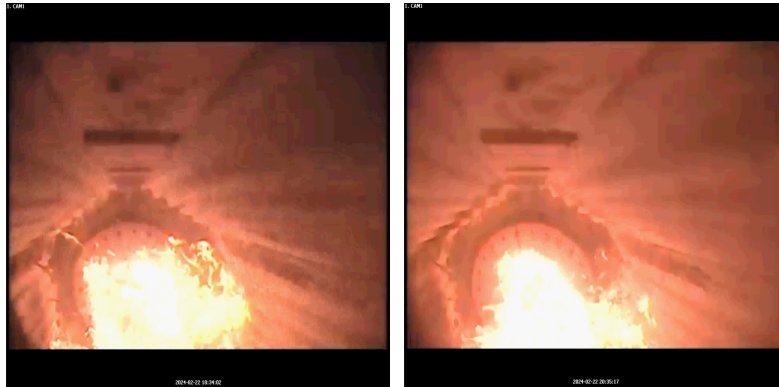
Fig. 7.13 Images of stable pulverized oxyfuel WS flames at $\dot{V}_{sec}/\dot{V}_{tet}$ = 5.6. Left: 27 vol% O_2 content in the oxidant at 460 kW$_\mathrm{th}$. Right: 33 vol% O_2 content in the oxidant at 500 kW$_\mathrm{th}$.

Fig. 7.14 shows three images of unstable WS flames under oxyfuel conditions. All flames show a highly asymmetric profile, are off-centered and have strong positional fluctuations. In addition, the flames appear torn apart as they do not have a closed luminous profile. These flames are not able to survive without a NG pilot flame.

The left image shows a flame at a thermal load of 400 kW and an oxygen concentration of 30 vol% in the oxidant. The low thermal load results in a low velocity ($u_{sec} = 11.8\,\mathrm{m/s}$) of the secondary stream which causes insufficient mixing. The picture in the middle shows an oxyfuel flame at a thermal load of 500 kW and is therefore in the range of nominal power. The oxygen content is only 25 vol% here. This causes the flame to emit less radiation, which can be seen in the dark appearance of the combustion chamber and the low luminosity of the flame. The CO emissions of this flame are almost 16000 ppm, which indicates poor combustion. The secondary velocity is 18.2 m/s and therefore should be high enough for a sufficient IRZ. The low oxygen concentration in the oxidant seems to be the cause for the instability of the flame. Therefore, the O_2 enrichment should be selected higher than 25 vol% in the oxidant at nominal

Fig. 7.14 Images of different unstable oxyfuel WS flames. Left: oxyfuel WS flame at 400 kW$_{th}$ with 30 vol% O_2 in the oxidant, $\lambda_{loc} = 1.2$. Middle: oxyfuel WS flame at 500 kW$_{th}$ with 26 vol% O_2 in the oxidant, $\lambda_{loc} = 1.0$. Right: oxyfuel WS flame at 460 kW$_{th}$ with 33 vol% O_2 in the oxidant, $\lambda_{loc} = 0.9$.

power for WS. In the picture on the right, the thermal load is 500 kW with an oxygen content of 32 vol% and a local equivalence ratio of 0.9 ($\dot{V}_{sec}/\dot{V}_{tet} = 0.8$). Due to the low equivalence ratio, less secondary flow is provided leading to a low secondary velocity ($u_{sec} = 11.2$ m/s) and poor mixing.

In Fig. 7.15 the oxygen content in the oxidant is plotted against the momentum ratio for WS. All trials, including those not discussed, are shown in the diagram. The stability limit is set here at a momentum ratio of 1.5 and an oxygen concentration in the oxidant of 27 vol%, since instabilities or high CO emissions occur below.
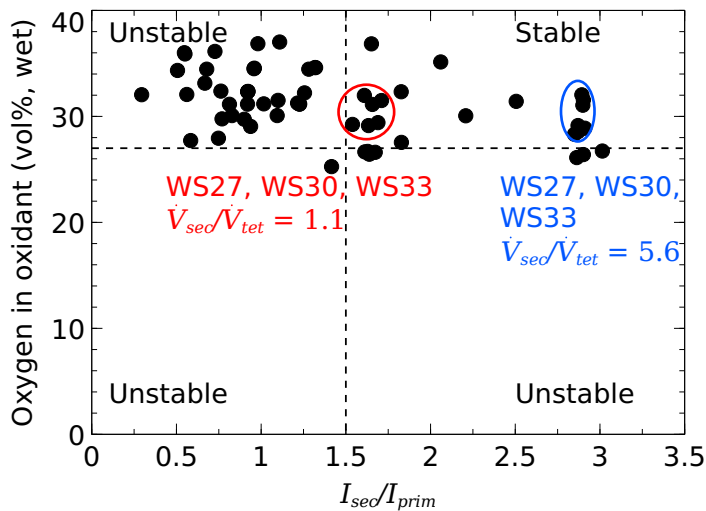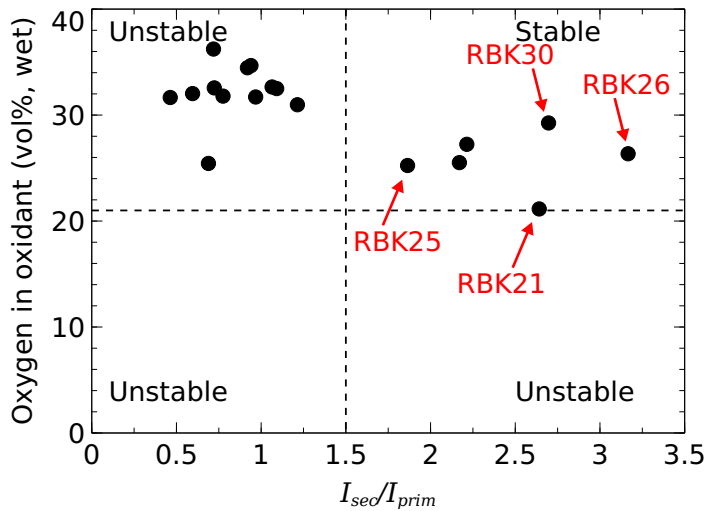

Fig. 7.15 Quantification of the stability for the WS flame under oxyfuel conditions based on the momentum ratio (abscissa) and the O_2 concentration in the oxidant (ordinate). The diagram is divided into stable and unstable zones (dashed lines).

The operating conditions for WS, which are presented in Section 7.1, are marked in red for low secondary to tertiary flow ratios and in blue for high secondary to tertiary flow ratios. Flames below 450 kW$_{th}$ generally show instabilities. A higher secondary flow (high λ_{loc}) increases the momentum ratio and thus the stability. Habermehl and co-workers came to the same conclusion, recognizing high CO content in the exhaust gas for low λ_{loc} [203]. The swirl number, on the other hand, shows no significant influence on the stability. In most cases, it was chosen as high as possible. Considering the oxygen concentration in the oxidant, it can be seen that a high oxygen concentration can lead to instabilities, as lower volume flows are

required to oxidize the same amount of fuel. This reduces the velocity of the secondary flow and decreases the momentum ratio. WS27, WS30 and WS33 are within the stable range for both local equivalence ratios, which also corresponds to the observations with the camera and the measurements of CO emissions.

7.2.3 Rhensih lignite

Fig. 7.16 shows three different oxyfuel flames with RBK. The left image shows the RBK25 flame discussed in the previous section. The flame is centered and shows a closed luminous profile. The flame can also be operated without NG support.
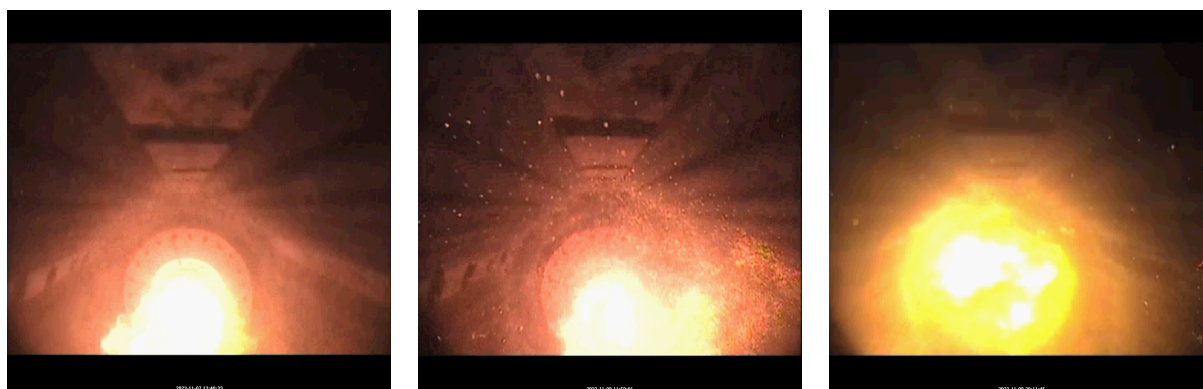
Fig. 7.16 Images of different RBK flames under oxyfuel conditions. Left: image of the RBK25 flame with a thermal power of 540 kW and 25 vol% O_2 content in the oxidant. Middle: image of a 300 kW$_{th}$ flame with 32 vol% O_2 content in the oxidant and 20 Nm^3/h NG support. Right: image of a 650 kW$_{th}$ flame with 49 vol% O_2 content in the oxidant.

The image in the middle shows a 300 kW$_{th}$ flame with an enrichment of 32 vol% oxygen in the oxidant. Even with a high NG support of 20 Nm^3/h, it shows instabilities, which can be recognized by a strongly asymmetrical flame pattern and incomplete burned particles. As the velocities are low at this thermal power, it can be assumed that there is no IRZ or at least insufficient recirculation of the fuel near the burner. The image on the right shows an oxyfuel flame with 650 kW$_{th}$ and an oxygen enrichment of 49 vol% in the oxidant. This causes the bright luminarity of the flame. This flame has pollutant emissions of 470 ppm CO and 540 ppm NO. Although this type of flame is not of practical use, it was studied due to academic interest. Due to the high oxygen content, lower volume flows are required, leading to lower secondary momentum and thus instabilities.

In Fig. 7.17 the oxygen content in the oxidant is plotted against the momentum ratio for RBK. All trials, including those not discussed, are shown in the diagram. The stability limit is set here at a momentum ratio of 1.5 and an oxygen concentration in the oxidant of 21 vol%, since instabilities or high CO emissions occur below.

Any thermal output below 400 kW is unstable because of the low momentum ratio. Oxygen enrichments of more than 30 vol% in the oxidant can also lead to instabilities, as can be seen in the diagram. The low momentum of the secondary flow at high oxygen concentrations can be

Fig. 7.17 Quantification of the stability for the RBK flame under oxyfuel conditions based on the momentum ratio (abscissa) and the O_2 concentration in the oxidant (ordinate). The diagram is divided into stable and unstable zones (dashed lines).

compensated with a higher local equivalence ratio or secondary to tertiary ratio, respectively. This was done for RBK30. Although RBK30 has a high oxygen content in the oxidant, the momentum of the secondary flow is increased through a higher local equivalence ratio. However, this measure is not advisable as this results in increased NO emissions due to more oxidizer in the flame core. RBK26 has the highest momentum ratio, but the highest CO emissions of the investigated RBK cases at the same time. However, this may also be related to fluctuations in the fuel dosing while constant oxidant flow (cf. Section 7.1). RBK21 has a high momentum ratio, although the O_2 content in the oxidant is close to the limit of the unstable zone. The experiments have shown that a further reduction in oxygen enrichment leads to a rapid increase in CO emissions. RBK25, which has in comparison to the biomass, a low O_2 enrichment of 25 vol% in the oxidant, is within the stable range at low CO emissions (650 ppm). The influence of the swirl number is difficult to assess, as maximum swirl was always aimed for. Low swirl numbers led to flame blow-off in the experiments.

7.2.4 Beech wood

In case of BW400 and BW520, it can be seen in Fig. 7.18 that the flame is surrounded by glowing particles falling downwards. This indicates insufficient recirculation of particles near the burner due to a low secondary velocity of approx. 10 m/s for both operating conditions. As a result, the particles are discharged from the reaction zone not able to follow the streamlines in the flame core.

In case of BW670, no particles can be seen on the image. The flame of BW670 shows a slight inclination and the visibility of the quarl suggests that there is a delayed ignition of the fuel. The inclination of the BW670 flame could be also caused by the purge gas of the measuring systems. However, it is difficult to determine how strong the inclination of the flame actually is from the perspective of the camera position. As BW400 and BW520 have shorter flames, which can be assessed using the inspection windows on the combustion chamber, the flames are less affected by the purge gas from the measuring systems.
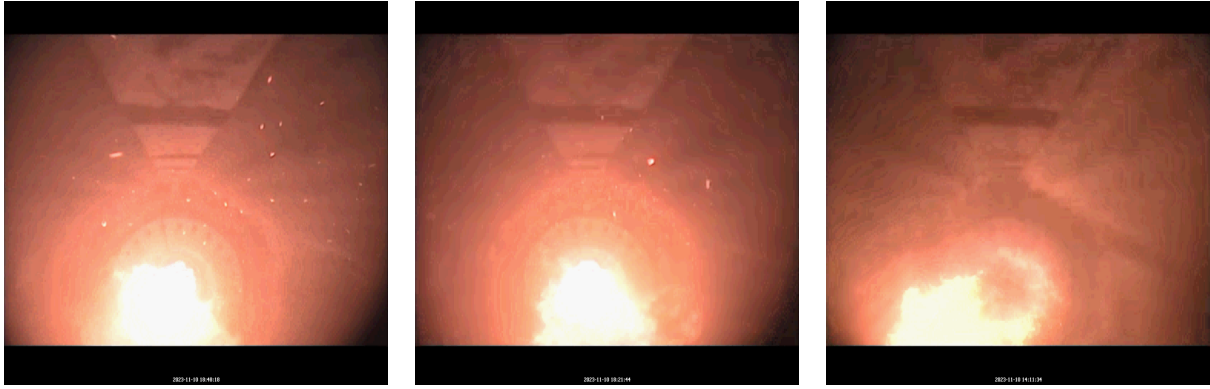
Fig. 7.18 Images of pulverized oxyfuel flames for BW. Left: image of the BW400 flame with a thermal output of 400 kW and 35 vol% O_2 content in the oxidant. Middle: image of the BW520 flame with a thermal output of 520 kW and 27 vol% O_2 content in the oxidant. Right: image of the BW670 flame with a thermal output of 670 kW and 35 vol% O_2 content in the oxidant.

Even though the data basis for BW is small, BW670 with a thermal output of 670 kW, 35 vol% O_2 and a global equivalence ratio of 1.7 shows the lowest CO emissions in these investigations, with a stable flame under oxyfuel conditions (cf. Section 7.1). The NO emissions are the highest for BW670. However, they can be reduced by air staging or adjustment of $\dot{V}_{sec}/\dot{V}_{tet}$, respectively. All BW trials had a local equivalence ratio above 1.3.

In Fig. 7.19 the oxygen content in the oxidant is plotted against the momentum ratio for BW. All trials, including those not discussed, are shown in the diagram. The stability limit is set here at a momentum ratio of 1.2 and an oxygen concentration in the oxidant of 28 vol%, since instabilities or high CO emissions occur below.
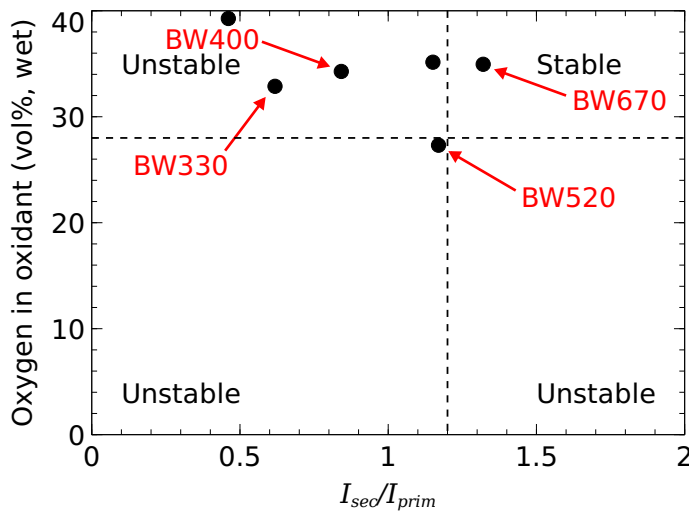
Fig. 7.19 Quantification of the stability for the BW flame under oxyfuel conditions based on the momentum ratio (abscissa) and the O_2 concentration in the oxidant (ordinate). The diagram is divided into stable and unstable zones (dashed lines).

The majority of operating points are in the unstable range despite BW670. Since all cases have a local equivalence ratio above one, the instability may be attributed to the high oxygen enrichment of 35 vol% in the oxidant. As already discussed for WS and RBK, high O_2 concentrations in the oxidant cause a low momentum of the secondary flow and thus insufficient recirculation of the fuel near the burner. This can also be recognized by the particles discharged by the flame, as they do not follow the streamlines in the flame core. For BW670,

a low secondary momentum is prevented by a high thermal output and consequently a high secondary to primary momentum ratio. BW520 shows the highest CO emissions for BW (cf. Section 7.1) although this case shows an almost stable flame. Nevertheless, a small number of glowing particles can still be seen surrounding the flame. However, these could also be due to large particles, as this fuel has high inhomogeneities concerning particle sizes. The swirl numbers are similar for all cases investigated. It is assumed that slight changes in the swirl number do not have a significant effect on the stability of the flame but low swirl numbers result in flame extinction. Nevertheless, the swirl number should be high to generate a strong IRZ.

Schneider et al. [14] compared the velocity field of RBK, WS and BW in the reference laboratory oxyfuel combustion chamber. The results show that the IRZ is most pronounced for RBK, as it has a large number of very fine particles. In contrast, the IRZ is more compact using WS and BW and most particles penetrate the IRZ. This could also explain why RBK has the lowest CO emissions compared to WS and BW in this work and a higher O_2 concentration in the oxidant is necessary to improve the oxidation of the larger biomass particles. However, the hypothesis in this work that the IRZ collapses with increasing oxygen content in the oxidant at constant thermal load can neither be proven nor disproven by the work of Schneider and co-workers, since the thermal power for a higher oxygen enrichment was increased in their experiments to keep the equivalence ratios ($\lambda_{loc} = 0.61$, $\lambda_{glob} = 1.25$) and the volume flows constant. In summary, a stable flame under oxyfuel conditions is obtained for the semi-industrial burner with a secondary to primary momentum ratio of greater than $1.2 - 1.5$ and an O_2 concentration in the oxidant of $\geq 21\,\text{vol}\%$ for RBK, $\geq 27\,\text{vol}\%$ for WS and $\geq 28\,\text{vol}\%$ for BW. The NG flame is stable for all tested combustion parameters. Adjustments to the O_2 concentration in the oxidant result in only minor temperature changes in the combustion chamber.

7.3   Radiative Heat Transfer

Due to the high amount of CO_2 in oxyfuel combustion, the radiation properties within the combustion chamber change compared to air-firing. To investigate the effects of this on radiative heat transfer during the combustion of biomass, lignite, and natural gas, measurements of the wall-incident radiative heat flux were carried out using a Gardon Gauge heat flux sensor (cf. Chapter 6). A brief overview of the state of the art regarding thermal radiation measurements in oxyfuel combustion is given below.

Zabrodiec et al. [153] carried out radiative heat flux measurements using an ellipsoidal radiometer. They investigated the combustion of RBK and torrefied biomass (TB) with a $40\,\text{kW}_{\text{th}}$ oxyfuel burner. The walls of the combustion chamber are refractory-lined and heated. The chamber has an interior diameter of $400\,\text{mm}$. The results for the radiative heat flux are

only presented in relative values. The TB shows a higher radiative heat flux compared to the RBK, both in the case of air and oxyfuel combustion. The firing of TB and RBK with air results in higher values for the radiative heat flux for both fuels than under oxyfuel conditions. An enrichment of 27 vol% oxygen was used in the oxidant. Ramadan et al. [204] investigated the temperature and radiative heat flux in a 200 kW$_{th}$ NG-fired combustion chamber with refractory-lined walls under air and oxyfuel conditions for different swirl numbers. They used an ellipsoidal radiometer for radiative heat flux measurement. The ratio of oxygen and CO_2 in their study is 17/83 mass per cent. They conclude that even under oxyfuel conditions, thermal radiation increases with increasing swirl. However, the values of wall-incident radiative heat flux for a comparable air-NG flame are 25 % higher than for an oxyfuel flame. Corrêa da Silva and Krautz [205] investigated various burner parameters at 400 kW$_{th}$ with dried lignite in a square 1×1 m boiler with water-cooled membrane walls. They used an ellipsoidal radiometer for the radiation measurements [205]. They concluded that an enrichment of 31 vol% O_2 in the oxidant results in similar radiative heat flux under oxyfuel conditions as for combustion with air. Smart et al. [206] investigated the influence of the flue gas recirculation rate on thermal radiation for a 500 kW$_{th}$ coal and saw dust co-firing under oxyfuel conditions. They carried out the measurements with a MEDTHERM digital radiation heat flux meter on a refractory-lined combustion chamber with a diameter of 800 mm [207]. Their investigation showed a decrease in radiative heat flux with increasing recirculation rate. During the combustion of coal and saw dust, the recirculated flue gas was enriched with oxygen targeting 3 vol% residual oxygen in the flue gas [184].

The above-mentioned studies were mainly carried out in combustion chambers with refractory-lined walls, with the exception of the work by Corrêa da Silva and Krautz [205] which do not correspond to industrial conditions, where water-cooled membrane walls made of steel are frequently used. As these represent a heat sink, the radiation exchange in the combustion chamber changes in comparison to refractory-lined walls. Furthermore, biomass is either co-fired with coal in an oxyfuel atmosphere to study the radiative heat flux, or torrefied biomass is used. The following section is intended to provide information about the radiation properties in a semi-industrial combustion chamber with water-cooled walls and the combustion of biomass with different combustion parameters in an oxyfuel and air atmosphere. Furthermore, the radiation of natural gas under oxyfuel and air conditions is investigated to show differences in gaseous and solid fuels. Since the EST500 burner is a up-scaled version of the WSA40 burner, the measurements of radiative heat flux are compared to each other [184].

7.3.1 Walnut shells

A constant thermal load of 510 kW was used to burn pulverized WS (cf. appendix Tab. C.3). Therefore, a mass flow rate of 110 kg/h was set. The secondary streams result in a swirl number of 0.95, and the global stoichiometric ratio is approx. 1.6 for air and oxyfuel WS

combustion. At lower equivalence ratios, a significant increase in CO emissions occurs for WS. The local stoichiometric ratio was changed between 0.8 and 1.0 for WS-air combustion and 0.8 to 1.4 for WS-oxyfuel combustion during the experiments. An oxygen concentration in the recirculated flue gas of 27 vol% (WS27), 30 vol% (WS30) and 33 vol% (WS33) was set. Fig. 7.20 shows the measurement results of the wall-incident radiative heat flux plotted against the axial distance to the burner quarl for WS-air and three WS-oxyfuel flames with different O_2 content in the oxidant [184].
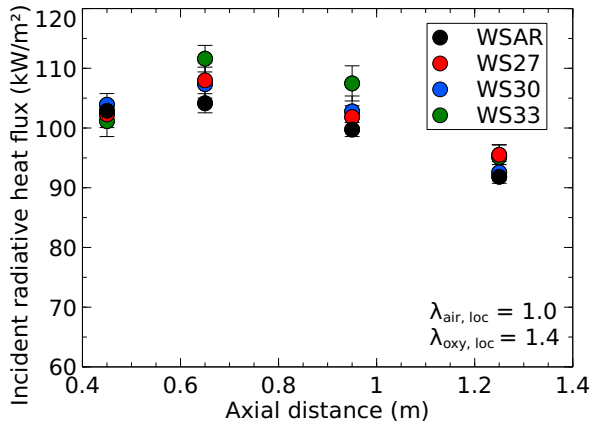
Fig. 7.20 Measured incident radiative heat flux of WSAR (black), WS27 (red), WS30 (blue) and WS33 (green) plotted against different axial distances to the burner quarl. The local equivalence ratio is 1.0 for air combustion, and 1.4 for oxyfuel combustion [184].
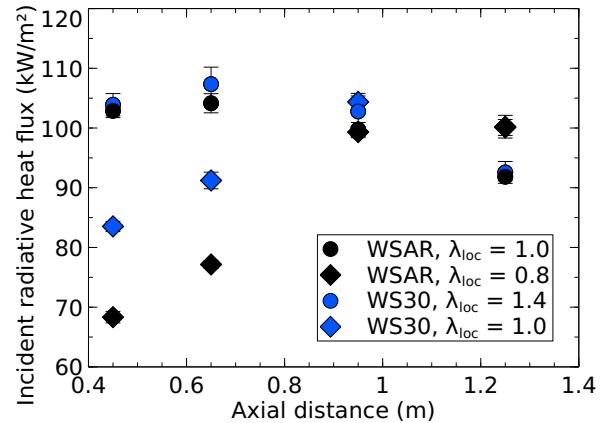
Fig. 7.21 Measured incident radiative heat flux of WSAR at local equivalence ratio of 1.0 (black circle) and 0.8 (black diamond); WS30 at local equivalence ratio of 1.4 (blue circle) and 1.0 (blue diamond). All operating conditions plotted against different axial distances to the burner quarl [184].

All measured flames show a maximum radiative heat flux at an axial distance of approx. 0.65 m. The radiative heat flux decreases continuously with increasing distance to the quarl. The highest value of 112 kW/m² is measured for WS33, as the O_2 enrichment is highest here and thus also the temperature. The results of all WS-oxyfuel flames are close to the results of the WS-air flame. It is assumed that the flame is longer than 1.25 m, as no identical radiative heat fluxes are measured for the different operating parameters at the lowest measuring port, as can be observed with short flames. This is the case for NG flames, for example, which will be discussed later. Only the background radiation is measured for NG flames at this position. The flame is also recognizable at all four sight windows, which are installed on the combustion chamber. Fig. 7.21 shows the comparison of air-firing and WS30 with low and high local stoichiometric ratio or $\dot{V}_{sec}/\dot{V}_{tet}$ ratio, respectively. The lower conversion of the carbon monoxide at this point indicates poor combustion and consequently reduced heat release which is also reflected in the radiative heat flux measurements. The WS-air and WS-oxyfuel flames both show far lower values compared to the flames with a higher local equivalence ratio, but otherwise the same boundary conditions. Changes in the oxidant distribution between the secondary and tertiary channels have a larger impact on the differences of thermal radiation in the WS-air case than in the WS-oxyfuel case. However, in the air-firing case the difference

between the local equivalence ratios is 0.2, while in the oxyfuel case the difference is 0.4. Fig. 7.22 shows the difference in heat release by means of gas temperatures near the chamber wall at measuring port T_2 [184].
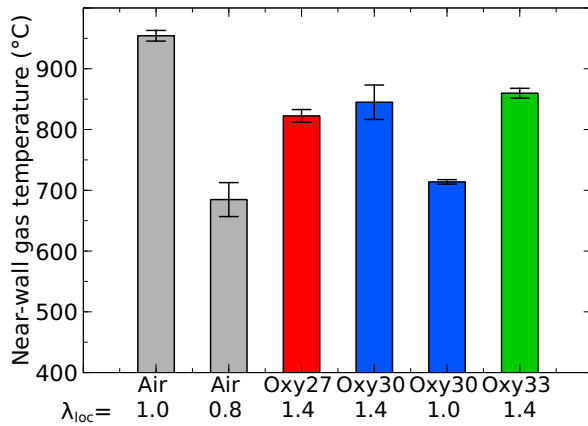
Fig. 7.22 Near-wall gas temperature of WS-air and WS-oxyfuel flames with different local equivalence ratios [184].

High temperatures are reached in the air-firing case with a local stoichiometric ratio of one. For the same operating condition at $\lambda_{loc} = 0.8$, the temperature is approx. 250 K lower. The slower velocity near the burner with lower local stoichiometric ratios can lead to insufficient mixing of fuel and oxidizer and thus to lower heat release rates, reflected in the temperature [184].

7.3.2   Rhensih lignite

The wall-incident radiative heat flux was measured for the RBK at an output of 500 kW$_{\text{th}}$, an equivalence ratio of $1.4 - 1.6$ and a swirl number of approx. 0.95. Two oxyfuel flames with 26 vol% (RBK26) and 30 vol% (RBK30) oxygen in the oxidant and one RBK-air (RBKAR) flame were investigated (cf. appendix Tab. C.4). In addition, the results of the radiative heat flux for RBK are compared with those of WS. Fig. 7.23 shows the measured incident radiative heat flux of two RBK-oxyfuel flames and one RBK-air flame plotted against the axial distance to the burner quarl [184].

All flames have the same tendency down the axis of the combustion chamber and reach the maximum radiative heat flux at 0.65 m. After the maximum is reached, all curves drop slightly, whereby the heat flux in the RBK-air flame drops rapidly. The reason for this are fluctuations in the fuel dosing. A temporarily reduced fuel mass flow is also noticeable due to decreasing temperatures inside the combustion chamber. The RBK-air flame reaches 92 kW/m² at 0.65 m, which is the highest measured value for the RBK. Both oxyfuel flames have lower heat flux values than the RBK-air flame. This could be due to endothermic Boudouard-reactions in the oxyfuel atmosphere, which reduce the temperature and thus the radiative heat transfer. Therefore, an oxygen content of over 30 vol% in the oxidant is necessary to achieve approx. the values of RBK-air combustion. As the RBK30 case is already close to the values of air combustion, this observation is consistent with the results of Corrêa da Silva and Krautz
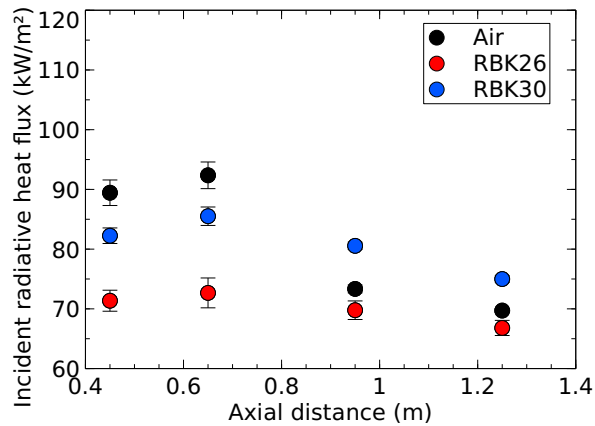
Fig. 7.23 Measured incident radiative heat flux of RBK-air (black), RBK26 (red) and RBK30 (blue) plotted against different axial distances to the burner quarl. Comparison of RBK-air and RBK-oxyfuel combustion considering wall-incident radiative heat flux [184].
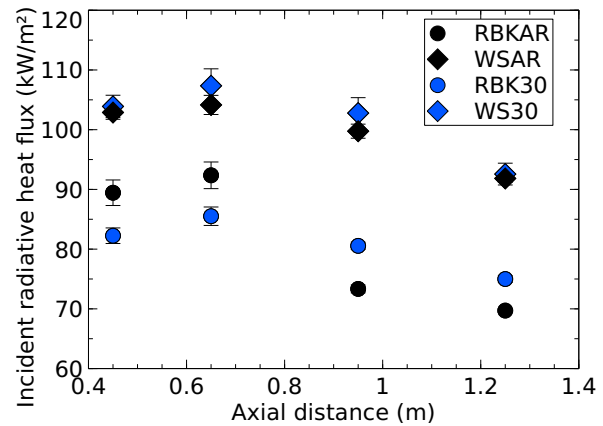
Fig. 7.24 Measured incident radiative heat flux of WSAR (black diamond) and WS30 (blue diamond); RBKAR (black circle) and RBK30 (blue circle). All operating conditions plotted against different axial distances to the burner quarl. Comparison of WS and RBK considering wall-incident radiative heat flux [184].

[205], who achieved values similar to those for air combustion with an enrichment of 31 vol% oxygen. Fig. 7.24 shows a comparison of the radiative heat flux for the solid fuels WS and RBK. Each fuel is investigated for air-firing and oxy-firing with 30 vol% O_2 in the oxidant. In the study of Zabrodiec et al. [153], the biomass also yielded higher values than the RBK at the same thermal output. Their assumption is that the thermal radiation, mainly emitted by the particles, is higher because the biomass has a lower calorific value and therefore a higher particle load is necessary to achieve the same thermal power as with the RBK [45]. However, it is also assumed that the higher volatile content in the biomass accelerates ignition of the fuel and therefore results in more intensive heat release, which in turn leads to higher radiative emissions [184]. Fig. 7.25 shows the gas temperature near the combustion chamber wall for the three RBK flames at measuring port T_2. Since the mentioned fluctuations in the fuel dosing occur and the temperature dropped, the temperature of RBK26 and RBKAR are close to each other. However, the temperature of RBK30 and RBK are not closely related, although the measured incident radiative heat fluxes are more similar than RBKAR and RBK26 [184].
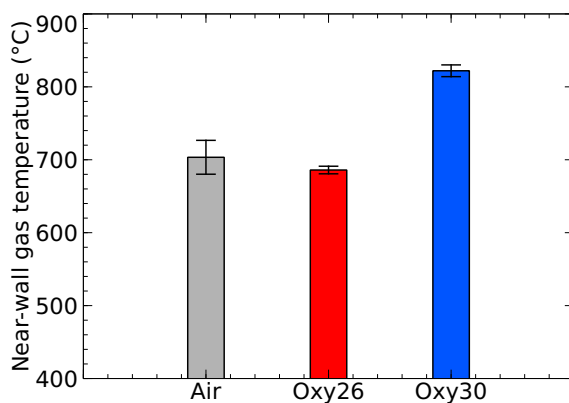
Fig. 7.25 Near-wall gas temperature of RBK-air and RBK-oxyfuel combustion with two different O_2 concentrations in the oxidant [184].

117

7.3.3   Natural gas

The wall-incident radiative heat flux of the NG flames was measured at a thermal output of 310 kW for NGAR, NG28, NG29 and NG30 (cf. appendix Tab. C.6). Fig. 7.26 shows the heat flux measurements plotted against the axial distance to the burner quarl for the NG-air flame and the three oxyfuel flames.
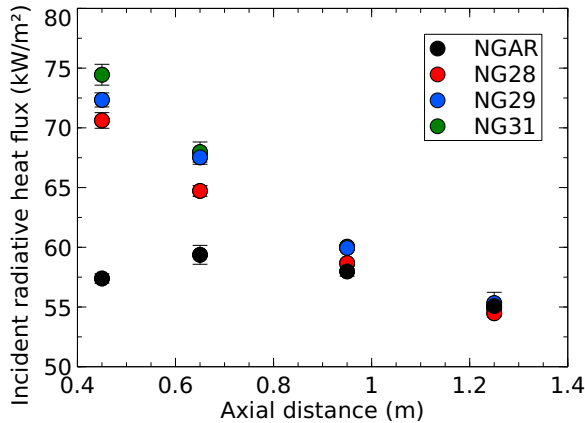
Fig. 7.26 Measured incident radiative heat flux of NGAR (black), NG28 (red), NG29 (blue), NG31 (green) plotted against the axial distance to the burner quarl. Comparison of a NG-air flame and NG-oxyfuel flames at different oxygen concentrations in the oxidant.
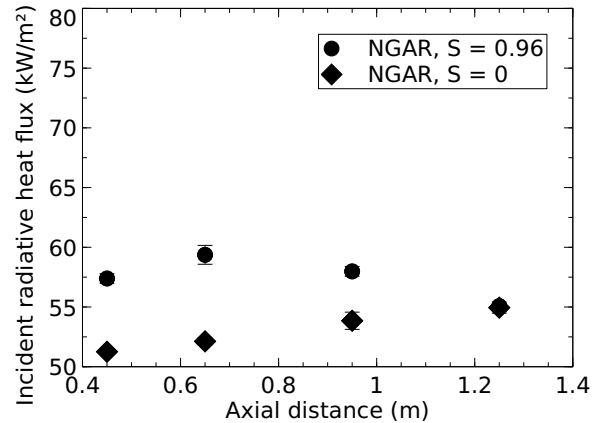
Fig. 7.27 Measured incident radiative heat flux of NGAR at $S = 0.96$ and $S = 0$ plotted against the axial distance to the burner quarl. Comparison of a swirled and non-swirled NG-air flame.

Compared to the NG-air flame, all NG-oxyfuel flames have a considerably higher radiative heat transfer near the burner quarl. While the radiative heat flux of the NG-air flame first rises along the combustion chamber axis, reaching a maximum at approx. 0.65 m and then decreases, the oxyfuel flames already show their maximum at the first measuring port (approx. 0.45 m). With increasing oxygen concentration in the oxidant, the measured radiative heat flux also rises. The difference in the maximum between NG31 and NG28 is approx. 4 kW/m². This result seems reasonable, as the theoretical adiabatic flame temperature also rises with increasing oxygen content in the oxidant. The measurement results at the 4th port overlap for all investigated gas flames. It is assumed that this position marks the end of the flame and only background radiation is measured. Due to the windows installed on the combustion chamber at the same height as the measuring ports, it can also be seen that the NG flames with high swirl are shorter than the particle loaded flames. Fig. 7.27 shows the radiative heat flux of the air-flame at high swirl and without induced swirl. The difference between these flames is up to 7.2 kW/m². Due to the reduced mixing of oxidizer and fuel in the type I flame (non-swirled NGAR), less heat is probably released locally, which leads to lower flame temperatures and thus to less heat transfer by radiation. A reduced O_2 enrichment in the oxidant requires more oxidant volume flow using a unchanged equivalence ratio. Higher CO_2 mass reduces the flame temperature and thus the emission of the flame. A higher oxygen content in the oxidant ensures a more intense reaction and heat release, which leads to higher

flame temperatures and faster ignition [184]. Fig. 7.28 shows the temperatures for air- and oxyfuel combustion at measuring port T_2.
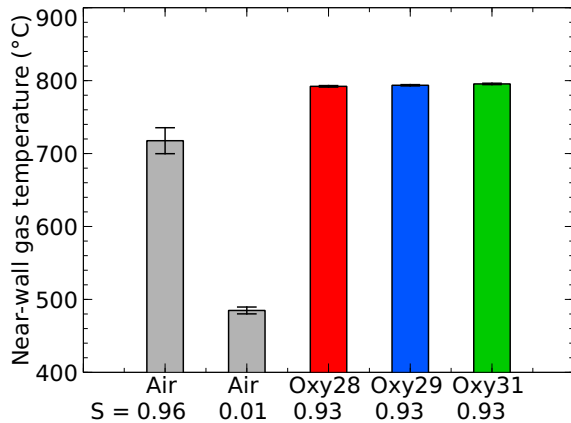
Fig. 7.28 Near-wall gas temperature of swirled NG-air and NG-oxyfuel flames with three different O_2 concentrations in the oxidant. In addition, a non-swirled NG-air flame [184].

The gas temperatures near the combustion chamber wall are almost identical for the oxyfuel flames, while the NG-air flame is approx. 80 K lower. The non-swirled NG-air flame is more than 300 K below the temperatures of the oxyfuel flames. In the work of Ramadan et al. [204] they also concluded that a higher swirl increases the temperatures and radiative emissions. They obtained higher temperatures and radiative heat transfer at the wall for air-firing, than using an oxidant with a 17/83 O_2 to CO_2 ratio. The recommendation of Ramadan and co-workers is to increase the O_2 content in the oxidant to achieve temperature and radiative heat flux levels similar to those of air combustion, since N_2 absorbs less radiation than CO_2 [184].

7.3.4 Reference burner

The measurements of the radiative heat flux with the up-scaled EST500 burner are compared to the reference burner WSA40. Zabrodiec et al. [153] performed radiative heat flux measurements with RBK and torrefied biomass (TB). As the combustion chamber of the WSA40 has refractory-lined walls and thus no comparable values are obtained in total terms, the comparison is carried out using relative values. The incident radiative heat flux (RHF) is normalized by the maximum measured value. The measurement results of Zabrodiec and co-workers for RBK and TB under air (RBK21 and TB21) and oxyfuel atmosphere (RBK27 and TB27) at an oxygen content of 27 vol% in the oxidant are compared to the measurements of RBK and WS in an air (RBKAR and WSAR) and oxyfuel atmosphere (RBK26 and WS26) at an oxygen content of 26 vol% in the oxidant. As the combustion chambers of the WSA40 and EST500 have different dimensions, the axial distance to the quarl is shown in dimensionless values (z/d). In addition, the measuring position of the maximum radiative heat flux is indicated. Fig. 7.29 shows the RHF results of RBK and WS plotted against the dimensionless axial distance to the quarl. Fig. 7.30 shows the RHF results by Zabrodiec et al. [153] of RBK and TB plotted against the dimensionless axial distance to the quarl [184].

The TB has a higher calorific value than the WS, so the results for RBK and TB may therefore
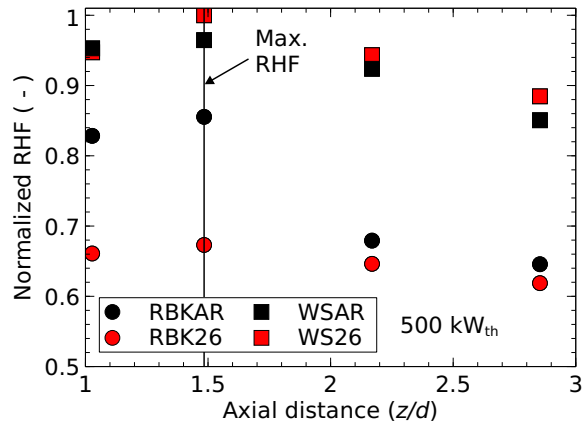
Fig. 7.29 RBKAR (black circle), RBK26 (red circle), WSAR (black square) and WS26 (red square) at a thermal output of 500 kW plotted against the dimensionless axial distance to the quarl. Comparison of WS and RBK for air and oxyfuel firing in terms of the dimensionless RHF. The maximum values are marked with a solid line [184].
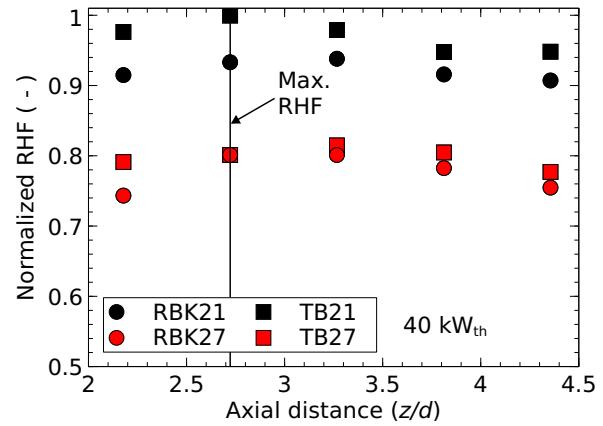
Fig. 7.30 RBK21 (black circle), RBK27 (red circle), TB21 (black square) and TB27 (red square) at a thermal output of 40 kW plotted against the dimensionless axial distance to the quarl. Comparison of TB and RBK for air and oxyfuel firing in terms of the dimensionless RHF. The maximum values are marked with a solid line [153].

be closer together than the results for RBK and WS. At the first two measuring positions of the combustion chamber of the WSA40, in the work of Zabrodiec et al. [153], the differences in RHF between RBK21 and RBK27 are 0.17 (z/d=2.18) and 0.13 (z/d=2.72). Compared with the first two measuring ports of the combustion chamber of the EST500, the difference in RHF between the RBK-air and RBK-oxyfuel flame is 0.17 (z/d=1.03) and 0.18 (z/d=1.48), respectively. Hence, a comparison of the radiative heat flux in relative values shows good agreement between both combustion chambers at different thermal loads. The remaining measuring positions are not comparable, since fluctuations in the fuel dosing occurred for the RBK21 case, which led to a distortion of the measured data. The difference between the TB-air and TB-oxyfuel flame for the RHF is between $0.14 - 0.2$ at 40 kW$_{th}$, while the difference for the walnut shells is between 0 and 0.04 at 500 kW$_{th}$ along all measurement positions. It is assumed that due to a 16 % higher carbon content in the TB fuel, the endothermic Boudouard-reaction is more pronounced under an oxyfuel atmosphere, compared to the WS. This reduces the temperature of the flame and therefore the difference of the measured wall-incident radiative heat flux between RBK and TB are greater than for RBK and WS. Another assumption is that the TB char burnout is insufficient and therefore less heat is released locally, which leads to a reduced flame temperature. The CO content measured by Zabrodiec and co-workers at the last measuring position z/d=4.35 for TB27 is considerably higher than for TB21, RBK21 and RBK27 [153]. The increased CO formation supports both theories [184].

8 Application of Radiation Models

The measured wall-incident radiative heat flux at the combustion chamber wall for air- and oxy-firing with NG (see Chapter 7) is used to validate the radiation models from Chapter 3. A CFD simulation of the combustion chamber is performed using the models from Chapter 4. Since this work focuses on the modeling of gas radiation under oxyfuel conditions, a natural gas flame is considered to exclude particle radiation, which dominates in pulverized fuel flames. The boundary conditions of NG28 are used for simulation of oxyfuel combustion, and the boundary conditions of NGAR at high swirl number ($S = 0.96$) are used for air combustion. The FSCK and WSGG[1] model from Chapter 3 are applied.

8.1 Boundary Conditions

As mentioned, the boundary conditions of NGAR and NG28 ($S = 0.96$) are used, which can be found in the appendix. Since the homogeneous combustion of NG does not require a pyrolysis and char combustion model, less models are necessary for the simulations. Furthermore, the chemical reactions for the combustion of volatiles, described in Chapter 4 are not used. Instead methane-specific reaction mechanisms are used. A two-step reaction is used to model methane combustion in order to keep the calculation time to a minimum. If H_2O and CO_2 are assumed as combustion products in a one-step reaction, the absolute heat release may be overestimated locally. It is known that hydrocarbons burn sequentially. The fuel is partially oxidized to CO and H_2, these species are not remarkable consumed until all hydrocarbon species have disappeared. Based on this background, Dryer and Glassman developed a two-step reaction model for the oxidation of methane in turbulent flows [208]:

$$CH_4 + 1.5\,O_2 \;\rightarrow\; CO + 2\,H_2O, \tag{8.1}$$

$$CO + 0.5\,O_2 \;\rightarrow\; CO_2. \tag{8.2}$$
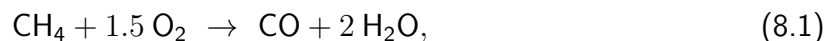
However, H_2 is not included as an intermediate product in this model. The reaction rates in Eq. (8.1) and Eq. (8.2) are taken from Andersen et al. [209] based on the work of Westbrook and Dryer [208]:

$$k_{8.1} = 1.59 \times 10^{13} \exp\left(-\frac{24088\,\mathsf{K}}{T}\right) [CH_4]^{0.7}[O_2]^{0.8}, \tag{8.3}$$

---

[1]WSGG parameters for oxyfuel combustion according to Bordbar et al. [73] are used.

$$k_{8.2} = 3.98 \times 10^{14} \exp\left(-\frac{20510\,\text{K}}{T}\right) [\text{CO}]^1 [\text{H}_2\text{O}]^{0.5} [\text{O}_2]^{0.25}. \tag{8.4}$$

Fixed wall temperatures are used for the simulations. The wall temperatures in the simulations are 720 °C for NGAR and 790 °C for NG28. These values correspond to the measurements of the wall temperature in the upper area of the combustion chamber near the wall. All simulations were carried out with the open-source code OpenFOAM® version 2006. The simulations were performed with an AMD Ryzen Threadripper 2950X 16-core processor, 3917 MHz. The 16 physical CPUs can be divided into 32 virtual cores. 24 cores were used for the simulations.

8.2 Numerical Mesh

The numerical mesh was created using the commercial software ANSYS®. The three dimensional numerical meshes were created as detailed as possible, but simplifications were nevertheless made. These relate to the wall of the combustion chamber, which does not take into account the cooling tubes of the membrane wall, the gaps between the individual quarl stones and sharp edges. A further simplification concerns the tiny nozzles of the gas lance in relation to the entire combustion chamber. Here, the nozzles of the lance are approximated as a single inlet patch. The geometry is only meshed up to the end of the radiation section of the combustion chamber. Three meshes with different cell numbers and element types were created for the mesh study. More information on the accuracy of the three meshes can be found in the appendix, Chapter A.2. The swirl channels of the burner made of tetrahedral elements for all three meshes. The remaining part of the combustion chamber is meshed with either tetrahedral or hexahedral cells. In comparison to Chapter 5, the entire geometry is modeled here instead of just one sixth of the chamber. Since a parameter study is carried out in Chapter 5, which requires several simulations, the computing time needs to be low. A partial section of the mesh with 2.5×10^6 cells is shown in Fig. 8.1.

8.3 Simulation Results

Fig. 8.2 shows the results for the wall-incident radiative heat flux obtained from the CFD simulations with the FSCK and WSGG model for NG28, plotted against the axial distance to the burner. The experimental results for NG28 are plotted for validation in the same diagram. The results of the FSCK model are in the average range of the experimental data, but do not capture the highest or lowest measured point. A peak can be seen at a distance of approx. 0.5 m, similar to the experimental data. However, the peak in the simulation results is not as pronounced as in the measurements. This could be due to uncertainties in the combustion model, which determines the heat release through chemical reactions. Since thermal radiation is strongly temperature-dependent, peaks can be expected in the area of high local heat release
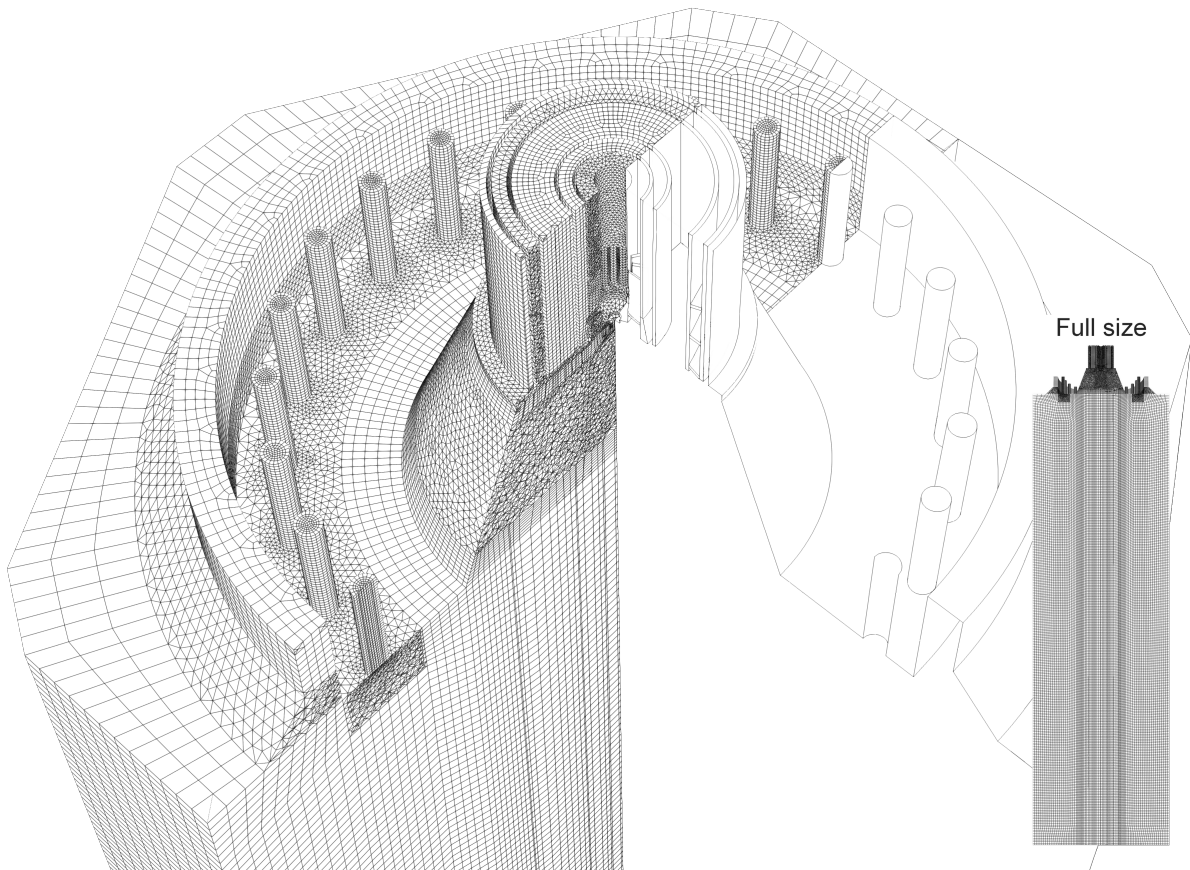
Fig. 8.1 Partial cut of the entire mesh and a partial cut of the geometry for better visualization. In addition, the entire cross-section of the whole EST combustion chamber mesh with 2.5×10^6 cells.
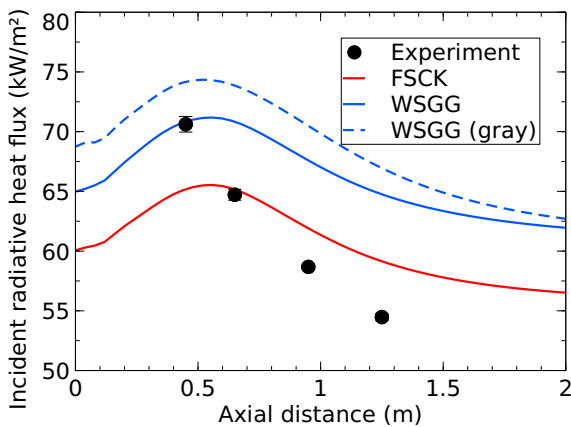

Fig. 8.2 Experimental (dots) and numerical (solid line) results of the wall-incident radiative heat flux for NG28 plotted against axial distance to the quarl.
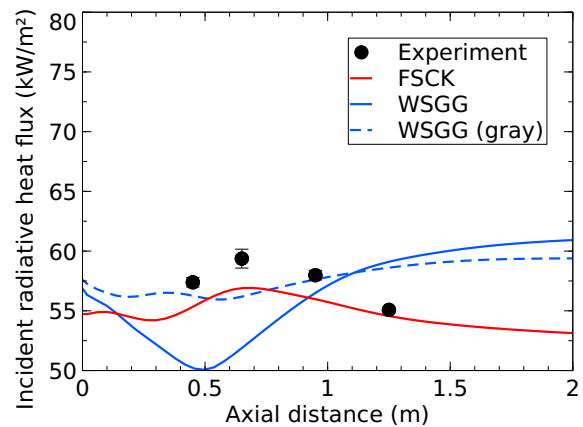

Fig. 8.3 Experimental (dots) and numerical (solid line) results of the wall-incident radiative heat flux for NRAG plotted against axial distance to the quarl.

and thus high local temperatures. Uncertainties in the turbulence model could also be a reason, as the prediction of the turbulent mixing has a direct impact on the combustion model. Another cause could be the soot concentration in this zone, which also cannot be accurately modeled by the combustion model. However, as the C/O ratio is low, soot can be expected to be of minor importance here. The WSGG model shows similar results as the FSCK model, but the

results are shifted vertically towards higher values for the wall-incident radiative heat flux. The gray formulation of the WSGG shows an additional vertical shift and exceeds the measured data. The fastest way to calculate the radiative properties in the CFD simulation is by using the WSGG model in its gray formulation. In comparison to the gray formulation, the WSGG where the RTE is solved individually for each gray gas requires 3.3 times the computing time and the FSCK model requires 8.1 times the computing time of the gray WSGG. Fig. 8.3 shows the simulation results with the FSCK and WSGG model for the NGAR case. The FSCK model shows a good approximation of the experimental data. Both the gray and the non-gray WSGG model show non-plausible results for the NGAR case. The WSGG parameters for oxyfuel do not seem to be suitable for application to air combustion. The FSCK model is used here unchanged as for the NG28 case. It is therefore universally applicable as long as the look-up table contains the necessary species concentrations, pressures and temperatures.

Fig. 8.4 shows the results for the temperature fields of the simulation case NGAR and case NG28 in the upper cross-section of the combustion chamber.
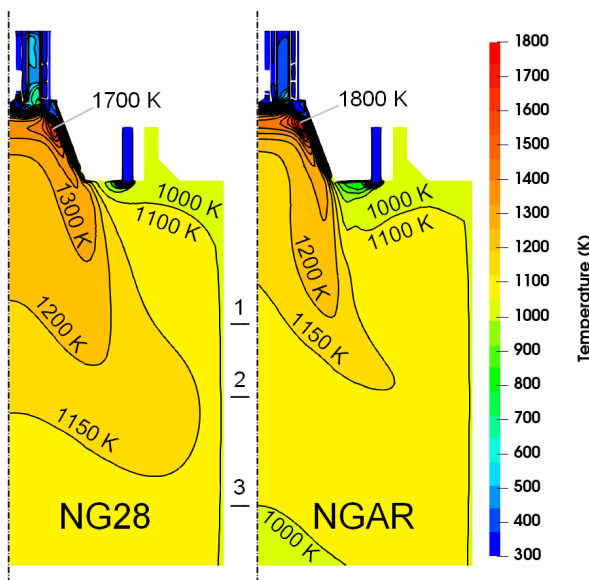
Fig. 8.4 Cross-section of the temperature field inside the combustion chamber. Left: temperature field of the NG28 case. Right: temperature field of the NGAR case. The first 3 measurement levels are marked.
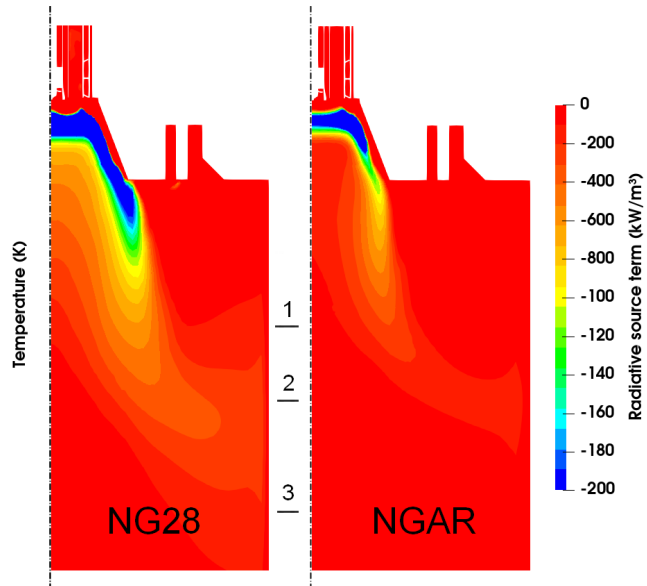
Fig. 8.5 Cross-section of the radiative source term distribution inside the combustion chamber. Left: radiative source term distribution of the NG28 case. Right: radiative source term distribution of the NGAR case. The first 3 measurement levels are marked.

As already discussed in Chapter 7, it is presumed that an earlier ignition of the NG occurs under oxyfuel conditions and therefore a higher heat release locally arises near the quarl. This assumption is based on the significantly higher wall-incident radiative heat flux measured in the upper part of the combustion chamber during oxyfuel combustion. The simulation, on the other hand, shows a higher local temperature for NG-air firing near the burner. In the NGAR case, the fuel-oxidant mixture therefore ignites earlier than in the oxyfuel case and releases its heat predominantly within the quarl, in which no radiation can be measured. The heat release

along the combustion chamber axis therefore decreases faster than in the oxyfuel combustion and lower temperatures are localized at the height of the measuring ports than in the oxyfuel case. The reason for the higher measured wall-incident radiative heat flux at NG28 could therefore be a delayed ignition and the region of highest heat release is at the height of the measuring ports.

Fig. 8.5 compares the radiative source term in the combustion chamber for NG28 and NGAR. The contour is scaled so that the thermal radiation emitted by the cells is clearly visible. It can be seen that the radiation source term for NGAR is concentrated in a small region within the quarl, while in the case of NG28 the radiative source term extends further into the combustion chamber along the combustion chamber axis. This could explain why higher wall-incident radiative heat flux are measured at the upper ports in the case of NG28 than in the case of NGAR.

Fig. 8.6 shows the temperature plotted against the mixture fraction of NG-oxyfuel firing with an oxygen concentration of 28 vol% in the oxidant and for the combustion with air in Fig. 8.7. The adiabatic flame temperature is shown simplified as a straight black line.
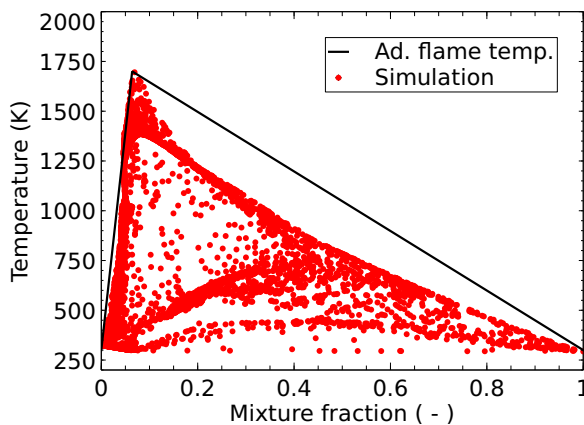
Fig. 8.6 Temperature scatter plot of NG-oxyfuel (NG28) combustion against mixture fraction. Adiabatic flame temperature drawn as black solid line.
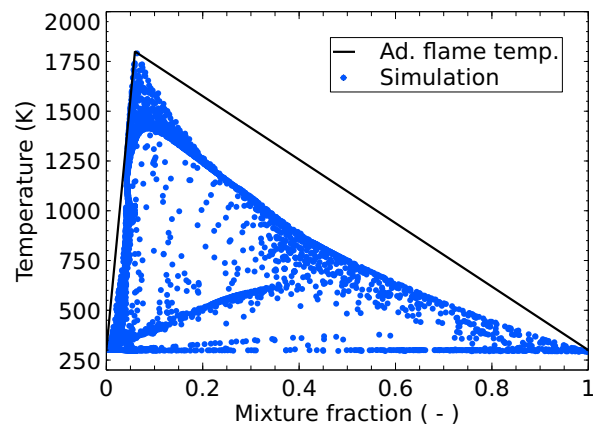
Fig. 8.7 Temperature scatter plot of NG-air (NGAR) combustion against mixture fraction. Adiabatic flame temperature drawn as black solid line.

It can also be seen from the mixture fraction diagrams that higher temperatures occur in the case of air-firing than for oxyfuel combustion. Below 750 K, a cloud of dots can be recognized that is clearly below the black curve, around which the majority of the dots accumulate. This area of localized flame extinction is much more pronounced for the oxyfuel case than for NG-air combustion. The deviations from the adiabatic flame temperature due to limitations in turbulent mixing are quite similar for the NG-air and NG-oxyfuel firing.

The EDC model from Chapter 4 and the equations described at the beginning of this chapter were used for turbulent combustion in the gas phase. As already described, this modeling is still subject to uncertainties, which is why it is recommended to evaluate this investigation in a future study with more complex models that are adapted to oxyfuel combustion.

9 Conclusions

In this work, a laboratory oxyfuel burner was scaled up to $500\,\mathrm{kW_{th}}$ and investigated in a semi-industrial combustion chamber with water-cooled membrane walls similar to commercial plants. Pulverized biomass was burned in an air and oxyfuel atmosphere to investigate the flame stability, radiative heat transfer, carbon monoxide and nitrogen monoxide emissions. In addition, the results of the radiative heat flux measurements were used to validate a customized CFD code including promising gas radiation models. Several studies on the combustion of coal and the co-firing of biomass in an oxyfuel atmosphere exist. So far, less attention has been paid to the combustion of pure pulverized biomass in an oxyfuel atmosphere and its application to industrial systems. For this reason, the scaling of an oxyfuel laboratory burner to a semi-industrial scale and the combustion of biomass was investigated in this thesis. The results are summarized and an outlook is given in the following paragraphs.

The FSCK radiation model is currently one of the most promising global models for the calculation of thermal radiation in combustion chambers regarding accuracy and calculation time. There are only a few studies on the applicability of the FSCK model in CFD. In most cases, the radiation source term is calculated separately to the reactive flow simulations, or only simple laboratory flames are considered [5, 96, 210]. Here, the FSCK and WSGG model are implemented, verified and tested in the open-source code OpenFOAM® for reactive flows. The WSGG was implemented and tested here to compare both global models for oxyfuel combustion.

The application of these models to a virtual oxyfuel boiler and a virtual oxyfuel flame shows that the FSCK model has the smallest deviations from the benchmark solution regarding the total radiative heat flux and the radiative source term. The WSGG using oxyfuel parameters also produce acceptable results. Applying the CFD code, including the radiation models, to an experimental investigated case in this work with an oxyfuel natural gas flame, the FSCK model yields results for the wall-incident radiative heat flux that are in the average range of the experimental data. The WSGG model yields values that are slightly higher than the FSCK model results. A pronounced peak that can be seen in the measurement data cannot be reproduced by both models. However, it is unclear whether this is due to the radiation models or the combustion model, which may predicts an insufficient local heat release. In terms of computing time, the WSGG is currently more beneficial for use in CFD simulations. The FSCK can be used for oxyfuel and air-firing, whereas different parameter sets are required for the WSGG.

In order to investigate scaling effects with focus on thermal radiation, a laboratory oxyfuel burner was scaled up to $500\,\mathrm{kW_{th}}$. Numerous correlations exist in the literature for the scaling of industrial burners, although these correlations assume that there are no geometric restrictions [159, 160]. To overcome these restrictions, a new approach was developed for up-scaling

of an oxyfuel burner with the aid of numerical simulation and the introduction of dimensionless parameters. The focus was on a comparable recirculation zone near the burner, which provides a significant contribution to flame stabilization of the flame. A similarity between the laboratory and semi-industrial burner was achieved through a numerical parameter study with the objective of obtaining identical dimensionless parameters. The results from the burner up-scaling were used as a basis for the construction of a semi-industrial oxyfuel burner. Furthermore, major modifications were made to the existing air-fired combustion system to enable oxyfuel operation with the semi-industrial plant.

The flame stability of biomass and lignite was investigated in a semi-industrial combustion chamber under oxyfuel conditions. The effect of thermal power, oxygen content in the oxidant, equivalence ratio, swirl number and pollutant emissions, which have an impact on the flame stability were analyzed. Investigations of the flame stability in oxyfuel combustion using different methods exist in the literature [154, 203]. However, an exact definition of flame stability cannot be specified for semi-industrial oxyfuel combustion from these studies. In this work, the flame stability for biomass and lignite under oxyfuel conditions was determined using qualitative and quantitative methods.

It is assumed that a high primary flow penetrates the IRZ and therefore no type II flame is formed. Similarly, at reduced thermal power where only a low volume flow is required for the oxidation of the fuel, this results in a minor momentum ratio between secondary flow and primary flow, which in turn leads to an extinction of the IRZ. The same effect occurs if the oxygen enrichment in the oxidant is too high. Lower volume flows are necessary for high O_2 concentrations, which in turn leads to less secondary momentum. However, it was also shown that the biomass requires relatively high oxygen concentrations in the oxidant in order to keep CO emissions in a moderate range compared to the lignite. Even with a low oxygen content in the oxidant, the lignite shows significantly less CO emissions than biomass. It is assumed that this is due to the higher proportion of fine particles, which improves the ignition of the lignite. Biomass, on the other hand, has a relatively high amount of large particles. In summary, oxyfuel firing in the semi-industrial combustion chamber requires a sufficiently high momentum ratio between secondary and primary flow for pulverized solid fuels in order to form a strong IRZ and transport of particles. Natural gas exhibits stable properties and low emissions for all conditions.

Compared to conventional air-firing, the radiative heat transfer in the combustion chamber changes under oxyfuel conditions due to the high amount of strongly absorbing gases. Investigations have been carried out by different authors on oxyfuel firing with coal and biomass co-firing, although most of the investigations were done in laboratory combustion chambers or refractory-lined chambers [153, 204, 206]. To approach industrial conditions and to investigate the radiation characteristics of pure biomass, the radiative heat flux was measured in the semi-industrial combustion chamber which has water-cooled walls.

The wall-incident radiative heat flux differs only slightly for the biomass at different oxygen enrichment in the oxidant. The highest values for the radiative heat flux are achieved at the highest O_2 enrichment and the lowest radiative heat flux at the lowest enrichment. By decreasing the secondary to tertiary volume flow ratio and thus the strength of the IRZ, the measured thermal radiation is significantly reduced for both air-firing and oxyfuel combustion. This indicates a lower heat release due to poor mixing of oxidizer and fuel, which is also reflected in the CO emissions previous mentioned. Lignite shows the highest incident radiative heat flux for air combustion. This could be due to endothermic Boudouard-reactions in the oxyfuel atmosphere, which reduce the temperature and thus the radiative heat transfer. Using an O_2 content of 30 vol% in the oxidant for oxy-firing, radiative heat fluxes were achieved that come close to those of air-firing with lignite. A comparison of the incident radiative heat flux of lignite and biomass shows that the results for biomass are significantly higher. It is assumed that the high volatile content in the biomass results in a higher heat release rate in the upper section of the combustion chamber, where the measurements are taken. The investigation of a natural gas flame in an oxyfuel and air atmosphere results in significantly higher incident radiative heat fluxes at the first two measuring ports, near the quarl, for oxyfuel combustion. At higher distances to the quarl, the measurements overlap for all investigated conditions. It is assumed that the reactions take place faster due to the high oxygen content in oxyfuel combustion and therefore a strong heat release near the quarl. A CFD simulation of this case, on the other hand, shows that the highest heat release during air combustion already takes place inside the quarl and therefore less heat is released outside the quarl. The comparison of the incident radiative heat flux between the reference laboratory combustion chamber and the up-scaled semi-industrial combustion chamber for lignite shows that in relative terms the difference between the radiative heat flux under air and oxyfuel conditions is similar for both combustion chambers.

Further research issues for future studies can be derived from the results of this work:

- Depending on the burner's secondary velocity and the fuel particle sizes, the particles are able to follow the streamlines or penetrate the IRZ. Therefore, it is advisable to take the particle size distribution into account during the burner scaling process.

- Flame stability can also be determined using optical methods. Measuring ports are installed on the combustion chamber for this purpose. In future studies, the flame stability from this work can be compared with results from optical measurements.

- A more precise investigation can be carried out to determine whether the relatively high radiative heat flux of biomass is caused by the higher particle mass flow or by the higher volatile content.

- Measurements of soot concentrations, temperature fields and species concentration fields inside the semi-industrial combustion chamber during biomass combustion under oxyfuel

conditions to validate CFD models. In addition, this measurement data can also be used to validate a radiation model more precisely.

Bibliography

[1] United Nations Framework Convention on Climate Change. *Paris Agreement*. United Nations. 2015.

[2] International Energy Agency. *World Energy Outlook 2019*. 2019.

[3] Bundesministerium für Wirtschaft und Klimaschutz. *EnArgus, Energieforschung*. https://www.enargus.de/. ↗ (Accessed: 2022-04-10).

[4] B. S. Rodriguez, P. Drummond, and P. Ekins. "Decarbonizing the EU Energy System by 2050: an Important Role for BECCS". In: *Climate Policy* 17.sup1 (2017), S93–S110. doi

[5] V. Kez. "Modelling of Radiative Heat Transfer in Oxy-Fuel Combustion Scenarios". PhD thesis. Technischen Universität Darmstadt, 2022.

[6] L. Chen, S. Z. Yong, and A. F. Ghoniem. "Oxy-Fuel Combustion of Pulverized Coal: Characterization, Fundamentals, Stabilization and CFD Modeling". In: *Progress in Energy and Combustion Science* 38.2 (2012), pp. 156–214. doi

[7] D. Toporov. *Combustion of Pulverised Coal in a Mixture of Oxygen and Recycled Flue Gas*. 1st ed. Waltham, London: Elsevier, 2014.

[8] D. Adams and J. Davison. *Capturing CO_2*. Tech. rep. International Energy Agency Greenhouse Gas R&D Programme, 2007.

[9] A. M. Bukar and M. Asif. "Technology Readiness Level Assessment of Carbon Capture and Storage Technologies". In: *Renewable and Sustainable Energy Reviews* 200 (2024), p. 114578. doi

[10] L. Strömberg et al. "Update on Vattenfall's 30 MW_{th} Oxyfuel Pilot Plant in Schwarze Pumpe". In: *Energy Procedia* 1.1 (2009), pp. 581–589. doi

[11] J. Guo et al. "Oxy-Fuel Combustion Characteristics of Pulverized Coal in a 3 MW Pilot-Scale Furnace". In: *Energy & Fuels* 32.10 (2018), pp. 10522–10529. doi

[12] Thyssenkrupp AG. *Startschuss für den Bau eines der ersten CO_2-neutralen Zementwerke weltweit – Thyssenkrupp liefert innovative „pure oxyfuel"-Technologie und ermöglicht CO_2-Abscheidung*. https://www.thyssenkrupp.com/. ↗ (Accessed: 2024-06-17).

[13] J. L. J. Ling, W. Yang, H. S. Park, H. E. Lee, and S. H. Lee. "A Comparative Review on Advanced Biomass Oxygen Fuel Combustion Technologies for Carbon Capture and Storage". In: *Energy* 284 (2023), p. 128566. doi

[14] H. Schneider et al. "Combined Flow, Temperature and Soot Investigation in Oxy-Fuel Biomass Combustion Under Varying Oxygen Concentrations Using Laser-Optical Diagnostics". In: *Fuel* 362 (2024), p. 130771. doi

[15]   B. Özer, D. Zabrodiec, R. Kneer, and A. Maßmeyer. "Experimental Investigation of 40 kW$_{th}$ Methane-Assisted and Self-Sustained Pulverized Biomass Flames". In: *Proceedings of the Combustion Institute* 39.3 (2023), pp. 3343–3351. **doi**

[16]   A. Kather and G. Scheffknecht. "The Oxycoal Process With Cryogenic Oxygen Supply". In: *Naturwissenschaften* 96 (2009), pp. 993–1010. **doi**

[17]   D. Toporov, M. Förster, and R. Kneer. "Combustion of Pulverized Fuel under Oxycoal Conditions at Low Oxygen Concentrations". In: *Third International Conference on Clean Coal Technologies for our Future*. Cagliari, Sardinia, Italy, May 2007.

[18]   F. Kluger, P. Mönckert, B. Krohmer, G. Stamatelopoulos, J. Jacoby, and U. Burchhardt. "Oxyfuel Pulverised Coal Steam Generator Development 30 MW$_{th}$ Pilot Steam Generator Commissioning and Testing". In: *First IEAGHG International Oxyfuel Combustion Conference, Cottbus, Germnay*. 2009.

[19]   H. Martin. *VDI-Wärmeatlas: Berechnungsblätter für den Wärmeübergang*. 9th ed. Berlin, Heidelberg: Springer Verlag, 2002. **doi**

[20]   F. Joos. *Technische Verbrennung*. Verbrennungstechnik, Verbrennungsmodellierung, Emissionen. 1st ed. Berlin, Heidelberg: Springer Verlag, 2006.

[21]   E. Laurien and H. Oertel. *Numerische Strömungsmechanik*. 5th ed. Wiesbaden: Springer Vieweg, 2013.

[22]   C. Akan. "Surface Mass Transfer in Large Eddy Simulation (LES) of Langmuir Turbulence". PhD thesis. University of South Florida, 2012.

[23]   A. Rasheed. "Turbulence Modeling: Large Eddy Simulation". In: *Web* (May 2011).

[24]   H. Pitsch. *Combustion Theory*. CEFRC Combustion Summer school, Princeton, 2014.

[25]   J. Warnatz, U. Maas, and R. W. Dibble. *Verbrennung*. 3rd ed. Berlin Heidelberg: Springer Verlag, 2001.

[26]   H. C. Hottel and W. R. Hawthorne. "Diffusion in Laminar Flame Jets". In: *Symposium on Combustion and Flame, and Explosion Phenomena*. Vol. 3. 1. Elsevier, pp. 254–266.

[27]   G. Damköhler. "Der Einfluss der Turbulenz auf die Flammengeschwindigkeit in Gasgemischen". In: *Zeitschrift für Elektrochemie und angewandte physikalische Chemie* 46.11 (1940), pp. 601–626. **doi**

[28]   V. Zimont and A. N. Lipatnikov. "A Numerical Model of Premixed Turbulent Combustion of Gases". In: 14 (Jan. 1995), pp. 993–1025.

[29]   D. Bradley, A. K. C. Lau, M. Lawes, and F. T. Smith. "Flame Stretch Rate as a Determinant of Turbulent Burning Velocity". In: *Philosophical Transactions of the Royal Society of London. series A: Physical and Engineering Sciences* 338.1650 (1992), pp. 359–387. **doi**

[30] M. Metghalchi and J. C. Keck. "Burning Velocities of Mixtures of Air With Methanol, Isooctane, and Indolene at High Pressure and Temperature". In: *Combustion and Flame* 48 (1982), pp. 191–210. 🔵

[31] R. Borghi. "On the Structure and Morphology of Turbulent Premixed Flames". In: *Recent Advances in the Aerospace Sciences: In Honor of Luigi Crocco on His Seventy-fifth Birthday*. Ed. by C. Casci and C. Bruno. Boston, MA: Springer US, 1985, pp. 117–138. 🔵

[32] S. Marinov. "Untersuchung der Flammenstabilität von geometrisch ähnlichen Brennern für zukünftige magere Triebwerksbrennkammerkonzepte". PhD thesis. Karlsruher Instituts für Technologie, 2013. 🔵

[33] N. Peters. *Combustion Theory*. CEFRC Combustion Summer school, Princeton, 2010.

[34] S. P. Burke and T. E. W. Schumann. "Diffusion Flames". In: *Industrial & Engineering Chemistry* 20.10 (1928), pp. 998–1004. 🔵

[35] R. H. Essenhigh, M. K. Misra, and D. W. Shaw. "Ignition of Coal Particles: a Review". In: *Combustion and Flame* 77.1 (1989), pp. 3–30. 🔵

[36] E. M. Suuberg, W. A. Peters, and J. B. Howard. "Product Compositions and Formation Kinetics in Rapid Pyrolysis of Pulverized Coal—Implications for Combustion". In: *Symposium (International) on Combustion* 17.1 (1979). Seventeenth Symposium (International) on Combustion, pp. 117–130. 🔵

[37] K. Görner. *Technische Verbrennungssysteme*. Grundlagen, Modellbildung, Simulation. 1st ed. Berlin, Heidelberg: Springer Verlag, 1991. 🔵

[38] R. Schneider. "Beitrag zur numerischen Berechnung dreidimensional reagierender Strömungen in industriellen Brennkammern". PhD thesis. Universität Stuttgart, 1998.

[39] C. Hasse, P. Debiagi, X. Wen, K. Hildebrandt, M. Vascellari, and T. Faravelli. "Advanced Modeling Approaches for CFD Simulations of Coal Combustion and Gasification". In: *Progress in Energy and Combustion Science* 86 (2021), p. 100938.

[40] K. L. Smith, L. D. Smoot, T. H. Fletcher, and R. J. Pugmire. *The Structure and Reaction Processes of Coal*. The Plenum Chemical Engineering series. Springer US, 2013.

[41] R. Günther. *Verbrennung und Feuerungen*. Berlin, Heidelberg: Springer Verlag, 1974.

[42] M. A. Hassan, M. A. Ismail, and F. C. Lockwood. "Pulverized-Coal Flame Stability: Effect of the Burner Quarl Cooling". In: *Chemical Engineering Science* 46.10 (1991), pp. 2543–2550. 🔵

[43] C. Schmid, R. Weber, and P. A. Roberts. *Interaction Between Primary Air Jets and Swirl Generated Vortices*. Tech. rep. Doc. No. K70/a/2. International Flame Research Foundation, IJmuiden, Netherlands, 1987.

[44] R. Weber, J. Dugué, and H. Horsman. *The Effect of Combustion on Swirling Expanding Flows: Results of the NFA 3-1 Investigations*. Tech. rep. Doc. No. F59/a/6. International Flame Research Foundation, IJmuiden, Netherlands, 1989.

[45] D. Zabrodiec. "Experimental Characterization of Turbulent Particle Laden Reactive Flows under Air and Oxy-Fuel Conditions". PhD thesis. RWTH Aachen University, 2021. 🔘

[46] K. Strauß. *Kraftwerkstechnik*. 6th ed. Berlin, Heidelberg: Springer Verlag, 2009.

[47] H. Effenberger. *Dampferzeugung*. 1st ed. Berlin, Heidelberg, New York: Springer Verlag, 2000.

[48] M. F. Modest. *Radiative Heat Transfer*. 3rd ed. New York, San Francisco, London: Academic Press, 2013.

[49] D. K. Edwards. "Molecular Gas Band Radiation". In: *Numerical Heat Transfer, Part B: Fundamentals* 12 (1976), pp. 115–193. 🔘

[50] J. Ströhle. "Spectral Modelling of Radiative Heat Transfer in Industrial Furnaces". PhD thesis. Universität Stuttgart, 2003.

[51] K. Spindler. *Thermophysikalische Stoffeigenschaften (Thermodynamik III)*. Lecture script. Universität Stuttgart, Institut für Thermodynamik und Wärmetechnik, 2016.

[52] C. L. Tien. "Thermal Radiation Properties of Gases". In: *Advances in Heat Transfer*. Ed. by T. F. Irvine and J. P. Hartnett. Vol. 5. Elsevier, 1969, pp. 253–324. 🔘

[53] M. F. Modest. "Narrow-Band and Full-Spectrum k-Distributions for Radiative Heat Transfer-Correlated-k vs. Scaling Approximation". In: *Journal of Quantitative Spectroscopy and Radiative Transfer* 76 (2003), pp. 69–83. 🔘

[54] C. L. Tien and B. L. Drolen. "Thermal Radiation in Particulate Media With Dependent and Independent Scattering". In: *Annual Review of Numerical Fluid Mechanics and Heat Transfer*. Vol. 1. Washington DC: Hemisphere Publishing Corp., 1987, pp. 1–32. 🔘

[55] G. Mie. "Beiträge zur Optik trüber Medien, speziell kolloidaler Metallösungen". In: *Annalen der Physik* 330 (1908), pp. 377–445. 🔘

[56] L. Rayleigh. "On the Light from the Sky, its Polarization and Colour". In: *Philosophical Magazine* 41 (1871), pp. 107–120, 274–279.

[57] Institut für Verbrennungstechnik (DLR). *Ruß*. https://www.dlr.de/vt/. ↗ (Accessed: 2022-03-30).

[58] A. F. Sarofim and H. C. Hottel. "Radiative Transfer in Combustion Chambers: Influence of Alternative Fuels". In: *International Heat Transfer Conference* 6 (1978), pp. 199–217. 🔘

[59] M. Kunugi and H. Jinno. "Determination of Size and Concentration of Soot Particles in Diffusion Flames by a Light-Scattering Technique". In: *Symposium (International) on Combustion* 11 (1967), pp. 257–266. doi

[60] T. Sato, T. Kunitomo, S. Yoshii, and T. Hashimoto. "On the Monochromatic Distribution of the Radiation from the Luminous Flame". In: *Bulletin of Japan Society of Mechanical Engineers* 12 (1969), pp. 1135–1143. doi

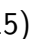[61] R. Wu, F. Xie, J. Wei, X. Song, H. Yang, P. Lv, and G. Yu. "Study on Soot Emission Characteristics of Methane/Oxygen Inverse Diffusion Flame". In: *ACS Omega* 6.36 (2021), pp. 23191–23202. doi

[62] V. Kez, J. L. Consalvi, F. Liu, J. Ströhle, and B. Epple. "Assessment of Several Gas Radiation Models for Radiative Heat Transfer Calculations in a Three-Dimensional Oxy-Fuel Furnace Under Coal-Fired Conditions". In: *International journal of Thermal Sciences* 120 (2017), pp. 289–302. doi

[63] A. Mbiock and R. Weber. *Radiation in Enclosures*. 1st ed. Berlin Heidelberg: Springer Verlag, 2000.

[64] J. Y. Murthy and S. R. Mathur. "Radiative Heat Transfer in Axisymmetric Geometries using an Unstructured Finite-Volume Method". In: *Numerical Heat Transfer, Part B: Fundamentals* 33 (1998), pp. 397–416. doi

[65] B. G. Carlson and K. D. Lathrop. "Transport Theory - The Method of Discrete Ordinates". In: *Computing Methods in Rector Physics*. Los Alamos, N.M.: Los Alamos Scientific Laboratory of the University of California, 1965.

[66] D. M. Christ. "The Effect of Char Kinetics on the Combustion of Pulverized Coal under Oxyfuel Conditions". PhD thesis. RWTH Aachen, 2013. doi

[67] B. Epple, R. Leithner, W. Linzer, and H. Walter. *Simulation von Kraftwerken und Feuerungen*. 2nd ed. Wien: Springer Verlag, 2012.

[68] Merced University of California. *Radiative Heat Transfer*. https://me.ucmerced.edu/. (Accessed: 2022-03-15).

[69] R. E. Marshak. "Note on the Spherical Harmonic Method as Applied to the Milne Problem for a Sphere". In: *Physical Review* 71 (1947), pp. 443–446. doi

[70] *ANSYS Fluent Theory Guide*. Canonsburg, 2013.

[71] H. C. Hottel and A. F. Sarofim. *Radiative Transfer*. 1st ed. New York: McGraw-Hill, 1967.

[72] V. Kez, F. Liu, J. L. Consalvi, J. Ströhle, and B. Epple. "A Comprehensive Evaluation of Different Radiation Models in a Gas Turbine Combustor Under Conditions of Oxy-Fuel Combustion With Dry Recycle". In: *Journal of Quantitative Spectroscopy and Radiative Transfer* 172 (2016), pp. 121–133. doi

[73] M. H. Bordbar, G. Węcel, and T. Hyppänen. "A Line by Line Based Weighted Sum of Gray Gases Model for Inhomogeneous $CO_2 - H_2O$ Mixture in Oxy-Fired Combustion". In: *Combustion and Flame* 161 (2014), pp. 2435–2445. doi

[74] T. Kangwanpongpan, F. H. R. França, R. Corrêa da Silva, P. Smith Schneider, and H. J. Krautz. "New Correlations for the Weighted-Sum-of-Gray-Gases Model in Oxy-Fuel Conditions Based on HITEMP 2010 Database". In: *International journal of Heat and Mass Transfer* 55 (2012), pp. 7419–7433. doi

[75] Y. Liu, G. Liu, F. Liu, and J. Consalvi. "Effects of the k-Calue Solution Schemes on Radiation Heat Transfer Modelling in Oxy-Fuel Flames Using the Full-Spectrum Correlated k-Distribution Method". In: *Applied Thermal Engineering* 170 (2020), p. 114986. doi

[76] M. F. Modest and H. Zhang. "The Full-Spectrum Correlated-k Distribution for Thermal Radiation From Molecular Gas-Particulate Mixtures". In: *Journal of Heat Transfer* 124 (2002), pp. 30–38. doi

[77] J. Cai and M. F. Modest. "Improved Full-Spectrum k-Distribution Implementation for Inhomogeneous Media Using a Narrow-Band Database". In: *Journal of Quantitative Spectroscopy and Radiative Transfer* 141 (2014), pp. 65–72. doi

[78] S. Leiser. "Numerical Simulation of Oxy-fuel Combustion". PhD thesis. Universität Stuttgart, 2010.

[79] B. Leckner. "Spectral and Total Emissivity of Water Vapor and Carbon Dioxide". In: *Combustion and Flame* 19.1 (1972), pp. 33–48. doi

[80] A. G. Clements, S. Black, J. Szuhánszki, K. Stęchły, A. Pranzitelli, W. Nimmo, and M. Pourkashanian. "LES and RANS of Air and Oxy-Coal Combustion in a Pilot-Scale Facility: Predictions of Radiative Heat Transfer". In: *Fuel* 151 (2015). The 10th European Conference on Coal Research and its Applications, pp. 146–155. doi

[81] L. S. Rothman et al. "The HITRAN 2004 Molecular Spectroscopic Database". In: *Journal of Quantitative Spectroscopy and Radiative Transfer* 96 (2005), pp. 139–204. doi

[82] L. S. Rothman et al. "The HITRAN2012 Molecular Spectroscopic Database". In: *Journal of Quantitative Spectroscopy and Radiative Transfer* 130 (2013), pp. 4–50. doi

[83] P. De Bièvre and Gallet M. "Isotopic Abundances and Atomic Weights of the Elements". In: *Journal of Physical and Chemical Reference Data* 13 (1984), pp. 809–891. doi

[84] M. Šimečková, D. Jacquemart, L. S. Rothman, R. R. Gamache, and A. Goldman. "Einstein A-Coefficients and Statistical Weights for Molecular Absorption Transitions in the HITRAN Database". In: *Journal of Quantitative Spectroscopy and Radiative Transfer* 98 (2006), pp. 130–155. doi

[85]   J. Tennyson et al. "Recommended Isolated-Line Profile for Representing High-Resolution Spectroscopic Transitions (IUPAC Technical Report)". In: *Pure and Applied Chemistry* 86 (2014), pp. 1931–1943. doi

[86]   N. H. Ngo, D. Lisak, H. Tran, and J. M. Hartmann. "An Isolated Line-Shape Model to go Beyond the Voigt Profile in Spectroscopic Databases and Radiative Transfer Codes". In: *Journal of Quantitative Spectroscopy and Radiative Transfer* 129 (2013), pp. 89–100. doi

[87]   L. S. Rothman et al. "HITEMP, the High-Temperature Molecular Spectroscopic Database". In: *Journal of Quantitative Spectroscopy and Radiative Transfer* 111 (2010), pp. 2139–2150. doi

[88]   P. Riviére and A. Soufiani. "Updated Band Model Parameters for H_2O, CO_2, CH_4 and CO Radiation at High Temperature". In: *International journal of Heat and Mass Transfer* 55 (2012), pp. 3349–3358. doi

[89]   G. Herzberg. *Molecular Spectra and Molecular Structure.* Vol. II: Infrared and Raman Spectra of Polyatomic Molecules. New Jersey: Van Nostrand, Princeton, 1945.

[90]   C. L. Tien and J. H. Lienhard. *Statistical Thermodynamics.* 1st ed. USA: CRC Press, 1979.

[91]   P. Rivière, A. Soufiani, and J. Taine. "Correlated-k and Fictitious Gas Methods for H_2O near 2.7 μm". In: *Journal of Quantitative Spectroscopy and Radiative Transfer* 48.2 (1992), pp. 187–203. doi

[92]   A. Soufiani and J. Taine. "High Temperature Gas Radiative Property Parameters of Statistical Narrow-Band Model for H_2O, CO_2 and CO, and Correlated-k Model for H_2O and CO_2". In: *International journal of Heat and Mass Transfer* 40.4 (1997), pp. 987–991. doi

[93]   A. Wang and M. F. Modest. "High-Accuracy, Compact Database of Narrow-Band k-Distributions for Water Vapor and Carbon Dioxide". In: *Journal of Quantitative Spectroscopy and Radiative Transfer* 93 (2005), pp. 245–261. doi

[94]   M. F. Modest and R. J. Riazzi. "Assembly of Full-Spectrum k-Distributions From a Narrow-Band Database; Effects of Mixing Gases, Gases and Nongray Absorbing Particles, and Mixtures With Nongray Scatterers in Nongray Enclosures". In: *Journal of Quantitative Spectroscopy and Radiative Transfer* 90 (2005), pp. 169–189. doi

[95]   H. Zhang and M. F. Modest. "Full-Spectrum k-Distribution Correlations for Carbon Dioxide Mixtures". In: *Journal of Thermophysics and Heat Transfer* 17 (2003), pp. 259–263. doi

[96] C. Wang, W. Ge, M. F. Modest, and B. He. "A Full-Spectrum k-Distribution Look-up Table for Radiative Transfer in Nonhomogeneous Gaseous Media". In: *Journal of Quantitative Spectroscopy and Radiative Transfer* 168 (2016), pp. 46–56. **doi**

[97] Y. Zhou, C. Wang, and T. Ren. "A Machine Learning Based Efficient and Compact Full-Spectrum Correlated k-Distribution Model". In: *Journal of Quantitative Spectroscopy and Radiative Transfer* 254 (2020), p. 107199. **doi**

[98] C. Wang, B. He, M. F. Modest, and T. Ren. "Efficient Full-Spectrum Correlated-k-Distribution Look-up Table". In: *Journal of Quantitative Spectroscopy and Radiative Transfer* 219 (2018), pp. 108–116. **doi**

[99] K. Levenberg. "A Method for the Solution of Certain Non-Linear Problems in Least Squares". In: *Quarterly of Applied Mathematics* 2 (1944), pp. 164–68. **doi**

[100] D. W. Marquardt. "An Algorithm for Least-Squares Estimation of Nonlinear Parameters." In: *Society for Industrial and Applied Mathematics* 11 (1963), pp. 431–41. **doi**

[101] H. D. Baehr and K. Stephan. *Wärme- und Stoffübertragung*. 3rd ed. Berlin Heidelberg New York: Springer Verlag, 1998.

[102] C. Wang, M. F. Modest, and B. He. "Full-Spectrum k-Distribution Look-up Table for Nonhomogeneous Gas-Soot Mixtures". In: *Journal of Quantitative Spectroscopy and Radiative Transfer* 176 (2016), pp. 129–136. **doi**

[103] P. J. Davis and P. Rabinowitz. *Methods of Numerical Integration*. 2nd ed. Orlando: Academic Press Inc, 1984.

[104] R. Porter, F. Liu, M. Pourkashanian, A. Williams, and D. Smith. "Evaluation of Solution Methods for Radiative Heat Transfer in Gaseous Oxy-Fuel Combustion Environments". In: *Journal of Quantitative Spectroscopy and Radiative Transfer* 111 (2010), pp. 2084–2094. **doi**

[105] J. Ströhle, B. Epple, and M. Orth. "Spectral Modelling of Radiative Heat Transfer in Oxy-Coal Combustion". In: *1st Oxyfuel Combustion Conference*. Cottbus, Germany, 2009.

[106] H. Chang and T. T. Charalampopoulos. "Determination of the Wavelength Dependence of Refractive Indices of Flame Soot". In: *Proceedings of the Royal Society A* 430 (1990), pp. 577–591. **doi**

[107] J. M. Beer, N. Afgan, and International Center for Heat and Mass Transfer. *Heat Transfer in Flames*. Washington DC: Scripta Book Company, 1974.

[108] S. J. Brookes and J. B. Moss. "Predictions of Soot and Thermal Tadiation Properties in Confined Turbulent Jet Diffusion Flames". In: *Combustion and Flame* 116 (1999), pp. 486–503. **doi**

[109]   OpenFOAM. *OpenFOAM 2.3.0: Physical Modelling*. https://openfoam.org/release/2-3-0/physical-modelling/. ☑ (Accessed: 2024-01-12).

[110]   T. Holzmann. *Mathematics, Numerics, Derivations and OpenFOAM*. ☑ (Accessed: 2018-06-15).

[111]   Wiki OpenFOAM. *The SIMPLE algorithm in OpenFOAM*. https://openfoamwiki.net/. ☑ (Accessed: 2022-03-15).

[112]   W. Sutherland. "LII. The Viscosity of Gases and Molecular Force". In: *The London, Edinburgh, and Dublin Philosophical Magazine and journal of Science* 36.223 (1893), pp. 507–531. ⓓⓞⓘ

[113]   I. Yimer, I. Campbell, and L. Jiang. "Estimation of the Turbulent Schmidt number From Experimental Profiles of Axial Velocity and Concentration for High-Reynolds-Number Jet Flows". In: *Canadian Aeronautics and Space journal* 48 (2002), pp. 195–200. ⓓⓞⓘ

[114]   B. E. Launder, G. J. Reece, and W. Rodi. "Progress in the Development of a Reynolds-Stress Turbulence Closure". In: *Journal of Fluid Mechanics* 68.3 (1975), pp. 537–566. ⓓⓞⓘ

[115]   H. Knaus. "Numerische Simulation von reagierenden turbulenten Zweiphasenströmungen in industriellen Feuerungen mit komplexen Geometrien". PhD thesis. Universität Stuttgart, 2000.

[116]   D. Toporov et al. "Detailed Investigation of a Pulverized Fuel Swirl Flame in CO_2/O_2 Atmosphere". In: *Combustion and Flame* 155 (2008), pp. 605–618. ⓓⓞⓘ

[117]   M. von Bohnstein, M. Richter, P. Graeser, M. Schiemann, J. Ströhle, and B. Epple. "3D CFD Simulation of a 250 MW_{el} Oxy-Fuel Boiler With Evaluation of Heat Radiation Calculation". In: *Renewable and Sustainable Energy Reviews* 137 (2021), p. 110601. ⓓⓞⓘ

[118]   H. Askarizadeh, H. Nicolai, D. Zabrodiec, S. Pielsticker, C. Hasse, R. Kneer, and A. Maßmeyer. "Numerische Untersuchung zur Relevanz von Teilmodellen für Pyrolyse und Koksabbrand in turbulenten drallbehafteten Flammen unter Oxyfuel Bedingungen". In: *Deutscher Flammentag*. Vol. 30. Hannover-Garbsen, Germany, Sept. 2021.

[119]   B. E. Launder and D. B. Spalding. "The Numerical Computation of Turbulent Flows". In: *Computer Methods in Applied Mechanics and Engineering* 3 (1974), pp. 269–289. ⓓⓞⓘ

[120]   S. H. El Tahry. "k-Epsilon Equation for Compressible Reciprocating Engine Flows". In: *Journal of Energy* 7 (1983), pp. 345–353. ⓓⓞⓘ

[121]   L. Davidson. *Fluid Mechanics, Turbulent Flow and Turbulence Modeling*. Department of Mechanics and Maritime Sciences Chalmers University of Technology SE-412 96 Göteborg, Sweden, 2018.

[122] CFD Online. *Turbulence length scale*. https://www.cfd-online.com/Wiki/. ⬀ (Accessed: 2022-03-15).

[123] CFD Online. *Turbulence intensity*. https://www.cfd-online.com/Wiki/. ⬀ (Accessed: 2022-03-15).

[124] OpenFOAM. *Extended Code Guide*. https://www.openfoam.com/. ⬀ (Accessed: 2022-03-15).

[125] API Guide OpenFOAM. *OpenFOAM: API Guide – The open source CFD toolbox*. https://www.openfoam.com/documentation/guides/latest/api/. ⬀ (Accessed: 2024-04-05).

[126] R. Barrett et al. *Templates for the Solution of Linear Systems: Building Blocks for Iterative Methods*. 2nd ed. Philadelphia: SIAM, 1994.

[127] H. A. van der Vorst. "Bi-CGSTAB: A Fast and Smoothly Converging Variant of Bi-CG for the Solution of Nonsymmetric Linear Systems". In: *SIAM journal on Scientific and Statistical Computing* 13.2 (1992), pp. 631–644. ⓓⓞⓘ

[128] R. Kasper. *Particle Simulation with OpenFOAM: Introduction, Fundamentals and Applications*. German OpenFOAM User meeting, Braunschweig, 2017.

[129] O. T. Stein et al. "Towards Comprehensive Coal Combustion Modelling for LES". In: *Flow, Turbulence and Combustion* 90 (2013), pp. 859–884. ⓓⓞⓘ

[130] W. E. Ranz and W. R. Marshall Jr. "Evaporation from Drops, Part I". In: *Chemical Engineering Progress* 48 (1952), pp. 141–146.

[131] W. E. Ranz and W. R. Marshall Jr. "Evaporation from Drops, Part II". In: *Chemical Engineering Progress* 48 (1952), pp. 173–180.

[132] A. D. Gosman and E. Ioannides. "Aspects of Computer Simulation of Liquid-Fueled Combustors". In: *Journal of Energy* 7.6 (1983), pp. 482–490. ⓓⓞⓘ

[133] S. S. Yoon, J. C. Hewson, P. E. DesJardin, D. J. Glaze, A. R. Black, and R. R. Skaggs. "Numerical Modeling and Experimental Measurements of a High Speed Solid-Cone Water Spray for Use in Fire Suppression Applications". In: *International journal of Multiphase Flow* 30 (2004), pp. 1369–1388. ⓓⓞⓘ

[134] CFD Direct. *Thermophysical models*. https://cfd.direct/openfoam/user-guide/thermophysical/. ⬀ (Accessed: 2022-03-15).

[135] H. D. Baehr and Kabelac S. *Thermodynamik*. 16th ed. Berlin Heidelberg: Springer Verlag, 2009.

[136] B. E. Poling, J. M. Prausnitz, and J. P. O'Connell. *The Properties of Gases and Liquids*. 5th ed. New York: McGraw-Hill, 2001.

[137] A. Kronenburg. *Grundlagen technischer Verbrennungsvorgänge (I+II)*. Lecture script. Universität Stuttgart, Institut für Technische Verbrennung, 2016.

[138] S. Badzioch and P. G. W. Hawksley. "Kinetics of Thermal Decomposition of Pulverized Coal Particles". In: *Industrial and Engineering Process Design and Development* 9 (1970), pp. 521–530. 📀

[139] R. J. Hamor, I. W. Smith, and R. J. Tyler. "Kinetics of Combustion of a Pulverized Brown Coal Char between 630 and 2200 °K". In: *Combustion and Flame* 21 (1973), pp. 153–162. 📀

[140] T. H. Fletcher. "Time-Resolved Temperature and Mass Loss Measurements of a Bituminous Coal During Devolatilization". In: *Combustion and Flame* 78 (1989), pp. 223–236. 📀

[141] D. B. Anthony, J. B. Howard, H. C. Hottel, and H. P. Meissner. "Rapid Devolatilization of Pulverized Coal". In: *Symposium (International) on Combustion* 15 (1975), pp. 1303–1317. 📀

[142] M. M. Baum and P. J. Street. "Predicting the Combustion Behaviour of Coal Particles". In: *Combustion Science and Technology* 3 (1971), pp. 231–243. 📀

[143] R. I. Backreedy, R. Habib, J. M. Jones, M. Pourkashanian, and Williams A. "An Extended Coal Combustion Model". In: *Fuel* 78 (1999), pp. 1745–1754. 📀

[144] F. C. Marincola. "Large Eddy Simulation of Coal Combustion". PhD thesis. Imperial College London, 2013.

[145] *ESTOS: Eulerian Simulation Tool for Solid Fuels*. TU Darmstadt, Fachgebiet für Energiesysteme und Energietechnik, 2005.

[146] H. Askarizadeh, M. Koch, H. Nicolai, S. Pielsticker, R. Kneer, C. Hasse, and A. Maßmeyer. "Influence of Gas Radiation, Particle Radiation Interactions, and Conversion-Dependent Particle Radiative Properties on Pulverized Solid Fuel Combustion". In: *Deutscher Flammentag*. Vol. 31. Berlin, Germany, Sept. 2023.

[147] I. R. Gran and B. F. Magnussen. "A Numerical Study of a Bluff-Body Stabilized Diffusion Flame. Part 2. Influence of Combustion Modeling And Finite-Rate Chemistry". In: *Combustion Science and Technology* 119 (1996), pp. 191–217. 📀

[148] B. F. Magnussen and B. H. Hjertager. "On Mathematical Modeling of Turbulent Combustion With Special Emphasis on Soot Formation and Combustion". In: *Symposium (International) on Combustion* 16 (1977), pp. 719–729. 📀

[149] D. Toporov, M. Förster, and R. Kneer. "Development of an Oxycoal Burner for Pulverized Fuel Combustion at low O_2-Concentrations". In: *Advances in Combustion Technology: Improving the Environment and Energy Efficiency American: Japanese Flame Research Committees International Symposium*. Kona, USA, Oct. 2007. 📀

[150]   H. Nicolai, P. Debiagi, X. Wen, L. Dressler, A. Massmeyer, J. Janicka, and C. Hasse. "Flamelet LES of Swirl-Stabilized Oxy-Fuel Flames Using Directly Coupled Multi-Step Solid Fuel Kinetics". In: *Combustion and Flame* 241 (2022), p. 112062. 🔘

[151]   X. Wen, H. Nicolai, P. Debiagi, D. Zabrodiec, A. Maßmeyer, R. Kneer, and C. Hasse. "Flamelet LES of a 40 kW$_{th}$ Pulverized Torrefied Biomass Furnace in Air and Oxy-Fuel Atmospheres". In: *Proceedings of the Combustion Institute* 39.4 (2023), pp. 4563–4572. 🔘

[152]   J. Hees et al. "Detailed Analyzes of Pulverized Coal Swirl Flames in Oxy-Fuel Atmospheres". In: *Combustion and Flame* 172 (2016), pp. 289–301. 🔘

[153]   D. Zabrodiec, A. Massmeyer, J. Hees, O. Hatzfeld, and R. Kneer. "Flow Pattern and Behavior of 40 kW$_{th}$ Pulverized Torrefied Biomass Flames under Atmospheric and Oxy-Fuel Conditions". In: *Renewable and Sustainable Energy Reviews* 138 (2021), p. 110493. 🔘

[154]   L. G. Becker et al. "Experimental Investigation of Flame Stabilization Inside the Quarl of an Oxyfuel Swirl Burner". In: *Fuel* 201 (2017). 1st International Workshop on Oxy-Fuel Combustion, pp. 124–135. 🔘

[155]   A. S. Doost et al. "Residence Time Calculations for Complex Swirling Flow in a Combustion Chamber Using Large-Eddy Simulations". In: *Chemical Engineering Science* 156 (2016), pp. 97–114. 🔘

[156]   H. Nicolai. "Towards Predictive Simulations of Low-Emission Reactive Solid Fuel Systems". PhD thesis. Technischen Universität Darmstadt, 2021.

[157]   S. Trespi, H. Nicolai, P. Debiagi, J. Janicka, A. Dreizler, C. Hasse, and T. Faravelli. "Development and Application of an Efficient Chemical Reactor Network Model for Oxy-fuel Combustion". In: *Energy & Fuels* 35.9 (2021), pp. 7121–7132. 🔘

[158]   L. G. Becker. "Untersuchung von gasassistierten Staubflammen mittels Lasermesstechnik". PhD thesis. Technischen Universität Darmstadt, 2019.

[159]   E. Drubetskoi, S. Eckart, and H. Krause. "Short Overview on Combustion Systems Scale-up With Emphasis on NO$_x$ Emissions of Gas-Fired Furnaces". In: *Energy Science & Engineering* 10.2 (2022), pp. 621–629. 🔘

[160]   R. Weber and M. Mancini. "On Scaling and Mathematical Modelling of Large Scale Industrial Flames". In: *Journal of the Energy Institute* 93.1 (2020), pp. 43–51. 🔘

[161]   W. R. Hawthorne, D. S. Weddell, and H. C. Hottel. "Mixing and Combustion in Turbulent Gas Jets". In: *Symposium on Combustion and Flame, and Explosion Phenomena* 3.1 (1948), pp. 266–288. 🔘

[162]   F. C. Maldonado. "Pilot Testing, Simulation, and Scaling of an Oxyfuel Burner for Cement Kilns". PhD thesis. Universität Stuttgart, 2021. 🔘

[163]   J. P. Smart and D. J. Morgan. "Exploring the Effects of Employing Different Scaling Criteria on Swirl Stabilised Pulverised Coal Burner Performance". In: *Combustion Science and Technology* 100.1-6 (1994), pp. 331–343. (doi)

[164]   Santanu Pramanik and R.V. Ravikrishna. "Investigation of novel scaling criteria on a reverse-flow combustor". In: *Energy* 206 (2020), p. 118156. (doi)

[165]   M. Richter, J. Ströhle, and B. Epple. "Up-Scaling of a Laboratory-Scale Pulverised Oxyfuel Burner to Semi-Industrial-Scale Through a Flow Similarity Approach". In: *Fuel* 371 (2024), p. 131809. (doi)

[166]   P. Heil, D. Toporov, H. Stadler, S. Tschunko, M. Förster, and R. Kneer. "Development of an Oxycoal Swirl Burner Operating at Low O_2 Concentrations". In: *Fuel* 88 (2009), pp. 1269–1274. (doi)

[167]   D. Zabrodiec et al. "Detailed Analysis of the Velocity Fields from 60 kW Swirl-Stabilized Coal Flames in CO_2/O_2- and N_2/O_2-Atmospheres by Means of Laser Doppler Velocimetry and Particle Image Velocimetry". In: *Combustion Science and Technology* 189.10 (2017), pp. 1751–1775. (doi)

[168]   E. Buckingham. "On Physically Similar Systems; Illustrations of the Use of Dimensional Equations". In: *Phys. Rev.* 4 (4 Oct. 1914), pp. 345–376. (doi)

[169]   Y. Tong, S. Chen, M. Li, Z. Li, and J. Klingmann. "Experimental Study on Bluff-Body Stabilized Premixed Flame with a Central Air/Fuel Jet". In: *Energies* 10 (2017). (doi)

[170]   R. Weber, A. N. Sayre, J. Dugué, and H. Horsman. *The Scaling-400 Study, Part II: the 12 MW Test Results*. Tech. rep. Doc. No. GRI-93/0079. GRI, IFRF, Chicago, USA, and IJmuiden, 1993.

[171]   J. F. Driscoll, W. J. A. Dahm, and M. S. Wu. *The Scaling-400 Study, Part III: the 30 kW Test Results*. Tech. rep. Doc. No. GRI-389443-9. GRI, IFRF, Chicago, USA, and IJmuiden, 1993.

[172]   A. Sayre, N. Lallemant, J. Dugué, and Weber R. *The Scaling-400 Study, Part IV: the 300 kW BERL Test Results*. Tech. rep. Doc. No. GRI-94/0186. GRI, IFRF, Chicago, USA, and IJmuiden, 1994.

[173]   M. Bertolo, A. N. Sayre, J. Dugué, and Weber R. *The Scaling-400 Study, Part V: the 4 MW Test Results*. Tech. rep. Doc. No. GRI-94/0187. GRI, IFRF, Chicago, USA, and IJmuiden, 1994.

[174]   A. Sayre. *The Scaling-400 Study, Part VI: the 1.3 MW Test Results*. Tech. rep. Doc. No. F40/y/13. International Flame Research Foundation, IJmuiden, Netherlands, 1995.

[175]   W. J. A. Dahm, J. F. Driscoll, and A. Hsieh. *The Scaling-400 Study, Part VII: the 300 kW Test Results*. Tech. rep. Doc. No. 389443-14. Department of Aerospace Engineering, The University of Michigan, 1995.

[176] P. K. Selvam. "Thermal Mixing Characteristics of Flows in Horizontal T-Junctions". PhD thesis. Universität Stuttgart, 2017. doi

[177] A. Isaev. "Experimentelle und numerische Untersuchung von Strömungsvermischungsvorgängen in einem Rohrleitungs-T-Stück". PhD thesis. Universität Stuttgart, 2021. doi

[178] A. Stroh, F. Alobaid, J. P. Busch, J. Ströhle, and B. Epple. "3-D Numerical Simulation for Co-firing of Torrefied Biomass in a Pulverized-fired $1\,MW_{th}$ Combustion Chamber". In: *Energy* 85 (2015), pp. 105–116. doi

[179] M. Stöllinger, B. Naud, D. Roekaerts, N. Beishuizen, and S. Heinz. "PDF modeling and simulations of pulverized coal combustion – Part 1: Theory and modeling". In: *Combustion and Flame* 160.2 (2013), pp. 384–395. doi

[180] S. P. Domino and P. J. Smith. "State Space Sensitivity to a Prescribed Probability Density Function Shape in Coal Combustion Systems: Joint -PDF Versus Clipped Gaussian PDF". In: *Proceedings of the Combustion Institute* 28.2 (2000), pp. 2329–2336. doi

[181] D. V. Flores and T. H. Fletcher. "The Use of Two Mixture Fractions to Treat Coal Combustion Products in Turbulent Pulverized-Coal Flames". In: *Combustion Science and Technology* 150.1-6 (2000), pp. 1–26. doi

[182] B. S. Brewster, L. L. Baxter, and L. D. Smoot. "Role of Coal Devolatilization in Comprehensive Combustion Models". In: *Prepr. Pap., Am. Chem. Soc., Div. Fuel Chem.; (United States), Vol. 32:3; Conference: 194. American Chemical Society national meeting, New Orleans, LA, USA.* 1987.

[183] Hukseflux Thermal Sensors BV. *Gardon Gauge Water-Cooled High Heat Flux Sensor.* https://www.hukseflux.com/. Accessed: 16-02-2024. 2023.

[184] M. Richter, D. König, J. Ströhle, and B. Epple. "Radiative Heat Flux Measurement in a Semi-Industrial Oxyfuel Combustion Chamber with Biomass and Coal". In: *Energies* 17.11 (2024), p. 2735. doi

[185] ISO 14934-3. *Calibration and use of Heat Flux Meters Part 3: Secondary Calibration Method.* 2012-05.

[186] R. Gardon. "An Instrument for the Direct Measurement of Intense Thermal Radiation". In: *Review of Scientific Instruments* 24.5 (1952), pp. 366–370. doi

[187] T. Fu, A. Zong, Y. Zhang, and H. S. Wang. "A Method to Measure Heat Flux in Convection Using Gardon Gauge". In: *Applied Thermal Engineering* 108 (2016), pp. 1357–1361. doi

[188] L. Li, J. Wang, and X. Fan. "Development of Integrated High Temperature Sensor for Simultaneous Measurement of Wall Heat Flux and Temperature". In: *Review of Scientific Instruments* 83.7 (2012), p. 074901. 🔘

[189] M. Busch, G. Eyb, and J. Messner. *Messtechnik an Maschinen und Anlagen*. Lecture script. Universität Stuttgart, Institut für Thermische Strömungsmaschinen und Maschinenlaboratorium, 2012.

[190] W. Rüdiger, C. Rathke, M. Ohland, and M. Crevatin. *High-Technology Workhorse: Advancing Contemporary Modular Gas Analyzer Technology With the Uras26 Photometer*. ABB Ltd., Zürich, Schweiz, 2008.

[191] M. Helbig. "Experimentelle Untersuchung des Langzeitverhaltens des Carbonate-Looping-Verfahrens im Megawatt-Technikum". PhD thesis. Technischen Universität Darmstadt, 2019.

[192] Open Grid Europe (OGE). *E-Netz Südhessen*. https://www.e-netz-suedhessen.de/. ⬈ (Accessed: 2024-04-09).

[193] D. W. van Krevelen and J. Schuyer. *Coal Science*. Elsevier publishing company, 1957.

[194] G. Trif-Tordai and I. Ionel. "Waste Biomass as Alternative Bio-Fuel – Co-Firing versus Direct Combustion". In: *Alternative Fuel*. Ed. by M. Manzanera. Rijeka, Croatia: IntechOpen, 2011. Chap. 12. 🔘

[195] H. Stadler et al. "Experimental Investigation of NO_x Emissions in Oxycoal Combustion". In: *Fuel* 90.4 (2011), pp. 1604–1611. 🔘

[196] F. Carrasco, S. Grathwohl, J. Maier, J. Ruppert, and G. Scheffknecht. "Experimental Investigations of Oxyfuel Burner for Cement Production Application". In: *Fuel* 236 (2019), pp. 608–614. 🔘

[197] P. Steffens et al. "LES of a Swirl-Stabilized $40\,kW_{th}$ Biomass Flame and Comparison to a Coal Flame". In: *Fuel* 372 (2024), p. 132098. 🔘

[198] S. R. Turns. *An Introduction to Combustion: Concepts and Applications*. 2nd ed. New York: McGraw-Hill Series in Mechanical Engineering, 2000.

[199] I. Glassman and R. A. Yetter. *Combustion*. 4th ed. London: Elsevier, 2008.

[200] P. Debiagi, C. Yildiz, M. Richter, J. Ströhle, B. Epple, T. Faravelli, and C. Hasse. "Experimental and Modeling Assessment of Sulfur Release From Coal Under Low and High Heating Rates". In: *Proceedings of the Combustion Institute* 38.3 (2021), pp. 4053–4061. 🔘

[201] A. Becker, M. Schiemann, S. Heuer, N. Vorobiev, V. Scherer, D. Haxter, and J. Mayer. "A Standardized Method for the Characterization of Coal Ignition Under Oxyfuel Conditions". In: *Pittsburgh Coal Conference*. Vol. 32. Pittsburgh, USA, Oct. 2015. 🔘

[202] J. Liu, Z. Liu, S. Chen, S. O. Santos, and C. Zheng. "A Numerical Investigation on Flame Stability of Oxy-Coal Combustion: Effects of Blockage Ratio, Swirl number, Recycle Ratio and Partial Pressure Ratio of Oxygen". In: *International journal of Greenhouse Gas Control* 57 (2017), pp. 63–72. 🔗

[203] M. Habermehl, J. Hees, A. Maßmeyer, D. Zabrodiec, O. Hatzfeld, and R. Kneer. "Comparison of Flame Stability Under Air and Oxy-Fuel Conditions for an Aerodynamically Stabilized Pulverized Coal Swirl Flame". In: *Journal of Energy Resources Technology* 138.4 (Mar. 2016), p. 042209. 🔗

[204] O. B. Ramadan, C. S. Lam, P. M. Hughes, P. Gogolek, and J. Wong. "Radiant Flux Measurements in the Pilot-Scale IFRF-NFA Burner Operating in a High CO_2 Environment at Different Swirl Settings". In: *CanmetENERGY, Natural Resources.* Ottawa, Canada, 2012.

[205] R. Corrêa da Silva and H. J. Krautz. "Experimental Studies on Heat Transfer of Oxy-Coal Combustion in a Large-Scale Laboratory Furnace". In: *Applied Thermal Engineering* 82 (2015), pp. 82–97. 🔗

[206] J. P. Smart, R. Patel, and G. S. Riley. "Oxy-Fuel Combustion of Coal and Biomass, the Effect on Radiative and Convective Heat Transfer and Burnout". In: *Combustion and Flame* 157.12 (2010), pp. 2230–2240. 🔗

[207] *Description and Operating Instructions Medtherm H-201 Heat Flux Meter, Model E.* Medtherm Corporation. Alabama, USA, 1987.

[208] C. K. Westbrook and F. L. Dryer. "Simplified Reaction Mechanisms for the Oxidation of Hydrocarbon Fuels in Flames". In: *Combustion Science and Technology* 27.1-2 (1981), pp. 31–43. 🔗

[209] J. Andersen, C. L. Rasmussen, T. Giselsson, and P. Glarborg. "Global Combustion Mechanisms for Use in CFD Modeling under Oxy-Fuel Conditions". In: *Energy & Fuels* 23.3 (2009), pp. 1379–1389. 🔗

[210] G. A. Clements, R. Porter, A. Pranzitelli, and M. Pourkashanian. "Evaluation of FSK Models for Radiative Heat Transfer Under Oxyfuel Conditions". In: *Journal of Quantitative Spectroscopy and Radiative Transfer* 151 (2015), pp. 67–75. 🔗

[211] N. F. Reith. "Flow Field Simulation of a Semi-Industrial Oxyfuel Swirl Burner using a Detailed Geometry Model". MA thesis. Institute for Energy Systems and Technology, Technische Universität Darmstadt, 2023.

A Additional Numerical Results

A.1 Results of the P_1 Model

Fig. A.1 – A.4 show the results for the P_1 radiation model (dashed lines) using the FSCK and WSGG gas absorption models applied to the test cases in Chapter 3. The WSGG models use the parameters of Kangwanpongpan et al. [74] and Bordbar et al. [73]. For comparison, the results of the FVM radiation model are shown in addition (solid lines).

Fig. A.1 Radiative source term plotted against the central axis of the geometry. Results of the FVM compared to the results of the P_1 model using FSCK and WSGG absorption models. The test case of Kez and co-workers is used for comparison [62].

Fig. A.2 Total radiative wall heat flux plotted against the central axis on the wall of the geometry. Results of the FVM compared to the results of the P_1 model using FSCK and WSGG absorption models. The test case of Kez and co-workers is used for comparison [62].

Fig. A.3 Radiative source term plotted against the central axis of the geometry. Results of the FVM compared to the results of the P_1 model using FSCK and WSGG absorption models. The test case of Porter and co-workers is used for comparison [104].
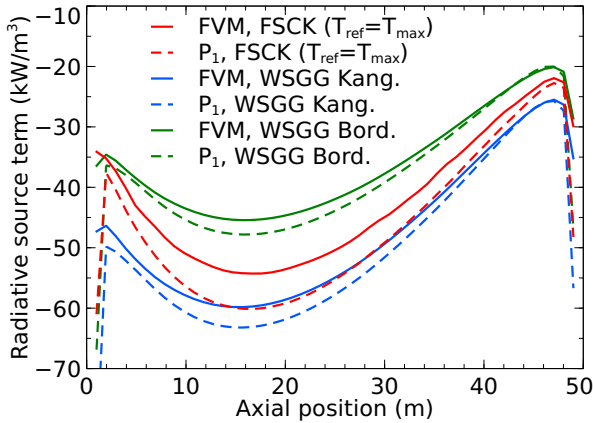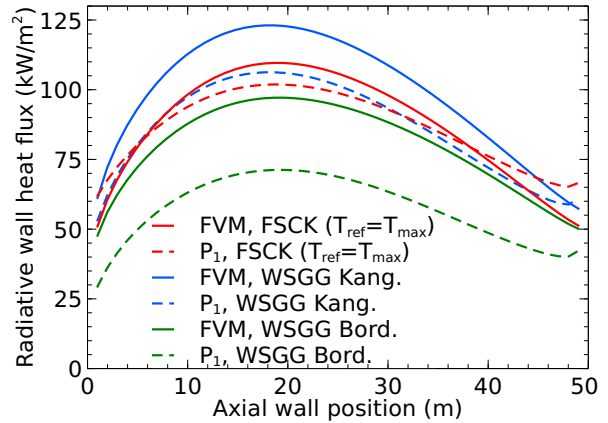

Fig. A.4 Total radiative wall heat flux plotted against the central axis on the wall of the geometry. Results of the FVM compared to the results of the P_1 model using FSCK and WSGG absorption models. The test case of Porter and co-workers is used for comparison [104].
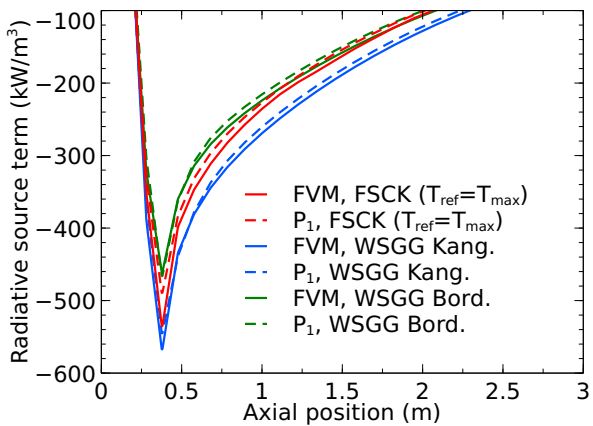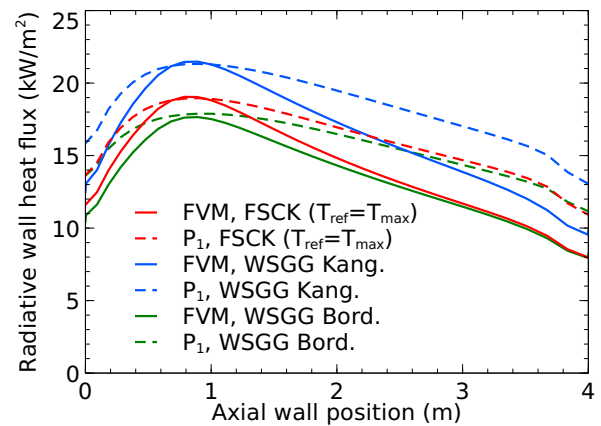
A.2   Results of the Mesh Study

The objective of the mesh study is to investigate the accuracy with regard to the computational effort. The solution is fully converged at 3000 iterations for all three meshes. Boundary conditions, listed in Tab. A.1, with an O_2 to CO_2 ratio of 21/79 are representative of oxyfuel combustion at a thermal load of 500 kW with RBK. For reasons of complexity, only simulations without particles, natural gas and combustion are carried out for the mesh study. Since the Lagrangian calculation of the particles, radiation and chemical reactions need a significantly higher computation time [211].

Tab. A.1 Boundary conditions for the mesh study [211].

Primary (swirled)	Solid fuel (carrier gas)	Cooling	Secondary (swirled)	Secondary (axial)	Tertiary nozzles
m^3/h	m^3/h	m^3/h	m^3/h	m^3/h	m^3/h
49.7	96.0	0	618.1	168.4	54.2

The number of elements for the three meshes, as well as their quality and computing time, is summarized in Tab. A.2.

Tab. A.2 Properties of the three numerical meshes for the EST combustion chamber [211].

	Number of elements	Type of element	Skewness	Orthogonal quality	Calculation time (h)
Mesh 1	7.3×10^6	Tetrahedral	0.20	0.80	87
Mesh 2	5.5×10^6	Hexahedral	0.14	0.93	50
Mesh 3	2.5×10^6	Hexahedral	0.17	0.91	18

All meshes are of sufficient quality for numerical simulation in terms of skewness and orthogonality. The computing time increases significantly as the number of cells increases, as can be seen in the table. In Fig. A.5, the axial velocities of the three meshes are plotted against the radius of the combustion chamber. In the left diagram, at an axial height of 0.425 m, which corresponds to the end of the qural, slight differences in velocity in the range of -0.3 to 0.3 m are visible for the three meshes. The IRZ can also be recognized from the curves, which show a reverse flow in the center by negative axial velocities and transition to positive values as the radius increases. In the right diagram, at an axial height of 1.425 m, which corresponds to an axial distance of 1 m to the end of the quarl, hardly any differences can be recognized between the three meshes. It is recognizable how the IRZ approaches 0 m/s in the center and marks the region where the IRZ ends [211]. Fig. A.6 shows the axial velocities, at the center axis, of the different meshes, plotted against the reciprocal number of mesh elements. The regression line through the three points is intended to show the exact solution for an infinite number of elements ($1/N = 0$) according to Richardson's approximation method [21].
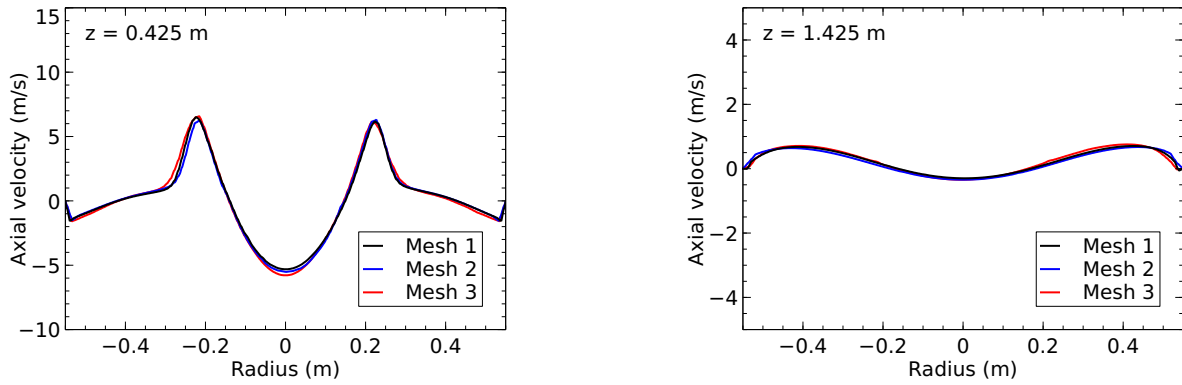
Fig. A.5 Comparison of the axial velocities of the three different meshes. Left: axial height of 0.425 m (end of the quarl). Right: axial height of 1.425 m (1 m axial distance to the end of the quarl). Velocities plotted against the combustion chamber radius [211].
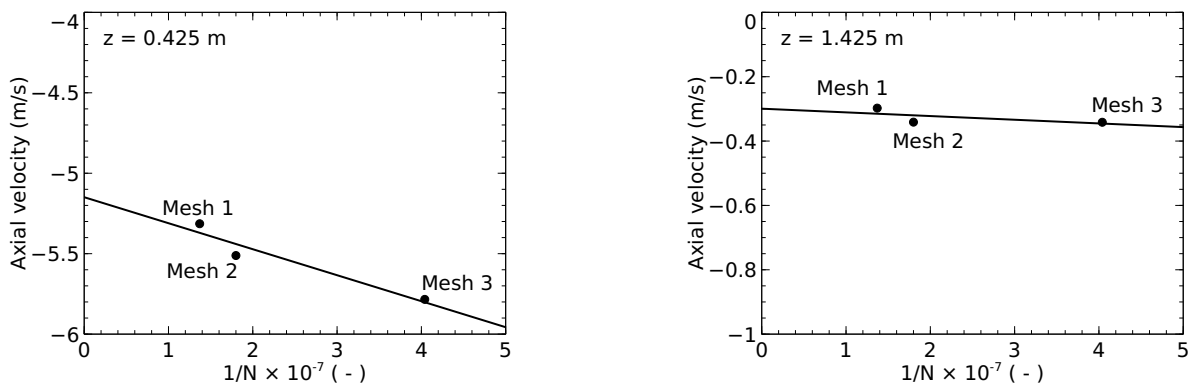
Fig. A.6 Richardson-extrapolation for the axial velocity at the center line plotted against the inverse number of numerical cells. Left: axial height of 0.425 m (end of the quarl). Right: axial height of 1.425 m (1 m axial distance to the end of the quarl).

At an axial position of 0.425 m, the difference between a theoretically exact solution and the coarsest mesh is 0.65 m/s. At a position of 1.425 m, the difference is even less than 0.05 m/s. Since the errors for all meshes using the Richardson approach are small, Mesh 3 with the lowest computational effort is used.

A.3   Comparison of Turbulence Models

Fig. A.7 and Fig. A.8 show the comparison of the turbulence models Standard k–ϵ and SST k–ω for the axial and tangential velocity along the combustion chamber radius at two different heights. The results presented relate to the conditions in Tab. A.1. While the results of the turbulence models differ slightly at the edges of the IRZ, the results in the center are almost identical. Due to the minor differences, the Standard k–ϵ model is used for the sake of simplicity [211].

Fig. A.9 shows a screenshot of the residuals plotted against the iteration steps, and the temperature at different axial positions in the combustion chamber plotted against the iteration steps for the RNG k–ϵ model (monitor points).
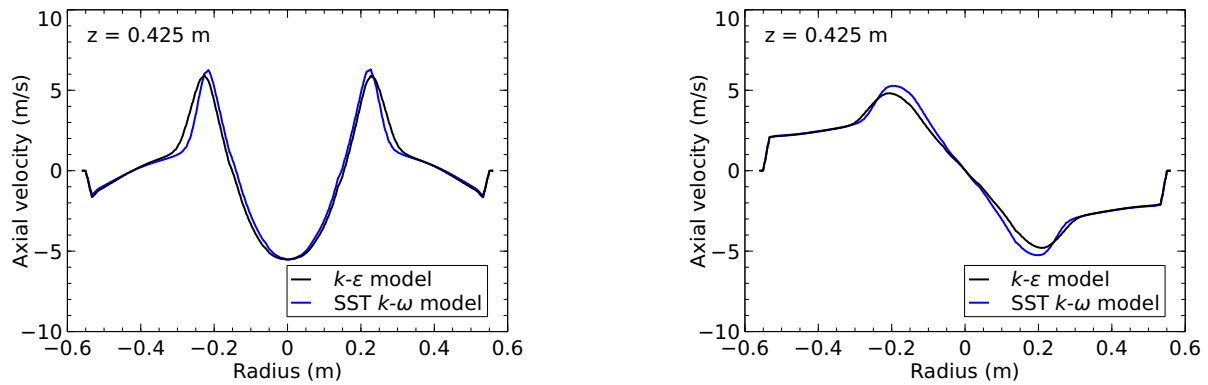
Fig. A.7 Left: results for the axial velocity of the Standard k–ϵ (black) and SST k–ω (blue) turbulence model at a height of 0.425 m plotted against the combustion chamber radius. Right: results for the tangential velocity [211].
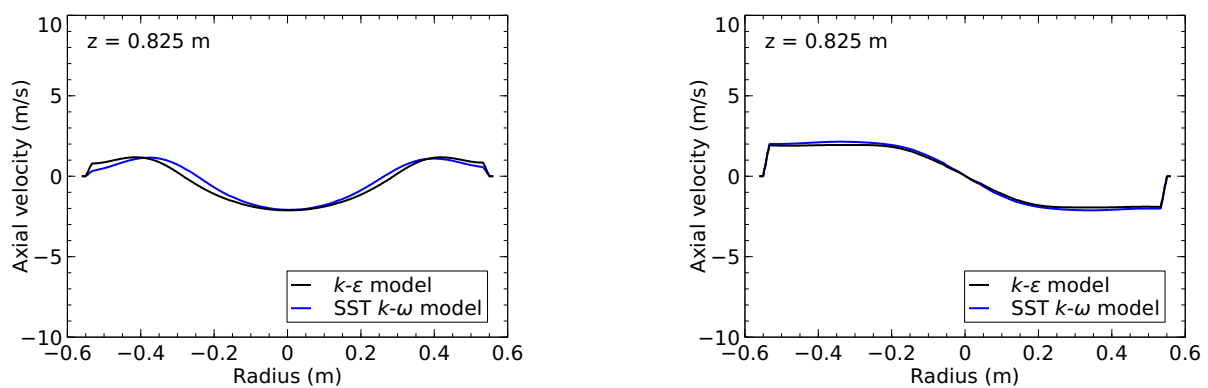
Fig. A.8 Left: results for the axial velocity of the Standard k–ϵ (black) and SST k–ω (blue) turbulence model at a height of 0.825 m plotted against the combustion chamber radius. Right: results for the tangential velocity [211].
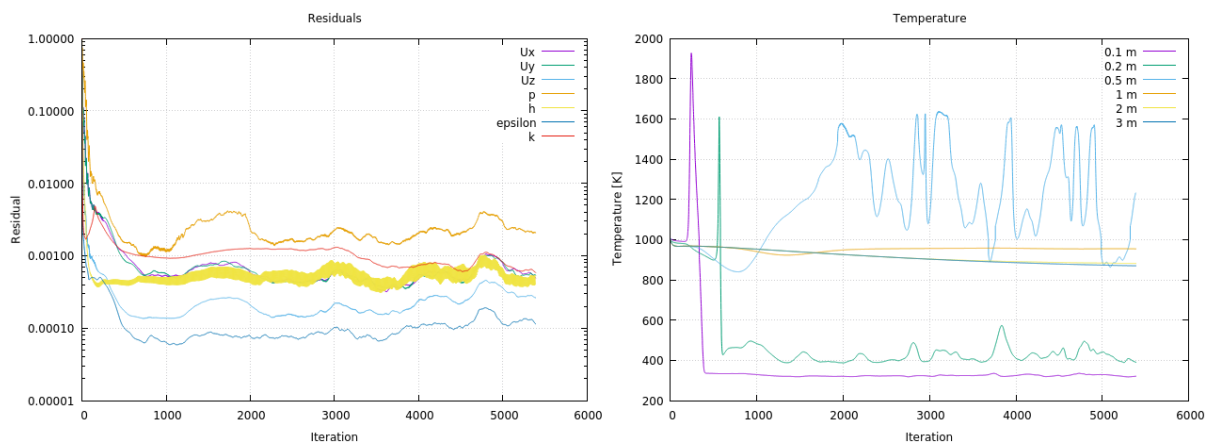
Fig. A.9 Screenshot of the residuals and temperature monitor points plotted against the iteration steps while using the RNG k–ϵ model.

The screenshot was taken during the simulation from Chapter 8 using the RNG k–ϵ model. Both the residuals and the monitor points of the temperature show significant instabilities, which caused the simulation to collapse. Instabilities also occurred for the Realizable k–ϵ model during the simulations. Consequently, these turbulence models were not used further in this work.

B Model Parameters

B.1 Weighted Sum of Gray Gases Parameters

Tab. B.1 shows the parameters according to Kanwangpongpan et al. [74] and Bordbar et al. [73] for the WSGG model in Chapter 3.

Tab. B.1 WSGG model parameters according to Kanwangpongpan et al. [74] and Bordbar et al. [73].

i		Kanwangpongpan et al. [74]			Bordbar et al. [73]				
i		$CK1_i$	$CK2_i$	$CK3_i$	$CK1_i$	$CK2_i$	$CK3_i$	$CK4_i$	$CK5_i$
1		0.0429	0.0093	-0.0018	0.0340429	0.0652305	-0.0463685	0.0138684	-0.0014450
2		0.3647	0.0790	-0.0150	0.3509457	0.7465138	-0.5293090	0.1594423	-0.0166326
3		3.7144	0.2565	-0.0509	4.5707400	2.1680670	-1.4989010	0.4917165	-0.0542999
4		105.31	-39.265	6.0877	109.81690	-50.92359	23.432360	-5.1638920	0.4393889
i	j	$C1_{i,j}$	$C2_{i,j}$	$C3_{i,j}$	$C1_{i,j}$	$C2_{i,j}$	$C3_{i,j}$	$C4_{i,j}$	$C5_{i,j}$
1	1	0.3947	-0.1214	0.0243	0.7412956	-0.5244441	0.5822860	-0.2096994	0.0242031
1	2	-0.4512	1.1420	-0.2296	-0.9412652	0.2799577	-0.7672319	0.3204027	-0.0391017
1	3	0.1492	-5.2222	1.0115	0.8531866	0.0823075	0.5289430	-0.2468463	0.0310940
1	4	1.8824	9.1820	-1.7493	-0.3342806	0.1474987	-0.4160689	0.1697627	-0.0204066
1	5	-2.3284	-6.9298	1.3038	0.0431436	-0.0688622	0.1109773	-0.0420861	0.0049188
1	6	0.7698	1.9063	-0.3549	–	–	–	–	–
2	1	-0.4974	0.1092	-0.0179	0.1552073	-0.4862117	0.3668088	-0.1055508	0.0105857
2	2	6.8986	-2.3198	0.4077	0.6755648	1.4092710	-1.3834490	0.4575210	-0.0501976
2	3	-19.988	8.0021	-1.4482	-1.1253940	-0.5913199	0.9085441	-0.3334201	0.0384236
2	4	26.2080	-11.007	2.0311	0.6040543	-0.0553385	-0.1733014	0.0791608	-0.0098934
2	5	-16.440	7.1199	-1.3278	-0.1105453	0.0464663	-0.0016129	-0.0035398	0.0006121
2	6	3.9847	-1.7876	0.3349	–	–	–	–	–
3	1	0.3189	-0.0720	0.0158	0.2550242	0.3805403	-0.4249709	0.1429446	-0.0157408
3	2	-0.7222	1.0304	-0.2478	-0.6065428	0.3494024	0.1853509	-0.1013694	0.0130244
3	3	1.5053	-1.9350	0.5931	0.8123855	-1.1020090	0.4046178	-0.0811822	0.0062981
3	4	-1.8378	1.6332	-0.6619	-0.4532290	0.6784475	-0.3432603	0.0883088	-0.0084152
3	5	1.0337	-0.7798	0.3857	0.0869309	-0.1306996	0.0741446	-0.0202929	0.0020110
3	6	-0.2107	0.1782	-0.0933	–	–	–	–	–
4	1	0.1648	0.0329	-0.0095	-0.0345199	0.2656726	-0.1225365	0.0300151	-0.0028205
4	2	-0.6012	0.6942	-0.0687	0.4112046	-0.5728350	0.2924490	-0.0798076	0.0079966
4	3	2.0308	-3.0960	0.3691	-0.5055995	0.4579559	-0.2616436	0.0764841	-0.0079084
4	4	-3.4361	4.7494	-0.5919	0.2317509	-0.1656759	-0.1052608	-0.0321935	0.0033870
4	5	2.5803	-3.1714	0.4017	-0.0375491	0.0229520	0.0160047	0.0050463	-0.0005364
4	6	-0.7069	0.7869	-0.1003	–	–	–	–	–

B.2 Particle Drag Coefficient

The particle drag coefficient C_d (cf. Chapter 4, Eq. (4.17)) is determined by Eq. (B.1):

$$C_D = \begin{cases} \frac{24}{\mathrm{Re}_p}\left(1 + \frac{1}{6}\mathrm{Re}_p^{2/3}\right) & \mathrm{Re}_p \leq 1000 \\ 0.424 & \mathrm{Re}_p > 1000 \end{cases}. \tag{B.1}$$

C Operating Conditions

A volume flow of $100\,Nm^3/h$ for the solid fuel transport gas at a temperature of approx. 22 – 25 °C is used for all trials with pulverized solid fuel. In the case of oxyfuel combustion, the transport flow consists of 15 vol% oxygen and 85 vol% carbon dioxide at a temperature of approx. 15 – 20 °C.

C.1 Walnut Shells Combustion Parameters

Tab. C.1 Operating conditions of the WS parameter study in an air atmosphere.

	WSI	WSII	WSIII	WSIV	WSV
Thermal output (kW)	285	500	600	420	420
Fuel mass flow (kg/h)	61	112	132	88	88
Swirl number (−)	0.91	0.97	0.97	0.98	0.97
Global λ (−)	1.7	1.7	1.7	1.7	1.5
Local λ (−)	1.1	1.0	1.0	1.4	1.2
$\dot{V}_{sec}/\dot{V}_{tet}$ (−)	1.3	1.1	1.2	4.0	4.0
Axial flow (Nm^3/h)	42	45	53	47	41
Swirl flow (Nm^3/h)	199	376	461	441	378
Tertiary flow (Nm^3/h)	179	374	442	121	105
Temp. oxidant (°C)	32	32	33	34	35

Tab. C.2 Operating conditions at constant velocity for air and oxyfuel combustion of WS at different oxygen concentrations in the oxidant and secondary to tertiary flow ratios.

	WSAR*	WSAR**	WS27*	WS30*	WS33*	WS27**	WS30**	WS33**
Thermal output (kW)	500	410	570	590	615	460	470	500
Fuel mass flow (kg/h)	110	90	123	128	135	100	102	108
O_2 in Oxidant (vol%)	−	−	27	30	33	27	30	33
Recirc. Ratio (%)	−	−	81	79	77	81	79	77
Swirl number (−)	0.96	0.98	0.96	0.96	0.96	0.98	0.98	0.98
Global λ (−)	1.7	1.7	1.75	1.8	2.0	1.8	1.9	1.9
Local λ (−)	1.0	1.5	1.0	1.0	1.1	1.6	1.6	1.6
$\dot{V}_{sec}/\dot{V}_{tet}$ (−)	1.1	5.5	1.1	1.1	1.1	5.6	5.6	5.6
Axial flow (Nm^3/h)	48.7	50.3	45.7	46.1	52.0	48.7	48.4	48.5
Swirl flow (Nm^3/h)	364.1	470.9	352.2	344.6	365.9	462.6	456.2	458.7
Tertiary flow (Nm^3/h)	363.5	95.3	353.8	345.3	366.9	91.9	90.7	91.3
Temp. oxidant (°C)	32	31	72	63	56	81	81	79

*Low $\dot{V}_{sec}/\dot{V}_{tet}$ ratio.
**High $\dot{V}_{sec}/\dot{V}_{tet}$ ratio.

Tab. C.3 Operating conditions at constant 510 kW$_{th}$ for air and oxyfuel combustion of WS at different oxygen concentrations in the oxidant and secondary to tertiary flow ratios.

	WSAR[*]	WSAR[**]	WS33	WS30	WS30	WS27
Thermal output (kW)	510	510	510	510	510	510
Fuel mass flow (kg/h)	110	110	110	110	110	110
O$_2$ in Oxidant (vol%)	–	–	33	30	30	27
Recirc. Ratio (%)	–	–	77	79	79	81
Swirl number (–)	0.94	0.94	0.94	0.94	0.94	0.95
Global λ (–)	1.4	1.4	1.7	1.6	1.6	1.5
Local λ (–)	0.8	1.0	1.4	1.4	1.0	1.3
$\dot{V}_{sec}/\dot{V}_{tet}$ (–)	1.1	3.8	5.4	5.6	1.1	5.4
Axial flow (Nm^3/h)	58.2	79.0	69.8	73.3	46.7	73.0
Swirl flow (Nm^3/h)	348.0	486.4	423.9	453.1	281.7	454.9
Tertiary flow (Nm^3/h)	361.9	149.4	91.9	93.1	292.9	98.0
Temp. oxidant (°C)	41	48	57	72	62	81

[*]Low $\dot{V}_{sec}/\dot{V}_{tet}$ ratio.
[**]High $\dot{V}_{sec}/\dot{V}_{tet}$ ratio.

C.2 Rhenish Lignite Combustion Parameters

Tab. C.4 Operating conditions for air and oxyfuel combustion of RBK at different oxygen concentrations in the oxidant and secondary to tertiary flow ratios.

	RBKAR	RBK21	RBK25	RBK26	RBK30
Thermal output (kW)	510	540	540	540	510
Fuel mass flow (kg/h)	96	102	102	102	96
O$_2$ in Oxidant (vol%)	–	21	25	26	30
Recirc. Ratio (%)	–	85	84	83	80
Swirl number (–)	0.94	0.94	0.93	0.95	0.95
Global λ (–)	1.4	1.4	1.6	1.5	1.6
Local λ (–)	1.2	0.9	1.1	1.3	1.3
$\dot{V}_{sec}/\dot{V}_{tet}$ (–)	3.7	1.8	1.8	4.1	4.1
Axial flow (Nm^3/h)	83.7	70.6	78.4	69.8	67.6
Swirl flow (Nm^3/h)	481.3	431.3	417.4	472.6	430.3
Tertiary flow (Nm^3/h)	151.2	273.1	264.8	132.9	122.4
Temp. oxidant (°C)	43	74.5	55.4	61.5	76.9

C.3 Beech Wood Combustion Parameters

Tab. C.5 Operating conditions for oxyfuel combustion of BW at different combustion parameters.

	BW670	BW520	BW400	BW330
Thermal output (kW)	670	520	400	330
Fuel mass flow (kg/h)	135	102	77	60
O_2 in Oxidant (vol%)	35	27	35	32
Recirc. Ratio (%)	75	84	78	79
Swirl number (−)	0.94	0.94	0.92	0.86
Global λ (−)	1.7	1.6	2.0	2.1
Local λ (−)	1.4	1.3	1.7	1.8
$\dot{V}_{sec}/\dot{V}_{tet}$ (−)	4.0	4.0	4.4	4.4
Axial flow (Nm³/h)	65.1	57.2	56.7	57.9
Swirl flow (Nm³/h)	367.8	331.6	266.4	218.2
Tertiary flow (Nm³/h)	110.9	94.6	72.2	62.2
Temp. oxidant (°C)	52	52	52	51

C.4 Natural Gas Combustion Parameters

Tab. C.6 Operating conditions for air and oxyfuel combustion of natural gas at different combustion parameters.

	NGAR[*]	NGAR[**]	NG28	NG29	NG31
Thermal output (kW)	310	310	310	310	310
Fuel volume flow (Nm³/h)	30	30	30	30	30
O_2 in Oxidant (vol%)	−	−	28	29	31
Recirc. Ratio (%)	−	−	78	77	75
Swirl number (−)	0.96	0	0.93	0.93	0.93
Global λ (−)	1.4	1.4	1.4	1.4	1.4
Local λ (−)	1.3	1.3	1.3	1.3	1.3
$\dot{V}_{sec}/\dot{V}_{tet}$ (−)	9.5	9.5	9.5	9.5	9.5
Axial flow (Nm³/h)	47.4	354.6	45.0	43.6	42.9
Swirl flow (Nm³/h)	354.2	48.1	240.3	237.1	228.5
Tertiary flow (Nm³/h)	41.1	42.0	29.3	29.6	29.6
Temp. oxidant (°C)	30	25	51	51	50

[*]High swirl number.
[**]No swirl.